JAEA-Conf 2017-001
INDC(JPN)-203
DOI:10.11484/jaea-conf-2017-001

Proceedings of the 2016 Symposium on Nuclear Data

November 17-18, 2016,

High Energy Accelerator Research Organization,

Tsukuba, Ibaraki, Japan

(Eds.) Toshiya SANAMI, Katsuhisa NISHIO, Masayuki HAGIWARA, Hiroshi IWASE
Satoshi KUNIEDA and Shoji NAKAMURA

Nuclear Science and Engineering Center
Sector of Nuclear Science Research

January 2018
Japan Atomic Energy Agency
日本原子力研究開発機構

JAEA-Conf

国立研究開発法人日本原子力研究開発機構 研究連携成果展開部 研究成果管理課
〒319-1195 茨城県那珂郡東海村大字白方 2 番地4
電話 029-282-6387, Fax 029-282-5920, E-mail:ird-support@jaea.go.jp

Institutional Repository Section,
Intellectual Resources Management and R&D Collaboration Department,
Japan Atomic Energy Agency.
2-4 Shirakata, Tokai-mura, Naka-gun, Ibaraki-ken 319-1195 Japan
Tel +81-29-282-6387, Fax +81-29-282-5920, E-mail:ird-support@jaea.go.jp

JAEA-Conf 2017-001
INDC(JPN)-203

Proceedings of the 2016 Symposium on Nuclear Data
November 17-18, 2016,
High Energy Accelerator Research Organization,
Tsukuba, Ibaraki, Japan

(Eds.) Toshiya SANAMI*, Katsuhisa NISHIO+, Masayuki HAGIWARA*,
Hiroshi IWASE*, Satoshi KUNIEDA and Shoji NAKAMURA

Nuclear Science and Engineering Center, Sector of Nuclear Science Research
Japan Atomic Energy Agency
Tokai-mura, Naka-gun, Ibaraki-ken

（Received October, 18）

The 2016 Symposium on Nuclear Data was held at Kobayashi Hall of High Energy Accelerator Research Organization, on November 17 and 18, 2016. The symposium was organized by the Nuclear Data Division of the Atomic Energy Society of Japan in cooperation with Radiation Science Center, High Energy Accelerator Research Organization, Nuclear Science and Engineering Center of Japan Atomic Energy Agency and North Kanto Branch of Atomic Energy Society of Japan. In the symposium, there were one tutorial, “Historical Evolution of Accelerators” and four oral sessions, “Overview of the ImPACT Program - Reduction and Resource Recycling of High Level Wastes through Nuclear Transmutation”, “Facilities and experiments for nuclear data in Japan”, “Nuclear data from measurement to application”, and “Progress of neutron nuclear data measurement and research for its basics and application”. In addition, recent research progress on experiments, evaluation, benchmark and application was presented in the poster session. Among 65 participants, all presentations and following discussions were very active and fruitful. This report consists of total 38 papers including 15 oral and 23 poster presentations.

Keywords: Nuclear Data Symposium 2016, Experiments, Nuclear Theory, Nuclear Data Evaluation, Benchmark Test, Nuclear Data Applications, ImPACT

+ Advanced Science Research Center
* High Energy Accelerator Research Organization

Organizers: T. Sanami (KEK, Chair), K. Nishio (JAEA, Vice-Chair), M. Hagiwara (KEK), H. Iwase (KEK), O. Iwamoto (JAEA), M. Aikawa (Hokkaido U.), N. Yamano (Fukui U.), J. Hori (Kyoto U.), I. Murata (Osaka U.), K. Nakajima (Kyoto U.), T. Hazama (JAEA), S. Kunieda (JAEA), H. Koura (JAEA), S. Chiba (Tokyo Tech.), S. Nakamura (JAEA), K. Kino (AIST)

JAEA-Conf 2017-001
INDC(JPN)-203

2016年度核データ研究会報告集

2016年11月17日～18日

高エネルギー加速器研究機構　つくばキャンパス

共通基盤研究施設　放射線科学センター　茨城県つくば市

日本原子力研究開発機構　原子力科学研究部門　原子力基礎工学研究センター

(編) 佐波　俊哉*、西尾　勝久+、萩原　雅之*、岩瀬　広*、國枝　賢、中村　詔司

（2017年10月18日受理）

2016年度核データ研究会は、2016年11月17日ー18日に、茨城県つくば市の高エネルギー加速器研究機構にて開催された。本研究会は、日本原子力学会核データ部会が主催、高エネルギー加速器研究機構、日本原子力研究開発機構原子力基礎工学研究センターと日本原子力学会北関東支部が共催した。今回、チュートリアルとして「加速器の進化」を、講演・議論のセッションとして「ImPACTプログラム　核変換による高レベル放射性廃棄物の大幅な減容・資源化の概要」、「核データ測定を行う施設と実験」、「核データの測定から応用まで」、「中性子核データの測定と基礎・利用研究の進展」の4件を企画し実施した。さらに、ポスターセッションでは、実験、評価、ベンチマーク、応用など、幅広い研究内容について発表が行われた。参加者総数は65名で、それぞれの口頭発表及びポスター発表では活発な質疑応答が行われた。本報告集は、本研究会における口頭発表15件、ポスター発表23件の論文をまとめている。

キーワード: 2016年度核データ研究会、実験、核理論、核データ評価、ベンチマークテスト、核データ応用、ImPACT

＋　先端基礎研究センター

＊　高エネルギー加速器研究機構

2016 年核データ研究会実行委員会：佐波俊哉（委員長、KEK）、西尾勝久（副委員長、原子力機構）、萩原雅之（現地委員、KEK）、岩瀬　広（現地委員、KEK）、岩本　修（原子力機構）、合川正幸（北大）、山野直樹（福井大）、堀　順一（京大）、村田　勲（阪大）、中島　健（京大）、羽様　平（原子力機構）、國枝　賢（原子力機構）、小浦寛之（原子力機構）、千葉　敏（東工大）、中村詔司（原子力機構）、木野幸一（産総研）

Contents

Papers presented at Oral sessions

Papers presented at Poster session

目 次

口頭発表論文

ポスター発表論文

1 Program of 2016 Symposium on Nuclear Data

Date : November 17(Thu)13:00 – 18(Fri), 2016
Venue :KEK Tsukuba Campus, Kobayashi Hall
Host : Nuclear Data Division, Atomic Energy Society of Japan
High Energy Accelerator Research Organization
Co-host : Nuclear Science and Engineering Center of JAEA
North Kanto Branch of Atomic Energy Society of Japan

November 17 (Thu), at Kobayashi Hall

13:00 – 13:10 Opening Address T. Sanami (KEK)

13:10 – 15:10
Session 1 : "Nuclear data measurement and simulation for LLFP nuclear transmutation"

【Chair: Y. Watanabe (Kyushu Univ.)】

1-1. Reduction and Resource Recycling of High Level Wastes through Nuclear Transmutation - Overview of the ImPACT Program - [30] R.Fujita (JST)
1-2. Reaction cross section measurement for the transmutation of Long-Lived Fission Products at RIBF [30] H.Otsu (RIKEN)
1-3. Simulation Study of Transmutation Processes of Long-lived FPs [30] K. Niita (RIST)
1-4. Research on Neutron Capture Cross Sections at J-PARC in ImPACT Project [30] S.Nakamura (JAEA)

15:10-15:20 Coffee Break [10]

15:30-17:30 Poster Session (Venue: Kobayashi hall lounge)

18:00-20:00 Convivial Gathering (Venue : KEK Shokuin Kaikan)

November 18 (Fri), at Kobayashi Hall

9:00 – 10:40

Session 2 : "Facilities and experiments for nuclear data in Japan" 【Chair: M.Hagiwara (KEK)】

2-1. Current Status of Nuclear Data Measurement at the KURRI-LINAC [25] J.Hori (Kyoto Univ.)
2-2. Nuclear Data Measurement at the JAEA Tandem Facility[25] K.Nishio (JAEA)
2-3. Nuclear Data Measurements at Center for Accelerator and Beam Applied Science, Kyushu University [25] N.Shigyo (Kyushu Univ.)
2-4. Research Activities with Neutron Beams at RCNP [25] T.Shima (RCNP)

10:40-11:00 Coffee Break

11:00-12:00 【Chair: H.Iwase (KEK)】

Tutorial : “Historical Evolution of Accelerators” [60] K.Takayama (KEK/Sokendai)

12:00-12:10 Photo [10]

13:00-14:30

Session 3 : “Nuclear data from measurement to application” 【Chair: N.Shigyo (Kyushu Univ.)】

3-1. Current Status of Pulsed Spallation Neutron Source of J-PARC [25] H.Takada (JAEA)
3-2. Current Status of carbon-ion radiotherapy in Japan [25] N.Matsufuji (NIRS)
3-3. High-energy neutron measurement and radiation experiment of particularity [40] K.Ishibashi (Kyushu Univ.)

14:30-14:40 Coffee Break

14:40-16:10
Session 4 : “Progress on neutron nuclear data measurement and research for its basics and Application” 【Chair: J.Hori (Kyoto Univ.)】

4-1. Space Nuclear Power and Nuclear data -Radioisotope Power Generator and Space Nuclear Reactor- [25] J.Nishiyama (Tokyo Tech.)
4-2. Fundamental and Applied Sciences Explored by Neutrons [25] Y.Nagai (QST)
4-3. Study on Neutron Capture Reaction using Pelletron and ANNRI [40] M.Igashira (Tokyo Tech.)

16:00 -16:10 Poster Award Nuclear Data Division, AESJ

16:10 -16:20 Closing Address K.Nishio (JAEA)

16:20 - 17:20 Facility Tour (KEK Accelerator test facility)

Poster Presentations

Date : November 17(Thu), 15:30-16:30

1. Sensitivity and Uncertainty Analysis of Fusion Neutronics Benchmark Problem with Deterministic Code System CBZ G.Chiba (Hokkaido Univ.)
2. Theoretical model analysis of composite-particle emission from deuteron-induced reactions S.Nakayama (JAEA)
3. Dynamical calculation for fission process of actinoid nuclei N.L.B.Anuar (Kindai Univ.)
4. Evaluation of neutron resonance parameters for Zr isotopes A.Ichihara (JAEA)
5. Evaluation of nuclear structure data with probable spin values for ^{124}Cd and ^{124}In in 124 mass chain W.T.L.S. Fernando (JAEA)
6. FENDL-3.1b test C.Konno (JAEA)
7. ENDF/B-VIIIβ2 benchmark test with shielding experiments at QST/TIARA S. Kwon (QST)
8. Production cross sections of ^{52}Fe isotopes in alpha particle induced reactions on ^{nat}Cr N. Ukon (Hokkaido Univ.)
9. Theoretical model analysis of (d,xn) reactions on ^{7}Li at 25, 40, and 102 MeV H. Sadamatsu (Kyushu Univ.)
10. Optimization of experimental system design for benchmarking of large angle scattering reaction cross section at 14MeV using two shadow bars N.Hayashi (Osaka Univ.)
11. Verification and Estimation of Thermal Neutron Capture Cross Section of ^{102}Ru A. Terashima (Tokyo Tech.)
12. Activation cross sections of alpha-induced reactions on natural zinc for ^{68}Ge production M. Aikawa (Hokkaido Univ.)
13. Development of an artificial neural network code for unfolding neutron spectra measured by multiple foils activation method Y.Sanzen (Kyushu Univ.)
14. Resonance analysis of cross section data measured by J-PARC/MLF using the modified REFIT code K.Mizuyama (JAEA)
15. Measurement and simulation of the neutron capture reaction using NaCl samples Kaoru Y. Hara(Hokkaido Univ.)
16. Dependence of activation products for decommissioning on fission neutron spectra H. Jojima (Tokyo Tech.)
17. Measurement of Double Differential Cross Section for Evaporated Charged Particles from Proton-Induced Reactions Y. Yamaguchi (Kyushu Univ.)
18. Consistency check of experimental data using evaluated photonuclear data N. Iwamoto (JAEA)
19. Gamma strength function of Ca-40 below the particle threshold for medical physics applications A. Makinaga (Hokkaido Univ./ JEIN Inst.)
20. Measurement of the neutron capture cross-section of ^{133}Cs as a part of the ImPACT project Brian Hales (JAEA)
21. Improvement of gross theory of beta-decay on single particle treatment H. Koura (JAEA)
22. Nondestructive Determination of Water Content in Concrete by Foil Activation Method Y. Nishiyama (Osaka Univ.)
23. Measurement of residual activities induced in copper by 148 MeV carbons H.Yashima (Kyoto Univ.)

This is a blank page.

2 Reduction and Resource Recycling of High Level Wastes through Nuclear Transmutation

- Overview of the ImPACT Program -

Reiko FUJITA
ImPACT Program, Japan Science and Technology Agency
e-mail: reiko.fujita@jst.go.jp

The high-level radioactive wastes (HLW) contain Minor actinides (MAs) and long-lived fission products (LLFPs). The aim of this program is to propose a new transmutation path for LLFPs without isotope separation and a reuse path.

This work was funded by ImPACT Program of Council for Science, Technology and Innovation (Cabinet Office, Government of Japan).

Keywords: ImPACT, Transmutation, LLFPs, HLW, RIBF, J-PARC, PHITS

1. Introduction

Cabinet office, Government of Japan has adopted 12 Program Managers (PMs) who will be producers in a different way from the usual researchers in order to encourage challenging R&D as Impulsing PAradigm Change through disruptive Technologies (ImPACT). "Reduction and Resource Recycling High-level Radioactive Waste through Nuclear Transmutation" program [1] was chosen for one of solutions on the issues in disposal sites for High level radioactive wastes (HLW). Partitioning and Transmutation technique (P&T) using reactors has been developed since 1980's in Japan. The project of P&T was named "Omega Project [2]" Self-Consistent Nuclear Energy System (SCNES) has been studied based on the isotope separation technique for LLFPs [3]. The aim of this program is to propose a new transmutation path for LLFPs without isotope separation process. The transmutation technique of MAs has been already started developing by Japan Atomic Energy Agency (JAEA) [4]. Recovery techniques of LLFPs from high-level liquid waste (HLLW) in a spent fuel reprocessing plant have been developed. The recovered LLFPs from HLLW still contain radioactive nuclides and are difficult to reuse. The other aim of this program is to propose a reuse path for LLFPs. This paper outlines "Reduction and Resource Recycling High-level Radioactive Waste through Nuclear Transmutation" program.

2. Overview of this program

The concept of "Reduction and Resource Recycling High Level Radioactive Waste through Nuclear Transmutation" program is shown in **Fig.1**. The goal is to be the first in the world to obtain nuclear reaction path for conversion to short- lived nuclides without isotope separation.

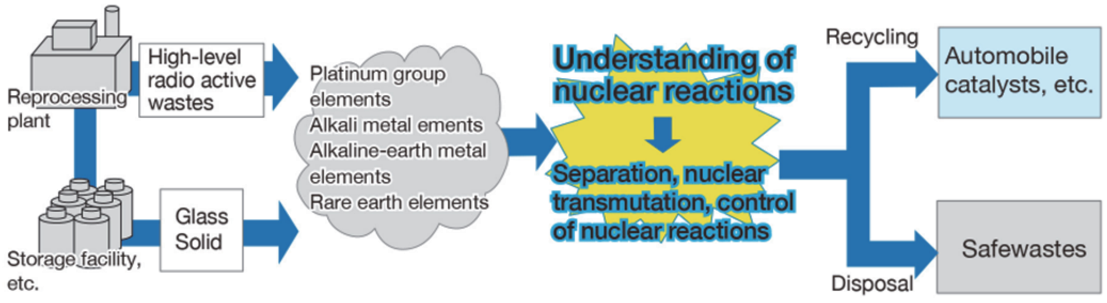

Figure 1 The concept of this program

LLFPs are recovered from high-level radioactive wastes in a spent fuel reprocessing plant and glass solids in storage facility. Recovered LLFPs are transmuted by new nuclear reaction paths and converted to short-lived nuclides or stable ones. The short-lived nuclides or stable one is used for resource materials, for example automobile catalysts.

This program has 5 projects, separation and recovery process from HLW in Project 1, new data measurements of nuclear reactions in Project 2, theoretical model and simulation code for nuclear reactions in Project 3, control method of nuclear reactions and accelerator developments in Project 4 and a proposal for conceptual plant design of LLFP recovery in HLW through transmutation process to ingot fabrication in Project 5.

3. Target LLFPs

Four target LLFPs were chosen in **Table 1**. Cesium-135 and Selenium-79 are contributed to safety and security of disposal with converting from HLW to Transuranium (TRU) wastes, namely Intermediate level radioactive wastes (ILW) or low level radioactive wastes.

Table 1 LLFPs targets

Nuclides	Half-life	Disposal	Resource recycling
Cs(Cesium)-135	2.3million year	Disposal of Ba (Barium) transmuted from Cs-135	
Cs(Cesium)-137	30.1year		
Sr(Strontium)-90	28.5 year	Disposal of Rb (Rubidium) -85,87 and Sr-86,88 transmuted from Sr-90	
Pd(Palladium)-107	6.5million year		Reuse of stable Pd transmuted from Pd -107 for catalysts for vehicles
Sn(Tin)-126	0.23million year	Transmutation for stable nuclides of Sn(Tin) or Sb(Antimony)	
Zr(Zirconium) - 93	1.53 million year		Reuse of stable Zr transmuted from Zr-93 for Zircalloy cladding and Channel boxes
Se(Selenium)-79	0.30million year	Stable Se transmuted from Se-79	
Tc(Technetium) -99	0.21million year	Ru (Ruthenium) -110 transmuted from Tc-99	
I (Iodine) -129	15.70 million year	Xe (Xenon) -130 transmuted from I-129	

Palladium-107 is transmuted by (n,2n) reaction after even-odd separation with laser technique. Zirconium-93 is also transmuted by (n,2n) reaction after even-odd separation in same one. Transmuted Pd and Zr are possible to be used for resource materials.

In the recycling process for resource materials, the contamination by a small amount of radioactive nuclides is unavoidable. It is necessary to determine a safe level of contamination named the clearance level for recovered materials. The investigation of the lifecycle and environmental behavior of Zr and Pd is carried out to obtain the necessary data for establishing the clearance levels for ^{93}Zr and ^{107}Pd.

4. Current progress in Project 2 and 3

By means of inverse kinematics, spallation cross sections on the proton and deuteron and coulomb dissociation reactions were obtained at RIKEN Radioactive Isotope Beam Factory in Project 2. The experimental data are compared with PHITS of Project 3 calculation implementing primary cascade-like Reactions followed by evaporation processes.

Cesium-133 was measured by J-PARC in JAEA and analyzed in order to obtain the cross section data of ^{135}Cs in Project 2.

5. Conclusion

Some of candidates for new desirable transmutation path will be proposed for ^{107}Pd, ^{93}Zr and ^{79}Se. A conceptual design of the process will be shown from LLFPs recovery in HLW converted to Short-lived nuclides or stable nuclides through new transmutation reactions by accelerator.

References

[1] www8.cao.go.jp/cstp/sentan/about-kakushin.html

[2] http://www.mext.go.jp/b_menu/shingi/gijyutu/gijyutu2/070/gijiroku/1352357.htm

[3] Y. FUJII-E et al., “A Self-Consistent Nuclear Energy Supply System “, Int'l. Specialists' Mtg. on Potential of Small Nuclear Reactors for Future Clean and Safe Energy Sources, Tokyo, 23-25 October (1991).

[4] http://www.aec.go.jp/jicst/NC/senmon/bunri/houkokusho-090428.pdf

This is a blank page.

3 Reaction cross section measurement for the transmutation of Long-Lived Fission Products at RIBF

H. Otsu[1*], H. Wang[1], H. Sakurai[1], N. Chiga[1], S. Kawase[2], Y. Watanabe[2], S. Takeuchi[3],
T. Nakamura[3], RIBF-ImPACT Collaboration

1: RIKEN Nishina Center, 2-1, Japan,

2: Department of Advanced Energy Engineering Science, Kyushu University, Kasuga, Japan,

3: Department of Physics, Tokyo Institute of Technology, Japan.

*otsu@ribf.riken.jp

Spallation reactions and Coulomb dissociation reactions for the long-lived fission products (LLFP) have been investigated for the purpose of nuclear waste transmutation. By means of inverse kinematics, spallation cross sections on the proton and deuteron and Coulomb dissociation reactions were obtained at the RIKEN Radioactive Isotope Beam Factory. The experimental data are compared with the PHITS calculation implementing primary cascade-like reactions followed by evaporation processes. For spallation reaction studies, lower energy data were recently obtained. Future prospects are also discussed.

This work was partially supported by the ImPACT program of Council for Science, Technology and Innovation (Cabinet Office, Government of Japan) and the grant MEXT Nuclear System Research and Development Program.

***Keywords*: ImPACT, LLFPs, Spallation reaction, Coulomb dissociation reaction**

1. Introduction

Reduction in the quantity of high-level radioactive waste in the spent fuel is one of the major issues for the use of a nuclear power plant. Research and development into the reduction of radioactive waste using partitioning and transmutation technology has been performed over recent decades. The LLFP nuclei have large radiotoxicities and long lifetimes, and they can be produced continuously even in the accelerator driven systems and next-generation nuclear reactors. It is essential to find effective reactions for the LLFP transmutation. However, experimental reaction data are currently lacking.

Nuclear physics plays an essential role in addressing the treatment on LLFP, because the reliable reaction data and models are necessary for LLFP reactions. In order to accumulate data and clarify the possible LLFP transmutation path, we have measured the proton- and deuteron-induced spallation reactions for LLFPs by means of inverse kinematics. We also take data for Coulomb dissociation reaction using the same experimental techniques. Our study on ^{137}Cs and ^{90}Sr [1] is the first attempt in the history of nuclear physics to solve the problem of the LLFP transmutation and has triggered the reaction studies for other long-lived fission products.

2. Experiments

The inverse kinematics technique was adopted to measure the spallation reaction and Coulomb dissociation reaction of LLFP. Radioactive beams of LLFP were produced at in-flight separator BigRIPS at the RIKEN Radioactive Isotope Beam Factory and identified by event by event. For measurement of spallation reaction, hydrogen or deuterium targets were used. For Coulomb dissociation reaction, lead target was used. Carbon target measurement was also taken for nuclear part subtraction. This technique allows us to study systematically on the target dependence, to unambiguously identify the reaction products, and to avoid the difficulties associated with using a highly radioactive target. In order to study the energy dependence, the cross-section measurements for ^{107}Pd were performed at reaction energies around both 200 and 100 MeV/nucleon. Very recently, we also succeeded to obtain 50 MeV/nucleon data. An example of particle identification for both beams and reaction products is displayed in Fig. 1 for ^{107}Pd at 100 MeV/nucleon.

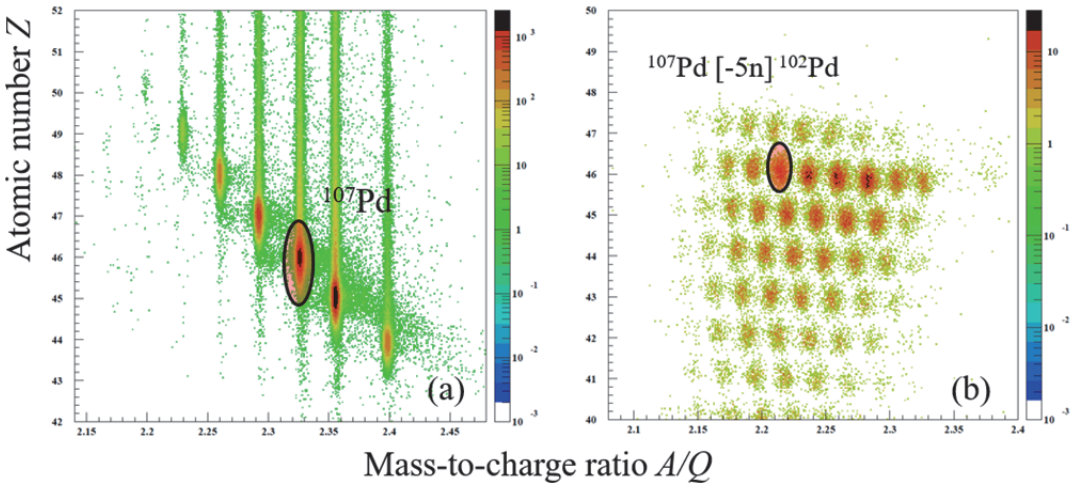

Figure 1 Particle identification plots for (a) the secondary beams in the BigRIPS separator and (b) the reaction products from the ^{107}Pd beam in the ZeroDegree spectrometer. Circles indicate (a) the ^{107}Pd beam, and (b) ^{102}Pd produced via the five-neutron removal reaction channel to guide the eyes.

3. Results and Discussion

For spallation reaction, both the target and energy dependences of cross sections have been investigated. The new results were compared with an intra-nuclear cascade and evaporation model using the PHITS code [2]. For Coulomb dissociation reaction, obtained results are compared with E1 and E2 responses. We plan to continue taking reaction data especially at lower incident energy in parallel with comparison between our data and model predictions and with discussion on their discrepancies.

References

[1] Wang H, Otsu H, Sakurai H, *et al.*, Phys. Lett. B, 2016;**754**(2):104.

[2] Sato T, *et al.*, J. Nucl. Sci. Technol., 2013;**50**:913

4 Simulation Study of Transmutation Processes of Long-lived FPs

K. Niita
Research Organization for Information Science and Technology
niita@rist.or.jp

The efficiency of transmutation of long-lived fission products by using proton, deuteron and carbon beam has been investigated based on the simulation study of macroscopic transmutation processes in the targets. The dual target systems have been proposed in order to improve the efficiency of the transmutation. This work was funded by ImPACT Program of Council for Science, Technology and Innovation (Cabinet Office, Government of Japan).

Keywords: ImPACT, Transmutation, LLFP, Nuclear Data, PHITS

1. Introduction

We are aiming to establish reasonable nuclear transmutation methods which enable long-lived fission products (LLFP) to be converted into stable or short-lived nuclides and also to be recycled as rare metals and other resources that are contained in the recovered products. For this purpose, we have investigate the efficiency of transmutation of LLFP by using proton, deuteron and carbon beam based on a macroscopic numerical simulation of the target systems. We propose dual target systems which can improve the efficiency of LLFP transmutation by using proton beam

2. Method and Results of Simple Target System

We have used the PHITS [1] code for macroscopic simulation of target systems bombarded by proton beams. As for the LLFP, only four nuclides, ^{137}Cs, ^{107}Pd, ^{93}Zr, ^{79}Se, are considered in this study. At first, we considered simple cylindrical targets consist of one of these four nuclides, where the length of the cylinder is determined by 1.1 times of the range of incident proton in each target, and the radius is fixed so as to equal the transmutation density for each target. In **Figure 1**, we plot the transmutation energy E/h, which is defined by the incident energy E of proton divided by the transmutation number h of target per the proton in the simulations, as a function of the incident proton energy. The figure shows that the transmutation energy decreases as the incident energy is increasing up to around 500 MeV. The reason of this behavior is that the range of incident proton is smaller than the mean free path of the proton in this energy range. Thus the transmutation energy may increase linearly as the beam energy increases above 500 MeV, if only the incident proton contributes to the transmutation of

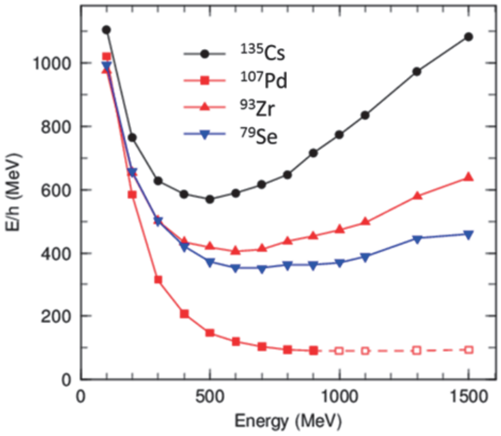

Figure 1 Transmutation energy as a function of incident proton energy

the target nuclide. However, the transmutation energy shows quite different behavior for each target nuclide. This is due to the contribution of secondary neutrons produced by the incident proton. **Figure 2** shows the energy spectra of neutron inside the target produced by the incident 1 GeV proton. This figure indicates the most probable neutron energy inside the target is from 200 keV to 2 MeV for each targets. For this energy range, the main transmutation channel caused by neutron is capture reactions, whose cross sections for each nuclide are shown in **Figure 3**. The capture cross sections are quite different for each nuclide by roughly one order of magnitude in this energy range from 200 keV to 2 MeV. This leads to the significant differences above 500 MeV in **Figure 1.**

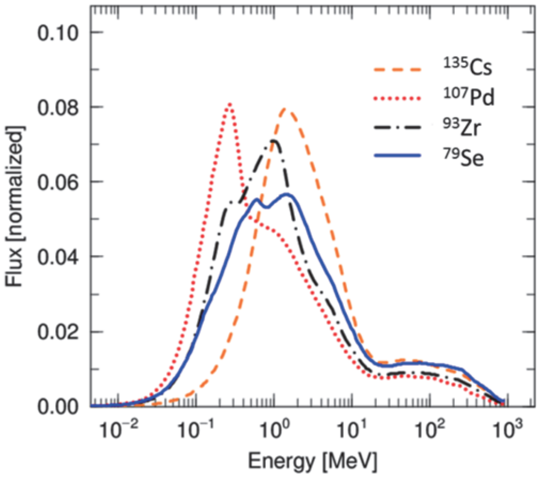

Figure 2 Energy spectra of neutrons inside the target

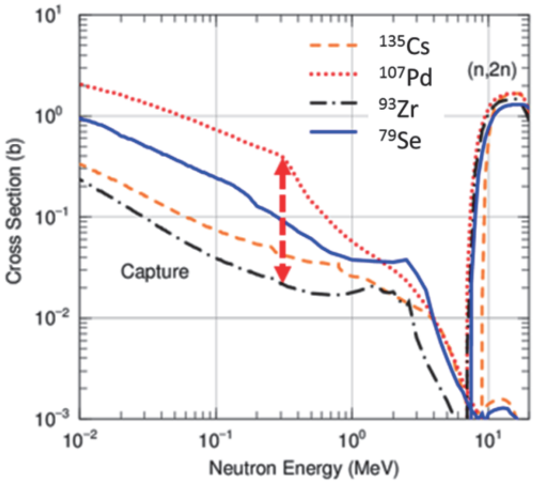

Figure 3 Capture cross section of neutron taken from JENDL-4.0

We have also compared the transmutation energy *E/h* for deuteron and carbon beam in the same condition as for proton in **Figure 4, 5, 6, 7** for each targets. In these figures, open symbols denote that the weight of the target is heavier than 300 kg. These figures show that the transmutation energy by deuteron beam below 500 MeV/u becomes the smallest for all targets.

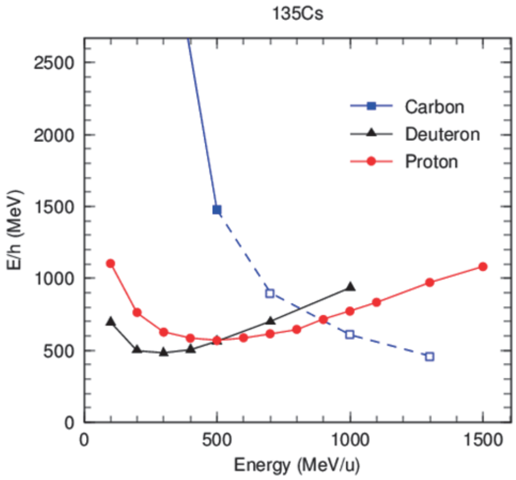

Figure 4 Transmutation energy for Cs target by proton, deuteron and carbon beam

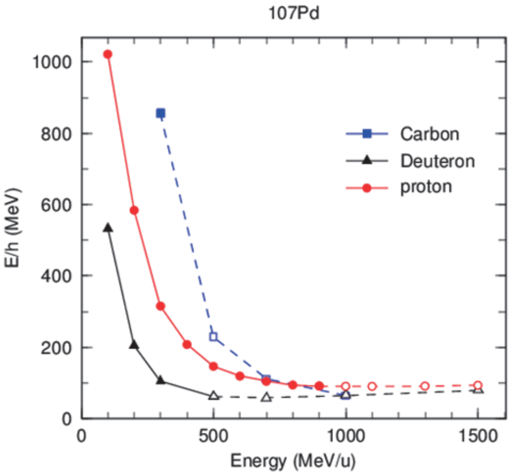

Figure 5 Transmutation energy for Pd target by proton, deuteron and carbon beam

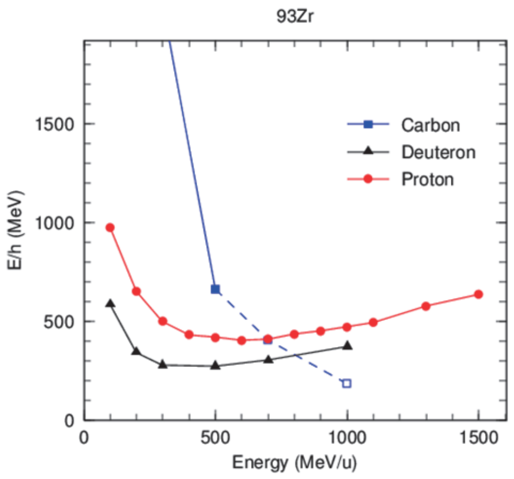

Figure 6 Transmutation energy for Zr target by proton, deuteron and carbon beam

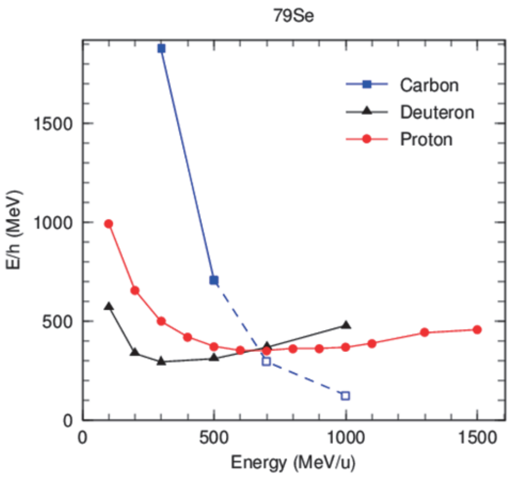

Figure 7 Transmutation energy for Se target by proton, deuteron and carbon beam

3. Results of Combinational Target and Conclusion

Base on the study in the simple target system mentioned above, we propose the dual target system which can enhance the efficiency of the transmutation of LLFP by using proton beam. We put LLFP with small capture cross section, e.g. ^{135}Cs, in the central part of cylindrical target, and LLFP with large capture cross section, e.g. ^{107}Pd, outside the cylinder. Conceptual 3D structure for the dual target system is shown in **Figure 8**. Proton beam bombards on the central part of target ^{135}Cs, which is transmuted and also produces secondary neutrons. These secondary neutrons transport to outer region of cylinder and cause the capture reactions on ^{107}Pd.

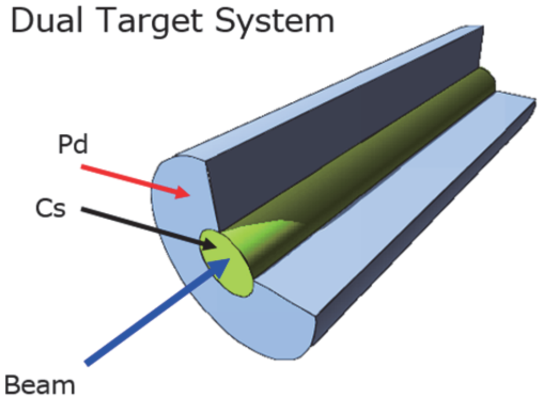

Figure 8 Conceptual 3D structure of dual target system

We have investigated three combinations, Cs-Pd, Zr-Pd, and Se-Pd systems as for dual target system. In **Figure 9**, we show the proton and neutron flux distributions for Cs-Pd and Zr-Pd systems bombarded by 1 GeV proton. The results of transmutation number *h* for these three dual target system are shown in **Table 1** compared with those of single target systems. In these simulations, we considered not only the isotope separation target and also the spent fuel components and even-odd mass separation target. The Cs-Pd dual target system enhanced the efficiency of transmutation 1.8 times, 1.9 times and 2.8 times compared with single two cylinder systems for the cases of isotope separation target, even-odd mass separation target and the spent fuel components, respectively. We also found that for the even-odd mass separation target case, only 40 % reduction of the transmutation efficiency compared with the isotope separation case. This suggests that this dual target system might be one of candidates for core system of the transmutation method of our aim. The efficiency of the dual target system by deuteron beam will be investigated in the near future.

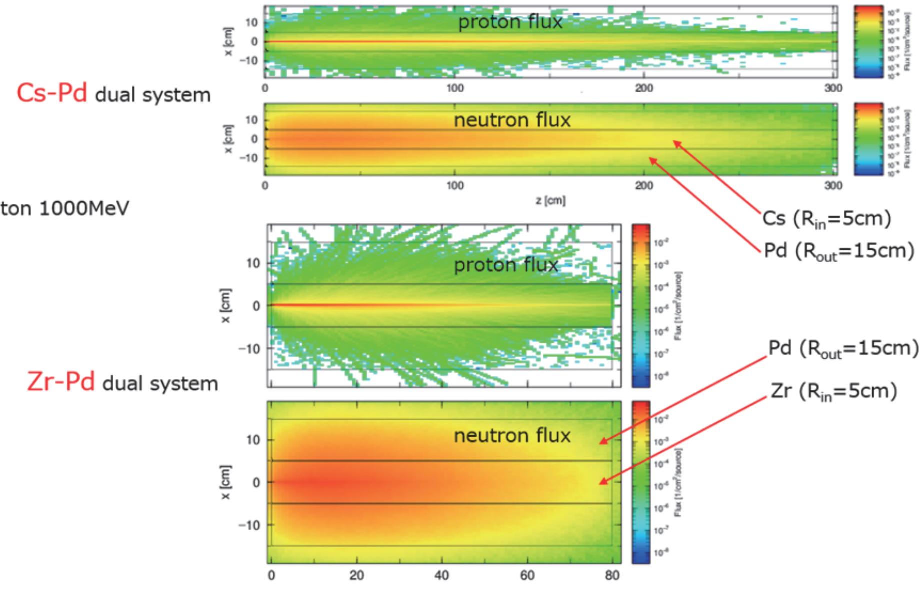

Figure 9 Proton and neutron flux distributions for Cs-Pd and Zr-Pd systems

Table 1 Transmutation number *h* for three dual target system compared with those of single target systems

	dual target			two single target		
element	fuel	even-odd	mono	fuel	even-odd	mono
Cs	0.15	0.15	1.35	0.14	0.142	1.29
Pd	1.98	3.91	10.8	1.38	4.21	12.1
	2.13	4.06	12.2	0.76	2.18	6.70
	sum	sum	sum	sum/2	sum/2	sum/2
	dual target			two single target		
element	fuel	even-odd	mono	fuel	even-odd	mono
Zr	0.40	1.37	2.55	0.375	1.31	2.40
Pd	0.96	2.92	8.52	1.37	4.21	12.1
	1.36	4.29	11.1	0.87	2.76	7.25
	sum	sum	sum	sum/2	sum/2	sum/2
	dual target			two single target		
element	fuel	even-odd	mono	fuel	even-odd	mono
Se	0.09	2.10	2.48	0.064	1.81	2.13
Pd	1.04	3.01	8.43	1.38	4.21	12.1
	1.13	5.11	10.9	0.72	3.01	7.12
	sum	sum	sum	sum/2	sum/2	sum/2

Reference

[1] T. Sato, K. Niita, N. Matsuda, S. Hashimoto, Y. Iwamoto, S. Noda, T. Ogawa, H. Iwase, H. Nakashima, T. Fukahori, K. Okumura, T. Kai, S. Chiba, T. Furuta and L. Sihver, "Particle and Heavy Ion Transport Code System PHITS, Version 2.52", J. Nucl. Sci. Technol., 2013 50:9, 913.

5 Research on Neutron Capture Cross Sections at J-PARC in ImPACT Project

Shoji Nakamura[1]*, Atsushi Kimura[1], Brian Yamada Hales[1], Osamu Iwamoto[1],
Yasuhiro Tsubata[1], Tatsuro Matsumura[1],
Yuji Shibahara[2], Akihiro Uehara[2], and Toshiyuki Fujii[3]

1) Japan Atomic Energy Agency, 2-4 Shirakata, Tokai-mura, Naka-gun, Ibaraki 319-1195
2) Research Reactor Institute, Kyoto University, 2-1010 Asashiro Nishi, Kumatori-cho, Sennan-gun, Osaka 590-0494
3) Osaka University, 2-1 Yamadaoka, Suita, Osaka 565-0871

*e-mail: nakamura.shoji@jaea.go.jp

Study on cross-section measurements has been promoted for ^{135}Cs among long-lived fission products in ImPACT Project. The feasibility study on ^{79}Se sample preparation also has been conducted to measure its cross sections in future. This paper reports research progresses on preparation of a radioactive ^{135}Cs sample, cross-section measurements of natural Cs, and feasibility study of ^{79}Se sample preparation.

This work was funded by ImPACT Program of Council for Science, Technology and Innovation (Cabinet Office, Government of Japan).

***Keywords*: ImPACT, transmutation, long-lived fission products, Cesium-135, capture cross section**

1. Introduction

The social acceptability of nuclear power reactors is related to the waste management of long-lived fission products (LLFPs) existing in spent nuclear fuels. The LLFPs are important in the nuclear waste management, because the presence of these nuclides induces long-term radiotoxicity because of their extremely long half-lives. The transmutation is one of the solutions to reduce the radiotoxicity of nuclear wastes. The ImPACT project [1] aims to realize a "large reduction and exploitation of resources in high-level nuclear waste by nuclear transmutation", by using an accelerator to accomplish nuclear transmutation of LLFPs. This project targets the major LLFPs: ^{107}Pd, ^{93}Zr, ^{135}Cs, ^{126}Sn, and ^{79}Se, as well as incidentally the medium-lived fission product ^{137}Cs. To perform accelerator-based nuclear transmutation effectively, it is necessary to acquire reaction cross-section data for the radionuclides across a wide spectrum of incident particle energies. Our concern was focused to measure the cross-sections of ^{135}Cs because of its long half-life (2.3×10^6 yr.[2]). However, it is impossible to obtain a pure ^{135}Cs sample because it is not supplied by available vendors. This is why the quantity of data is so scarce [3-9] for ^{135}Cs as shown in **Figure 1**. As seen from Fig.1, the thermal-neutron cross section and some resonance parameters have been measured, but no energy-dependent cross section data have been obtained. In order to realize measurements for ^{135}Cs, the ^{135}Cs sample should be firstly prepared. When the sample is prepared, the neutron-capture cross-section measurements of ^{135}Cs will be performed by the Time-Of-Flight method. In addition, to accurately measure the cross sections of ^{135}Cs, the cross sections of ^{133}Cs must also be measured, which is expected to be contained as a carrier in the ^{135}Cs sample. Therefore, during the sample preparation, the neutron-capture cross sections of ^{133}Cs were also measured. Furthermore, ^{79}Se is one of the important LLFPs, but there is no data because of the difficulty of obtaining the sample of ^{79}Se. Thus, we decided to make feasibility study whether or not the ^{79}Se sample could be prepared.

This paper reports the progress of the project.

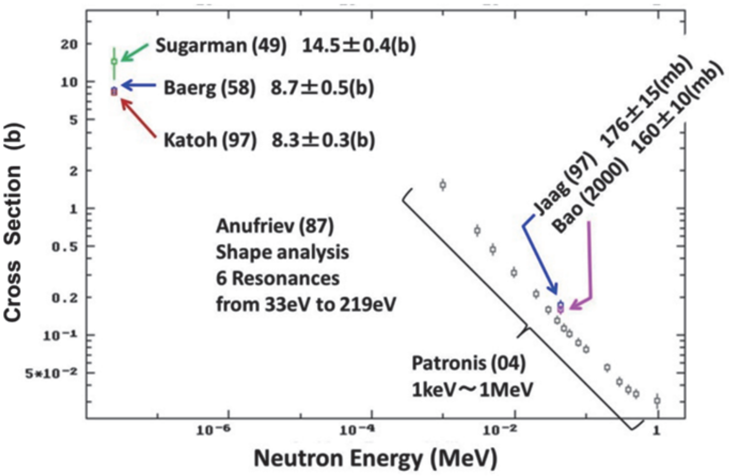

Figure 1 Current status of data for ^{135}Cs cross-sections reported in the past

2. Preparation of radioactive Cs sample

Since the ^{135}Cs sample was not supplied, it was considered to use ^{135}Cs, which would be included as an impurity in a ^{137}Cs sample that can be available. Since Isotope separation is difficult, ^{137}Cs and ^{135}Cs would be present in a ratio of 1:1 from the viewpoint of nuclear fission yield. Cesium-137 has a half-life of 30.08 years. If the samples deteriorated over time, it would be advantageous for the measurement because the ^{135}Cs abundance ratio is larger than unity. It was found that Russia's Isotope Research Institute had ^{137}Cs solutions about 30 years old. Therefore, ^{137}Cs solutions of 200 MBq were extracted and pelletized with yttrium oxide (Y_2O_3) as a binder, and then the Cs pellet was fabricated as a sealed source of aluminum disk shape. The radiation source was delivered in March, 2017. **Figure 2** shows the sealed ^{137}Cs source produced in this project. The radioactivity amount of the sealed Cs source was confirmed to be 200.7±2.5 MBq by measurement of 662-keV γ ray in comparison with a ^{137}Cs calibration source.

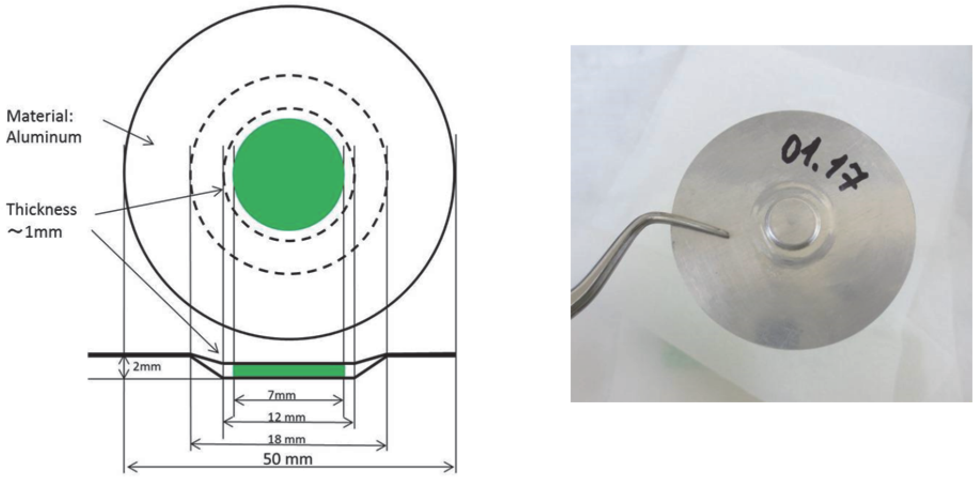

Figure 2 A sample design (left), and the sealed ^{137}Cs source of 200MBq actually manufactured in this project (right).

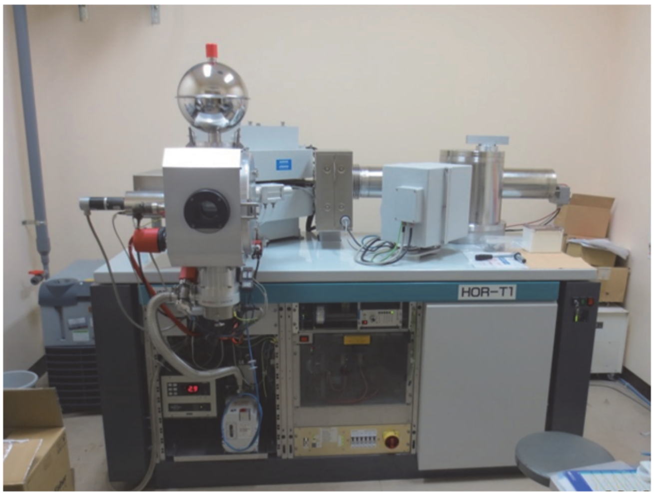

Figure 3 TRITON mass spectrometer installed in KURRI

Isotope separation of ^{135}Cs and ^{137}Cs is difficult, and therefore ^{135}Cs is expected to be included as an impurity in available ^{137}Cs samples. By measuring the isotope abundance of ^{135}Cs and ^{137}Cs in a standard ^{137}Cs source by mass spectrometry, the amount of ^{135}Cs can be obtained from the isotope abundance and yields of 662-keV decay γ rays emitted from ^{137}Cs. Collaborators of Kyoto University Research Reactor Institute (KURRI) have started to apply mass spectrometry to a very small amount of radioisotope sample, and to confirm its effectiveness. The mass spectrometer TRITON (Thermo Fisher Scientific Inc.) was used for this analysis, which is shown in **Figure 3**. For demonstration experiments, a standard solution of ^{137}Cs (370 kBq in activity) was used as a preliminary sample, which was obtained through the Japan Radioisotope Association. An appropriate amount of the ^{137}Cs solution was dispensed, and then converted to nitrate by a chemical processing. In order to suppress contamination of the mass spectrometer from radioactive ^{137}Cs and ^{135}Cs, an extremely small amount of sample should be used. However, it is necessary to perform highly precise mass-analysis even in as small amount as possible. For this reason, a small amount of the chemically processed solution, slightly about 10 Bq, was pipetted onto a Rhenium (Re) filament with a TaO (Tantal Oxide) activator, and then dried. The filaments were attached onto the ion source of the mass spectrometer. **Figure 4** shows the resulting mass spectrum of the standard ^{137}Cs solution. The red line shows the spectrum of the sample before the chemical treatment, and the black line shows the spectrum after the chemical treatment. One finds that false peaks appeared on tails of the Cs peaks were not observed after the chemical treatment. From the yields of the mass spectral peaks, the ^{135}Cs/^{137}Cs isotope ratio was obtained as 0.868±0.004 (±2σ). This experiment successfully got the isotope ratio with an accuracy of 0.5% using a standard solution of ^{137}Cs. This technique makes it possible to analyze a very small amount of radioactive sample, expectantly picogram order. We obtained the ^{137}Cs solution of 370 kBq extracted from the same batch as the sealed ^{137}Cs source. We plan to perform mass analysis with this solution at KURRI, and derive the ^{135}Cs/^{137}Cs ratio.

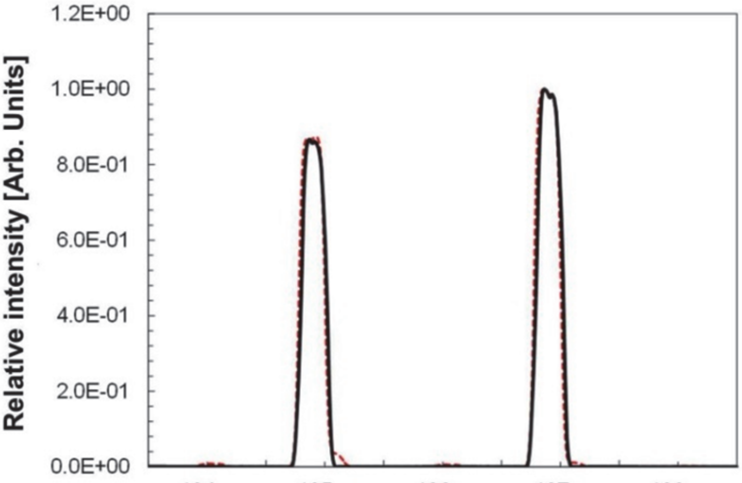

Figure 4 Result of mass spectrum of a standard ^{137}Cs solution

3. Experiments with natural Cs

During the preparation of the radioactive ^{137}Cs sample, we decided to measure the neutron cross sections of ^{133}Cs, which is assumed to be contained in the sample. Experiments were performed by the experimental apparatus called “Accurate Neutron Nucleus Reaction measurement Instrument (ANNRI)” at the Beam Line No.4 (BL04) of the MLF in the J-PARC. The ANNRI has a large Ge detectors array, which consists of two cluster-Ge detectors, eight coaxial-shaped Ge detectors and BGO Compton suppression detectors as shown in **Figure 5**. The ANNRI has an advantage for the neutron cross-section measurements because the MLF facility can provide the highest pulsed neutron intensity in the world when the 1-MW operation would be achieved [10]. In addition of the highest pulsed neutron intensity, ANRRI has another advantage by introducing High speed data acquisition system [11]. The Ge spectrometers were composed of two cluster-Ge detectors, eight coaxial-Ge detectors, and Compton suppressing BGO detectors. Its energy resolutions for 1.33-MeV γ ray are 5.8 keV in on-beam and 2.4 keV in off-beam conditions. Its peak efficiency for 1.33-MeV γ-ray is 3.64±0.11% as a nominal value [12].

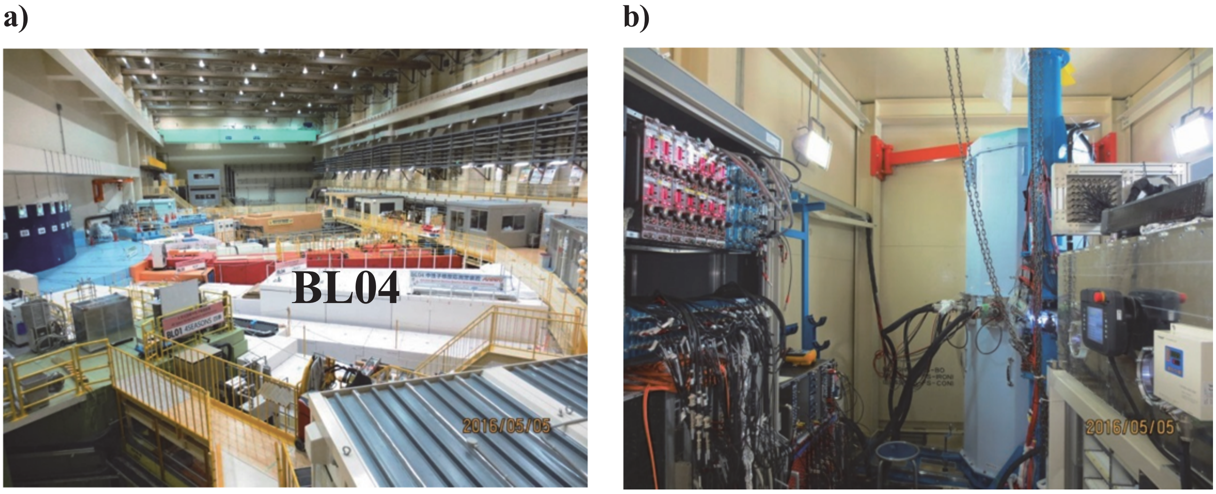

Figure 5 **a)** An experimental apparatus called “Accurate Neutron Nucleus Reaction measurement Instrument (ANNRI)” at BL04 in MLF of J-PARC **b)** the Ge spectrometers installed with ANNRI

The ^{133}Cs sample used in this experiment was 17.2 mg in weight, 5.04 mm in diameter, 0.329 mm in thickness, and its chemical form is Cs_2CO_3. The Cs sample was sealed with a FEP(fluoroethylene polymer) film under Argon gas atmosphere. The neutron capture cross sections of ^{133}Cs have been measured using the Ge spectrometer installed in ANNRI. The sample was placed at a flight path of 21.5 m. In the experiment of ^{137}Cs, it is necessary to perform experiments by shielding 662-keV γ rays. To simulate the ^{137}Cs experiments, lead blocks of 5cm in thickness were piled around the beam duct at the sample position as shown in **Figure 6**. The accelerator of J-PARC was operated in 150-kW power and in single bunch mode.

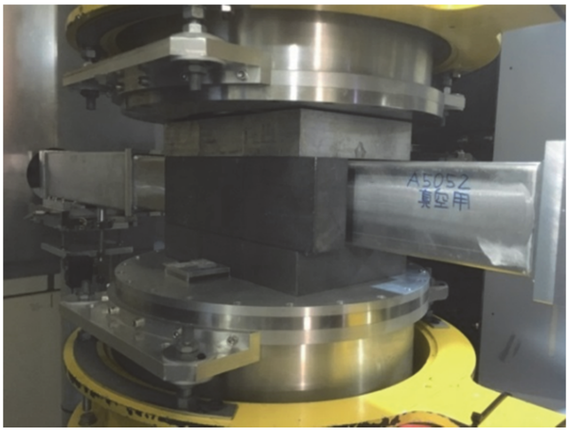

Figure 6 Shielding condition around the sample position

Figure 7 shows the result of neutron capture cross section of ^{133}Cs for neutron energies ranging from 0.01 to 300 eV. Here, the results obtained in June 2016 experiment are plotted together with the evaluation of JENDL-4.0[13]. The experimental data obtained in this study resulted in supporting JENDL-4.0. However, as shown in **Figure 8**, several resonance peaks reported in past were not observed. Even in the preliminary experiment conducted before in November 2015, it was confirmed that there is no resonance peaks at neutron energies near 140 eV and 373 eV. In measurements reported in the past, it is possible that the resonances caused by impurities might be miss-assigned to those due to ^{133}Cs.

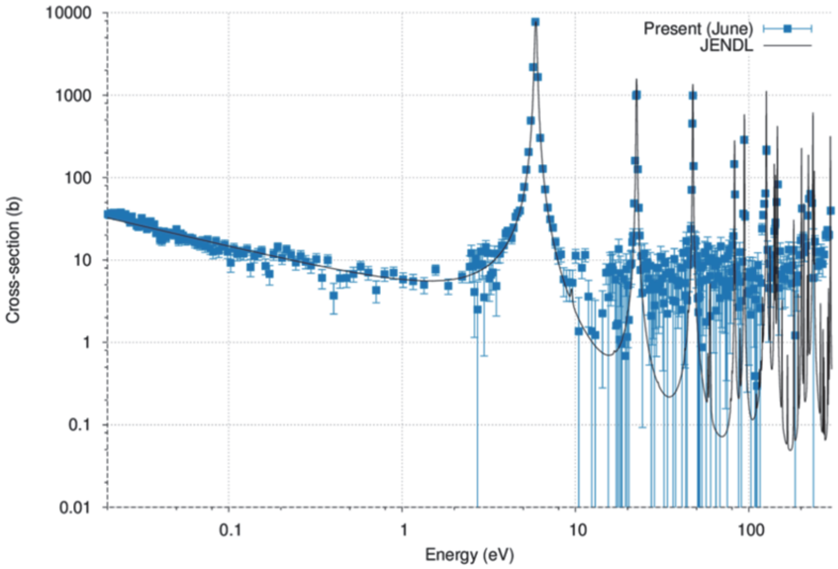

Figure 7 Preliminary results of neutron capture cross sections for ^{133}Cs together with the evaluated data of JENDL-4.0

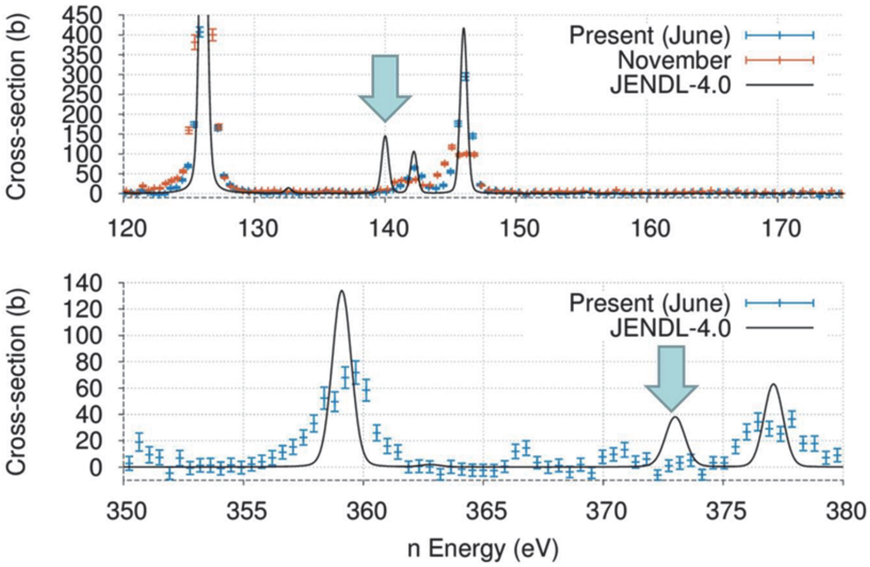

Figure 8 Some of miss-assigned resonance peaks sited in the JENDL-4.0 evaluation

4. Feasibility study of Se-79 sample preparation

It is extremely difficult to obtain a ^{79}Se sample, and therefore it is impossible to measure the cross sections of ^{79}Se. This is why the cross-section measurements were performed only for stable Se isotopes (^{74,77}Se [14]) at J-PARC. Even in activation experiments, there are only measurements of stable ^{80}Se nuclides [15]. Thus, we decided to study the possibility of sample preparation of ^{79}Se including the possibility of the process of separating and recovering the required amount for cross-section measurements from irradiated nuclear fuels, the scale of a facility, and equipment at an actual scale level

Present situation for the research and development on Se separation from irradiated fuels was examined. In the research filed of fuel reprocessing and group partitioning, a study to separate a coherent amount of Se from irradiated fuels has not been conducted at least in Japan. There is no example of aggressive separation and recovery studies. Regarding analysis of slight amount of ^{79}Se contained in radioactive wastes, there are some cases of examination from the viewpoint of waste management including JAEA.

Based on the above situation, the following items are considered.

1) Estimation of the amount of Se contained in spent fuel by combustion calculations
2) Estimation of the amount of spent fuel required to recover 10 mg of ^{79}Se
3) Issues in separation process at existing facilities of JAEA
4) Examination of separation and recovery methods

Using the combustion calculation code ORIGEN, the abundance of Se contained in an irradiated fuel was estimated. The code ORIGEN-2.2UPJ and JENDL - 4.0 base library PWR47J40 [16] were used for this calculations. **Table 1** lists the results of the weight ratio of Se isotopes contained in irradiated fuel of light water reactors PWR under conditions of burnup of 45 GWd/t and cooling for 10 years. The irradiated fuel 1,000 kgUpr* contained 46.4 kg of fission products, in which Se was only 72.6 g (0.156% of the total FP) [17]. The ^{79}Se among FPs was only 5.9 g. From the results, 1.7 kgUpr of irradiated fuel is required to obtain 10 mg of Se, if the recovery rate from dissolved nuclear fuels with nitric acid is assumed to be 100%. It is not so easy to achieve 100% recovery ratio. Then, if the recovery rate is assumed to be around 10%, 17 kgUpr will be required.

Table 1 Amount of Se isotope contained in irradiated fuel of 1 ton

Se Isotopes	Weight (g)	Weight fraction (wt%)	Half Life [2]
^{76}Se	0.006	0.0084	stable
^{77}Se	1.02	1.4	stable
^{78}Se	3.0	4.1	stable
^{79}Se	5.9	8.1	2.95×10^{5} yr
^{80}Se	17.6	24	stable
^{81}Se	0	0	18.45 min
^{81m}Se	0	0	57.28 min
^{82}Se	45	62	8.3×10^{19} yr

*kgUpr : weight conversion of metal uranium before irradiation

Here, it is assumed that Se is separated and recovered from irradiated fuels at Nuclear Fuel Cycle Safety Engineering Research Facility (NUCEF) in Nuclear Science Research Institute of JAEA. In the αγ cell installed in the NUCEF, there is permission to handle irradiated fuels from light water reactors, and experiences of dissolution and separation tests with fuels of several hundred grams per batch up to now [17]. An overview of process is drowning in **Figure 9**.

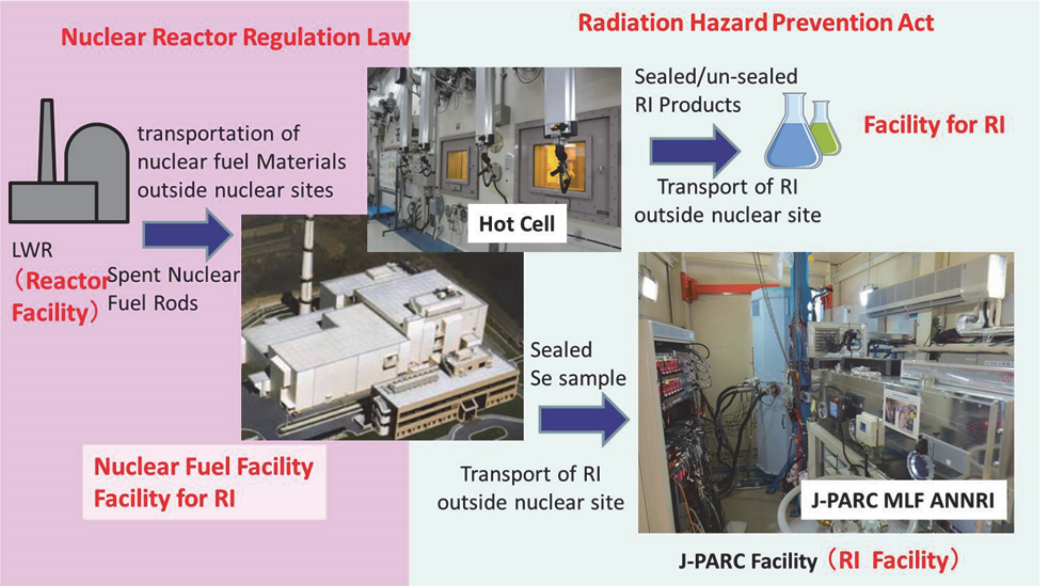

Figure 9 An overview of process

Including separation methods, the current issues are extracted and summarized as follows:

1) It is assumed to use irradiated LWR fuels currently stored in JAEA. Although it is sufficient as the holding amount, permission and approval by each right holder is necessary.
2) The problem was examined assuming separation on solvent extraction and column separation. It will be possible to use solvent extraction methods using TBP (tributylphosphate) and DGA (diglycolamide) extractant, for removing U, Pu, MA from dissolved irradiated fuel.
3) In order to reliably purify Se sample at the final stage, other elements, ex. U, Pu, Mo, Zr, Ru, Cs, and Ln *etc*. should be eliminated in separation stages, and technical problems should be simplified.
4) From the viewpoint of "waste volume reduction", it is required not to add new elements as much as possible. (Use reagents mainly composed of C, H, O, and N.)
5) When solvent extraction by continuous operation is frequently conducted, efficient disposal of used solvent (TBP, DGA or hydrocarbons) and estimation of total waste amount are also subjects.
6) In order to frequently transport nuclear materials such as U, Pu etc. inside the Nuclear Science Research Institute of JAEA, it is necessary to extract issues relating to safeguards and nuclear material accountancy.
7) Under the supervision of the Nuclear Regulation Authority, work on new regulatory standards for nuclear fuel facilities is underway at each plant including Nuclear Science Research Institute of JAEA. It is also necessary to grasp trends for the permission of amount of nuclear fuels and reduction in facility size for earthquake and tsunami countermeasures, and to respond to the regulation strengthening.

5. Summary

In the ImPACT project, we have been promoting neutron-capture cross section measurements of ^{135}Cs. Considering the use of ^{135}Cs contained as an impurity in the ^{137}Cs sample, the sealed ^{137}Cs source with 200 MBq in radioactivity was made. In near future, we will transport the sealed ^{137}Cs source to J-PARC and carry out irradiation experiments.

In order to derive the isotopic ratio ^{135}Cs to ^{137}Cs in the sealed source with high accuracy, the mass spectrometry analysis has been carried out in KURRI. Using a ^{137}Cs standard solution, we succeeded in measuring the isotopic ratio ^{135}Cs to ^{137}Cs with an accuracy of 0.5%. We plan to conduct the mass analysis with the same sample as the sealed ^{137}Cs source.

During the preparation of the radioactive samples, the neutron capture cross sections of ^{133}Cs contained as impurities in the sealed source were measured, and the neutron capture cross section data were obtained in the neutron energy ranging from 0.01 eV to 300 eV. It was found that some of the reported ^{133}Cs resonances were incorrectly identified because they were not obviously measured in this work.

To consider the possibility of preparation of ^{79}Se sample, a feasibility study was conducted on the assumption that ^{79}Se is separated and recovered using facilities of Nuclear Science Research Institute of JAEA. The works of processing a Se sample were considered to be a long-term project with high hurdles for national approval.

Acknowledgment

The authors would like to appreciate the staff of J-PARC and Kyoto University Research Reactor Institute for their support.

References

[1] http://www.jst.go.jp/impact/index.html
[2] R.B. Firestone *et al.*, Table of Isotopes, 8th ed. Update, John Wiley and Sons, New York, (1998).
[3] N. Sugarman, Pysical Review, **75**, 1743(1945).
[4] A.P. Baerg *et al.*, Canadian Journal of Physics, **36**, 863(1958).
[5] T. Katoh *et al.*, J.Nucl.Sci.Technol., **34**, 431(1997).
[6] V.A. Anufriev *et al.*, Soviet Atomic Energy, **63**, 851(1988).
[7] Z.Y. Bao *et al.*, Atomic Data and Nuclear Data Tables, **76**, 70(2000).
[8] S. Jaag *et al.*, Nuclear Physics A, **621**, 247(1997).
[9] N. Patronis *et al.*, Physicsal Review C, **69**, 025803(2004).
[10] K. Kino *et al.*, NIM-A, **626**, 58 -66 (2011).
[11] T. Nakao *et al*, ND2016, **R130**, (2016).
[12]T. Kin *et. al.*, *the 2009 NSS-MIC Conf. Rec.*, N24-2, (2009).
[13] K. Shibata *et al.*, *J.Nucl.Sci. Technol.*, **48**(1), 1-30 (2011).
[14] J. Hori, H. Yashima, S. Nakamura *et al.*, Nuclear Data Sheets, **119**, 128-131 (2014).
[15] S. Nakamura *et al.*, J.Nucl. Sci.Technol., **45**, 116 (2008).
[16] K. Okumura *et a*l., ORLIBJ40, JAEA-Data/Code 2012-032, (2013).
[17] Committee of Handbook on Process and Chemistry of Nuclear Reprocessing, JAEA-Review 2015-002, 2015.

6 Current Status of Nuclear Data Measurement at the KURRI-LINAC

Jun-ichi Hori
Research Reactor Institute, Kyoto University
Kumatori-cho, Sennan-gun, Osaka 590-0494
E-mail: hori@rri.kyoto-u.ac.jp

The electron linear accelerator at the Research Reactor Institute, Kyoto University (KURRI-LINAC) established in 1965 has been used as various types of particle beam source such as electrons, neutrons and photons. The electron beam is generated by a thermionic gun and accelerated to a maximum energy of 46 MeV in two accelerator tubes by L-band microwave. The pulse width is variable from 2 ns to 4 μs. The linac produces a maximum power of 6 kW electron beam with an energy of 30 MeV. A water-cooled Ta target assembly surrounded by light water moderator is used as a white neutron source. There are three flight paths of 10, 12 and 22 m for neutron capture or total cross section measurements with the time-of-flight technique. There is also a lead slowing-down spectrometer for fission cross section measurements. Systematic studies on neutron cross sections of minor actinides (MAs) and long-lived fission products (LLFPs) have been performed for nuclear transmutation of nuclear waste. In the presentation, previous activities on nuclear data measurement at the KURRI-LINAC will be outlined.

Recently, we have started basic and application researches on nuclear data in the frameworks of two projects. One is the project entitled as "Research and development for Accuracy Improvement of neutron nuclear data on Minor ACtinides (AIMAC)". In the project, neutron cross sections of MA are cross checked by integral measurements using variable neutron flux fields. Moreover, we try to determine the resonance parameters of MA by combining total and capture cross section measurements. Another is the project entitled as "Development of Non-Destructive Methods Adapted for Integrity test of Next generation nuclear fuels (N-DeMAIN)". In the project, we aim at the development of non-destructive assays for nuclear materials from the point of view of nuclear densitometry, neutron and X-ray imaging, and temperature measurement using a Doppler broadening effect. The current status of those projects will be also introduced.

7 Nuclear data measurement at the JAEA tandem facility

K. Nishio

Advanced Science Research Center, Japan Atomic Energy Agency

Tokai, Ibaraki 319-1195, Japan

e-mail : nishio.katsuhisa@jaea.go.jp

The activity of nuclear data measurements at the JAEA tandem facility is presented. We are promoting a surrogate reaction measurement to obtain neutron-induced fission data using multi-nucleon transfer induced fissions. This approach has an advantage that fission data for various nuclei are obtained in one experiment, some of which are impossible to take using a neutron beam. Also in the reaction, excitation energies of the initial compound nucleus are populated widely below the fission threshold up to around 60 MeV, allowing us to generate neutron-energy dependence up to equivalent neutron energies. Fission fragment mass distributions for various nuclei and excitation energies are shown. We are also running a program to measure prompt fission neutrons by installing liquid scintillation detectors around the fission chamber. Correlation between fission fragments and neutrons will be obtained, which is also important to develop a fission model.

1. Introduction

Nowadays, the surrogate reaction technique has been widely used for the measurement of fission and capture cross sections, see for example the review article [1]. When these cross sections cannot be measured directly or predicted reliably, this indirect method becomes useful to obtain these data. Difficulty in obtaining neutron-induced cross sections comes from the short life-times of the nuclei of interest. In spite of many activities to apply the surrogate method in cross section measurements, it was quite recently that the surrogate reaction technique was applied in the fission fragment mass distributions (FFMDs) for the first time [2] at the JAEA tandem facility.

Multi-nucleon transfer (MNT) reactions applied in the JAEA experiment, promoted by advanced science research center of JAEA, are now based on the ^{18}O beam bombarded to various actinide target nuclei. Experimental data for ^{18}O + ^{232}Th, ^{238}U, ^{248}Cm, ^{237}Np, ^{249}Cf were taken, some of which are under analysis. The FFMDs and their excitation energy dependence for more than fourteen nuclei can be obtained in one experiment. In addition to FFMDs, fission barrier height can be determined from the threshold in the excitation functions of the fission probability, which is of crucial importance to benchmark a fission model. From the analysis of fission fragment angular distributions with respect to the recoil direction of the fission nucleus, we observed the angular anisotropy of fission-fragment emission angles, due to nuclear rotation driven by the MNT reaction. As the anisotropy has information on the average square of angular momentum, information on spins of the fissioning system would be obtained. This is important for the surrogate-reaction method that decay properties of excited nucleus depend not only on the excitation energy but also spin and parity of a state. Recently, our measurement setup is upgraded so as to obtain prompt neutron multiplicity and energy spectrum and neutrons accompanied generated in multi-chance fission by installing liquid organic scintillation detectors.

In this report, experimental method and results from the JAEA setup is shown to highlight the activity of the JAEA tandem facility.

2. Experimental Setup

Figure 1 shows the experimental setup for the surrogate fission measurement at the JAEA tandem facility. Thin targets (^{232}Th, ^{238}U, ..) were irradiated by an ^{18}O beam at energy of about 9MeV/u.

Transfer channels were identified by detecting the projectile-like nucleus using a silicon ΔE-E detector array which was mounted to the forward direction of the target. The thickness of the ΔE detector is 75 μm. Twelve pieces of the ΔE detectors were mounted conically around the beam axis to make an efficient collection of the projectile-like nuclei after MNT reaction. Particles passing through the ΔE detector were detected by a silicon strip E detector (SSD) with thickness of 300 μm are mounted to measure residual energy (E_{res}). The E detector has the annular shape, and the telescope covers the scattering angle from 17.2° to 30.9° relative to the beam direction. The SSD has 16 annular strips within the active area, and each strip define the scattering angle θ of the particle with respect to the beam. Figure 2 shows an example of the projectile-like nuclei plotted on the ($\Delta E+E_{\mathrm{res}}$, ΔE) plane. Oxygen isotopes are clearly separated as well as those of lighter-element isotopes. By choosing a specific transfer channel, we can assign the corresponding compound nucleus by assuming a binary reaction process.

Fission fragments were detected using four multi-wire proportional counters (MWPCs). Each MWPC has an active area of 200×200 mm^2. The MWPC consists of the central cathode which is sandwiched by two wire planes. The wire planes were designed to detect the incident position of a fission fragment. The MWPCs were operated with an isobutene gas of about 1.5 Torr. The operation gas was shielded by an aluminum-coated Mylar window of 2.0 μm thickness. Induced charge in the cathode was used to separate fission fragments from scattered particles and/or lighter ions. Time difference signal, ΔT, from the two facing MWPCs was recorded. Fission fragment masses were determined kinematically using ΔT value and fission fragment directions.

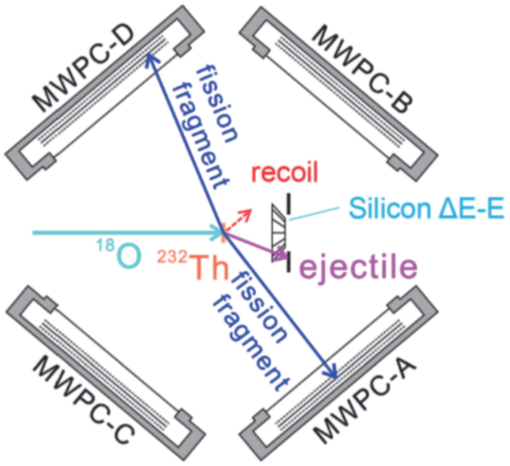

Fig.1 Experimental setup for the surrogate fission measurement at the JAEA tandem

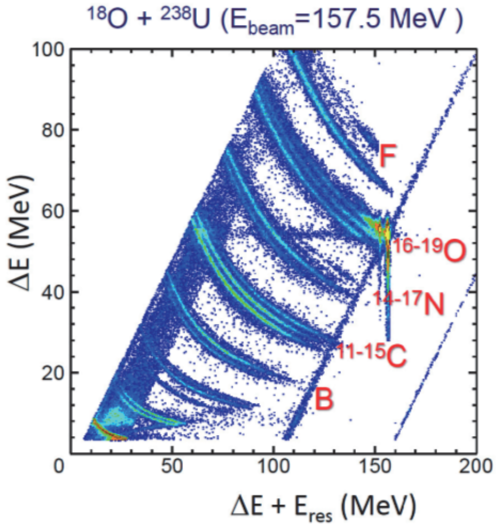

Fig.2 Plot of the projectile nuclei on the ($\Delta E+E_{\mathrm{res}}$, ΔE) plane obtained in the ^{18}O + ^{238}U reaction

3. Experimental Results and Discussions

As an example of the results of the FFMD, data for ^{239}U* are shown in Fig. 3. The nucleus is populated by the $^{18}\mathrm{O} + {}^{238}\mathrm{U} \rightarrow {}^{17}\mathrm{O} + {}^{239}\mathrm{U}^*$ channel. Fission events are plotted on the fragment mass and excitation energy (E^*) of the compound nucleus. Light and heavy fragment groups are clearly visible.

Similar analysis was carried out for the other different transfer channels (fissioning nuclides) in the ^{18}O+^{238}U reaction, and the FFMDs for uranium isotopes ^{237,238,239,240}U* and their excitation energy dependence are shown in Fig.4. The FFMD for ^{240}U* were obtained for the first time. Predominantly asymmetric fission is observed at low excitation energies, with a gradual increase of the asymmetric fragments toward high excitation energy, due to the smearing of the shells responsible for the mass-asymmetric fission.

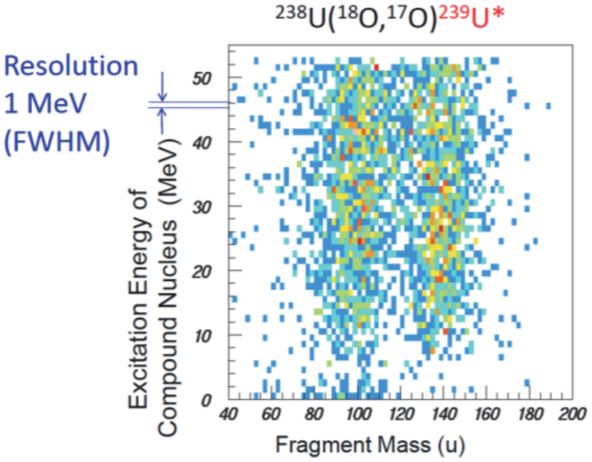

Fig.3 Fission events registered on the fragment mass and excitation obtained in the ^{238}U(^{18}O,^{17}O)^{239}U* channel. Light and heavy fragment groups are separately visible

To understand the behavior of FFMDs, the spectra are compared with a calculation based on the fluctuation-dissipation fission model developed in [3]. In this model, the evolution of a nuclear shape, defined by three parameters (charge-center distance, mass-asymmetry and fragment deformation), is traced with time by solving the Langevin equations from the initial state down to the scission point, and the FFMD is generated by accumulating events in the Monte Carlo method. The temperature (excitation energy) dependence of the potential energy landscape, resulting from the smearing of the shell-correction energy, was taken into account to find the evolution of FFMD with excitation energy.

The calculated results are shown in Fig. 4 by blue lines. The results can account for the FFMDs only for the lowest excitation energy E^*=10-20 MeV. The deviation, however, is already evident at the next excitation-energy range, E^*=20-30 MeV. At the highest energy the calculation shows structure-less symmetric fissions in contrast to the measurement.

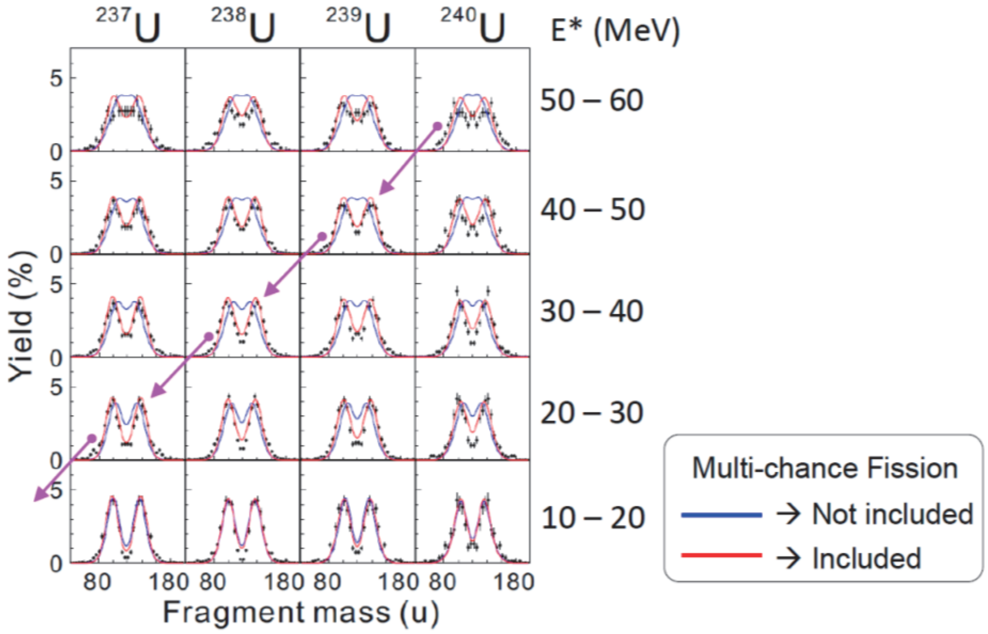

Fig.3 Fission fragment mass distributions of $^{237\text{-}240}$U* obtained in the multinucleon transfer reactions. Excitation energy ranges on the same line are indicated on the right side. The arrows connecting the FFMD show a link of multi-chance fissions entering in the high-energy fission of ^{240}U* (E^*=50-60

MeV).

In order to account for the double-humped shape in the FFMDs which remains at the highest excitation energies, the concept of multi-chance fission (MCF) was introduced in the analysis. When an initially populated nucleus has larger excitation energy than the neutron-binding energy, fission and neutron evaporation compete with each other. The latter populates a less excited nucleus, which can also fission when its excitation energy is higher than the fission barrier, known as the second-chance fission. This process successively continues until fission channel no longer opens. In the experimental setup for this run, the number of the emitted neutrons in the multi-chance fission cannot be identified, thus the data should include the contributions from all the possible chance-fissions. In order to incorporate the MCF, the fraction (probability) of each MCF was determined by the GEF code [4]. In each step of MCFs, decrease of excitation energy and the change of potential energy caused by neutron removal were considered.

The Lagevin calculation taking into account the MCF are shown by red curves in Fig.4. In contrast to the calculation without MCF (thin blue curves), the combination of MCF and the calculation well explains the mass-asymmetric structure remaining at the higher excitation energies. It was found in this calculation that the double-humped shape in FFMDs observed at high excitation energies comes from the fission of lower-excited lighter isotopes. For example, the double-humped shape of ^{240}U* at E^*=45 MeV, mainly originates from the lower-excited fission of the lighter isotopes of ^{235,236,237}U*.

Data for ^{18}O + ^{232}Th are published in [2]. Data analysis is in progress for the other studied reactions of ^{18}O + ^{237}Np, ^{248}Cm, ^{249}Cf. In the ^{18}O+ ^{237}Np, we are finding that thirty ejectile nuclei could be separated in the MNT channels, and the FFMDs for corresponding fissioning nuclides are obtained.

In near future, we are planning a measurement in the ^{18}O+ ^{254}Es reaction, which allows us access populate Fm isotopes, where sharp transition from double-humped (e.g. ^{256}Fm) to sharp-peaked symmetric fissions (e.g. ^{258}Fm) were observed in spontaneous fission [5]. New data from MNT fission in this region, which covers widely the nuclides and excitation energies, would unveil the unique phenomenon in nucleus.

4. Summary

At the JAEA tandem facility, nuclear data measurements using the surrogate reaction technique have been carried out, mainly to obtain fission fragment mass distributions and their incident neutron energy dependence. In the facility, radioactive target nuclei, such as Th, U, Np, Am, Cm, Cf can be used. These targets are irradiated by the ^{18}O beam, from which almost all the nuclei involved in the ADS technologies can be investigated, by taking advantage of various transfer channels opening in the reaction. More higher-energy data would be obtained by increasing the incident beam energy.

Acknowledgements

The authors thank the crew of the JAEA-tandem facility for the beam operation. This work is supported by the program ‘Comprehensive study of delayed-neutron yields for accurate evaluation of kinetics of high-burn up reactors’ and ‘Development of prompt-neutron measurement in fission by surrogate reaction method and evaluation of neutron-energy spectra’ by the Ministry of Education, Sports, Science and Technology of Japan (MEXT).

References

[1] J. Escher, J. Burke, F. S. Dietrich, N.D. Scielzo, Rev. Mod. Phys. **84**, 353 (2012).
[2] R. Léguillon et al., Phys. Lett. B, **761**, 125 (2016).
[3] Y. Aritomo and S. Chiba, Phys. Rev. C, **88**, 044614 (2013).
[4] K.-H. Schmidt et al., Nuclear Data Sheets, **131**, 107 (2016).
[5] D.C. Hoffman, Nucl. Phys. **A502**, 21c (1989).

8 Nuclear Data Measurements at Center for Accelerator and Beam Applied Science, Kyushu University

Nobuhiro SHIGYO
Department Applied Quantum Physics and Nuclear Engineering, Kyushu University
Motooka, Nishi-ku, Fukuoka, 819-0395, Japan
e-mail: shigyo@kune2a.nucl.kyushu-u.ac.jp

The tandem accelerator was constructed at Department of Physics in Hakozaki Campus, Kyushu University in 1972. Various experiments related to nuclear data have been performed in the accelerator facility. For example, measurements of cross section and analyzing power p + d scattering, reaction cross section of ^{4}He(^{12}C, ^{16}O)γ below 3 MeV. For engineering purpose, double differential neutron energy spectra were measured below 9 MeV deuteron incidence. Experiment of neutron angle differential thick target yield measurement was also performed for study of medical radioisotope production using accelerator neutrons. Center for Accelerator and Beam Applied Science was newly built in Ito Campus in 2008. The center has been upgrading a tandem accelerator and an FFAG synchrotron for the progress of beam science and engineering.

1. Introduction

The Tandem Accelerator was constructed at Department of Physics in Hakozaki Campus, Kyushu University in 1972. The accelerator was home-made and its terminal voltage and maximum beam current was 11 MV and 1.6 μA, respectively.

Various experiments related to nuclear data have been performed in the accelerator facility. For engineering purpose, double differential neutron energy spectra were measured for 9 and 5 MeV deuteron incidence to investigate neutron yields as source term in shielding design of IFMIF-EVEDA and systematics of neutron yields in the wide target mass range [1, 2]. Experiment of neutron angle differential thick target yield measurement using activation techinque was also performed for study of medical radioisotope production using accelerator neutrons[3].

A neutron source is one of essential equipment for engineering purpose as mentioned above. A quasi-monoenergetic neutron source using ^{1}H(^{13}C, n) reaction was developed[4]. This neutron source supplied 7.2 MeV neutrons by 59.3 MeV ^{13}C beam.

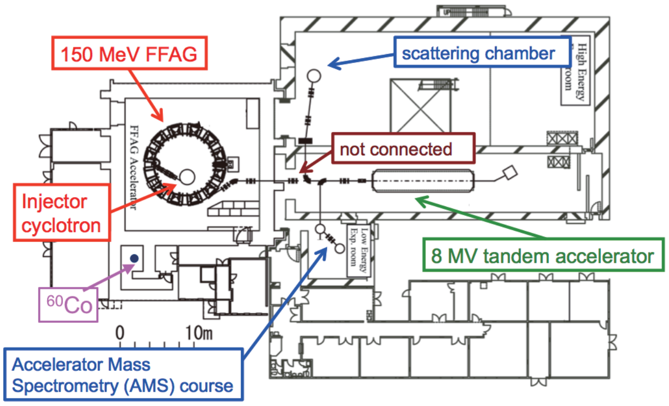

Figure 1 Plan view of building of Center for Accelerator and Beam Applied Science, Kyushu University

As examples of other kinds of experiments, reaction cross section of ^{4}He(^{12}C, ^{16}O)γ below 3 MeV, which is important to determine evolution of a star[5] had been measured using a recoil mass separator over 20 years.

The accelerator in Hakozaki Campus was completely shut down in 2015 because of campus relocation. In order to continue study using accelerators, Center for Accelerator and Beam Applied Science was newly built in Ito Campus to reconstruct accelerator facilities in Department of Physics and Department of Nuclear Engineering in 2008[6].

Figure 1 illustrates the plan view of the building of the center. The center has an 8 MV 1 nA tandem accelerator and 150 MeV 2 nA FFAG accelerator. There are two experimental rooms. An accelerator mass spectrometer is located in the smaller room. A scattering chmaber is currently in the larger room. Most of magnets and chambers on the beam lines were transfered from Hakazaki campus. This facility also has a 185 TBq ^{60}Co γ-ray source.

Some of experiments mentioned above on nuclear data in the Hakozaki Campus is introduced in the following sections.

2. Measurements of Thick Target Neutron Yields for Deuteron Incidence by scintillator

Neutron yields using deuteron incident reaction is useful for intense neutron sources and radiation source term in the shielding design such asThe IFMIF-EVEDA activities. However, experimental data of deuteron induced neutron yields were scarce below 10 MeV. The double differential neutron thick target yields for 9 and 5 MeV.

Figure 2 shows the target and detetctor arrangement for the series of measurements[1]. The deuteron beam from the tandem accelerator was delivered to a compact vacuum target chamber. The chamber was insulated from other experimental apparatus and the ground of the experimental room in order to acquire the deuteron beam current. The beam currents were 10 - 100 nA according to combination of beam and target material. Various types of target materials were chosen from carbon to tungsten to cover neutron yields in the wide target mass range. The thickness of each target was chosen for deuteron to stop completely in the target.

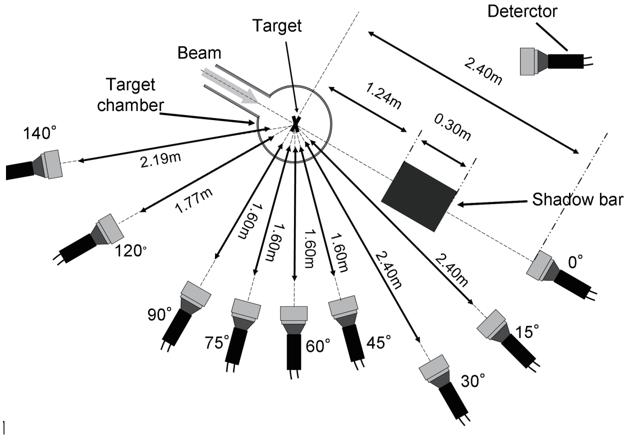

Figure 2 Experimental arrangements of measurements of thick target neutron yields for deutron incidence[1].

An NE213 liquid organic scintillator 50.4 mm thick and 50.4 mm was adopted as a neutron detector. The pulse signal of light output of the scintillator was recorded as integrated charge into 2 ADCs with different length of gates. The measurement directions were 9 directions from 0° to 140°. The distances from the target and the neutron detector were from 1.6 to 2.4 m. To obtain contribution of neutrons from floor and wall in the experimental room, the measurement with an iron shadow bar 150 mm 150 mm and 300 mm thick was set between the target and the scintillator for each direction as background measurement.

As an example of results, neutron energy spectra from 9 MeV Al(d, n) reaction is indicated in Fig. 3. One can see that PHTIS[7] code reproducs the experimental energy spectra for all directions reasonably to some extent.

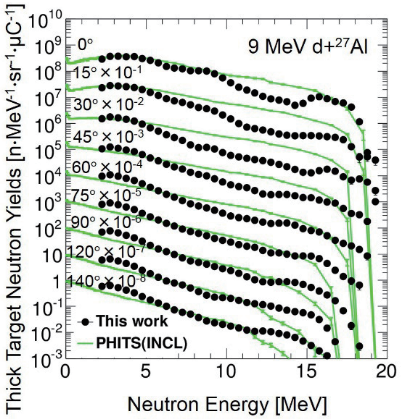

Figure 3 Thick target neutron yields for 9 MeV deutron incidence on an aluminum target[2].

3. Measurements of Thick Target Neutron Yields for Deuteron Incidence with activation technique

Medical radioisotopes have been widely used for in diagnosis, therapy. The isotopes are usually produced by nuclear reactors or by small-sized accelerators. However, there are problems of stable supply and cost. To reduce risks on the problems, a production method of isotopes using accelerator neutrons has been studied.

For reliable prediction of medical radio isotpes with accelerator neutrons, thick target neutron yields are highly essential. However, experimental data of neutron yields are not sufficient. Some theoretical models predict neutron yields with not high accuracy. To overcome the situation, the angle-differential thick target neutron yields of C(d, n) reaction at $E_d = 12$ MeV using a multiple-foil activation unfolding method[3].

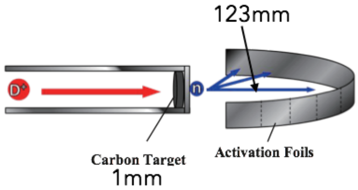

Figure 4 Experimental setup for measurement of neutron yield by activiation technique[3].

Figure 4 stands for experimental setup of measurments of neutron yields by activation technique[3]. The neutrons were generated by a 1 mm thick grahite target which is longer than the range of deuteron in the graphite and irradiated activation foils located at 123 mm downstream from the target. The foils were arranged from 0 to 90 degrees. Materials of the foils were ^{197}Au, ^{59}Co, ^{27}Al, ^{93}Nb, ^{nat}Fe and ^{nat}Ni. Decay γ-rays were measured by a HP-Ge detector.

The neutron thick target yields were deviled from unfolding the activation yield of all foils using JENDL-4.0 cross sections as response functions. Figure 5 shows thick target neutron yields of this experimental data and PHITS calculation at 0° and existing one at 3.5°[8]. the shape of the unfolded energy spectrum was in generally good agreement with the existing data and PHITS calculation.

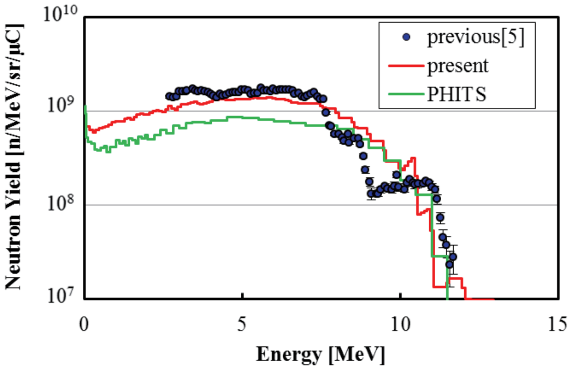

Figure 5 Measured neutron thick target yield for 12 MeV C(d, n) reaction at 0° with PHITS and exsisting data at similar direction[3].

4. Development of Neutron Source

Accelerator based neutron sources are utilized in science and engineering. D(d, n) and T(d, n) reactions are used to produce monoenergetic neutrons. However, the reactions are not able to produce monoenergetic neutrons in the energy region from 8 to 14 MeV. Therefore, only few neutron cross section data had been available in this energy range.

New types of monoenergetic neutron sources with heavy ion beams have been proposed as one of the candidates to fill in the energy region. This kind of reactions has advantages of enhancement of 0° neutron emission and small fraction of lower energy neutrons than desired ones.

The neutron source using the ^{1}H(^{13}C, n) reaction was tested[4]. The reaction was chosen as a candidate suitable for the Kyushu University Tandem Accelerator Laboratory from consideration about the performance of accelerator.

The schematic view of the neutron source using ^{1}H(^{13}C, n) reaction is illustrated in Fig. 6. The gas cell was made of 0.5 mm thick stainless steel and had the effective size of 30 mm long and 30 mm in diameter. The entrance window was made of tantalum foil of 3 μm in thickness and 12 mm in diameter on a cylinder shape frame. A 0.2 mm thick tantalum disk was used as the beam stopper. Escape of the electrons produced by beam bombardment on the entrance window was suppressed by permanent magnets.

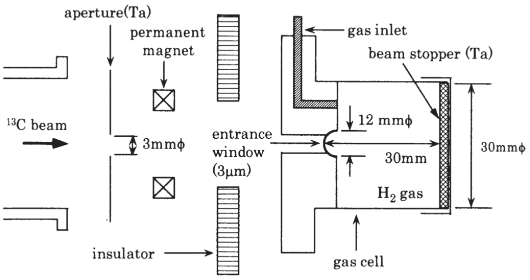

Figure 6 Schematic view of the neutron source using ^{1}H(^{13}C, n) reaction[4].

The neutron energy spectrum from 59.3 MeV ^{13}C beam incident on ^{1}H target at 0° is shown in Fig. 7. The peak energy of 7.2 MeV agreed with the simulation result. The energy resolution was about 1.5 MeV, which is due mainly to the intrinsic resolution of the NE213 scintillator used in the measurement. It is found that this neutron source was useful as a monoenergetic neutron source.

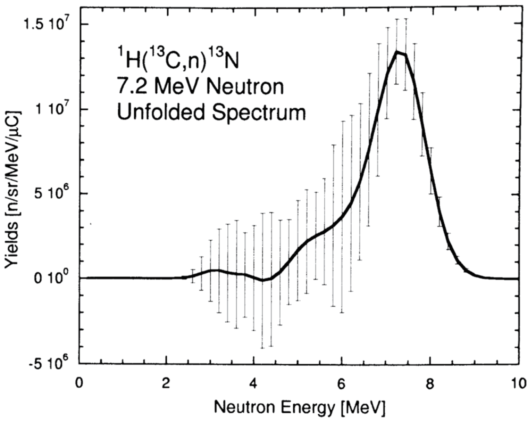

Figure 7 Measured and calculated neutron energy spectra for 59.3 MeV ^{1}H(^{13}C, n) reaction at 0°[4].

5. Measurements of ^{4}He(^{12}C, ^{16}O)γ Cross Sections

The reaction of ^{4}He(^{12}C, ^{16}O)γ around E$_{cm}$ = 0.3 MeV plays an important role in the helium burning in massive stars. To estimate the reaction cross section around E$_{cm}$ = 0.3 MeV by extrapolation, cross sections down to 0.7 MeV with high accuracy are requied. The ^{4}He(^{12}C, ^{16}O)γ cross sections had been measured in the tandem accelerator laboratory over 20 years.

Figure 8 illustrates the experimental setup of ^{4}He(^{12}C, ^{16}O)γ reaction cross section measurements[5]. It was essential to improve signal to noise ratio because the reaction cross section is very small. A ^{12}C beam from the tandem accelerator was incident on a windowless ^{4}He gas target. The ^{12}C and ^{16}O were separated by a recoil mass spectrometer and the ^{16}O were detected by a Si detector.

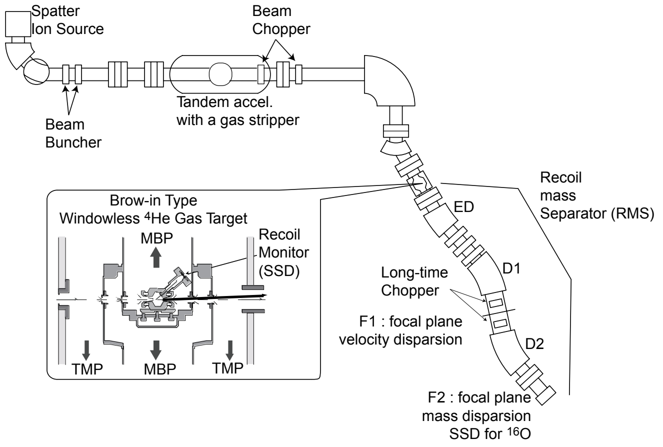

Figure 8 Experimental setup of measurements of ^{4}He(^{12}C, ^{16}O)γ reaction cross sections[5].

Figure 9 stands for the cross sections of ^{4}He(^{12}C, ^{16}O)γ reaction below 5 MeV. Cross sections of ^{4}He(^{12}C, ^{16}O)γ reaction at E$_{cm}$ = 2.4 and 1.5 were obtained in the experiments. The cross section at E$_{cm}$ = 1.5 MeV is the lowest energy data.

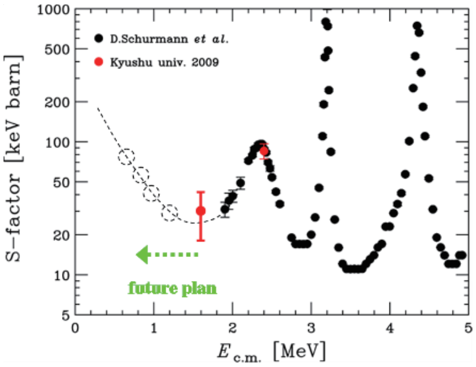

Figure 9 Cross section of ^{4}He(^{12}C, ^{16}O)γ reaction below 5 MeV[9].

6. Summary

The tandem accelerator had been used for measurements in engineering and science purposes and many important nuclear data had been acquired for a long time.

As a near future plan, beam current of the tandem accelerator will be increased to 1 μA. It is enable to develop a neutron source for science and engineering. The tandem accelerator will be also used as an injector of heay ion beam to the FFAG accelerator. A beam extraction line is under construction in the FFAG accelerator. Threre is a long-term plan the FFAG accelerator groduces 1 μA proton beam.

Acknowledgement

I would like to express my gratitude to Prof. Ishibashi, Prof. Watanabe, Prof. Ikeda, Prof. Noro, Prof. Teranishi and Prof. Kin at Kyushu University for details of the experiments on the facility.

References

[1] N. Shigyo, K. Hidaka, K. Hirabayashi, et al., Measurement of Deuteron Induced Thick Target Neutron Yields at 9 MeV, *J. Kor. Phys. Soc.*, 59 (2011) pp. 1725-1728.

[2] S. Araki, Y. Watanabe, T. Kin, et al., Measurement of Double Differential Neutron Yields from Thick Aluminum Target Irradiated by 9 MeV Deuteron, *Energy Procedia*, 71 (2015) pp. 197-204.

[3] T. Kawagoe, T. Kin, S. Araki, et al., Measurement of neutron yield by multiple-foil activation unfolding method for medical radioisotopes production using accelerator neutrons, *JAEA-Conf* 2015-003 (2015) pp. 297-302.

[4] Y. Watanabe, Y. Matsuoka, H. Nakamura, et al., Development of Quasi-Monoenergetic Neutron Source Using the ^{1}H(^{13}C,n) Reaction, *Eng. Sci. Rep. Kyushu Univ.*, 23 (2001) pp. 285-290.

[5] K. Sagara, T. Teranishi, H. Oba, et al., Direct measurement of ^{4}He(^{12}C, ^{16}O)γ reaction cross section around E_{cm} = 2.4 MeV at KUTL, *Nucl. Phys.*, A758 (2005) pp. 427c-430c.

[6] Website of the Center for Accelerator and Beam Applied Science, Kyushu University <https://www.cabas.kyushu-u.ac.jp>.

[7] T. Sato, K. Niita, N. Matsuda, et al., Particle and Heavy Ion Transport Code System PHITS, Version 2.52, *J. Nucl. Sci. Technol.*, 50 (2013) pp. 913-923.

[8] K. A. Weaver, J. D. Anderson, H. H. Barschall, et al., *Nucl. Sci. Eng.*, 52 (1973) p. 35.

[9] Website of the Kyushu University Tandem Acccelerator Laboratory [in Japanese], <http://ne.phys.kyushu-u.ac.jp/SubGroups/Astro/src/kenkyuu.html>

9 Research Activities with Neutron Beams at RCNP

Tatsushi SHIMA
Research Center for Nuclear Physics, Osaka University
10-1, Mihogaoka, Ibaraki, Osaka 567-0047, Japan
e-mail: shima@rcnp.osaka-u.ac.jp

Research Center for Nuclear physics of Osaka University provides opportunities for a variety of research fields by generating high-quality neutron beams in a wide energy range from sub μeV to a few hundred MeV. In this paper, the specifications of those beams and examples of the researches will be outlined.

1. Introduction

As a national Joint Usage/Research Center, the Cyclotron Facility (CF) at Research Center for Nuclear Physics (RCNP) of Osaka University provides research opportunities for fundamental science as well as for applications in the fields of engineering, medicine, radiation safety, and so on. One of the unique feature of RCNP-CF is its capability to generate high-quality/high-intensity neutron beams in a wide energy ranging over fifteen orders of magnitude, from sub μeV to a few hundred MeV. So far, the following neutron beams have been developed and utilized to various experiments.

(1) Quasi-monoenergetic pulsed neutrons at the N0 course
(2) “White” neutrons at the WS course
(3) Ultra-cold neutrons at the ES course (completed in JFY2015)

In what follows, the specifications and the research activities of those beam courses will be briefly outlined.

2. Beam Courses

2.1. Quasi-monoenergetic pulsed neutrons at the N0 course

The N0 course was constructed in 1996 [1] originally for high-resolution studies of nuclear spin-isospin responses via (p, n) reactions [2-6]. As shown in **Fig. 1**, it is provided with a 100 m long tunnel for measurement of the flight times of the emitted neutrons, offering opportunities for high-precision experiments on nuclear reactions associated with neutron emissions and absorptions in the energy range from a few MeV up to 400 MeV. Angular distribution measurements are available with use of a movable target system.

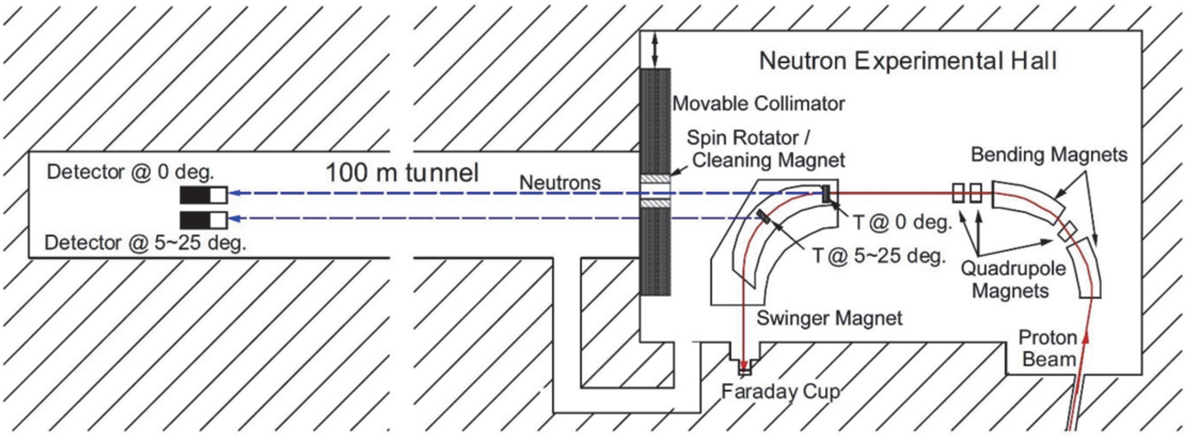

Figure 1 Schematic view of the N0 course (top view). "T" denotes a target.

The N0 course is equipped with a neutron polarimeter NPOL3 [7] for measurement of the nuclear polarization transfer observables in the (p, n) reactions with a spin polarized proton beam. NPOL3 consists of position-sensitive organic scintillators covering an area of 1 m×1 m. The effective analyzing powers A_y(eff.) are typically 0.37-0.43 and 0.13-0.15 for (n, n) and (n, p) channels, respectively.

The N0 course is also useful as one of the world-brightest sources of quasi-monoenergetic MeV neutrons. Employing the ^{7}Li(p, n)^{7}Be reaction, a quasi-monoenergetic neutrons in the energy range from a few MeV to about 400 MeV with intensities of ~2×10^9 /MeV/sr/μC and ~10^{11} /μC for the peak component and for all the range in the energy spectrum, respectively [8,9]. The primary proton beam impinges upon a lithium target with a typical repetition rate of 16 MHz, which can be divided down to 1 MHz for the neutron time-of-flight (TOF) measurement at low energies. The time spread of the proton pulse is 200 ps (FWHM), leading to typical energy resolutions with the TOF method of 660 keV and 2.1 MeV (FWHM) at the neutron energies of 198 MeV and 389 MeV, respectively. The neutron beams have been used for studies of the cross sections of neutron-induced nuclear reactions [10-14], performances of the materials for neutron shields [15], responses of neutron detectors [16,17], and so on.

2.2. White neutrons at the WS course

At the WS course, neutrons with continuous energy distributions are generated via the spallation reaction caused by a 400 MeV proton beam and a 65 mm thick tungsten target. As shown in **Fig. 2**, the spallation neutron has a similar energy distribution and more than eight orders of magnitude higher intensity compared to cosmogenic neutrons detected on the Earth's surface, and therefore it is quite useful to perform accelerated tests for the influence of cosmogenic neutrons on semiconductor devices, LSIs, *etc* [18].

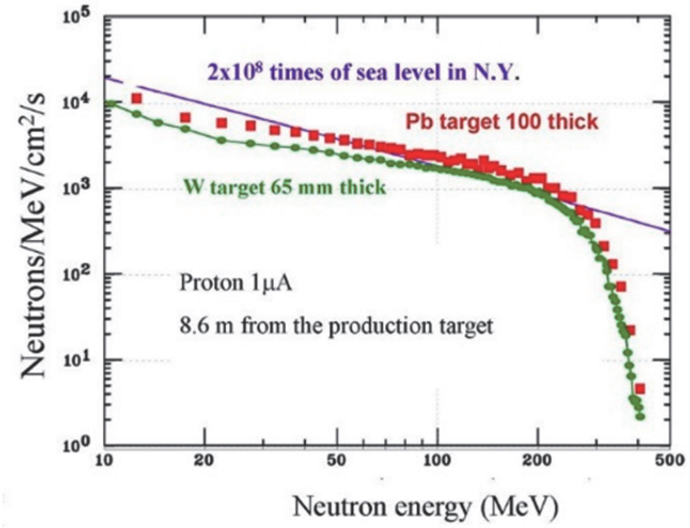

Figure 2 Energy spectra of spallation neutrons compared with cosmogenic neutrons at sea level in New York. Note that the spectrum of cosmogenic neutrons is emphasized by a factor of 2×10^8 from the real observed flux.

2.3. Ultra-cold neutrons at the ES course

The neutron with kinetic energy below about 200 neV, called an ultra-cold neutron (UCN), can be totally reflected on a surface of a material which has the Fermi's pseudo-potential higher than the kinetic energy of UCN [19]. Due to this unique feature, UCN is expected to be useful for a variety of experiments in the fields of fundamental physics, such as high-precision measurement of the neutron lifetime, the test of the time-reversal invariance via the measurement of the neutron electric dipole moment (nEDM), quantization of the neutron wave function in the Earth's gravitational potential, and the test of the baryon number conservation via the neutron-antineutron oscillation. In RCNP, a new method called the super-thermal method with a converter made of superfluid helium (He-II) has been developed. The principle of the method is based on the energy exchange between cold neutrons and phonons that takes place very efficiently at the crossing point of the curves of the dispersion relation (see **Fig. 3**) [20].

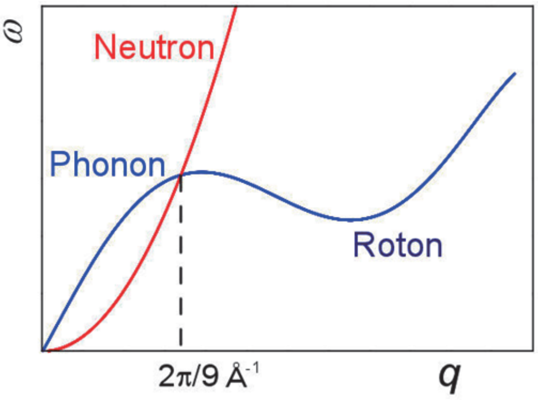

Figure 3 Dispersion relations of neutrons (red) and quasi-particles (blue) in superfluid helium.

At the ES course, a 400 MeV proton beam was stopped in a thick lead target to produce MeV-energy neutrons via the spallation reaction. Those energetic neutrons were cooled down to cold neutrons using moderators made of graphite and heavy water whose temperature was kept at 20 K. After the moderation, cold neutrons were introduced into the UCN converter made of He-II. **Table 1** compares the density of UCNs with the kinetic energy less than 90 neV produced in the UCN sources in the world.

Table 1 Summary of the UCN sources in the world

Facility	Source Type	Beam Power [kW]	Converter Type	UCN density [/cm^3] (below 90eV)
ILL [21]	Reactor	60000	Doppler Shifter	1
LANL [22]	Spallation	2.4	Super-thermal (solid D_2)	12
PSI [23]	Spallation	12	Super-thermal (solid D_2)	432
RCNP [24]	Spallation	0.4	Super-thermal (He-II)	260
TRIUMF	Spallation	20	Super-thermal (He-II)	> 5000 (plan)

As shown in Table 1, a good performance of the He-II super-thermal method was demonstrated in RCNP [24]. Based on the result, a new plan of a UCN source with the He-II super-thermal method was proposed, and now is in progress at TRIUMF in Canada. The project aims to achieve the nEDM sensitivity better than 10^{-28} e·cm by generating UCNs with the density of more than 5000 /cm^3.

2.4. New beam line for epithermal ~ keV neutrons (E-course)

A new project for development of the accelerator-driven boron neutron-capture therapy (BNCT) has recently started in RCNP with financial supports from Kyoto Medical Technology Inc. and Toyoda Radiation Laboratory Inc. This project will develop neutron beams in the epithermal and keV energy regions which is suitable to be delivered to a disease part locating deep inside of a human body. R&D on the following items are to be performed;

- accelerator dedicated to BNCT,
- epithermal ~ keV energy neutron sources based on the proton-induced spallation reaction and/or the ^{7}Li(p, n)^{7}Be reaction,
- detectors and imaging for fast neutrons,
- shielding for fast neutrons, and
- related component technologies.

For the above developments, the E course is going to be constructed in the M-experimental room of the RCNP AVF cyclotron building. **Figure 4** shows the layout of the E course in the M experimental room.

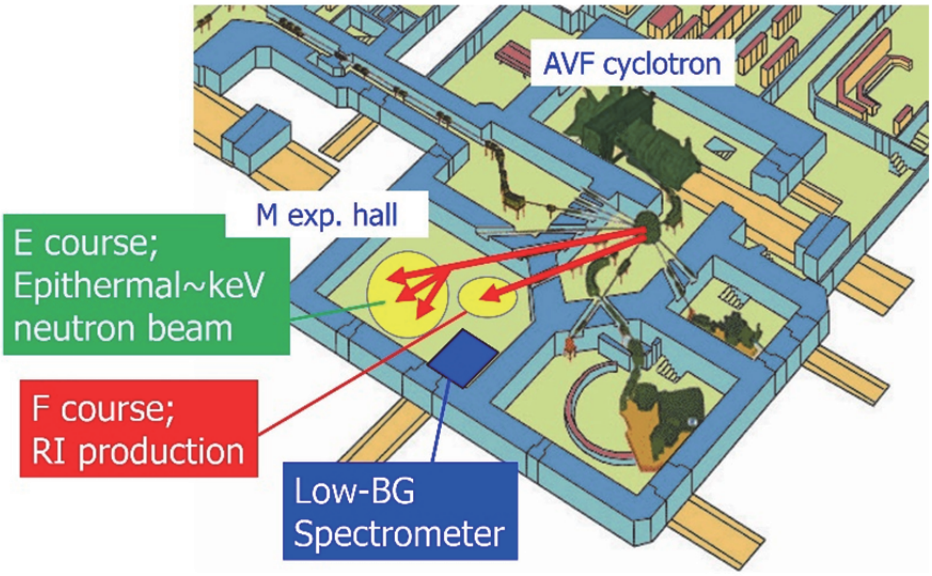

Figure 4 Layout of the E course

The E course has three branches, two for R&D of the neutron source and the neutron imaging for BNCT, and the other one for general use of epithermal neutrons, which can be used in combination with the existing F course for RI production and a low-background detector system.

3. Summary

Due to the wide coverage of neutron energy and the availability of various types of neutron sources, RCNP-CF is playing a role as a center for neutron science. In the Japanese fiscal year 2018, large-scale repair and improvement of the AVF cyclotron are scheduled. After one-year silence, the neutron sources will be resumed with higher intensities as well as better efficiencies.

References

[1] H. Sakai *et al*., Nucl. Instrum. Methods in Phys. Res. A369, pp.120-134 (1996).
[2] T. Wakasa *et al*., Phys. Rev. C77, 054611 (2008).
[3] E. Ihara *et al*., Phys. Rev. C78, 024607 (2008).
[4] M. Sasano *et al*., Phys. Rev. C79, 024602 (2009).
[5] K. Yako *et al*., Phys. Rev. Lett. 103, 012503 (2009).
[6] M. Sasano *et al*., Phys. Rev. C85, 061301(R) (2012).
[7] T. Wakasa *et al*., Nucl. Instrum. Methods in Phys. Res. A547, pp.569-582 (2005).
[8] Y. Iwamoto *et al*., Nucl. Instrum. Methods in Phys. Res. A629, pp.43-49 (2011).
[9] Y. Iwamoto *et al*., Nucl. Instrum. Methods in Phys. Res. A804, pp.50-58 (2015).
[10] H. Yashima *et al*., Proc. Radiochim. Acta, 1, pp.135-139 (2011).
[11] K. Ninomiya *et al*., Proc. Radiochim. Acta, 1, pp.123-126 (2011).

[12] S. Sekimoto *et al*., Prog. Nucl. Sci. Tech., 1, pp.89-93 (2011).

[13] S. Sekimoto *et al*., Nuclear Data Sheets 119, pp.197-200 (2014).

[14] H. Yashima *et al*., Rad. Prot. Dosim. 161, pp.139-143 (2014).

[15] M. Hagiwara *et al*., Prog. Nucl. Sci. Tech. 4, pp.327-331 (2014).

[16] A. Masuda *et al*., IEEE Trans. Nucl. Sci. 59,pp.161-166 (2012).

[17] V. Mares *et al*., IEEE Trans. Nucl. Sci. 60, pp.299-304 (2013).

[18] C.W. Slayman, IEEE Trans. Nucl. Sci. 57, pp.3163-3168 (2010).

[19] Ya.B. Zel'dovich, Sov. Phys.-JETP, 9, 1389 (1959).

[20] R. Golub and J. Pendlebury, Phys. Lett. A 62, 337 (1977).

[21] C.A. Baker *et al*., Phys. Rev. Lett. 97, 131801 (2006).

[22] A. Saunders *et al*., Rev Sci Instrum. 84, 013304 (2013).

10 Historical Evolution of Accelerators

Ken TAKAYAMA
Accelerator Laboratory, High Energy Accelerator Research Organization
Oho 1-1, Tsukuba-shi, Ibaraki-ken 305-0801 Japan
e-mail: takayama@post.kek.jp

Historical evolution of modern accelerators is described.

1. Introduction

These days many species of quantum beam are provided by various accelerators. Primary quantum beams are classified into four generations due to mass ratio as seen in Fig.1. The 1st generation is electron, the 2nd generation is proton, the 3rd generation is heavy ion, and the 4th generation is cluster ion. Although secondary particles such as photon, neutron, pion, and radio isotope are not included in the generations, applications of the primary generations and their secondary productions expand to the extensive fields from high energy physics to heavy ion mutation as described in Fig.1.

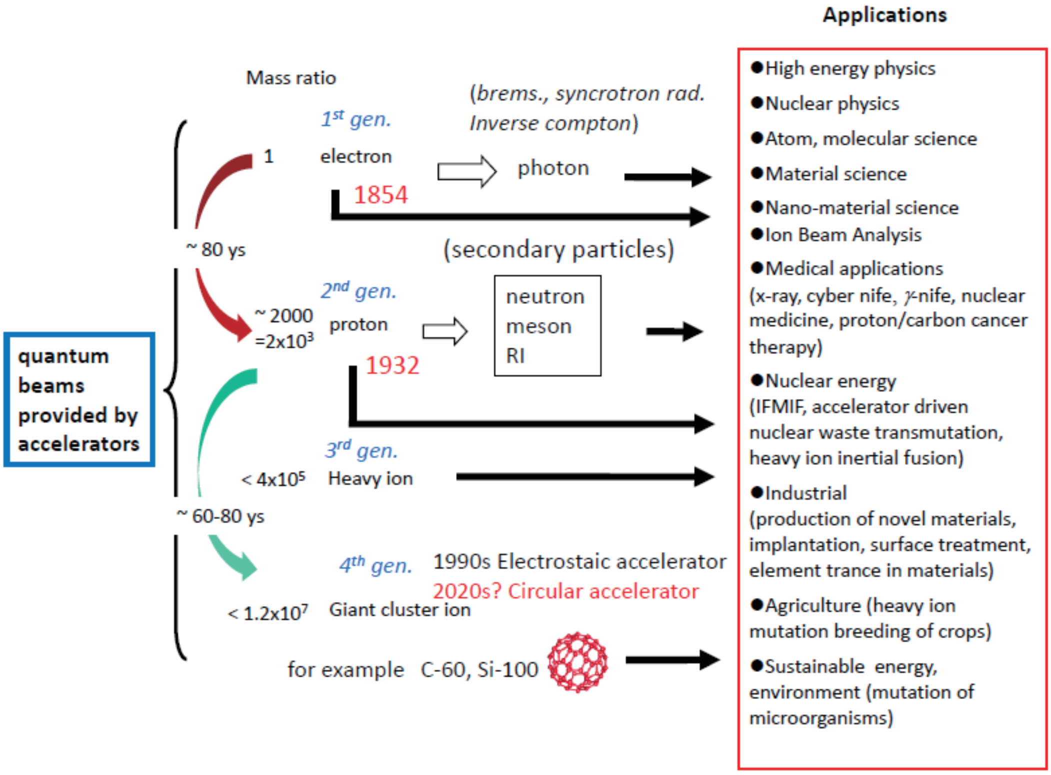

Figure 1: Generation of the quantum beams and their applications

Historically the quantum beam related science has been initiated since the entry of the 1^{st} generation and discretely and quickly evolved by the entry of succeeding generations. Large mass difference among the generations results in notable varieties of acceleration technology discussed in details later. In addition, the big difference of mass-to-charge ratio between the generations and even among the same generation poses significant restrictions on acceleration technique, since the mass-to-charge ratio straightforwardly determines acceleration efficiency. Consequently, a desired type of accelerator depends on the generations and a mass-to-charge ratio of accelerated ion.

The accelerators that have been invented and utilized so far can be clearly classified by the characteristics of accelerating electric field or the physics law that governs an operation principle of their acceleration devices. There are three sorts of electric field (EF) of static EF, induced pulse EF, and oscillating EF. The electrostatic EF is governed by the Gauss law, the induced pulse EF by the Faraday law, and the last oscillating EF by a full set of Maxwell equations with boundary conditions. The induced pulse EF and oscillating EF change in time; the former is produced in a way of transformer and the latter is excited in a resonant cavity. Here we call accelerators employing the induced pulse EF and the oscillating EF a resonant type and non-resonant type, respectively. In addition, the accelerators are divided into two groups of linear accelerator and circular accelerator from their geometrical configuration. It is well-known that electrostatic accelerators had been established just after their demonstration and resonant type accelerators had quickly evolved with a help of extensive developments in microwave and RF technology during World War II since their inventions. Classification of accelerators is summarized in Fig.2.

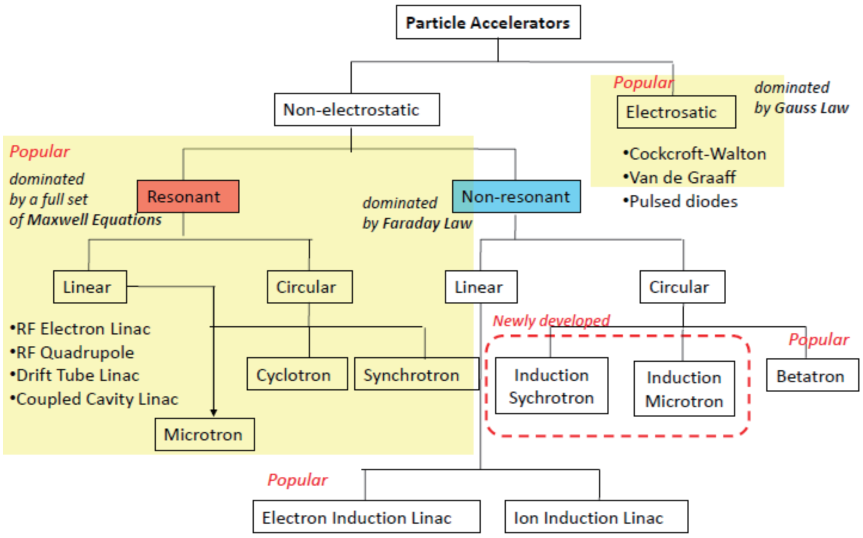

Figure 2: Classification of accelerators [1]

Through the following sections, let us follow more details of the historical evolution, focusing on what is their root?, who are primary contributors?, and how do they interrelate with various type of accelerators?,

2. Evolution from the dawn of accelerator to World War II

The first quantum beam was generated by J. Plucker in 1854 using his invention, the cathode ray tube. At that time, however, he didn't realize what the beam was. The cathode ray tube is an ancestor of all accelerators that have since been developed. It is a single gap accelerator and, of course, its beam is an electron beam—a fact that was recognized by J. J. Thomson in 1897. The X-rays emitted as Bremsstrahlung when an electron accelerated over a few tenths of a kilovolts hits a metal, also known as Röntgen rays, have been used for medical applications. These days, the direct use of electron beams and converted X-rays or γ-rays is quite popular.

Anticipating the need for further high-energy acceleration, G. Ising proposed a two-gap accelerator in 1924 but was not able to demonstrate the idea himself. Instead, R. Widerøe, who was a doctoral student in Karlsruhe University, demonstrated the concept in 1928 by successfully accelerating hydrogen ions, and published his experimental results in German. The history of multi-gap acceleration started with this demonstration and this two-gap accelerator is the forebear of microwave linear accelerators for electrons and RF linear accelerators for hadrons, both of which were rapidly developed after World War II because microwave/radio frequency (RF) technology had been extensively developed as part of the war effort. In his thesis in 1928, Widerøe proposed the betatron, in which temporally ramping guide fields provide an acceleration voltage induced along a circular beam orbit following Faraday's law, although he couldn't build one. The betatron was experimentally realized by D. Kerst of the State University of Illinois in 1941. It quickly became popular as a driver accelerator of electrons to generate hard X-rays. As a matter of fact, one US vendor provided 20 MeV betatrons to the lithography market during and after World War II.

E. Lawrence found the original paper of Widerøe in the library and immediately noticed that the idea could be employed in a circular accelerator. In one week, he summarized his idea of a cyclotron and then tried to demonstrate his idea with the help of his graduate student. In 1931 they demonstrated the palm-top baby cyclotron, which is exhibited in the Lawrence Berkeley National Laboratory (LBNL) museum. The cyclotron quickly evolved in the following 10 years and Lawrence was awarded the 1939 Nobel Prize in Physics for the invention of the cyclotron and its applications. After that, many cyclotrons were constructed and used to accelerate second-generation quantum beams of protons and third-generation quantum beams of heavy ions for nuclear physics and the production of radioisotopes in the US, Europe, and Japan.

Today, lower energy proton cyclotrons (< 20 MeV) are used as driver machines in nuclear medicine for positron emission tomography (PET) and single-photon emission computed tomography (SPECT). Medium-energy neutron cyclotrons (~ 30 MeV) are used as drivers for boron neutron capture therapy (BNCT). Higher energy cyclotrons (200 MeV) are typical cancer therapy proton drivers, and much higher energy heavy ion cyclotrons (> 20 MeV/au) are extensively used to induce mutations for research in Japan.

An electron cyclotron, which was later called the microtron, was proposed by V. Veksler of the USSR in 1944. The idea of using fixed magnetic fields for beam guidance is the same as that of the cyclotron but the acceleration fields are microwaves rather than RF waves. Its later name originates from the use of microwaves. A similar concept was independently proposed by J. Schwinger and L. Schiff in 1946, and by Japanese physicists J. Ito and D. Kobayashi in 1947. Since its first demonstration in Canada, it has become popular as a medium- to high-energy electron driver for nuclear physics. The guiding magnet in recent high-energy microtrons is split into two or four pieces to reduce the size of the accelerator; the resulting shape of the accelerator has led to it being called the racetrack microtron. Such machines are provided by several vendors as small synchrotron light sources.

At the same time, electrostatic accelerators were being developed to accelerate second- and third-generation quantum beams. Using the so-called Schenkel circuit, J. Cockroft and E. Walton constructed an extremely high-voltage generator (690 kV) to accelerate protons in 1932. They realized the first artificial nuclear reaction using their device, and were awarded the 1951 Nobel Prize in Physics. This type of high-voltage generator is now called a Cockloft-Walton generator and is a standard device for obtaining a stable, high voltage. Another type of accelerator is the Van de Graaff generator, which is named after its inventor. It is a unique device where charge is mechanically transferred to an electrode to generate an extremely high voltage between the electrode and the ground.

Van de Graaff demonstrated the original 1.5 MV device in 1931 but the rubber belt employed in the device quickly wears out and has to be replaced. R. Herb invented a metal/ceramic pellet belt to use instead of the rubber belt in 1965; this type of accelerator has been called a Pelletron. Van de Graaff also invented a tandem accelerator into which negative ions are injected from the ground potential side, negative charge is stripped through a loaded gas chamber placed in the center of the device, and the positive ions propagate in the other direction while being further accelerated. The voltage stability of electrostatic accelerators is excellent. This is the main reason why ion beam analysis, such as accelerator mass spectrometry, relies on electrostatic accelerators. In addition, electrostatic accelerators allow acceleration of any ion species with all their possible charge states, which is not possible when using RF accelerators employing time-varying electric fields as an acceleration medium. In the early days of synchrotron development, this type of electrostatic accelerator used to be employed as a pre-injector in the synchrotron accelerator complex. However, these days many low-voltage Cockroft-Waltons (100-300 kV) are used as heavy ion implantation drivers. A limited number of vendors share the world market.

3. after World War II

E. McMillan, who had been working on the Manhattan Project and had just started to consider rebuilding his science career after returning to the Berkeley campus, invented the synchrotron in 1945. Veksler also came up with the same concept in the same year. In a synchrotron, stability in the moving direction is guaranteed by the sinusoidal RF voltage profile. The synchrotron is characterized by its constant beam orbit throughout the entire acceleration period. The beam orbit is supported by time-varying magnetic guide fields and the RF frequency has to be changed as the beam is accelerated. This is the exact opposite of the cyclotron, where the beam orbit follows a spiral path and the RF frequency is constant in the low-energy case. The characteristic of a fixed beam orbit from injection to extraction means that the beam energy can, in principle, be increased without limit by increasing the number of guiding magnets. Thus, the concept of the synchrotron opened up the path to extremely large accelerators. The US Atomic Energy Commission approved the construction of two large synchrotrons (the 3 GeV Cosmotron and the 6 GeV Bevatron, proposed by Brookhaven National Laboratory (BNL) and LBNL, respectively) in 1948. The revolutionary idea of the strong focusing principle, which allows a remarkable reduction in the size of guiding magnets and had originally been found by Christofilos in 1950, was independently recognized by E. Courant, H. Snyder, and M. Livingston of BNL in 1952. One month after publication of the paper describing the strong focusing principle, T. Kitagaki of Tohoku University added the further crucial idea of separating the functions in the guiding magnet: the bending magnet with a gradient is split into a flat bending magnet and a pure quadrupole magnet. Thus, most of the essential concepts, without which modern synchrotrons such as hadron colliders, high-intensity proton drivers, synchrotron radiation sources, and cancer therapy drivers would never have been realized, were in place by the early 1950s. McMillan was awarded the 1951 Nobel Prize in Chemistry.

It must be pointed out that the synchrotron is available for all generations of quantum beams once their revolution frequencies fall in the RF bandwidth. In this sense, the synchrotron is universal. However, an injector accelerator is required to meet the bandwidth limitation. This injector may be a linear or electrostatic accelerator in many cases.

Now let us return to linear accelerators. It is clear that there are different evolution paths for electron and hadron linear accelerators. Since an accelerated electron immediately achieves a relativistic speed close to the speed of light, a traveling wave linac is quite typical. In such a linac, the acceleration tube is energized with fixed frequency microwaves. Historically, S-band microwaves are common because the Stanford two-mile accelerator, which has long been a leading electron linac, chose 2.856 GHz. R&D of linear colliders has strongly promoted the introduction of high gradient linacs. It is well known that high-frequency microwaves, such as C-band and X-band microwaves, are an effective means for obtaining a high acceleration gradient. So far, spin-offs from this technology include compact electron drivers in X-ray sources for cancer therapy and in X-ray/neutron sources for nondestructive analysis.

Linear accelerators for hadrons are very different from electron linear accelerators because of the particles' larger masses. As the particle's velocity gradually increases under the constant accelerating fields, the accelerating structure itself must be changed so as to maintain synchronization with time-varying, constant-frequency RF fields. The drift tube linac (DTL), which meets this demand, has been extensively developed since 1945. L. Alvarez and W. Panofsky played an important role in the construction of the first full-scale DTL in 1947, which accelerated a proton beam to 32 MeV at 200 MHz.

This has been the standard model of proton linear accelerators since then. In 1970 M. Kapchinsky and V. Teplyakov invented the radio-frequency quadrupole (RFQ) which simultaneously provides the necessary acceleration fields and focusing forces in the transverse direction. However, fabrication of complicated electrodes varying along the beam orbit could not be realized without a numerically controlled milling machine; but the RFQ quickly became popular in the accelerator community after its first demonstration at Los Alamos National Laboratory (LANL) in 1980 and replaced most of the Cockroft-Walton and Van de Graaff generators being used as pre-injectors for synchrotron accelerator complexes. These days a lot of RFQs are used in low- and medium-energy stand-alone proton accelerators to generate neutrons or radioisotopes. Alvarez was awarded the 1968 Nobel Prize in Physics for his decisive contributions to elementary particle physics.

Finally, we have to see what has evolved from the original betatron. In the 1950s, Christofilos and Veksler independently proposed a linear betatron or induction linac, in which the voltage induced at the secondary loop of a single one-to-one pulse transformer is used as an acceleration medium and many pulse transformers are connected in series along the beam path. The biggest induction linac, which is called the Advanced Test Accelerator and is capable of accelerating a 10 kA electron beam up to 50 MeV, was constructed at Lawrence Livermore National Laboratory (LLNL) in 1983. A small-scale ion induction linac is under development by an LBNL and LLNL collaboration. The aim is to create a heavy ion inertial fusion driver. The induction synchrotron−in which a pulse transformer capable of generating the necessary acceleration voltage pulses at 1 MHz instead of RF is introduced into a conventional RF synchrotron−was demonstrated at the High Energy Accelerator Research Organization (KEK) in 2006. Since this novel accelerator has no frequency bandwidth limitation, any ion species with all its possible charge states can be accelerated just as in electrostatic accelerators. This allowed us to realize a compact synchrotron without a large-scale injector, such as an RFQ or RFQ/DTL. Recent high-power solid-state switching devices, such as Si-MOSFETs or SiC-JFETs, that trigger the switching power supply energizing the pulse transformer play a crucial role in 1 MHz operation.

The requirement for high energies has been the continuous driving force in accelerator design. Now fourth-generation of quantum beams, consisting of cluster ions with a large mass-to-charge ratio of 100-1000, has appeared. Cluster ions accelerated by low-voltage

(< 300 kV) electrostatic accelerators are known to be very effective for surface manipulation of materials. Their acceleration to high energy by introducing a novel circular induction accelerator, such as an induction microtron, is under development. Although the research is in its early stages, high-density energy deposition by cluster ions, such as C-60 and Si-100, in a target material is expected to create extreme non-equilibrium states resulting in novel materials.

Figure 3a and 3b summarize the above explanation in a simple manner.

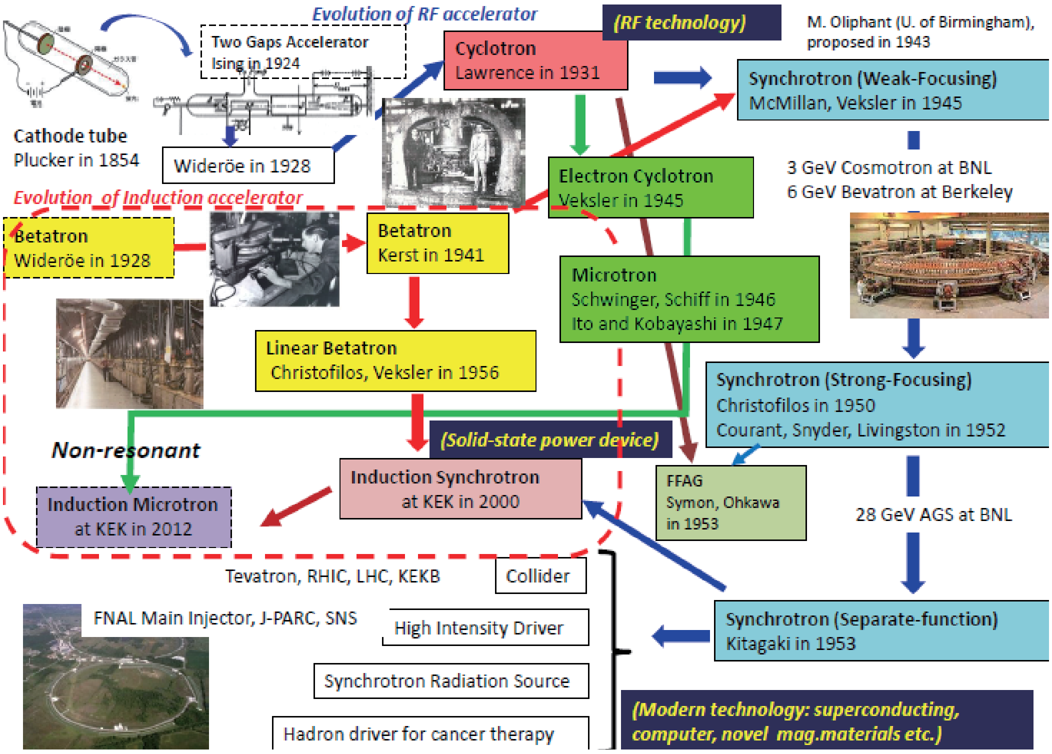

Figure 3a: Historical evolution of circular accelerators

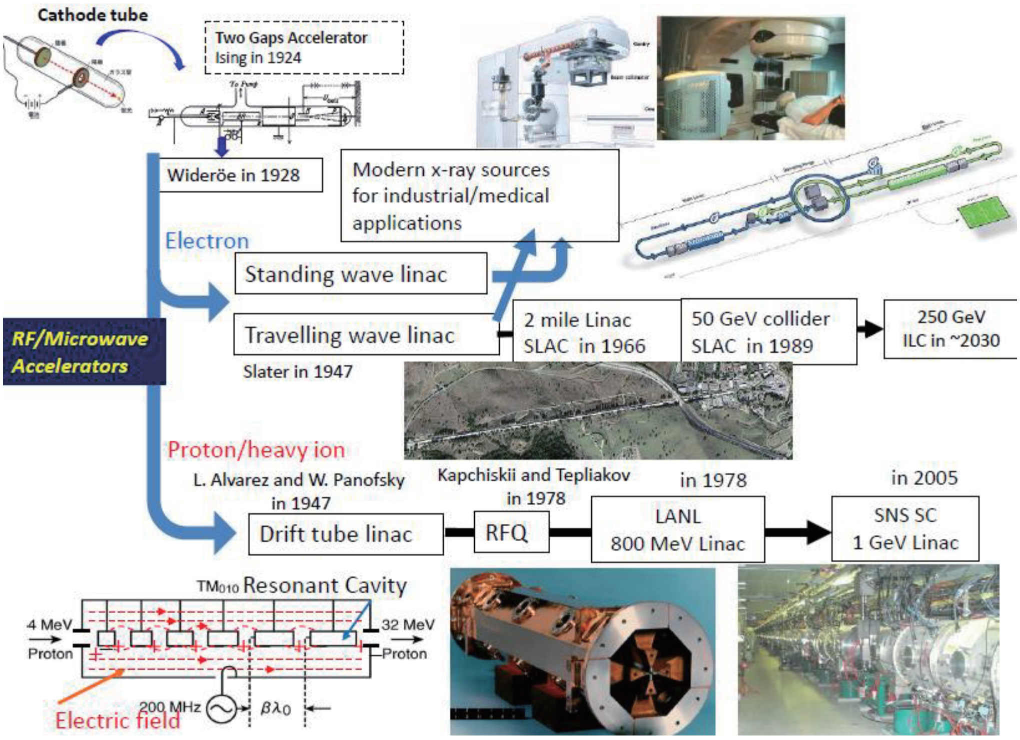

Figure 3b: Evolution of linear microwave/RF accelerators

Reference

[1] Ken Takayama and Richard J. Briggs: Induction Accelerators, (Springer, Berlin Heidelberg, 2011).

This is a blank page.

11 Current Status of Pulsed Spallation Neutron Source of J-PARC

Hiroshi TAKADA
J-PARC Center, Japan Atomic Energy Agency
Tokai-mura, Naka-gun, Ibaraki-ken 319-1195 Japan
e-mail: takada.hiroshi90@jaea.go.jp

Neutronic performance of the pulsed spallation neutron source of J-PARC and the efforts to achieve the goal of operating the mercury target system with a 1 MW proton beam are overviewed.

1. Introduction

At the Japan Proton Accelerator Research Complex (J-PARC), a pulsed spallation neutron source[1] has been operated by a 3 GeV proton beam at a repetition rate of 25 Hz since 2008. A neutron production mercury target and three types of liquid hydrogen moderators surrounded by a reflector with inner beryllium and outer iron are key components to provide high intensity and/or narrow-width neutron pulse. Actually, it was measured at a low power operation that high neutron intensity of 4.5 x 10^{12} n/cm^2/s/sr could be emitted from the coupled moderator surface for the 1 MW operation, and a superior resolution of $\Delta d/d$ = 0.035% was achieved at the beamline BL08 with the poisoned moderator, where d is the d-spacing of reflection.[2] Toward the goal to achieve the facility operation at 1 MW for 5000 h in a year, there are some critical issues on the target operation. One is to mitigate cavitation damage on the target vessel front, which was made of 3 mm thick 316L stainless steel, by the pressure wave generated in mercury by the pulsed proton beam injection. The other is to re-design the target vessel structure because there were failures twice[3] in the water shroud of the target vessel during operating periods at 500 kW in 2015. Furthermore, reducing the amount of gaseous radioactive materials released in the target replacement is important. The Spallation Neutron Source (SNS)[4] at the Oak Ridge National Laboratory has already accomplished the user program at 1 MW using the mercury target system. Considering the repetition rate of proton beam is 2.4 times lower than that of SNS (60 Hz), the power region above 500 kW is still untraversed in the world for the mercury target of J-PARC.

2. Neutronic performance of target-moderator-reflector system

Figure 1 shows the 3-D view of the neutron source station, in which the mercury target and liquid hydrogen moderators surrounded by the reflector are enlarged. Neutroics and shielding designs were conducted in early 2000s using the Nucleon Meson Transport Code NMTC/JAM[5] with the neutron-photon transport code MCNP-4C[6]. The accuracy of the code system was evaluated to be less than a factor of two by the results of a series of spallation experiments[7] with a thick mercury target conducted at Brookhaven National Laboratory.

The moderator size was optimized to generate high intensity and/or good pulse-shaped cold neutrons for 100% para-hydrogen as moderator material. Each moderator has following distinctive features[2]: 1) the coupled moderator (CM) has cylindrical shape with 14 cm diameter and 12 cm long for providing high intensity neutrons to wide angles of 50.8 degree from a cylindrical surface and 45 degree from the reverse one, 2) the de-coupled moderator (DM) equips neutron absorber made from Ag-In-Cd alloy on the outside to make pulse width narrower and pulse tails lower, with a decoupling energy of 1 eV, and 3) the poisoned moderator (PM) equips 2 mm thick Cd plate inside to make pulse shape shorter than the CM. To maximize the neutron intensity, the CM was arranged beneath the mercury target while DM and PM were placed upper side of the target. An inner beryllium with outer iron reflector was chosen, where the inner and outer diameter was 50 cm and 100 cm, respectively. In Figure 2, neutron flux spectrum measured at the neutron instrument BL10 which views the PM are plotted with calculated one.

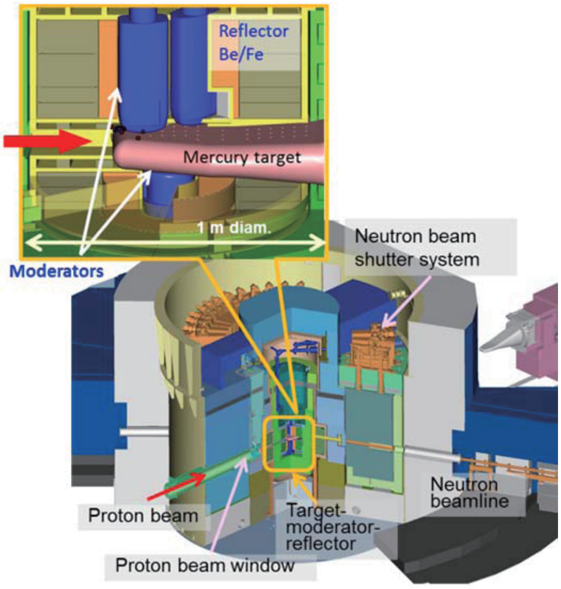

Figure 1 Three dimensional view of the target station of the pulsed spallation neutron source of J-PARC

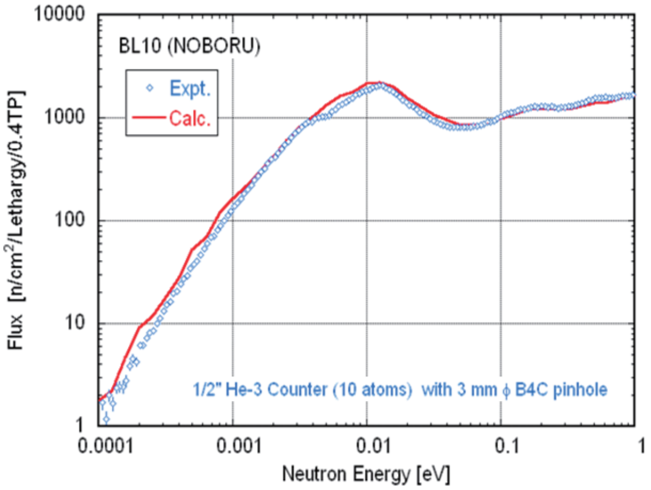

Figure 2 Neutron spectra measured at neutron instrument BL10 with a 1/2 inch diameter ^{3}He counter in comparison with calculated one[2]

3. Efforts to mitigate cavitation damage on target vessel front

For mitigating cavitation damage on the target vessel, a technology to use gas micro-bubbles has been developed at J-PARC.[8] Mitigation mechanisms with micro-bubbles are as follows: 1) absorption of thermal expansion of mercury at the incidence of proton beam pulse, pressure wave, attenuation of pressure wave by volume oscillation of the bubbles and the thermal dissipation between bubbles and mercury. As a result of off-beam[9] and on-beam[10,11] experiments, it was demonstrated that the pressure wave could be mitigated effectively by supplying micro-bubbles with a diameter less than 100 μm so as to occupy the void fraction of 10^{-5} to 10^{-4} at the target vessel front. In order to make bubbles distribute uniformly in mercury, especially in vertical direction because bubbles are subject to strong buoyancy due to mercury has large density of 13.3 g/cm^3, a swirl type bubbler was developed.[12] Figure 3 shows an illustration of mercury circulation system. The helium gas enclosed in the surge tank is pressurized by a compressor, and so could flow towards the bubbler in the target vessel. Figure 4 shows the displacement velocity measured on the target vessel at the moment that a pulsed proton beam was injected. The displacement velocity for the 1 MW case with the gas micro-bubbles injection (red line) is equivalent to the velocity obtained for the 310 kW case without the gas micro-bubbles injection (blue line), indicating that the pressure wave generated in mercury for the 1 MW operation could be mitigated to one-third owing to the gas micro-bubbles injection.

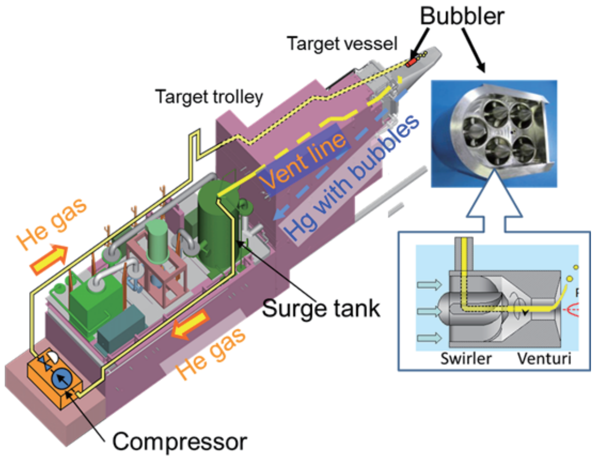

Figure 3 Three dimensional illustration of the mercury circulation system. Pictures of the swirl bubbler are also depicted

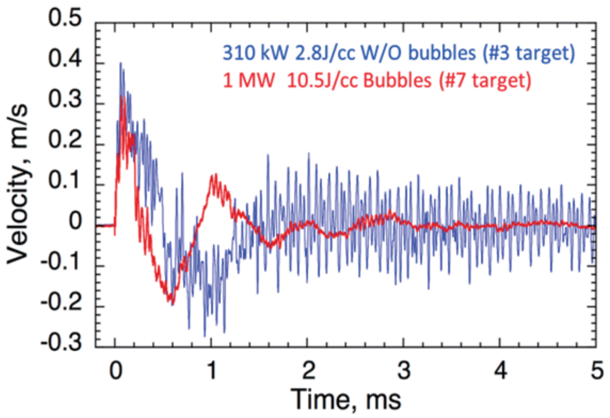

Figure 4 Displacement velocities of the mercury target vessel measured with a laser Doppler vibrometer

Furthermore, structure of the target front was modified to have double wall[13] so as to make faster mercury flow in a narrow channel with a gap of 2 mm, because it was demonstrated in the experiments[10,14] that cavitation damage could be suppressed in the narrow channel. Actually, no serious cavitation damage was observed in the actual target of the SNS for the1 MW operation. The effect of the narrow channel on the cavitation damage mitigation will be studied by cutting out a specimen from the target vessel front after operation.

4. Re-design of target vessel

The mercury target vessel is covered with a water shroud to confine mercury inside the interstitial space between them what if it is leaked from the mercury target vessel, where the water shroud consists of internal and external vessels with 3 mm thick each to have coolant channel in it. There are ribs on the internal vessel and their top surfaces are fixed with the external vessel by diffusion bonding. Then, the water shroud is bolted on the mercury vessel at 177 positions to endure an inner helium gas pressure of 0.2 MPa.

For the first failure, the location was specified at a welded interface between the internal and external shroud vessel in the vicinity of a bold on target vessel's bottom. (see Figure 5).[3] Our analyses confirmed that the diffusion bonding interface was detached by welding thermal deformation in the fabrication process, followed by seal welding failure by the crack propagation induced by repeated thermal stress caused by beam trips. Because the structure of the next target vessel was the same, we repaired the seal welding around all bolts to the full penetration welding before replacement.

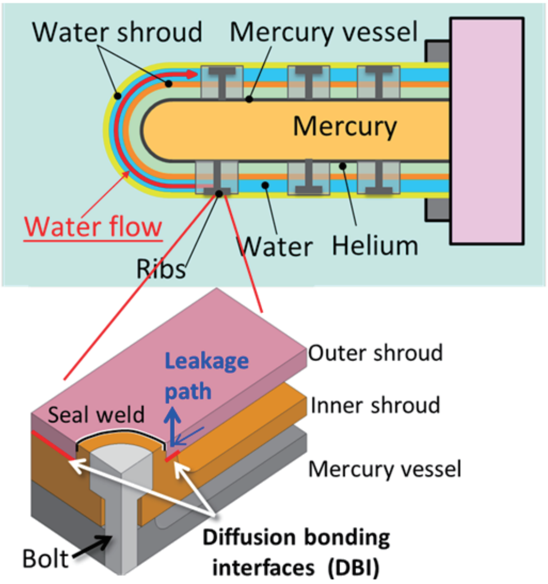

Figure 5 Schematic drawing of the specific location of the failure on the water shroud of the target vessel

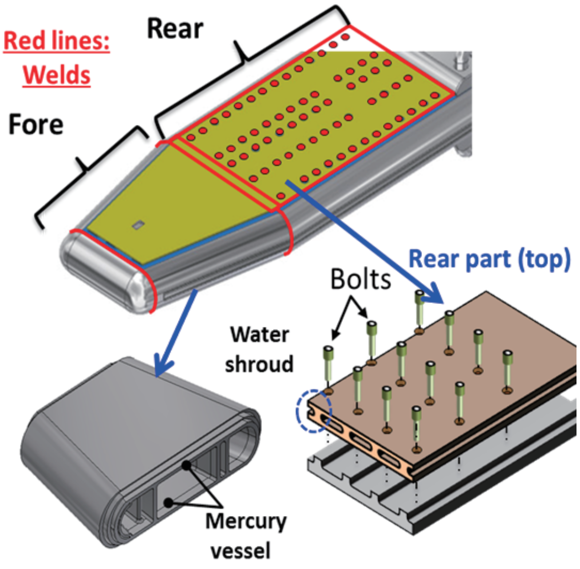

Figure 6 Schematic drawing of the re-designed target vessel structure

However, the second failure took place in the inner water shrouds of the replaced target. It was difficult to inspect the inside of target vessel at J-PARC, After reviewing the fabrication process and analytical studies, possible cause was that pressure wave induced stress might have expanded a crack existed at certain welding location to a leak path.

Based on these lessons, we have re-designed the target vessel structure to improve robustness. The fore part was changed to be a monolithic structure of mercury vessel and water shroud to eliminate welds and bolts from high stress region (see Figure 6). The water shroud of the rear part was also changed to be monolithic. We will improve the inspection process to employ radiation tests and ultrasonic test much more.

5. Efforts to reduce tritium release from target vessel replacement[15]

It was estimated that 1 x 10^{14} Bq (100,000 GBq) of ^{3}H might be generated in the mercury target after irradiation of 5000 MWh, the design lifetime. The allowable value for the ^{3}H release is 25000 GBq per 3-month at the stack of the building. An off-gas processing system[16] is equipped to collect gaseous radioactive materials, especially Xe-127 and ^{3}H into tanks from the cover gas of the mercury circulation loop before removing the target vessel at the replacement. At the first target replacement in 2011, about 150 GBq of ^{3}H was released unexpectedly from the stack although the accumulated beam power was low of 450 MWh.

Major mechanism of the ^{3}H release was the isotope exchange reaction between ^{3}H stuck in the target vessel and the moisture in air that comes into the target vessel at the moment of removal. At the target vessel #3 replacement after the irradiation of 2050 MWh in 2014, we took measures to suppress ^{3}H release: 1) filling helium gas in the target system slightly above 0.1 kPa, 2) evacuating the target system by the off-gas process system, and 3) plugging the open holes (ca. 5 cm diameter) after the specimen cut-out and those of mercury pipes (150A x2) after the target vessel removal, respectively.

In the end, radioactivity of ^{3}H released uncontrollably was suppressed to be 39 GBq as a result of analyzing the silica gel at the stack of the building. This amount is only about 6% of that released from the first replacement in 2011. On the other hand, 4200 GBq of ^{3}H was collected in the off-gas system according to a measurement with an ionization chamber. The collected ^{3}H was released from the stack with controlling the daily amount to be released.

6. Conclusions

The pulsed spallation neutron source of J-PARC has demonstrated at a low power operation that it could provide high neutron intensity of 4.5x10^{12} n/cm^2/s/sr from the coupled moderator with 100% para hydrogen for the 1 MW operation. Also, it is providing the neutron pulse with superior resolution of $\Delta d/d = 0.035\%$ from the poison moderator. Those neutronic performances were in good agreement with the value obtained in the neutronic design.

To achieve the goal to operate the mercury target with 1 MW proton beam, we have been making efforts to mitigate the pressure waves induced in the mercury target with injecting gas micro-bubbles less than 100 μm in diameter. We are also paying attention to suppress the amount of ^{3}H release through the target vessel replacement operation in view of radiation safety. So far, promising results were obtained for both subjects.

At present, re-design to improve the robustness of the mercury target is urgent issue to recover operational beam power higher than 500 kW. New target vessel eliminating welds and joint with bolts from high stress region in the target front is under fabrication.

Acknowledgements

The author would like to thank the staff of neutron source section of the J-PARC center of JAEA for their contributions to the target-moderator-reflector system operations. He also appreciates the staff of radiation safety section of the J-PARC center for their cooperation to measure tritium during the target replacement.

References

[1] Neutron Source Section: "Technical Design Report of Spallation Neutron Source Facility in J-PARC, "JAEA-Technology 2011-035 (2012).
[2] F. Maekawa, *et al.*: Nucl. Instrm. Methods. Phys. Res. A 620, 159 (2010).
[3] J-PARC Center: "J-PARC ANNUAL REPORT 2015 Vol.2: Materials and Life Science Experimental Facility," J-PARC 17-01 (2017).
[4] J.R. Haines, *et al.*: Nucl. Instrm. Methods Phys. Res. A 764, 94 (2014).
[5] K. Niita, *et al.*: Nucl. Instrm. Methods Phys. Res. B 184, 406 (2001).
[6] J.F. Briesmeister (ed.): "A General Monte Carlo N-Particle Transport Code, Version 4C," LA-13709-M (2000).
[7] H. Nakashima, *et al.*: J. Nucl. Sci. Technol. Suppl. 2, 1155 (2002).
[8] For example, T. Naoe, *et al.*: J. Nucl. Sci. Technol., 48, 865 (2011).
[9] M. Futakawa, *et al.*: J. Nucl. Sci. Technol., 45, 1041 (2008).
[10] B. Riemer, *et al.*: J. Nucl. Mater., 377, 162 (2008).
[11] B. Riemer, et al.: J. Nucl. Mater., 450, 192 (2014).
[12] H. Kogawa, *et al.*: J. Nucl. Sci. Technol., 56, 1461 (2015).
[13] K. Haga *et al.*: JPJ Conf. Proc. 8, 051008 (2015).
[14] T. Naoe, *et al.*: Transactions of the JSME, 80, FE0025 (2014). (in Japanese).
[15] H. Takada, *et al.*: "Progress of Target System Operation at the Pulsed Spallation Neutron Source in J-PARC," Proc. of AccApp'15, Washington D.C., November 10-13, 2015, p.297 (2016).
[16] T. Kai, *et al.*: Prog. Nucl. Sci, Technol., 4, 380 (2014).

12 Current Status of Carbon-ion Radiotherapy in Japan

Naruhiro MATSUFUJI
National Institute of Radiological Sciences,
National Institutes for Quantum and Radiological Science and Technology
9-1, Anagawa-4, Inage-ku, Chiba-shi Chiba 263-8555 Japan
e-mail: matsufuji.naruhiro@qst.go.jp

Carbon-ion radiotherapy was started in 1994 in Japan and more than 10,000 patients have been treated so far. Reflecting the unique physical and biological characteristics of the ion beams, the clinical outcomes show superior efficacy of this modality even against radioresistant tumour while keeping the quality of life at high level. Meanwhile, hardware and software technology related to the carbon-ion radiotherapy have been continuously improved such as 3D scanning beam-delivery technique with superconducting rotating gantry, or microdosimetry-based radiobiological modeling for treatment planning. As of 2016, in total five carbon-ion radiotherapy facilities have been in operation in Japan.

1. Introduction

Elevating energy loss of ion beams traveling in a matter toward its range end, known as Bragg curve, is attractive characteristics to treat deep-seated tumour in a patient's body while sparing surrounding normal tissues at the same time. By physics nature, as the incident ion gets heavier, the width of the Bragg peak gets sharper due to suppressed multiple scattering. On the other hand, the height of the peak gets substantially reduced due to increased nuclear fragmentation. The extent of the dose localization therefore reaches the optimum at certain ion species depending on therapeutic situation. In addition, ions in proximity to carbon has favourable characteristics from biological viewpoint. Their RBE (relative biological effectiveness) gradually increases as the energy loss increases, *i.e.,* from entrance to the Bragg peak. This increase in RBE tends to enhance the peak-to-plateau ratio of the Bragg curve from therapeutic viewpoint. This enhancement of the peak-to-plateau ratio weighted by RBE is not significant for lighter ions and, gets diminished in reversal for further heavier ions, known as the overkill effect because of delivering too much energy locally than required to inactivate a cell. From these aspects among various ion species, carbon ion is regarded to be one of the most advantageous ion species for therapeutic application as a method to achieve both high clinical effect on tumour and low toxicity on normal tissues at the same time.

The first ion-beam radiotherapy (ion-beam RT) was accomplished by the Lawrence Berkeley Laboratory (LBL) [1] with the Bevatron synchrotron dedicated for physics study. When the pioneering clinical trials at the LBL came to the end in 1993, world's first accelerator dedicated for ion-beam RT, HIMAC (Heavy Ion Medical Accelerator in Chiba) [2], was established at NIRS (National Institute of Radiological Sciences) and started carbon-ion radiotherapy (C-ion RT) in 1994. Soon after, German first C-ion RT facility was built at the Gesellschaft für Schwerionenforschung mbH (GSI) in Darmstadt and started clinical trials in 1997 [3]. As of 2016, 10 ion-beam RT facilities have been in operation in the world with carbon ions [4].

2. Status of C-ion RT in Japan

2-1. Facility status

The HIMAC project was aimed at establishing the optimum ion-beam RT modality. Figure 1 shows the bird's eye view of the HIMAC facility. The main synchrotron ring is doubled and can be operated independently. HIMAC has 3 treatment rooms (room A, B and C) in the building. Rooms A and C are equipped with one vertical or horizontal port, respectively while room B has both ports. In addition, experimental rooms for physics and biology are prepared and open for fundamental research with ion beams. HIMAC supplies only carbon ion beams to treatment rooms for therapeutic purpose in daytime, and various ion beams ranging from H to Xe up to 800 MeV/n for the experimental research in night time.

Next to HIMAC, Hyogo Ion Beam Medical Centre (HIBMC) [5] project was started. HIBMC offers both proton and C-ion RT in one machine first in the world since 2003 and 2004, respectively. Successively, development of hospital-based compact C-ion RT machine was funded in the third decade of the cancer control strategy started in 2004. In this framework, the GHMC (Gunma University Heavy Ion Medical Centre) project [6] has been carried out C-ion RT since 2010. SAGA HIMAT (Saga Heavy Ion Medical Accelerator in Tosu) [7] also adopted the similar design and has started the clinical operation in 2013. The newly developed techniques at NIRS have been continuously transferred to the successive facilities. i-ROCK [8], C-ion RT facility at Kanagawa Cancer Centre has started the C-ion RT in the end of 2015 with the updated beam-delivery technique, 3D scanning.

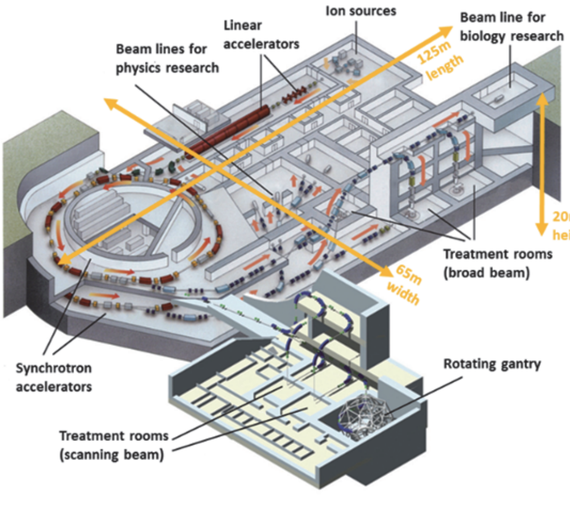

Figure 1 Bird's eye view of HIMAC facility

2-2. Clinical status

Figure 2 shows the patient distribution statistics treated at HIMAC at the end of FY2016. The first majority of patients treated so far is those suffered from prostate cancer, followed by those with solid tumours occurred at various sites. Most of clinical trials have been promoted to clinical practice by the approval by Government of Japan as the "Advanced Medical Technology" in 2003. Under this category, 3.14 M JPY is charged per treatment. Since 2016, C-ion RT for inoperable bone and soft tissue sarcoma has been covered by Japanese national health insurance.

Because of the superior dose localization, one of the theme on clinical trials at HIMAC is to exploit the possibility of the hypofractionation regime. In each fraction schedule, dose escalation study was carried out in order to find the optimum dose level to prescribe by carefully observing the normal tissue response. The ultimate is the non-small cell lung cancer treatment. The treatment with carbon ions was carried out in 18 fractions in 6 weeks at the beginning but now completed by successive 4 portal irradiations within one hour [9]. Throughout these clinical experiences [10], it was confirmed that normal tissue response is tolerable in most cases and QOL (quality of life) after the treatment has been kept at high level even under hypofractionation.

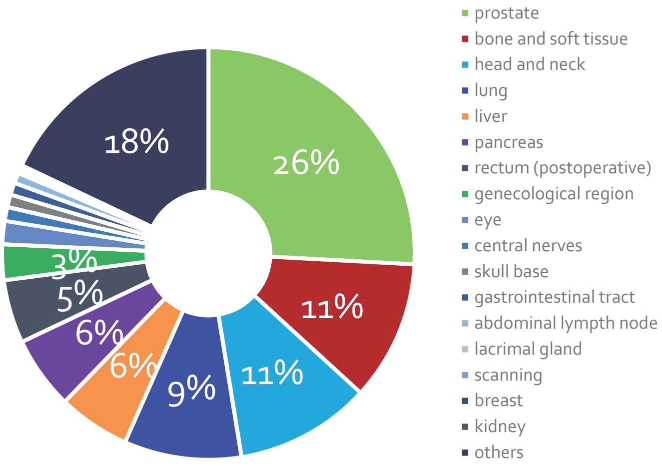

Figure 2 Distribution of patients at HIMAC by 2016

2-3. Improvements for C-ion RT

While promoting the C-ion RT, HIMAC has been kept on updating as a research facility. From the hardware viewpoint, the beam-delivery system has been improved to realize more localized and flexible dose delivery to tumour. At HIMAC, the therapeutic ports was originally configured based on a broad-beam irradiation method [11] to deliver the carbon-ion beam to tumour. In this method, a pencil-like beam extracted from the accelerator is at first circulated by a pair of dipole wobbler magnets. Then this ring-like beam passes through a thin metal foil as a scatterer inserted downstream of the wobbler magnets. At the isocenter located about 10 m downstream from the scatterer, beam size is broadened up to 200 mm in diameter with uniformity better than 95 %. This now dish-like beam is axially spread out up to 150 mm in water so that the spread out Bragg peak (SOBP) region covers the maximum target thickness by passing through a ridge filter made of tapered aluminium blades lined in parallel.

The resultant laterally and axially broadened beam is finally tailored by a collimator and a compensator manufactured to match the bulk beam to the cross section and distal plane of the individual target, respectively. In case of lung or liver cancer treatment, the beam is delivered only at the expiration phase.

The irradiation field by the broad-beam method is stable in time and space, which is favourable especially for the treatment of moving target by respiration [12]. On the other hand, the rigidness of the irradiation field made it difficult to optimize the dose distribution for individual patient. Due to the constant SOBP width irrespective to the difference in tumour thickness point by point, some portion of normal tissues inevitably receives full dose. In addition, the leading time necessary for manufacturing the collimator or the compensator also made it difficult to promptly adapt to the change in tumour shape. In order to overcome the problems, the development of the 3D scanning method [13] was started in 2007. In the method, a pencil-like beam extracted from the accelerator is directly delivered to appropriate position in the target and whole volume is scanned by the beam. A pair of scanning magnets is used to control the lateral position while the axial stopping point is adjusted by the accelerator by changing the beam energy dynamically within one extraction phase from 430 MeV/n down to 56 MeV/n in 250 steps. It should be noted that it was generally regarded difficult to apply the scanning method for the irradiation to the moving target because the interplay between the scanning process and target motion can spoil the dose uniformity easily. The 3D scanning technique developed at HIMAC tries to overcome this problem by a combination of gating and rescan feature [14]. During the irradiation, the position of the target is frequently monitored on an X-ray transmission imager [15]. The scanning irradiation takes place selectively when the target comes within a planned area in the expiration phase where the respiration motion is minimized. Trivial extent of movement within the expiration phase is statistically smeared out by swiftly repeating the scanning irradiation of one layer for several times in one expiration phase. In order to make the rescan possible, the scan speed reaches to 100 mm / 1 ms to the irradiation field size of 220 mm square. The scanning irradiation ports have been installed to a vertical and horizontal port of newly built room E and F in an annex building of HIMAC (see Fig. 1) in 2011 and used for routine C-ion RT since 2011.

There is one more treatment room in preparation as room G in the annex building. While the rooms E and F are identically equipped with stationary scanning irradiation ports, room G will have a rotating gantry [16] that enables irradiating beam from 360 degrees. The rotating gantry is *de-facto* standard configuration in modern intensity-modulated X-ray RT (IMRT) machine, and getting popular even for proton therapy, however, challenging for C-ion RT due to the large $B\rho$ value required for magnets to bend the therapeutic carbon-ion beam in a relativistic energy range. HIT (Heidelberg Ion Therapy Centre) [17] has realized the world's first rotating gantry applicable for C-ion RT. The construction has about 600 t of rotating weight with 20 m in diameter. The size of the gantry at HIMAC is reduced to be comparable to proton gantry, *i.e.*, 200 t in weight and 11 m in diameter by making use of compact superconducting magnets. Some of the magnets are designed as a hybrid of a dipole and a quadrupole in one magnet in order to further save the geometrical space. The 3D scanning technology is also integrated to the rotating gantry. The gantry will be enrolled in C-ion RT in 2017.

Effort has been paid also for software issues. As mentioned in the introduction, it is requisite to estimate the changing RBE value of carbon ions quantitatively and precisely to conduct the C-ion RT effectively and safely. In initiating the C-ion RT at HIMAC, the RBE value of human salivary gland (HSG) cells were chosen as the reference biological endpoint. The RBE value at the 10 % clonogenic survival level of the HSG cells was experimentally studied by changing the LET (linear energy transfer) of the carbon ions step by step. The derived dose-survival relationship at each LET was fitted with a commonly-used LQ model $S=exp(-\alpha D-\beta D^2)$ where S and D is the survival probability and the absorbed dose, respectively, and α and β are the fitting parameters. The derived α and β were tabulated as a function of LET, and looked up in designing the SOBP beam by mixing various residual-energy beams [11].

This approach was practically useful for estimating the RBE of therapeutic carbon-ion beams, however, the model was not appropriate for causal understanding between the "input", *i.e.*, radiation quality of the incident beam and the "output", observed radiosensitivity. From the viewpoint, the original model was updated to the Microdosimetric Kinetic Model (MKM) [18] when starting the scanning irradiation at HIMAC. The model introduces a micrometre scale unit region "domain". The number of biological lesions produced in the domain is associated with the specific energy z deposited there, and the cell survival probability is given from Poisson statistics when none of the domains in a cell nucleus develop any single lesion. The dose-survival relationship by MKM reaches to the following equation with α_0 and β as the LQ parameters for LET=0 radiation and z_{1D}^* as the saturation-corrected dose-averaged single event specific energy [19].

$$S(D) = \exp\{-[(\alpha_0 + \beta z_{1D}^*)D + \beta D^2]\}$$

Because specific energy z is measurable or calculable quantity for incident radiation, MKM makes it possible to estimate the extent of biological effectiveness of any radiation. MKM is tuned to harmonize with the original model [20] and now routinely utilized in a treatment planning system for both broad-beam and scanning irradiation [21].

3. Conclusion

C-ion RT has been carried out since 1994 in Japan. In more than two decades of experience, C-ion RT has been proven to be advantageous especially in treating radioresistant tumours such as bone and soft-tissue sarcoma, as well as in safely completing the course of the therapy even in short period as hypofractionation regime [22]. The high QOL and high clinical effectiveness of the C-ion RT will be advantageous in terms of cost effectiveness and contribute to sustainable development of the society. At the same time, research and development has been continuously carried out in order to further improve the ion-beam RT and further reduce the facility cost.

Acknowledgments

The Author wishes to acknowledge all the members at NIRS HIMAC.

References

[1] J. R. Castro, *Radiat. Environ. Biophys.* **34** 45-8 (1995).

[2] Y. Hirao *et al., Nucl. Phys.* A **538** 541-50 (1992).

[3] G. Kraft, *Nucl. Instr. and Method in Phys. Res. Sect.* A **454** 1-10 (2000).

[4] Particle Therapy Co-Operative Group (PTCOG), website URL: https://www.ptcog.ch/

[5] Y. Hishikawa *et al., Radioth. Oncol.* **73** S38-40 (2004).

[6] T. Ohno *et al., Cancers* **3** 4046-60 (2011).

[7] S. Kudo *et al., Int. J. Particle Therapy* **2** 464-7 (2016).

[8] Y. Nakayama *et al., Int. J. Particle Therapy* **2** 478-80 (2016).

[9] M. Karube *et al.*, *Int. J. of Radiat. Oncol. Biol. Phys.* **95** 542-8 (2016).

[10] H. Tsujii and T. Kamada, *Jpn. J. of Clin. Oncol.* **42** 670-85 (2012).

[11] T. Kanai T *et al., Int. J. of Radiat. Oncol. Biol. Phys.* **44** 201-10 (1999).

[12] S. Minohara *et al.*, *Int. J. of Radiat. Oncol. Biol. Phys.* **47** 1097-1103 (2000).

[13] T. Furukawa *et al., Med. Phys.* **37** 5672-82 (2010).

[14] T. Furukawa *et al., Med. Phys.* **37** 4874-9 (2010).

[15] S. Mori *et al., Int. J. of Radiat. Oncol. Biol. Phys.* **95** 258-66 (2016).

[16] Y. Iwata *et al., Nucl. Instr. and Method in Phys. Res. Sect.* B **317** 793-7 (2013).

[17] S. E. Combs *et al.*, *Radioth. Oncol.* **95** 41-44 (2010).

[18] R. B. Hawkins, *Radiat. Res.* **140** 485-96 (1994).

[19] Y. Kase *et al.*, *Radiat. Res.* **166** 629-38 (2006).

[20] T. Inaniwa *et al., Phys. Med. Biol.* **60** 3271-86 (2015).

[21] T. Inaniwa *et al.*, *Phys. Med. Biol.* **55** 6721-37 (2010).

[22] T. Kamada *et al., Lancet Oncol.* **16** e93-100 (2015).

13 High-Energy Neutron Measurement and Radiation Experiment of Particularity

Kenji ISHIBASHI

Department of Applied Quantum Physics and Nuclear Engineering, Kyushu University
Motooka, Nishi-ku, Fukuoka 319-0395 Japan
e-mail: kisibasi@nucl.kyushu-u.ac.jp

The author has studied for a long time in Kyushu University together with students and with supports of researchers of other universities and institutions. Before compulsory retirement, impressive works were recalled in the field of nuclear data and radiation measurement.

1. Introduction

After arrival at Department of Nuclear Engineering, Kyushu University, in 1982, the author was requested to start new research in Nuclear Engineering. As work in university, basic investigation was chosen on accelerator-driven subcritical reactor (ADS) for nuclear fuel breeding and transmutation of nuclear waste.[1] The field was not established in the nuclear engineering at that time, but it was anticipated to give a dream of new nuclear system to young students. The work in early time is summarized in this paper.

In the meanwhile, the author was interested in experimental search of new natural energy source in relation to weak interaction. After the preliminary measurement,[2] the experimental study has been suspended for more than ten years. Since it is not an established field, the work is classified into radiation measurement of particularity. The experiment was again carried out at nuclear reactor site in this fiscal year. The recent data and additional consideration are briefly presented, although detailed consideration are not fixed completely.

2. Neutron measurement and nuclear data

The ADS system requires a reliable accelerator which produces high-energy (~GeV) and high-intensity (~mA) protons. Experimental data on proton-incident neutron-production double-differential cross sections were required for the engineering purposes. Experiments on proton-incident proton-production cross-sections have already been carried out at KEK. However, low-energy nucleon emission data are available only by neutron measurement.

Our group measured the cross-sections at KEK 12-GeV proton synchrotron in the proton range of 0.8 to 3 GeV.[3] The experimental layout is illustrated in Fig. 1. A special care was taken to eliminate the floor scattered neutron effect. A short distance Time-of-Flight was adopted. The larger detectors were mounted at upward location on a frame being apart from the floor as seen in Fig. 2.

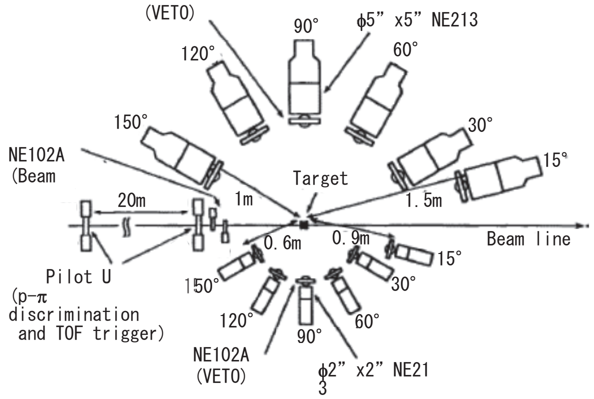

Fig. 1 Illustration of short range Time-of-flight neutron experiment for incident protons of 0.8 to 3 GeV

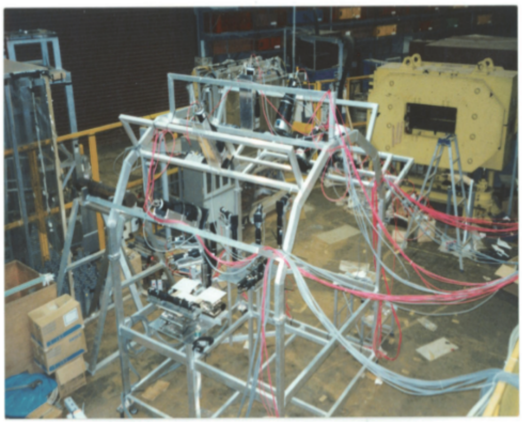

Fig. 2 Picture of neutron detectors. The larger detectors were mounted on upward position.

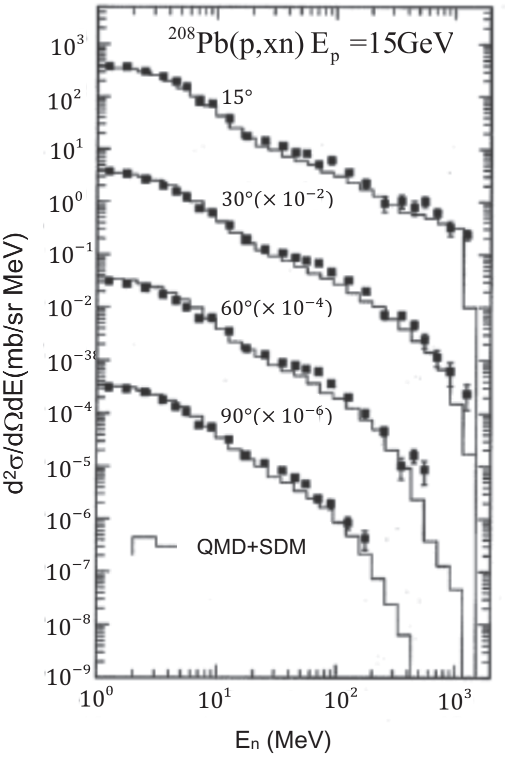

Fig. 3 Experimental data on proton-incident neutron-production cross section and calculation by K. Niita. S. Chiba et al.[4]

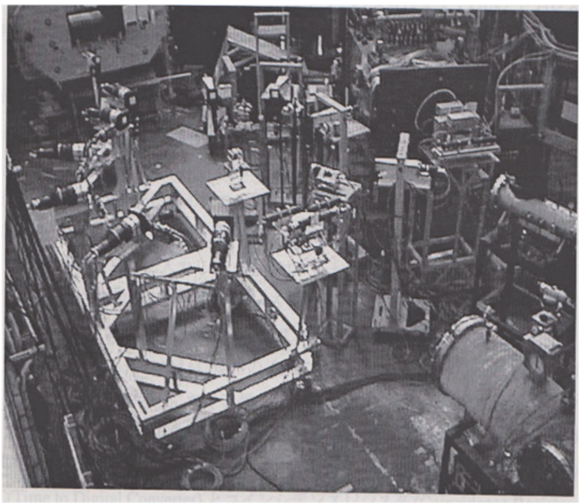

Fig. 4 Experimental layout adopted in later measurement. Floor scattering effect was eliminated by shadow bar experiment.

The cross section data may contribute to development of Quantum Molecular Dynamics code[4] of JAERI (JAEA), as shown in Fig. 3. The code was later utilized for nuclear data evaluation for JENDL High Energy File. The floor scattered neutron effect was confirmed to be eliminated by shadow bar experiment. For this reason, later measurement was carried out in a simple flat arrangement in Fig. 4, for pion incident experiments.[5] Neutron measurements were continued in such facilities as HIMAC and LANSCE WNR.

3. Radiation experiment of particularity

The radiation experiment of particularity was initiated for find a possible natural source of low-density power generation.[1] Experimental electrochemical device is shown in Fig. 5. The device was assembled in a Teflon container, and contained electrochemical gold and carbon electrodes with biological product of raw silk immersed in purified water. The experimental data are shown in Fig. 6. The lower cross and upper square marks stand for data under environmental circumstance and those at Advance Thermal Reactor FUGEN (165MWe, a distance of 18m) in the previous measurement.[1] The circular marks show the results at Pressurized Water Reactor (1GWe, a distance of 26m) in this fiscal year. Both reactor measurements (ATR, PWR) were performed in non-radiation control area, i.e. gamma rays and neutrons were well shielded down to background level. For this reason, the increase of signal at reactor sites is considered to be attributed to weak interaction near nuclear reactors.

The current by lower cross marks in Fig. 6 was observed under the environmental circumstance. The signal generation in environmental circumstance may also be ascribed to a kind of neutrinos (hereafter called as environmental neutrinos). However, neutrinos themselves should have quite small interaction cross sections, typically 10^{-44} cm^2 (E/MeV).

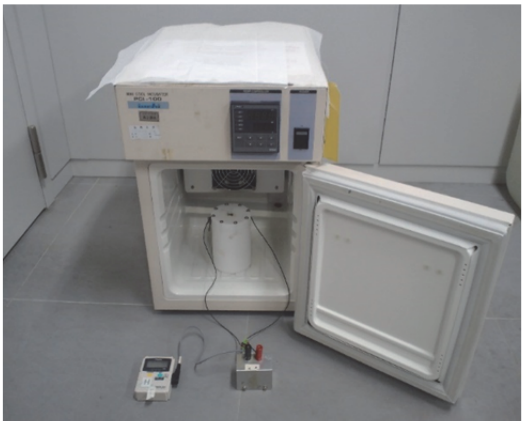

Fig. 5 Electrochemical device in an incubator for constant temperature. The device was assembled in a Teflon container.

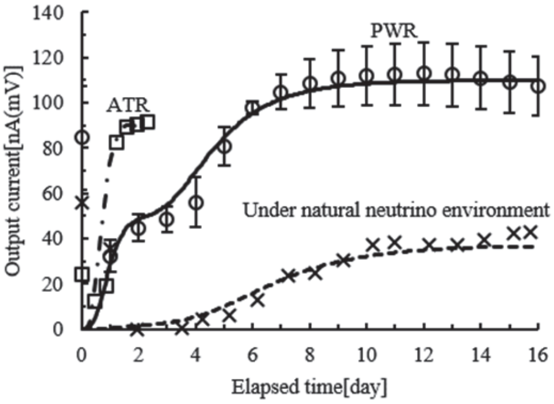

Fig. 6 Experimental results and simulated time-evolution of output current. The cross, square and circles marks stand for the data in environmental circumstance, and at Advanced Thermal Reactor and Pressurized Water Reactors. The calculation of three lines is based on half-cell model.[6]

Neutrino oscillation experiments have recently been made for reactor neutrinos (electron antineutrinos). The experimental results clarified the oscillation length to be 3 km for typical antineutrinos of 3 MeV[7] under assumption of flavor mixing model. Reproduction of the oscillation length was attempted to be calculated with use of subspace model with five neutrino constituents.[8,9] A table in Fig. 7 lists one of typical results on the constituents with their mass values. The internal and external auxiliary fields B^0 in AV type were formulated to work to give kinetic mass to neutrino constituents. The adjustable parameter in calculation was natural external auxiliary field B^0_{ext} in AV type. The quantity B^0 has a dimension of magnetic field, and the value of B^0_{ext} utilized was around 0.1 μT. The constituents have two types of situations (cases 1 and 2), appearing alternatively as oscillation, i.e. accelerating and deaccelerating phases. Figure 7 indicates the mass states are kept for mostly 75 fm in positive time increment, then 150 fm in total. This duration time of 150 fm corresponds to a flight distance of 3 km in the laboratory frame. It should be recalled that such neutrinos seldom make interaction to other materials.

There is another measurement data on neutrino oscillation which reveals an oscillation length of 100 km for 3 MeV range. [7] The neutrino constituent mass should be lowered to $1/\sqrt{33} \approx 1/6$ in comparison to the other oscillation mode of 3 km. To achieve neutrino situation of the lower mass states, a weak-lepton particle of Vector type with negative mass may be combined to the original neutrino system. The lepton particle seemed to be dissociated under appreciably high B^0_{ext} value, which may be supplied by the biological product of raw silk and be in an increased situation near the nuclear reactors. In this case, the interaction in the electrochemical devise is considered as in Fig. 8. It is noted that the neutrino itself is not capable of making interaction again. The binding between electron and week lepton particle should be consistent to non-dimensional coupling constant of weak interaction, i.e. 10^{-5} of electromagnetic fine structure constant.

The weak-lepton particle should be reside on a space [8,9] of gamma 0 matrix with Vector-type motion and V-type spin, making only magnetic interaction. In this situation, the weak-lepton particle is combined with usual electron with spin interaction. Existence of the weak-lepton particle works to disturb the hydroxide ion from the direct recombination with hydro ion. When electron and weak-lepton particle are transferred the gold electrode, an oxygen molecule is generated from four hydroxide. After oxygen molecules diffuse to the other carbon electrode, they combine with hydro ions with receiving electrons conducted through external circuit, and generate the output voltage between electrodes. The three lines in Fig. 6 indicate the results of simulation calculation, with use of three adjustable reaction rates.[6]

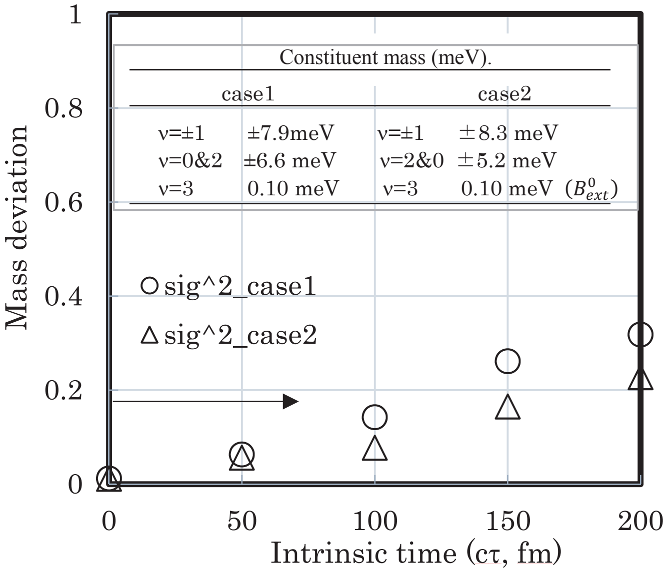

Fig. 7 Calculated kinetic mass deviation $\sigma^2 = \sum\left\{\left(m_{\nu,kin} - E^{mag}_{\nu,spin}\right)/E^{mag}_{\nu,spin}\right\}^2$ from spin magnetic energy during flight. The horizontal axis is drawn in the intrinsic time of the neutrino system multiplied by light velocity.

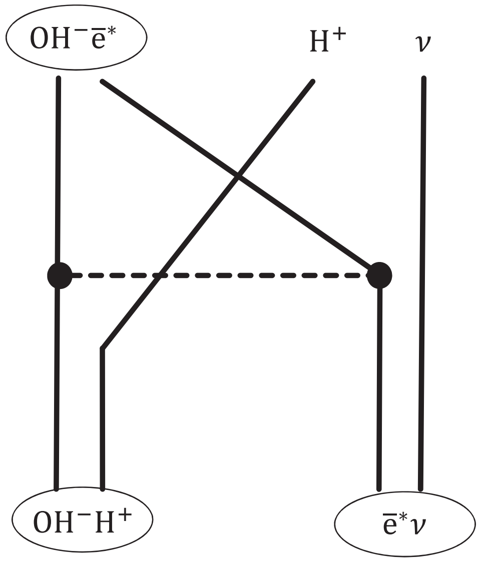

Fig. 8 Suggested interaction for environ-mental neutrinos with water molecule under sufficiently high B^0_{ext} field

4. Summary

The proton-incident neutron-production cross section down to low energy range was useful for the nuclear engineering including the basic study on accelerator driven subcritical reactor (ADS). The research on neutron measurement for GeV-range protons seemed to be a good choice as university study.

As for radiation experiment in relation to weak interaction, the new measurement was carried out at PWR. Although interesting data and suggestion were obtained, the investigation was not completed. Further study is required for fixing the suggestion.

Acknowledgements

The author gives its thanks to staff of nuclear data symposium organizer for given the chance of this talk. For the neutron measurement at KEK, the author expresses the gratitude for researchers of KEK, JAEA, Tohoku University and Kyushu University as well as graduate students of our laboratory. For the experiment at nuclear reactors, the author thanks to the staff of FUGEN decommission center and KAERI.

References

[1] T. Nakamura, K. Shouda, I. Fujiwara et al., Journal of Atomic Energy Society of Japan Vol.32 562(1990).
[2] Liu Wei, K. Ishibashi et al., “Possible Detection of Natural Neutrinos by Use of Small Apparatus”, J. Nucl. Sci. Technol., Suppl.4, 487 (2004).
[3] K. Ishibashi, H. Takada et al., J. Nucl. Sci. Technol., Vol.34, 529(1997).
[4] K. Niita, S. Chiba, et al., Phys. Rev. C 52, 2620(1995).
[5] Y. Iwamoto, N. Shigyo, et al., Phys. Rev. C70, 024602(2004).
[6] S. Suda, K. Ishibashi et al., "Study on the Output Current for Electrochemical Low-Energy Neutrino Detector with Regards to Oxygen Concentration", J. Radiat. Prot. Res. 41(4), 1 (2016).
[7] M.C. Gonzalez-Garcia, M. Maltoni, T. Schwetz: Nucl. Phys. B908 199(2016).
[8] K. Ishibashi, N. Terao et al., "Neutrino Properties and Their Usefulness Suggested by Recent Electrochemical Neutrino Detection Results", Progress in Nucl. Sci. Technol. Vol.1, 348(2011).
[9] K. Ishibashi, S. Suda et al., "Analysis of Reactor-Neutrino Oscillation Experiment from Consideration of Internal Constituent Motion", Presented at 9th International Symposium for Radiation Safety and Detection.

This is a blank page.

14

Space Nuclear Power and Nuclear Data -Radioisotope Power Generator and Space Nuclear Reactor-

Jun NISHIYAMA
Laboratory for Advanced Nuclear Energy, Institute of Innovative Research,
Tokyo Institute of Technology,
2-12-1-N1-19 Ookayama, Meguro-ku, Tokyo 152-8550, Japan
E-mail: jun-nishiyama@lane.iir.titech.ac.jp

Historically, plutonium-238 has been proven to be the best radioisotope for the provision of space nuclear power because of its high specific power (540 W/kg), enough half-life (87.7 years), low radiation levels, and stable fuel form at high temperature. However, current concerns over the limited supply and difficult treatment of ^{238}Pu have increased the need to explore alternative isotopes for space nuclear power applications.

Polonium-209 has the possibility to be an alternative material of ^{238}Pu. It has enough half-life of 102 years and the specific power of 490 W/kg. The production method by ^{209}Bi (p, n)^{209}Po reaction with proton accelerators is independent of fissile materials. The production rate of Po isotopes with proton accelerators was evaluated using the PHITS code. As the results, the beam current of 14 A with 40 MeV proton energy was required for annual production of 1kg ^{209}Po. The production rate using the reaction chain of ^{209}Bi (n, γ)^{210}Bi (β decay) ^{210}Po (n, 2n)^{209}Po was also estimated. This reaction may be possible in a system to use nuclear reactor such as a Lead-Bismuth cooled fast reactor or an Accelerator Driven system (ADS) with Lead-Bismuth target. To evaluate the production rate, calculations for the reaction rate of Bi and Po isotopes in Lead-Bismuth cooled fast reactors were performed using the MVP code. The TENDL nuclear data library was used for neutron reaction cross section of the Po isotopes. The calculation results showed that the amount of ^{210}Po in the equilibrium state was 1.4 (kg/m^3) assuming the averaged neutron flux level of 10^{16} (1/cm^2/s). In this situation, annual production per unit volume was 5.4×10^{-4} $R_{c/l}$ (kg/m^3/y), where $R_{c/l}$ is the volume ratio of Lead-Bismuth coolant in the core and in the loop.

On the other hand, nuclear reactors is also solution. We propose a small CANDLE burnup reactor as a heat source to be an alternative of ^{238}Pu. The CANDLE burnup strategy was proposed by Sekimoto et al., which does not require a burnup reactivity control instrument such as control rods or drums. In this study, we designed a small CANDLE reactor without any dynamic instrument nor coolant. The heat by fission reactions is directly converted to electrical energy by thermoelectric devices as same as radioisotope thermoelectric generators. As the results, the total core weight was 224 kg and the specific power was 89 W/kg. In this design, the moving speed of burning region was 0.64 cm/year. This study showed that the CANDLE burnup reactor was feasible for such small reactor core.

15 Fundamental and Applied Sciences Explored by Neutrons

Yasuki NAGAI
Quantum Beam Science Research Directorate, National Institutes for Quantum and Radiological Science and Technology, Tokai, Ibaraki 319-1106 Japan
e-mail: nagai.yasuki@qst.go.jp

Neutrons in the energy range from 0.3 μeV to a few GeV are playing an important role in the studies of various fields such as research, education, industry and commercial applications. In fact an accurate value of the neutron's half-life which could be measured by using an ultra-cold neutron with an energy of 0.3 μeV is known to be important in the calculation of the elemental abundance of light elements such as ^{4}He and ^{7}Li formed in the Big Bang nucleosynthesis and also in revealing new physics beyond the Standard model of particle physics. Elements heavier than iron is believed to be synthesized in stars via a neutron capture process at a temperature of about 10^8 °K. Hence, the neutron capture cross section measurement has been carried out using neutrons in the energy range from a few keV up to about 100 keV. The isovector E2 giant resonance state in nucleus was studied by the neutron capture reaction using neutrons with energy up to about 20 MeV. Recently we have shown that neutrons in the energy range from a few MeV to ~20 MeV obtained from an accelerator play an important role in the production of medical radioisotopes. It is also known since 1980th that atmospheric neutrons with energy up to a few GeV which penetrate shielding of building can cause soft errors in integrated circuits. The study of soft error rate testing of devices has been carried out using neutrons with energy up to ～800 MeV. In this paper we briefly describe the measurement of the neutron capture cross section of ^{16}O by means of a prompt γ-detection method from an interest in nuclear astrophysics and the medical radioisotope production using neutrons obtained from an accelerator.

1. keV Neutrons in Nuclear Astrophysics

It has been believed that galaxies form stars when they evolve. Namely, galactic chemical evolution (GCE) is the evolution of the transformation of gas into stars and of the resulting evolution of the chemical composition of a galaxy. Chemical abundances are considered to provide a fossil record of a galaxy's star-forming history. In order to construct models of chemical evolution of the Galaxy the abundance of the slow (s-) process isotopes for various metallicity stars has been extensively measured. In the models of the chemical evolution of the s-process istopes the abundant light nuclei such as ^{12}C, ^{16}O nd ^{20}Ne which are the direct product of He-burning in stars are considered to play an important role in the nucleosynthesis of elements heavier than iron [1]. Namely if the neutron capture cross section of these light isotopes would be large, the yields of the heavy elements would decrease. These abundant light elements would be neutron poison and affect significantly in the nucleosynthesis heavier than iron. Therefore the neutron capture cross section of these light isotopes at a stellar temperature is very important to construct the models of chemical evelution of the *s*-process isotopes. It is aslo claimed that the production yields of *p*-process isotopes woud also decrase because the *s*-process istotopes are the immediate predecessors of the *p*-process isotopes.

Before we made the measurement of the ^{16}O(n,γ)^{17}O reaction cross section at a stellar temperature, Maxwellian averaged cross section at kT = 30 keV, a very small value of 0.2 ± 0.1 μb was reported [1]. In order to remeasure such a small cross section we employed a prompt γ-ray detection method by using a highly sensitive anticompton NaI(Tl) γ-ray spectrometer developed by Igashira et al. [1]. The γ-ray branching ratio from the keV neutron capturing state to a low-lying state is quite dfferent from that of thermal neutron as shown in Fig. 1. In fact, the cross section at kT = 30 keV was obtained to be 34 ± 4 μb, 170-times larger than the reported value. The result is found to significantly affect the estimation of the s-process heavy elemens in especially metal-deficient stars due to a strong neutron poison of ^{16}O. It also provides an important role of the nonresonant direct *p*-wave neutron capture process of a nucleus [1].

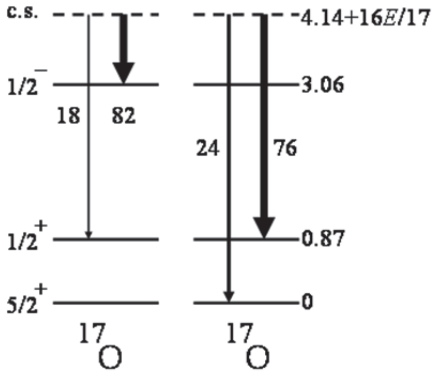

Fig. 1 Gamma-ray branching ratio from the thermal neutron capture reaction (left) and the pressent result (right), respectively. Note that the direct γ-ray from capture of neutron in ^{16}O strongly feeds to the 0.871 MeV state with a spin-parity 1/2^{+} in the keV neutron capture process. Whereas the direct gamma-ray feeds to the 3.055 MeV state with a spin-parity 1/2^{-} in the thermal neutron capture process. From the comparison it can be understood that the non-resonant direct p-wave neutron capture process plays an important role in the keV neutron capture process of ^{16}O [1].

Smilarly to the case of the neutron capture reaction of ^{16}O it was found that the non-resonant direct capture process plays an important role in the neutron capture reaction of ^{12}C [2]. The measured cross section of ^{12}C at a stellar temperature also played a crucial role in the yield calcualtion of elements heavier than iron in metal-deficient stars. It should be mentioned that the velocity of ion in stellar conditions is assumed to be the Maxwellian-Boltzman distribution. Hence in order to estimate the production yields of s-process isotopes one has to calculate the Maxwellian averaged neutron capture cross section at kT = 30 keV using an evaluated neutron capture cross section such as JENDL-4.0.

2. MeV Neutrons in Radioisotope Production for Medical Use

It is well known that an early diagnosis of diseases such as cancer, brain disease, and heart disease etc., is carried out using ^{99m}Tc ($T_{1/2}$ = 6 h) which is the daughter nuclide of ^{99}Mo ($T_{1/2}$ = 66 h) [3]. In Japan, about 0.7 to 0.9 million diagnostic procedures are performed using ^{99m}Tc [4]. ^{99m}Tc and ^{99}Mo is usually produced in ^{99}Mo/^{99m}Tc generators. Most ^{99}Mo has been produced by a fission reaction of highly enriched ^{235}U (HEU) in research reactors around the world. A shortage of ^{99}Mo due to the unexpected shutdown of two of the reactors triggered discussions to look for alternative ^{99}Mo and ^{99m}Tc production methods without HEU [5].

We proposed a new route to produce ^{99}Mo by the ^{100}Mo(n,2n)^{99}Mo reaction using neutrons obtained from an accelerator with a minimum level of radioactive waste [6]. Using ~14 MeV neutrons high-quality ^{99}Mo was produced with a minimum level of radioactive wastes without ^{235}U. Neutrons with most probable energy of 14 MeV with an intensity of 10^{14} n/s which is necessary to produce a large amount of ^{99}Mo can be produced by the ^{nat}C(d,n) reaction using 40 MeV intense deuterons. However, a specific-activity of the ^{99}Mo is low of about 37 GBq/(g Mo), which is a typical value in any alternative ^{99}Mo production methods without the fission reaction of uranium and which is about 1/5000 of the fission-^{99}Mo [7] Therefore we separated ^{99m}Tc from the irradiated ^{100}MoO$_3$ sample containing a low-specific activity of ^{99}Mo by employing a thermo-chromatography method to obtain a high radioactive concentration ^{99m}Tc free from any chemical impurities.

We checked the quality of ^{99m}Tc obtained from ^{99}Mo produced by the ^{100}Mo(n,2n)^{99}Mo reaction: the radionuclide purity of ^{99m}Tc obtained from ^{99}Mo produced by the ^{100}Mo(n,2n)^{99}Mo reaction was higher than 99.99% by γ-spectroscopy, and the labeling efficiency of ^{99m}Tc radiopharmaceutical was also higher than 96.7% by thin-layer chromatography. These values were shown to exceed the United States Pharmacopeia requirements for a fission product, ^{99}Mo. The result supports the new route that a ^{99m}Tc radiopharmaceutical preparation formed by using the ^{100}Mo(n,2n)^{99}Mo reaction can be a promising substitute for the fission product ^{99}Mo.

In discussing the alternative ^{99}Mo production route by the ^{100}Mo(n,2n)^{99}Mo reaction, we noticed that co-production of other radioisotopes than ^{99}Mo is possible using fast neutrons, because the traveling range of neutrons is much longer than that of a charged particle. In fact, we proposed new routes to produce carrier-free medical radioisotopes of ^{90}Y, ^{64}Cu, and ^{67}Cu using fast neutrons from an accelerator. Note that a radiopharmaceutical agent (Zevarin®) containing a radionuclide ^{90}Y ($T_{1/2}$=64h) is used for cancer therapy. ^{67}Cu ($T_{1/2}$=61.8h) is a promising radionuclide to treat small distant metastases. ^{64}Cu ($T_{1/2}$=12.7h) is a promising radionuclide suitable for labeling many radiopharmaceuticals for PET imaging. Among the radioisotopes, we note the production of ^{67}Cu. So far many studies were conducted to produce a large amount of ^{67}Cu by using reactors and accelerators via the ^{68}Zn(p,2p)^{67}Cu, ^{68}Zn(γ,p)^{67}Cu, ^{67}Zn(n,p)^{67}Cu, ^{70}Zn(p,α)^{67}Cu and ^{70}Zn(d,αn)^{67}Cu reactions. The ^{68}Zn(p,2p)^{67}Cu reaction is currently used to produce ^{67}Cu. Note that the proton energy used in the ^{68}Zn(p,2p)^{67}Cu reaction is high (see Fig. 2), a large amount of impurity radionuclide of ^{64}Cu is produced by ^{68}Zn(p,αn)^{64}Cu. Kin et al. proposed a new route to produce ^{67}Cu with very little radionuclide impurity via the ^{68}Zn(n,x)^{67}Cu reaction [8].

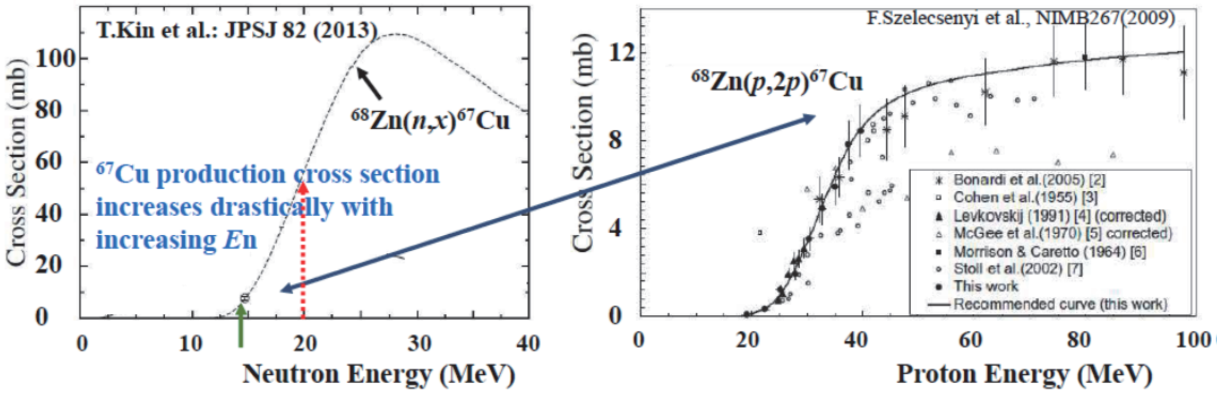

Fig. 2 The excitation function of the ^{68}Zn(n,x)^{67}Cu reaction and the ^{68}Zn(p,2p)^{67}Cu reaction. Note that the ^{68}Zn(n,x)^{67}Cu reaction cross section significantly increase with increasing neutron energy.

In fact the quality of ^{67}Cu was experimentally studied by measuring the radionuclide purity of ^{67}Cu produced by the ^{68}Zn(n,$n'p$+d)^{67}Cu reaction. It was found to be high with a minimum level of impurity of ^{64}Cu. Quite recently ^{67}CuCl$_2$ obtained by the reaction mentioned above was used to determine the biodistribution in colorectal tumor-bearing mice. High uptake of ^{67}Cu in the tumor was found. Here it should be mentioned that the neutron that is produced by the ^{nat}C(d,n) reaction with 40 MeV deuteron beams has a wide range of neutron energy with a most probable energy of 14 MeV. Hence in order to calculate the production yield of ^{99}Mo we used the evaluated cross section of ^{100}Mo(n,2n)^{99}Mo, given in the 4-th version of Japanese Evaluated Nuclear Data Library (JENDL-4.0).

3. Summary

On the basis of the results mentioned above, a new prototype system for the generation of radioisotopes with accelerator neutrons by deuterons (GRAND) has been proposed [9]. The system consists of an azimuthally variable field (AVF) cyclotron with a carbon converter to produce intense accelerator neutrons with a most probable energy of 14 MeV. The system has unique features in the production of a wide variety of radioisotopes, including ^{99}Mo, useful for nuclear medicine diagnosis procedures. High-quality radioisotopes can be produced continuously using fast neutrons from an accelerator with a minimum level of radioactive waste, and without using uranium. The system has a potential for the co-production of other radioisotopes at the same time. The proposed system is compact in size, and easy to operate, and therefore could be used in many countries for medical radioisotopes production.

Acknowledgements

I thank N. Iwamoto, O. Iwamoto, F. Minato, S. Shibata for their useful discussions. This work was supported by a Grant-in-Aid for Specially Promoted Research from the Japan Ministry of Education, Culture, Sports, Science, and Technology (23000005) and in part by the Adaptable and Seamless Technology Transfer Program through Target-driven R&D (A-STEP) of the Japan Science and Technology Agency (JST).

References

[1] M. Igashira, Y. Nagai, K. Masuda, T. Ohsaki, H. Kitazawa, Astrophys. J. 441 (1995) L89.
[2] Y. Nagai, M. Igashira, K. Takeda, N. Mukai, S. Motoyama, F. Uesawa, H. Kitazawa and T. Fukuda, Astrophys. J. 372 (1991) 683.
[3] F. F. Knapp, Jr. and S. Mirzadeh: Eur. J. Nucl. Med. 21 (1994) 1151.
[4] Report by Science Council of Japan (July 24, 2009) [in Japanese].
[5] K. Bertsche: Proceedings of IPAC'10, Kyoto, Japan. (2010) 121.
[6] Y. Nagai and Y. Hatsukawa: J. Phys. Soc. Jpn. 78 (2009) 033201.
[7] F. Minato and Y. Nagai: J. Phys. Soc. Jpn. 79 (2010) 093201.
[8] T. Kin *et al.*: J. Phys. Soc. Jpn. 82 (2013) 034201.
[9] Y. Nagai *et al.*: J. Phys. Soc. Jpn. 82 (2013) 064201.

This is a blank page.

16 Study on Neutron Capture Reaction using Pelletron and ANNRI

Masayuki IGASHIRA
Laboratory for Advanced Nuclear Energy, Institute of Innovative Research,
Tokyo Institute of Technology
2-12-1-N1-26 Ookayama, Meguro-ku, Tokyo 152-8550, Japan
e-mail: iga@nr.titech.ac.jp

Study on neutron capture reaction using the 3UH-HC Pelletron accelerator of the Tokyo Institute of Technology and the ANNRI of the MLF of the J-PARC is reviewed briefly. In particular, E1 and/or M1 gamma-ray strength functions derived from measured keV-neutron capture gamma-ray spectra of medium and heavy nuclei and non-resonant p-wave neutron capture by light nuclei are reviewed based on studies using the Pelletron. Concerning studies using the ANNRI, measurements of neutron capture cross sections of minor actinides and long-lived fission products are reviewed.

1. Introduction

Neutron capture cross sections are indispensable for the research and development of innovative nuclear energy systems, study on the nucleosynthesis in the universe, etc. Neutron capture gamma-ray spectra are also indispensable for the evaluation of gamma-ray heating in innovative nuclear energy systems, study on neutron capture mechanism, etc. Therefore, we have measured those physical quantities using the 3UH-HC (3 Units, Horizontal and High Current) Pelletron accelerator of the Tokyo Institute of Technology and the ANNRI (Accurate Neutron-Nucleus Reaction Measurement Instrument) of the MLF (Materials and Life Science Experimental Facility) of the J-PARC (Japan Proton Accelerator Research Complex).

In the present paper, E1 (Electric Dipole) and/or M1 (Magnetic Dipole) gamma-ray strength functions derived from measured keV-neutron capture gamma-ray spectra of medium and heavy nuclei, non-resonant p-wave neutron capture by light nuclei, and neutron capture cross sections of minor actinides and long-lived fission products are reviewed.

2. Study using 3UH-HC Pelletron

2.1. 3UH-HC Pelletron accelerator and gamma-ray spectrometer

The 3UH-HC Pelletron accelerator with the maximum high voltage of 3 MV was installed at the Tokyo Institute of Technology in 1976 JFY (Japanese Fiscal Year), but it required three more years to succeed in accelerating ns (nano second) pulsed proton beams, which were used for keV-neutron generation by the ^{7}Li(p,n)^{7}Be reaction. At present, the width and peak current of the pulsed proton beam are typically 1.5 ns (FWHM) and 2 mA, respectively. As for the pulse repetition rate, 4 or 2 MHz is usually used.

An anti-Compton NaI(Tl) gamma-ray spectrometer with a heavy shield was developed for fast-neutron experiment [1], and has been improved several times. The size of the present main NaI(Tl) detector is 15.2 cm in diameter and 30.5 cm in length. The outer diameter and length of Compton suppression NaI(Tl) detector are 33.0 cm and 35.6 cm, respectively. The present anti-Compton NaI(Tl) gamma-ray spectrometer has better sensitivity than the original one by about ten times.

2.2. E1 and/or M1 gamma-ray strength functions of medium and heavy nuclei

The capture gamma-ray spectra of Ag, In, Sb, I, Cs, Pr, Tb, Ho, Lu, Ta, and Au were measured at the neutron energies of 10 to 800 keV, using a TOF (Time Of Flight) method with the ^{7}Li(p,n)^{7}Be reaction pulsed neutron source and the original anti-Compton NaI(Tl) gamma-ray spectrometer [2,3]. A part of the spectra are shown in **Fig. 1**, where an anomalous bump, so-called the pygmy resonance, is clearly observed in all spectra. Combining the present data with the previous ones for Gd, ^{169}Tm, Re, Hg, Tl, and ^{206}Pb [4-7], remarkable features of the pygmy resonance were found to be that the resonance energy and the E1 strength exhausted in the resonance increase with neutron number but these quantities decrease precipitously around the neutron magic number N = 82, as shown in **Fig. 2**. Dots in the figure show the pygmy resonance energies (E_p) and vertical bars show the resonance widths (Γ_p).

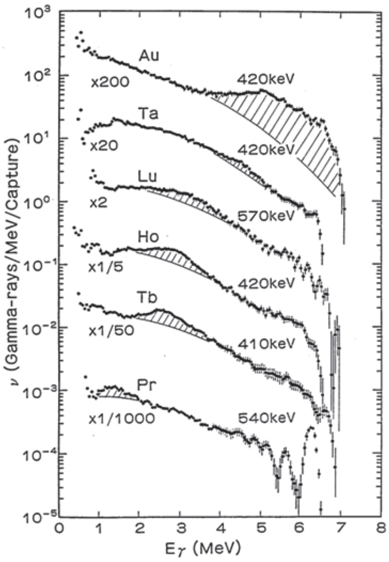

Fig. 1 Typical keV-neutron capture gamma-ray spectra

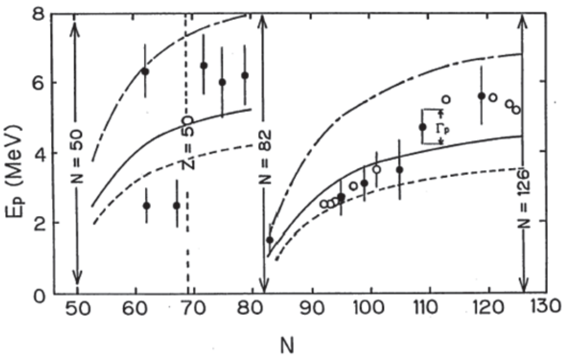

Fig. 2 Systematics of pygmy E1 resonance energies

Mohan *et al*. [8] proposed a three-fluid model for the E1 pygmy resonance. In their model, all the protons in a nucleus form one proton fluid, and neutrons form two fluids: one is called the blocked neutron fluid, which is formed by the neutrons that fulfil the same orbits as protons, the other is called the excess neutron fluid, which is formed by the neutrons that are above the highest proton orbit. The E1 pygmy resonance was explained as the oscillation of the excess neutron fluid against the proton and blocked neutron fluids in their model.

Since the neutron magic number effect was observed in the systematics of the pygmy resonance, as shown in Fig. 2, we revised the three-fluid model of Mohan *et al*.: the excess neutron fluid was formed by the neutrons above the highest major shell in the nucleus. Calculated pygmy resonance energies by the revised model are shown by lines in Fig. 2. Solid lines show the calculated results with the same coupling constants among the three fluids as Mohan *et al*. By changing the coupling

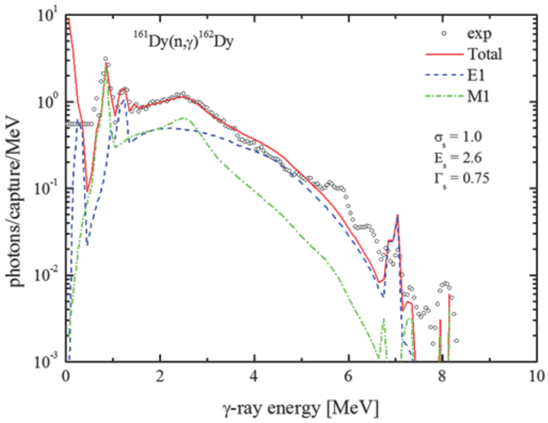

Fig. 3 Neutron capture gamma-ray spectra of ^{161}Dy

constants between the excess neutron and proton fluids and between the excess neutron and blocked neutron fluids, the calculation was also performed. The calculated results are shown by dashed lines and dash-dotted lines. The solid lines well reproduce the observed pygmy resonance energies. Concerning the ratios of the E1 pygmy resonance strength to the E1 sum rule [9], the calculation overestimated by about one order.

The anomalous bump around 3 MeV as well as that around 5.5 MeV was attributed to the E1 pygmy resonance in the above discussion. However, an M1 scissors mode excitation was theoretically predicted around 3 MeV [10], and the M1 excitations from the ground state to excited states around 3 MeV were observed for deformed nuclei through (e,e'), (γ,γ'), and (n,n'γ) reactions [11]. Then, we measured the keV-neutron capture gamma-ray spectra of deformed nuclei such as ^{145}Nd [12], ^{161}Dy [13], and ^{167}Er [14], and analyzed the anomalous bump around 3 MeV as the M1 scissors mode [15]. For example, the statistical model calculation of capture gamma-ray spectrum for ^{161}Dy is compared with the experimental spectrum in **Fig. 3**. In the calculation, a small resonance was introduced in the M1 gamma-ray strength function so as to reproduce the experimental spectrum. From the fitted parameters of the M1 small resonance, *i.e.* energy (E_s), width (Γ_s), and peak cross section (σ_s), the reduced M1 transition strength, B(M1), was derived for each residual nucleus, as shown in **Fig. 4**, where the horizontal axis shows the square of the ground state quadrupole deformation parameter, β_2 [16], of the residual nucleus. Solid dots show the present (n,γ) results and open dots show the results through (γ,γ') experiment [17], and both results well agree with each other, which means the anomalous bump around 3 MeV in the gamma-ray spectra of ^{145}Nd, ^{161}Dy, and ^{167}Er should be attributed to the M1 scissors mode excitation.

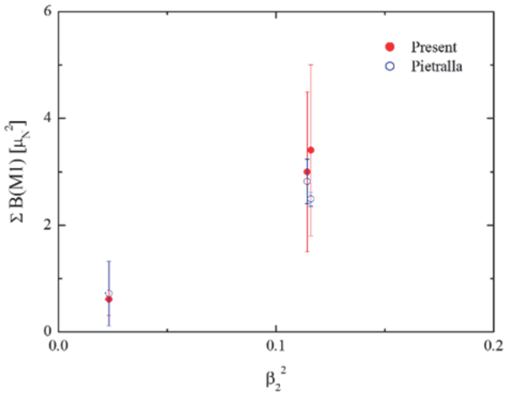

Fig. 4 Σ B(M1) versus β_2^2

2.3. Non-resonant p-wave neutron capture by light nuclei

The neutron capture cross sections around 30 keV of ^{12}C and ^{16}O are very important for the study on the s-process (slow neutron-capture process) of the nucleosynthesis in stars, because those nuclei are very abundant in s-process sites. However, the situation of measurements for those cross sections was very poor, because those cross sections were very small and the measurement was very difficult. For example, the capture cross section of ^{12}C was measured around 30 keV as 200 +- 400 μb [18], although the theoretical prediction with the thermal neutron capture cross section and the 1/*v* law (*v*: the velocity of incident neutron) was about 3 μb. A new measurement for ^{12}C [19] gave an upper limit of 14 μb around 30 keV. Then, we tried to measure those cross sections by using the TOF method described above [20-23].

A PH (pulse-height) spectrum obtained from the measurement for ^{12}C is shown in **Fig. 5**, where the gamma rays due to the primary transitions from the capture state (c.s.) to the ground state (g.s.) and from the c.s. to the first excited state (1st) are clearly observed together with cascade transition gamma rays.

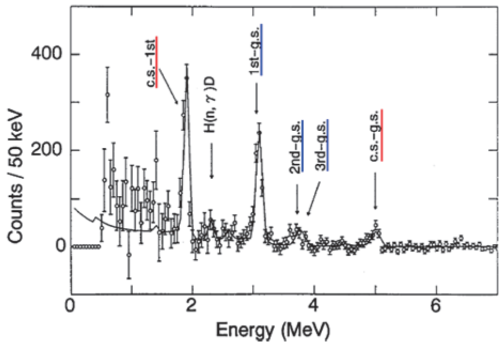

Fig. 5 ^{12}C(n,γ)^{13}C PH spectrum at 40 keV

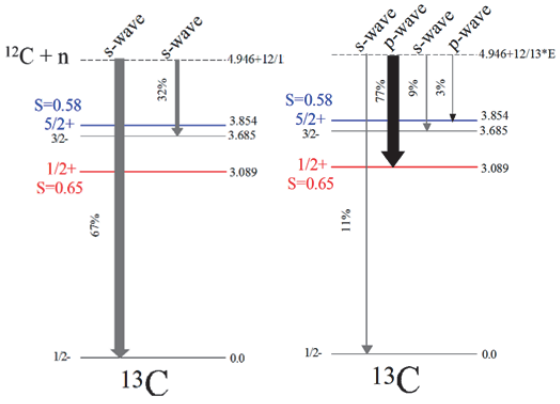

Fig. 6 Branching ratios of the capture state of ^{13}C at 40 keV (right) and at thermal (left)

From the analysis of the PH spectrum, the primary transitions from the 40-keV neutron capture state were derived, as shown in **Fig. 6**, where those from the thermal neutron capture state [24] are also shown. From the figure, it is found that the transition from the 40-keV neutron capture state to the first excited state (1/2$^+$) with a large neutron spectroscopic factor is dominant, whereas the ground state (1/2$^-$) transition is dominant in the case of the thermal neutron capture. It implies that the p-wave neutron direct capture is important for the 40-keV neutron capture. **Figure 7** shows the neutron energy dependence of the partial capture cross sections to the ground and first excited states of ^{13}C. The partial capture cross section to the first excited state shows the *v* dependence, whereas that to the ground state shows the 1/*v* dependence. This *v* dependence of the dominant partial capture cross section to the first excited state indicates that non-resonant p-wave neutron capture is essential in the keV-neutron capture of ^{12}C. Summing up the measured partial capture cross sections, finally, the total capture cross section of ^{12}C was derived as15.4 +- 1.0 μb [21] for kT = 30 keV.

As for the capture cross section of ^{16}O, using the same experimental technique as ^{12}C, it was derived as 34 +- 4 μb [23] for kT = 30 keV. The present value is larger than the previous measurement [25] by 170 times. The primary transitions from the 40-keV neutron capture state to the ground state (5/2$^+$) and the first excited state (1/2$^+$) were 24% and 76%, respectively. Here, these states have a large neutron spectroscopy factor. These strong transitions mean that non-resonant p-wave neutron capture is also essential in the keV-neutron capture of ^{16}O. In the case of the thermal neutron capture of ^{16}O, the primary transition to the second excited state (1/2$^-$) is dominant, *i.e.* about 80%, and the total capture cross section is 0.190 +- 0.019 mb [26].

It is worthy of note that, in the case of the keV-neutron capture of ^{7}Li, the s-wave, not p-wave, neutron capture is essential [27]. Since the residual nucleus, ^{8}Li, has only two bound states: the ground state (2$^+$) and the first excited state (1$^+$), and the spin and parity of the p-wave neutron capture state is 0$^+$, 1$^+$, 2$^+$, or 3$^+$, the E1 transition from the p-wave neutron capture state to the ground nor first excited state is forbidden. This is reason why the s-wave neutron capture is essential in the keV-neutron capture of ^{7}Li.

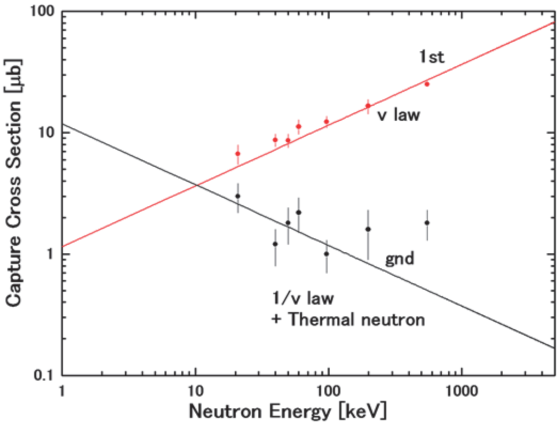

Fig. 7 Neutron energy dependences of the partial capture cross sections to the ground and first excited states of ^{13}C

3. Study using ANNRI

3.1. ANNRI and gamma-ray spectrometers

ANNRI was installed at the BL04 (Beam Line #04) of MLF [28,29]. Two spectrometers were installed in ANNRI: one is a 4π Ge spectrometer at 22 m from the spallation neutron source of MLF and the other is an NaI(Tl) spectrometer at 27 m. The 4π Ge spectrometer is composed of two cluster Ge detectors and eight coaxial Ge detectors, *i.e.* totally 22 Ge crystals. The NaI(Tl) spectrometer is composed of two NaI(Tl) detectors: one with a diameter of 33.0 cm and a thickness of 20.3 cm at 90 degree with respect to the neutron beam direction, the other with a diameter of 20.3 cm and a thickness of 20.3 cm at 125 degree. Those spectrometers are surrounded by neutron and gamma-ray shields.

The aim of the maximum proton beam power at MLF is 1 MW, which is much higher than those of other facilities, *e.g.* LANSCE (Los Alamos Neutron Science Center: 80 kW) and n_TOF/CERN (9 kW), but the time resolution of proton beam, 100 ns, at MLF is worse compared to those of other facilities. Therefore, the design concept for ANNRI was to make the best use of the high proton beam power. The neutron intensity at the sample position for the 4π Ge spectrometer is compared with those at other facilities in **Fig. 8**, where the intensity corresponding to 200 kW proton beam power is shown for ANNRI. The neutron intensity at ANNRI is higher than those at the other facilities by one or two orders above 0.5 eV, as shown in Fig. 8.

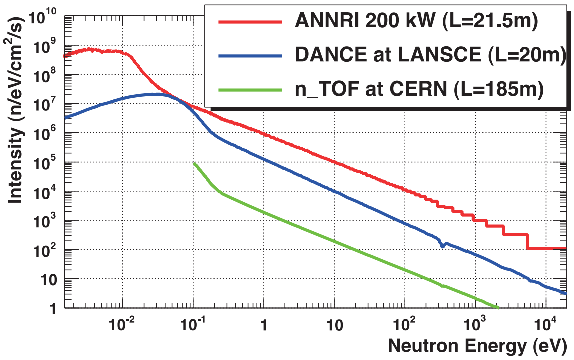

Fig. 8 Comparison of neutron intensities

3.2. Neutron capture cross sections of minor actinides and long-lived fission products

The neutron capture cross sections of minor actinides and long-lived fission products are very important for the research and development of nuclear transmutation technology for long-lived radioactive wastes which are generated in fission reactors. Therefore, the first mission of ANNRI is to measure those cross sections accurately.

The neutron capture cross sections of ^{237}Np, ^{241}Am, ^{243}Am, ^{244}Cm, and ^{246}Cm (minor actinides) and those of ^{93}Zr, ^{99}Tc, ^{107}Pd, and ^{129}I (long-lived fission products) have been measured, using the 4π Ge spectrometer and the NaI(Tl) spectrometer. Moreover, stable isotopes contained in the capture samples of long-lived fission products have been measured to correct for impurity effects on the capture yields of long-lived fission products. The neutron energy region for the measurements using the 4π Ge spectrometer was typically from thermal to several 100 eV, and that for the measurements using the NaI(Tl) spectrometer was typically from thermal to several 100 keV.

For example, the capture cross sections of ^{244}Cm obtained from the measurement using ANNRI [30] are shown in **Fig. 9**, where those from the previous measurement [31] and the evaluations of JENDL-4.0 are also shown. The previous measurement used a nuclear device as the neutron source. The present results below 20 eV are the first measurements in the world. It is worthy of note that the amount of

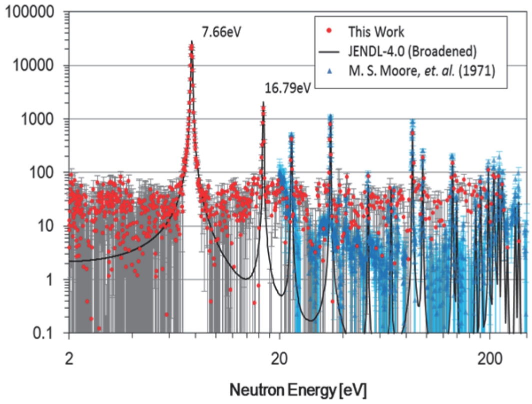

Fig. 9 Neutron capture cross sections of ^{244}Cm. The present results below 20 eV are the first measurements in the world

the ^{244}Cm sample was very small, *i.e.* 0.6 mg, but its radioactivity was very high, *i.e*. 2.0 GBq.

4. Summary

Study on neutron capture reaction using the 3UH-HC Pelletron of the Tokyo Institute of Technology was reviewed briefly. In particular, E1 and/or M1 gamma-ray strength functions derived from measured keV-neutron capture gamma-ray spectra of medium and heavy nuclei and non-resonant p-wave neutron capture by light nuclei were reviewed. Concerning the gamma-ray strength functions, it was pointed out that the M1 scissors mode excitation was important for the deformed nuclei in the medium and heavy mass regions. On the other hand, the E1 pygmy resonance was semi-quantitatively explained as the oscillation of the excess neutron fluid against the proton and blocked neutron fluids in a modified three-fluid model. As for the capture reaction by light nuclei, it was pointed out that the non-resonant p-wave neutron capture was essential for light nuclei except for the capture by ^{7}Li.

Measurements of neutron capture cross sections of minor actinides and long-lived fission products using ANNRI/MLF/J-PARC was also reviewed briefly. The measurements were performed in the energy region from thermal to several 100 keV. As an example, the capture cross sections of ^{244}Cm measured using the 4π Ge spectrometer of ANNRI were shown. The results below 20 eV were the first measurements in the world. ANNRI will play an important role in the nuclear data field in the world.

References

[1] M. Igashira *et al*., *Nucl. Instr. Meth*., **A245** (1986) 432.
[2] M. Igashira *et al*., *Nucl. Phys*., **A457** (1986) 301.
[3] M. Igashira, Doctoral thesis, Tokyo Institute of Technology, 1987 [in Japanese].
[4] J. Voignier *et al*., *Nucl. Sci. Eng*., **93** (1986) 43.
[5] I. Bergqvist and N. Starfelt, *Nucl. Phys*., **39** (1962) 353; 529.
[6] G. A. Bartholomew *et al*., *Can. J. Phys*., **46** (1970) 687.
[7] S. Joly *et al*., *Phys. Rev*., **C20** (1979) 2027.
[8] R. Mohan *et al*., *Phys. Rev*. **C3** (1971) 1740.
[9] J. S. Levinger and H. A. Bethe, *Phys. Rev*., **78** (1950) 115.
[10] N. Lo Iudice and F. Palumbo, *Phys. Rev. Lett*., **41** (1978) 1532.
[11] for example, U. Kneissl, *Prog. Part. Nucl. Phys*., **28** (1992) 331.
[12] T. Veerapaspong *et al*., *J. Nucl. Sci. Technol*., **36** (1999) 855.
[13] S. Mizuno *et al*., *J. Nucl. Sci. Technol*., **36** (1999) 493.
[14] A. K. M. Harun-ar-rashid *et al*., *J. Nucl. Sci. Technol*., **37** (1999) 421.
[15] M. Igashira et al., *Proc. the 11-th Int. Symp. on Capture Gamma-Ray Spectroscopy and Related Topics, 2002*, ed. J. Kvasil et al. (World Scientific, 2003) 258.
[16] S. Raman *et al*., *At. Data Nucl. Tables*, **36** (1987) 1.
[17] N. Pietralla *et al*., *Phys. Rev*., **C52** (1995) 2317.
[18] R. L. Macklin and J. H. Gibbons, *Phys. Rev*., **159** (1967) 1007.
[19] R. L. Macklin, *ApJ*., **357** (1990) 649.
[20] Y. Nagai *et al*., *ApJ*,, **372** (1991) 683.
[21] T. Ohsaki *et al*., *ApJ*., **422** (1994) 912.
[22] T. Kikuchi *et al*., *Phys. Rev*., **C57** (1998) 2724.
[23] M. Igashira *et al*., *ApJ*., **441** (1995) L89.
[24] M. A. Lone, *Proc. the 4th Int. Symp. on Capture Gamma-Ray Spectroscopy and Related Topics,*

1981, ed. T. von Egidy et al. (Inst. Phys. Conf. Ser. No. 62) 383.

[25] B. J. Allen and R. L. Macklin, *Phys. Rev*., **C3** (1971) 1737.

[26] S. F. Mughabghab, *Atlas of Neutron Resonances, Resonance Parameters and Thermal Cross Sections Z = 1-100* (Elsevier 2006).

[27] Y. Nagai *et al*., *ApJ*., **381** (1991) 444.

[28] M. Igashira *et al*., *Nucl. Instr. Meth*., **A600** (2009) 332.

[29] Y. Kiyanagi, *J. Korean Physical Society*, **59** (2011) 779.

[30] A. Kimura et al., *J. Nucl. Sci. Technol*., **49** (2012) 708.

[31] M. S. Moore and G. A. Keyworth, *Phys. Rev*., **C3** (1971) 1656.

This is a blank page.

17 Sensitivity and Uncertainty Analysis of Fusion Neutronics Benchmark Problem with Deterministic Code System CBZ

Go CHIBA
Faculty of Engineering, Hokkaido University
Kita-13 Nishi-8, Kita-ku, Sapporo, Hokkaido, 060-8628 Japan
e-mail: go_chiba@eng.hokudai.ac.jp

Sensitivity and uncertainty analyses are conducted for fusion neutronics benchmark problem focusing on copper with a deterministic code system CBZ. The present sensitivity analysis suggests that evaluation on Cu-65 inelastic scattering cross section in high energy range are different between ENDF/B-VIII.b3 and other recent libraries, and this difference has a large impact on spatial distributions of high-energy neutron flux. It also suggests that different evaluations on Cu-65 elastic scattering cross section among the recent libraries affect spatial distribution of low-energy neutron flux.

1. Introduction

Nuclear data sensitivity and uncertainty (S/U) analysis with (generalized) adjoint neutron flux (or importance function) has been well established and widely used in nuclear fission reactors applications. This methodology of the S/U analysis is also applicable to fusion neutronics problems[1], but such activities are quite few in Japan. In the present study, the S/U analysis methodology is applied to the copper fusion neutronics benchmark problem of the Fusion Neutronics Source (FNS) in the Japan Atomic Energy Agency[2]. This benchmark problem is numerically calculated with several recent evaluated nuclear data libraries, and energy group- and nuclear data-wise contributions to the difference in numerical results among different libraries are quantified by virtue of sensitivity profiles calculated from forward and generalized adjoint neutron fluxes. Nuclear data-induced uncertainties of energy-integrated neutron fluxes are also quantified with one of these recent libraries, TENDL-2015.

2. Numerical procedure of CBZ

All the calculations are performed with a deterministic code system CBZ[3], which is under development at Hokkaido University. A 421-energy group library is produced by the NJOY-99 code[4] from point-wise cross section data, which are generated by the PREPRO code[5]. Note that PREPRO can process resonance parameter data provided by the R-matrix limited theory (LRF=7) whereas NJOY-99 cannot.

A 421-group self-shielded cross section set is calculated with infinite homogeneous medium assumption, and this set is used in the following neutron transport calculations by a SNRZ solver based on the diamond-difference discrete-ordinate method. Scattering anisotropy is considered up to the third Legendre order. The benchmark system is simplified into a homogeneous copper cylinder with a neutron source of small volume. Air region between the source and the copper cylinder is also explicitly considered. Energy group-dependent angular quadrature sets are used; Double Legendre and Chebyshev quadrature set with 4,000 discrete points ($\mathrm{DP}_{100}\mathrm{T}_{10}$) is used above 12.88 MeV to remedy the ray-effect, and low-order angular quadrature sets are used in lower energy ranges. In order to calculate sensitivity profiles by the (generalized) perturbation theory, generalized adjoint neutron flux is necessary. The generalized adjoint neutron flux is calculated with the low-order quadrature set to save calculation time. In CBZ, several neutron disappearance reactions with high energy neutrons, such as (n,p) and (n,t) reactions, are added to (n,γ) cross sections, so sensitivities not to (n,γ) cross sections but to neutron disappearance cross sections are calculated. Sensitivities to inelastic scattering cross section are calculated only for total cross sections, and those to partial inelastic scattering cross sections are not taken into account.

3. Results

Neutron flux energy spectra at several spatial positions were measured through the experiment. For comparison between the measurement data and calculation results, neutron fluxes integrated over specific energy ranges are considered.

3.1 Verification of CBZ calculations

In order to confirm applicability of CBZ to fusion neutronics problems, energy-integrated neutron fluxes calculated with CBZ are compared with the reference results which were obtained by Konno with continuous-energy Monte Carlo calculations[2]. JENDL-4.0 is used in both the calculations. Results are shown in **Fig. 1**. The CBZ results agree with the references within 10% differences and numerical calculations with CBZ are well verified.

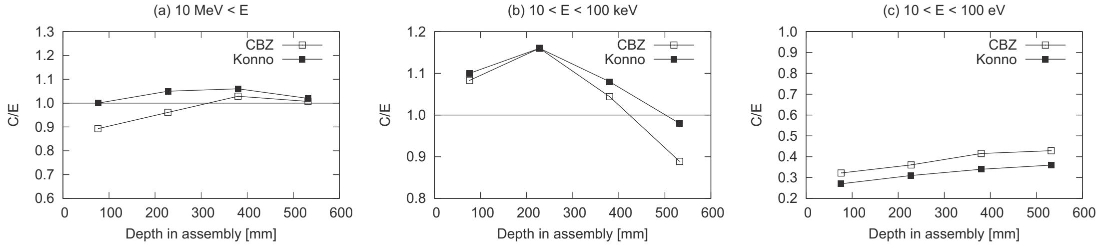

Fig. 1: C/E values obtained with JENDL-4.0

3.2 Calculations with various libraries and comparisons with measurement data

Numerical calculations are carried out with four recent evaluated nuclear data libraries: JENDL-4.0, JEFF-3.2, ENDF/B-VII.1 and the β-3 version of ENDF/B-VIII (ENDF/B-VIII.b3). Calculation results with JENDL-4.0 and the measurement data of neutron flux energy spectra at four different spatial positions are shown in **Fig. 2**.

C/E values on energy-integrated neutron flux at different spatial positions are shown in **Fig. 3**. Note that differences in the C/E values between JENDL-4.0 and ENDF/B-VII.1, whose evaluation for copper is the same as those in ENDF/B-VII.0, are consistent with the previous work by Konno[2].

3.3 Sensitivity analysis

In order to investigate differences in C/E values between different libraries, sensitivity profiles are multiplied by differences in cross sections between two libraries and then the differences in C/E values can be decomposed into nuclide-wise and nuclear data-wise differences contributions.

First the C/E differences are decomposed into nuclide-wise ones. Results are shown in **Fig. 4**. These figures show how much calculation results are altered when nuclear data of specific nuclide

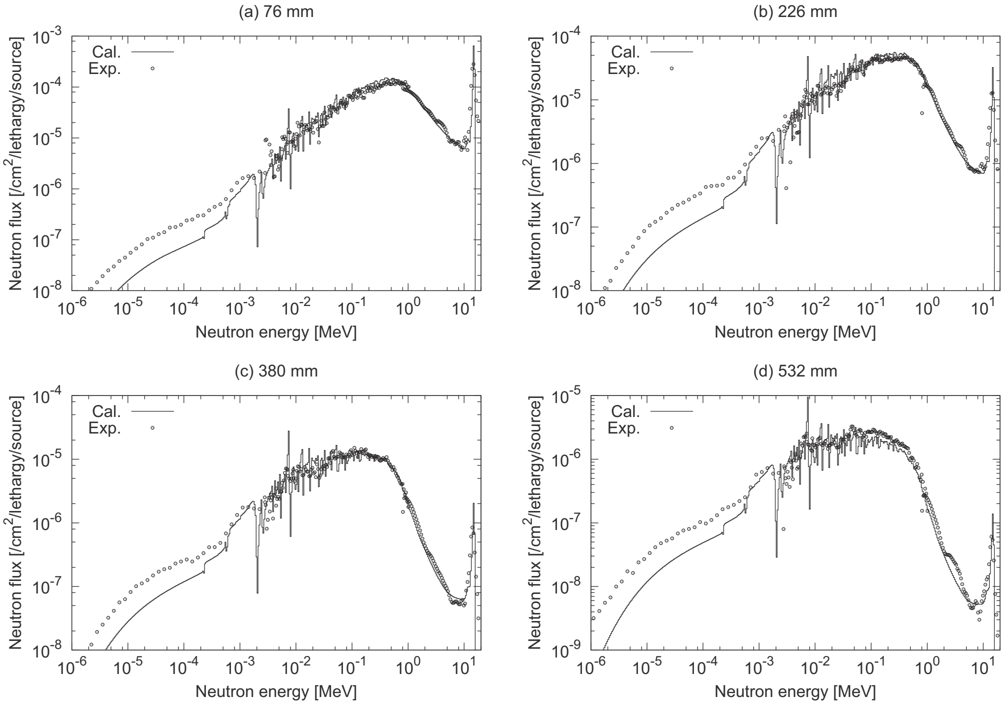

Fig. 2: Comparisons in neutron flux energy spectra between measurement data and calculation results with JENDL-4.0

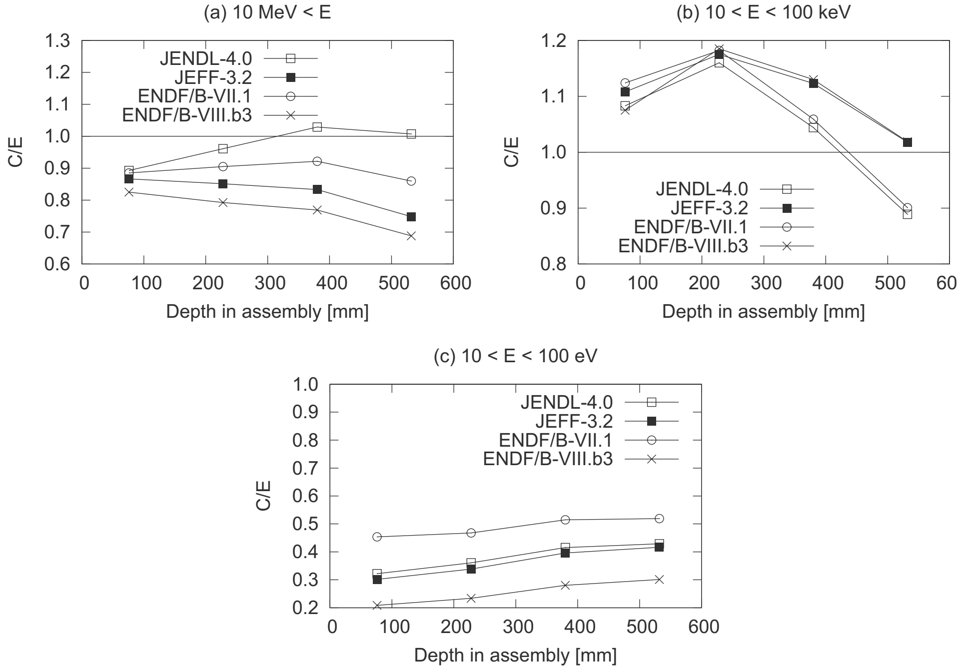

Fig. 3: C/E values obtained with several different nuclear data libraries

is replaced from JENDL-4.0 to JEFF-3.2 or ENDF/B-VIII.b3. It is interesting to point out that nuclear data difference in Cu-63 and that in Cu-65 are canceled out with each other in the integrated neutron flux below 100 eV between JENDL-4.0 and the other two libraries.

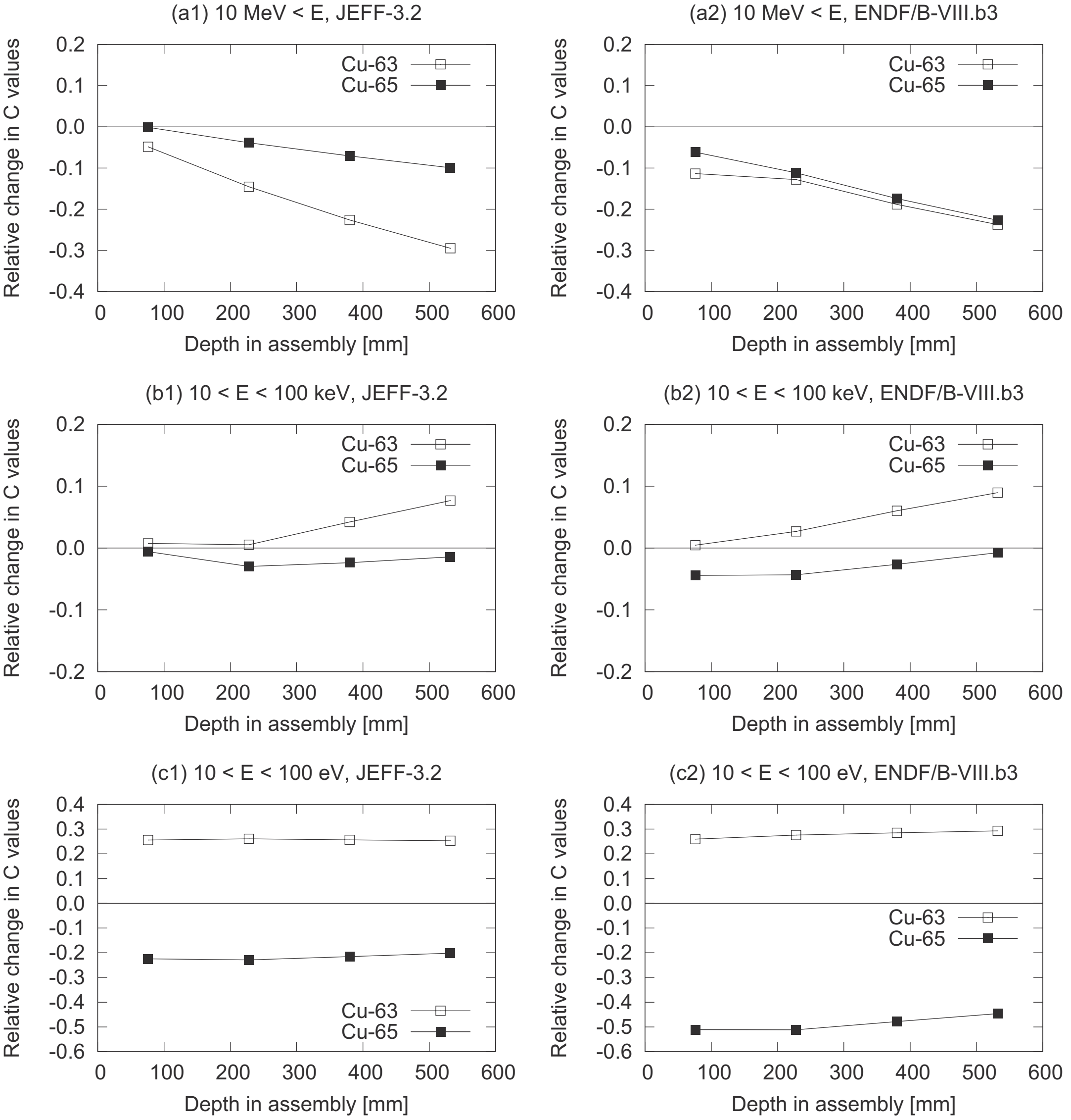

Fig. 4: Nuclide-wise contribution of effect of nuclear data difference on calculation results. Differences from the JENDL-4.0 results are shown.

Next the C/E differences are further decomposed into nuclear data-wise ones. Results are shown in **Fig. 5**. In these figures, "(n,disap)" and "(n,ine)" stand for neutron disappearance cross section and inelastic scattering cross section, respectively. From these results, it can be found that evaluation on Cu-65 inelastic scattering cross section in high energy range are different between ENDF/B-VIII.b3 and other recent libraries, and this difference has a large impact on spatial distributions of neutron flux above 10 MeV. On the low energy range, different evaluations on Cu-65 elastic scattering cross section have strong impact on neutron flux.

Finally energy group-wise contributions of differences in Cu-65 elastic scattering cross section to energy-integrated neutron flux below 100 eV are calculated. Results are shown in **Fig. 6**.

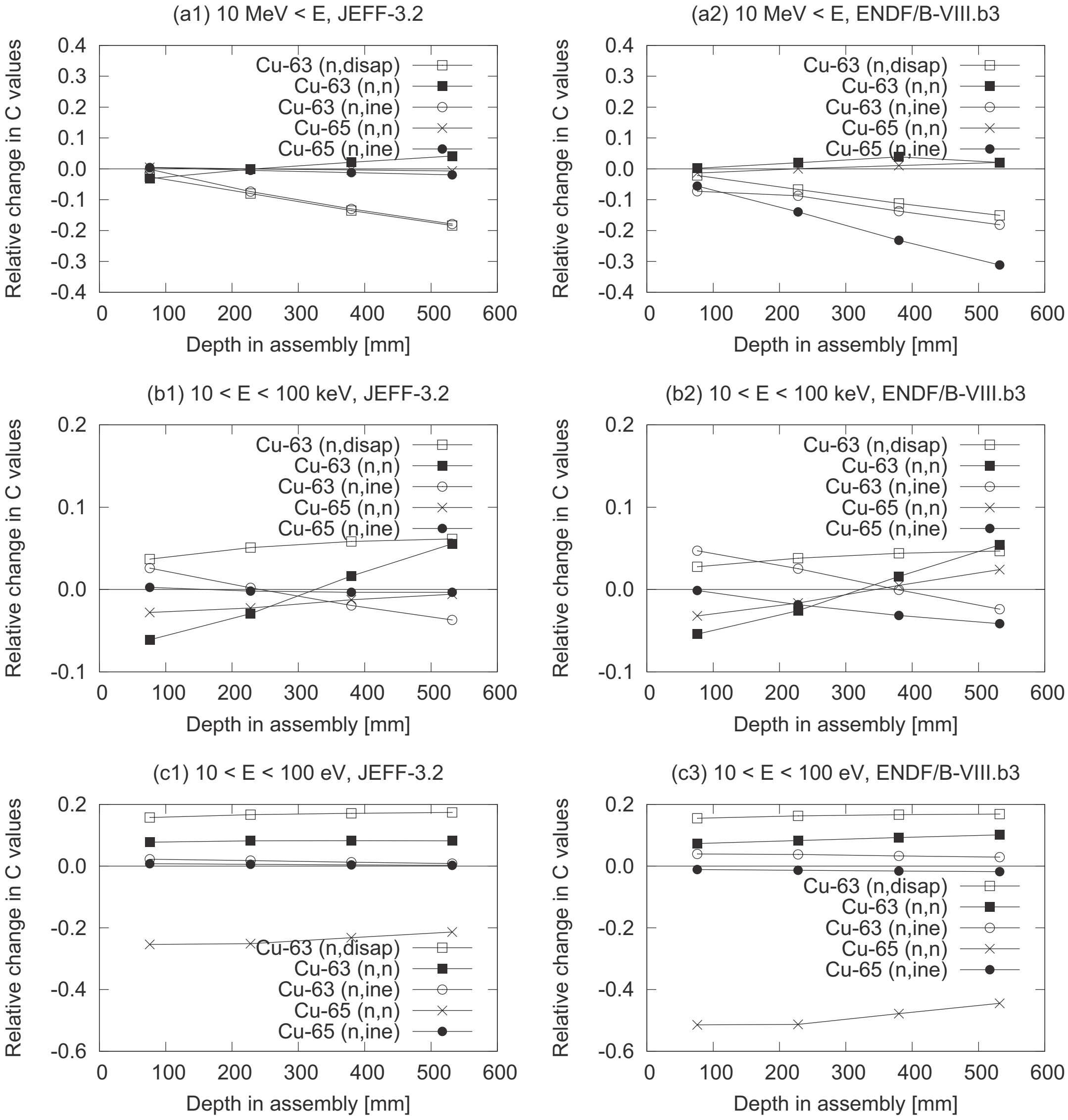

Fig. 5: Nuclide data-wise contribution of effect of nuclear data difference on calculation results. Differences from the JENDL-4.0 results are shown.

3.4 Uncertainty analysis

The TENDL-2015 library provides the covariance data for copper, so C/E values and nuclear data-induced uncertainties in the numerical results, which are obtained from sensitivity profiles and covariance data of the nuclear data, are calculated with TENDL-2015. Results are shown in **Fig. 7**, where error bars correspond to 1σ of nuclear data-induced uncertainties. Since the sum of neutron disappearance reactions are considered as (n,γ) reactions in CBZ, covariance matrices are reconstructed for the neutron total disappearance cross sections. Uncertainties in neutron flux over 10 MeV mainly come from uncertainties of Cu-63 inelastic scattering cross section, and those in neutron flux below 100 eV mainly come from those of Cu-65 elastic scattering cross section.

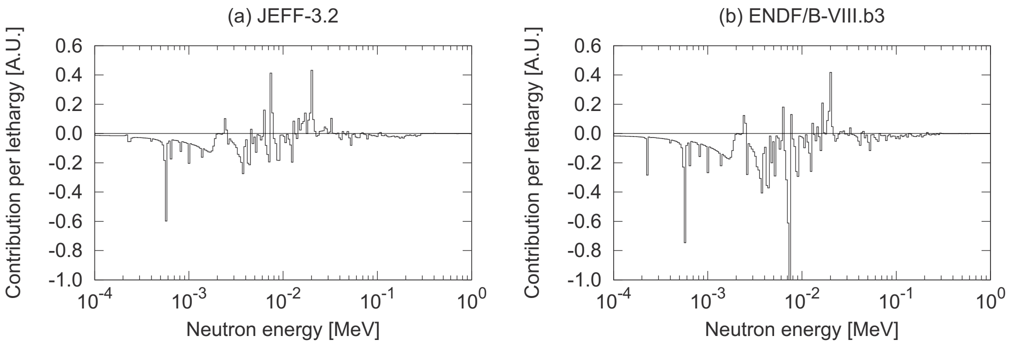

Fig. 6: Energy group- and nuclide data-wise contribution of effect of nuclear data difference on calculation results. Difference from the JENDL-4.0 results is shown.

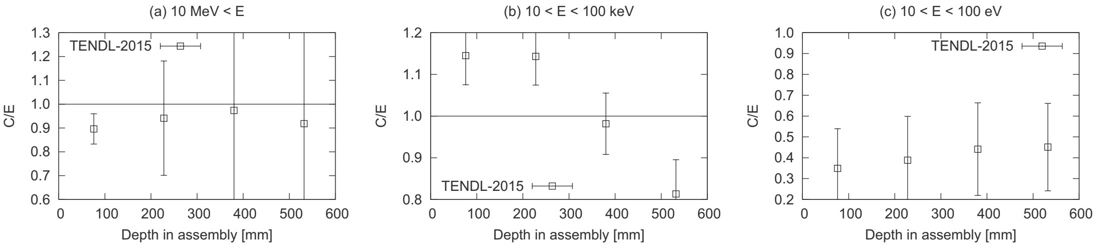

Fig. 7: C/E values and their nuclear data-induced uncertainties obtained with TENDL-2015

4. Conclusion

Sensitivity and uncertainty analyses have been successfully conducted for the FNS copper benchmark problem with the CBZ code system. Through the sensitivity analysis, it has been found that evaluation on Cu-65 inelastic scattering cross section in high energy range are different between ENDF/B-VIII.b3 and the other recent libraries, and this difference has a large impact on spatial distributions of high-energy neutron flux. It has also suggested that different evaluations on Cu-65 elastic scattering cross section among the recent libraries affect spatial distribution of low-energy neutron flux.

The author believes that these results and other previous works related to copper[6, 7] are useful and beneficial for future update of the JENDL library.

References

[1] I. Kodeli, *et al.*: *Fusion. Eng. Design*, 109-111, 1222 (2016).

[2] C. Konno, *et al.*: *Prog. Nucl. Sci. Technol.*, 2, 346 (2011).

[3] G. Chiba, *et al.*: *Ann. Nucl. Energy*, 96, 277 (2016).

[4] R.E. MacFarlane, *et al.*: LA-12740-M (1994).

[5] D.E. Cullen: IAEA-NDS-39, Rev. 13 (2007).

[6] S. Kwon, *et al.*: *Fusion Eng. Design*, 109-111, B, 1658 (2016).

[7] M. Angelone, *et al.*: *Fugion Eng. Design*, 109-111, A, 843 (2016).

18 Theoretical model analysis of composite-particle emission from deuteron-induced reactions

Shinsuke Nakayama[1*], Osamu Iwamoto[1], and Yukinobu Watanabe[2]
[1]*Nuclear Data Center, Japan Atomic Energy Agency*
[2]*Department of Advanced Energy Engineering Science, Kyushu University*
*e-mail: nakayama.shinsuke@jaea.go.jp

Toward evaluation of deuteron nuclear data, we have been developing a code system dedicated for the deuteron-induced reactions, called deuteron-induced reaction analysis code system (DEURACS). In the present work, we make an improvement in DEURACS and apply it to composite-particle emission from deuteron-induced reactions. The calculation using DEURACS reproduces the experimental double-differential cross sections of (d, xd), (d, xt), (d, $x\,^3$He), and (d, $x\alpha$) reactions on ^{27}Al and ^{58}Ni at incident energy of 80 MeV quantitatively well. From the results of the analyses, it is shown that the treatment of inelastic scattering and pick-up reaction processes is important in the calculation of deuteron-induced composite-particle emission.

1. Introduction

Recently, intensive neutron sources using deuteron accelerators have been proposed for various neutron beam applications such as transmutation of long-lived radioactive waste [1] and production of medically useful radioisotopes [2]. In the design of such neutron sources based on deuteron accelerators, accurate and comprehensive deuteron nuclear data over wide ranges of target mass number and incident energy are indispensable. Therefore, we have been developing a code system dedicated for the deuteron-induced reactions, called deuteron-induced reaction analysis code system (DEURACS). Double-differential cross sections (DDXs) of (d, xn) reactions are critically important in the engineering design of neutron sources. Therefore, we have so far focused on nucleon emission from deuteron-induced reactions. In our previous work, DEURACS was successfully applied to analysis of (d, xp) and (d, xn) reactions at incident deuteron energies up to 100 MeV [3-5].

In order to extend the applicability of DEURACS and to take advantage of it for comprehensive evaluation of deuteron nuclear data, analysis of reaction channels other than nucleon emission is also necessary. Especially, accurate prediction of triton emission is important for estimation of tritium production. In the present work, thus, we make an improvement in DEURACS and apply it to analyses of DDXs for (d, xd), (d, xt), (d, $x\,^3$He), and (d, $x\alpha$) reactions measured systematically at 80 MeV [6]. Validation of the present modelling adopted in DEURACS is discussed through comparison of the calculation results with the measured data.

2. Models and methods

A. Structure of DEURACS

First, we briefly explain the structure of DEURACS. It consists of several calculation codes based on theoretical models to describe respective reaction mechanisms involved in deuteron-induced reactions. Optical model calculation is done with the CCONE code [7,8], and direct inelastic scattering is also calculated with it. Elastic breakup and nonelastic breakup reactions are calculated using the codes based on the continuum-discretized coupled-channels method (CDCC) [9] and the Glauber model [10,11], respectively. In addition, DWUCK4 [12], which is the calculation code based on conventional zero-range distorted wave Born approximation (DWBA), is used to calculate (d, p) and (d, n) transfer reactions to bound states in the residual nuclei. Finally, pre-equilibrium and evaporation components from highly excited compound nuclei are calculated using the two-component exciton model and the Hauser-Feshbach model implemented in CCONE. In the following sections, we attempt to improve the CCONE code integrated in DEURACS so that composite-particle emission from deuteron-induced reactions can be described reasonably well.

B. (*d*, *xd*) reactions

In DEURACS, DDXs of (d, xd) reactions are expressed as follows:

$$\frac{d^2\sigma^{(d,xd)}}{dEd\Omega} = \frac{d^2\sigma_{EL}}{dEd\Omega} + \frac{d^2\sigma_{DIR}}{dEd\Omega} + \frac{d^2\sigma_{PE+CN}}{dEd\Omega}, \tag{1}$$

where $d^2\sigma_{EL}/dEd\Omega$, $d^2\sigma_{DIR}/dEd\Omega$, and $d^2\sigma_{PE+CN}/dEd\Omega$ correspond to DDXs for the components of elastic scattering (EL), direct inelastic scattering (DIR), and pre-equilibrium (PE) and compound nucleus (CN), respectively. It should be noted that there is no contribution from deuteron breakup reactions in the case of composite-particle emission. The EL component is calculated with the optical model implemented in the CCONE code. As to the DIR component, DWBA approach with a global parametrization by Kalbach [13] is used in CCONE to calculate the DIR component for giant resonance states, and we adopt the approach. In this work, the DIR component for the discrete levels in the residual nuclei is not considered.

The contribution from PE and CN processes is calculated by combining the Glauber model and the CCONE code. In the calculation, three different compound nuclei (*i.e.*, n+A, p+A, and d+A) are taken into consideration since they can be formed by absorption of a neutron, a proton in the incident deuteron, or the deuteron itself. Since the neutron or the proton absorbed in the target nucleus by the nonelastic breakup reactions has a certain energy distribution, the DDXs for the PE and CN components are calculated in the following way:

$$\frac{d^2\sigma_{PE+CN}}{dEd\Omega} = \int dE_n R_n(E_n) \frac{d^2\sigma^{(n,xd)}_{PE+CN}(E_n)}{dEd\Omega} + \int dE_p R_p(E_p) \frac{d^2\sigma^{(p,xd)}_{PE+CN}(E_p)}{dEd\Omega} + R_d \frac{d^2\sigma^{(d,xd)}_{PE+CN}}{dEd\Omega}, \tag{2}$$

where E_n and E_p are energies of the neutron and proton absorbed in the target, R_n, R_p, and R_d denote the formation fractions of three different compound nuclei, which are calculated with the Glauber model, and $d^2\sigma^{(n,xd)}_{PE+CN}/dEd\Omega$, $d^2\sigma^{(p,xd)}_{PE+CN}/dEd\Omega$, and $d^2\sigma^{(d,xd)}_{PE+CN}/dEd\Omega$ are the DDXs for the PE and CN components of (*n*, *xd*), (*p*, *xd*), and (*d*, *xd*) reactions calculated with the CCONE code, respectively.

In the present work, we have made an improvement in CCONE. In the CCONE code, the semi-empirical model proposed by Kalbach [14] is implemented. The model was originally developed for the (*α, α'*) inelastic scattering process and it expresses the effect of excitation of a nucleon in the target nucleus by the incident particle. Since this effect is not included in the exciton model, we extend the model to calculation of (*d, d'*) inelastic scattering process. In the extension, we have adopted the original model itself and the adjustable parameters used in it. Only the atomic and mass numbers of the incident and emitted particles are changed to those of (*d*, *d*') inelastic scattering. The contribution from the model is added to the PE component.

Each calculation model integrated in DEURACS contains some input parameters. In the Glauber model, nucleon optical potentials (OPs) at half the incident deuteron energy are necessary. We have chosen the Koning and Delaroche (K-D) OPs [15] for both neutron and proton. In the CCONE calculation, the OPs are taken from the K-D for nucleon, the An and Cai [16] for deuteron, the folding OPs from the K-D for triton and ^{3}He, and the Avrigeanu et al. [17] for *α*-particle, respectively. Default values in the CCONE code are employed for other input parameters such as the level-density parameter, the single-particle state density parameter, and so on.

C. (*d*, *xt*), (*d*, *x* ^{3}He), and (*d, xα*) reactions

In the case of (*d*, *xt*), (*d*, *x* ^{3}He), and (*d*, *xα*) reactions, there is no contribution from elastic and inelastic scattering components. Therefore, DDXs of these three reactions are described by only the PE and CN components and they are calculated by the same manner as Eq. (2). The direct pick-up reactions to bound states in the residual nuclei are not considered since there are few experimental differential cross sections of the reactions and it is difficult to extract corresponding spectroscopic factors necessary to determine the absolute values of the cross sections.

Since the Kalbach's semi-empirical model [14] describes also pick-up reactions induced by nucleon, we extend the model to calculate pick-up reactions induced by deuteron. As in the case of (*d*, *xd*) reactions, we have adopted the model and the adjustable parameters in it, and only the atomic and mass numbers of the incident and emitted particles are changed to the corresponding ones. Input parameters in the Glauber model and the CCONE code are the same as those used in the (*d*, *xd*) reactions.

3. Results and discussion

Figure 1 shows comparisons between calculated and experimental DDXs for the ^{58}Ni(*d*, *xd*) reactions at 80 MeV. Experimental data are taken from Ref. [6]. In the figure, the calculation results of the CCONE code introducing the Kalbach's model are presented by the dash-dotted lines. Here after, this version of the CCONE code will be referred to as "the modified CCONE code". The calculation results of the original CCONE code are also shown by the dashed lines. The peaks seen in the highest energy region arise from the elastic scattering (EL) component. In addition, the broad peaks located around 60 and 45 MeV in both calculations are attributed to the direct inelastic scattering (DIR) component for giant resonance states. A distinct difference can be seen between the two CCONE calculations in the energy region above 20 MeV. This difference comes from the inelastic scattering component calculated with the Kalbach's model.

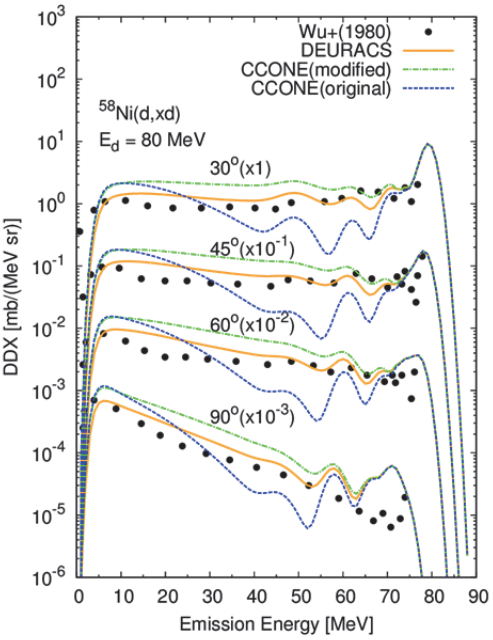

Fig. 1 Calculated and experimental DDXs for ^{58}Ni(*d*, *xd*) reactions at 80 MeV

The solid lines represent the calculation results of DEURACS, in whose framework the modified CCONE code is integrated. As shown in the figure, DEURACS reproduces the experimental (*d*, *xd*) spectra better than the modified CCONE code over the whole emission energy range. In the original and modified CCONE code, the compound nucleus formation cross section is given by subtraction of the direct inelastic scattering cross section from the deuteron total reaction cross section. However, the incident deuteron flux is fed into other direct reaction channels such as elastic and nonelastic breakup reactions. As described in Eq. (2), this effect is properly taken into account in the framework of DEURACS. This results in reduction of the cross sections of the PE and CN processes and good agreement with the experimental DDX of (*d*, *xd*) reactions. These results indicate the two important points in calculation of (*d*, *xd*) reactions: deuteron inelastic scattering with excitation of a nucleon in the target, and feeding of the incident deuteron flux into breakup channels.

In Fig. 2, calculated and experimental DDXs for the ^{27}Al(*d*, *xt*), ^{27}Al(*d*, *x* ^{3}He), and ^{58}Ni(*d*, *xα*) reactions at 80 MeV are shown, respectively. The peaks observed around the high emission energy end correspond to the direct pick-up reactions to bound states in the residual nuclei. Since this component is absent in the present calculation, some discrepancies are seen in the highest energy region. As in the case of (*d*, *xd*) reactions, cross sections in the energy region above 20 MeV increase in calculation of the modified CCONE code. This is due to the Kalbach's model introduced to calculate pick-up reaction. And also, by considering feeding of the incident deuteron flux into breakup channels, DEURACS reproduces the experimental data better than the modified CCONE code over the whole emission energy range.

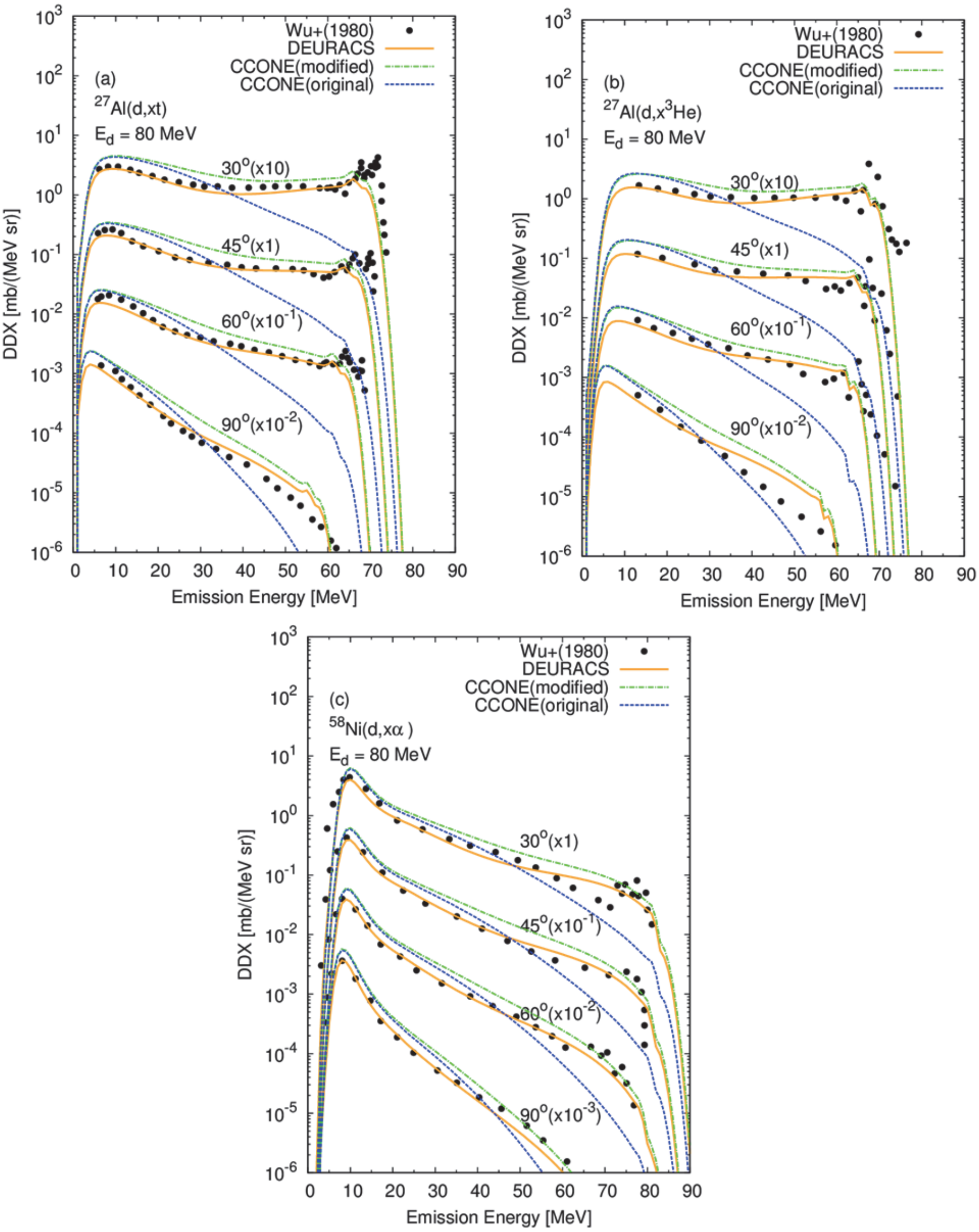

Fig. 2 Same as Fig. 1 but for (a) ^{27}Al(*d*, *xt*), (b) ^{27}Al(*d*, *x* ^{3}He), and (c) ^{58}Ni(*d*, *xα*) reactions

4. Summary and outlook

We have analyzed double-differential cross sections (DDXs) for (*d*, *xd*), (*d*, *xt*), (*d*, $x\,^3$He), and (*d*, $x\alpha$) reaction using deuteron-induced reaction analysis code system (DEURACS). In the calculation of the DDXs, the Kalbach's semi-empirical model implemented in the CCONE code has been extended to deuteron-induced reactions, and the modified CCONE code has been integrated in DEURACS. The calculation results of DEURACS has reproduced the experimental (*d*, *xd*), (*d*, *xt*), (*d*, x^3He), and (*d*, $x\alpha$) data at 80 MeV quantitatively well. The analysis results demonstrated that it is of importance in deuteron nuclear data evaluation to consider both inelastic scattering and pick-up reaction processes. Since we have confirmed that DEURACS is successfully applicable to all particle emissions from deuteron-induced reactions, we plan to perform deuteron nuclear evaluation using DEURACS in the future.

References

[1] R. Fujita, J. Atomic Energy Soc. Jpn., **58**, 93 (2016) (in Japanese).

[2] Y. Nagai, K. Hashimoto, Y. Hatsukawa et al., J. Phys. Soc. Jpn. **82**, 064201 (2013).

[3] S. Nakayama and Y. Watanabe, J. Nucl. Sci. Technol. **53**, 89 (2016).

[4] S. Nakayama, H. Kouno, Y. Watanabe, O. Iwamoto, and K. Ogata, Phys. Rev. C **94**, 014618 (2016).

[5] S. Nakayama, H. Kouno, Y. Watanabe, O. Iwamoto, T. Ye and K. Ogata, EPJ Web of Conferences **146**, 12025 (2017).

[6] J. R. Wu, C. C. Chang, and H. D. Holmgren, Phys. Rev. C **19**, 370 (1979).

[7] O. Iwamoto, J. Nucl. Sci. Technol. **44**, 687 (2007).

[8] O. Iwamoto, N. Iwamoto, S. Kunieda, F. Minato, and K. Shibata, Nucl. Data Sheets **131**, 259 (2016).

[9] M. Yahiro, K. Ogata, T. Matsumoto, and K. Minomo, Prog. Theor. Exp. Phys. **2012**, 1A206 (2012).

[10] T. Ye, Y. Watanabe, and K. Ogata, Phys. Rev. C **80**, 014604 (2009).

[11] T. Ye, S. Hashimoto, Y. Watanabe, K. Ogata, and M. Yahiro, Phys. Rev. C **84**, 054606 (2011).

[12] P. D. Kunz, computer code DWUCK4, http://spot.colorado.edu/~kunz/DWBA.html.

[13] C. Kalbach, Phys Rev. C 62, 044608 (2000).

[14] C. Kalbach, Z. Phys. A **283**, 401 (1977).

[15] A. J. Koning and J. P. Delaroche, Nucl. Phys. A **713**, 231 (2003).

[16] H. An and C. Cai, Phys. Rev. C **73**, 054605 (2006).

[17] V. Avrigeanu, P.E. Hodgson, and M. Avrigeanu, Phys. Rev. C **49**, 2136 (1994).

19 Dynamical Calculation for Fission Process of Actinoid Nuclei

N.L.B. Anuar, T. Aoki, S. Kobayashi, Y. Hayashi, J. Nakagawa, S. Sawada, S. Tanaka, T. Tanaka, Y. Aritomo, K. Nishio[1]

Faculty of Science and Engineering, Kindai University, Higashi-Osaka, Osaka, Japan
[1] *Japan Atomic Energy Agency, Tokai, Ibaraki, 319-1195, Japan*

Contact e-mail : aritomo@ele.kindai.ac.jp

Abstract

Mass distributions of fission fragments (MDFF) at low excitation energies are studied using a dynamical model based on the fluctuation-dissipation theorem formulated as Langevin equations. We investigate the MDFF of the isotopes in actinoid nuclei over a wide range, which is the first attempt with the Langevin calculation. We develop the model taking into account the change of the neutron number in the system by neutron emission, and investigate the multi chance fission. Moreover, we introduce the microscopic transport coefficient in the dynamical equation, and take into account the independent deformation of fission fragments using the four-dimensional Langevin calculation.

1. Introduction

Fission of uranium was discovered in 1938 [1, 2], and the principle of this phenomenon has been investigated. The application of the fission process to the supply of power was realized soon after its discovery. Because of the nuclear power plant accident at Fukushima in 2011, it is required to quantitatively prediction of the amounts of heavy elements and radioactive fission products in the remains of the power plant.

To perform the theoretical estimations of fission products, we employ the dynamical model based on the fluctuation-dissipation theorem [3]. Using the Langevin equation, we investigate the time evolution of the nuclear shape during the fission process starting from a nearly spherical shape and finishing at the scission region via the fission saddle point. This method takes account of friction, inertia mass and multi-dimensional potential energy surfaces.

Using the dynamical model, mass distribution of fission fragments (MDFF) of actinoid nuclei and isotopes at low excitation energies are studied with potential energy landscape of the two-center shell model. The overall trend of the asymmetric mass distribution of ^{236}U and ^{240}Pu were reproduced [4]. It was found that the shell effect of the potential energy landscape has a dominant role in determining the mass distribution. Using the model, we investigate the MDFF of the isotopes in actinoid nuclei over a wide range, which is the first attempt with the Langevin calculation. We find the characteristic tendency of the MDFF with the numbers of neutron and proton. We develop the model and investigate the multi chance fission. Moreover, we investigate the fission process using the microscopic transport coefficient in the dynamical model, and take into account the independent deformations of fission fragments using the four-dimensional Langevin calculation.

The paper is organized as follows. In Sec. 2, we detail the framework of the model. In Sec. 3, we show the results for MDFF of actinoid nuclei at low excitation energy by the dynamical model. In Sec. 4, we present a summary of this study and further discussion.

2. Model

We use the fluctuation-dissipation model and employ Langevin equations [3] to investigate the dynamics of the fission process. The nuclear shape is defined by the two-center parametrization [5, 6], which has three deformation parameters, z_0, δ, and α to serve as collective coordinates: z_0 is the distance between two potential centers, while $\alpha = (A_1 - A_2)/(A_1 + A_2)$ is the mass asymmetry of the two fragments, where A_1 and A_2 denote the mass numbers of heavy and light fragments [3]. The symbol δ denotes the deformation of the fragments, and is defined as $\delta = 3(R_{\|} - R_{\perp})/(2R_{\|} + R_{\perp})$, where $R_{\|}$ and $R_{\perp}$ are the half length of the axes of an ellipse in the z_0 and ρ directions of the cylindrical coordinate, respectively, as shown in Fig. 1 in Ref. [5]. We assume in this work that each fragment has the same deformation. This constraint is relaxed in the section 3.4 since the deformations of the heavy and light fragments in the fission of U region are known to be different from each other. In order to reduce the computational time, we employ the coordinate z defined as $z = z_0/(R_{CN}B)$, where R_{CN} denotes the radius of a spherical compound nucleus and B is defined as $B = (3 + \delta)/(3 - 2\delta)$. We use the neck parameter $\epsilon = 0.35$, which is recommended in Ref. [6] for the fission process. The three collective coordinates may be abbreviated as q, $q = \{z, \delta, \alpha\}$.

For a given value of a temperature of a system, T, the potential energy is defined as a sum of the liquid-drop (LD) part, a rotational energy and a microscopic (SH) part;

$$V(q, \ell, T) = V_{\mathrm{LD}}(q) + \frac{\hbar^2 \ell(\ell+1)}{2I(q)} + V_{\mathrm{SH}}(q, T), \tag{1}$$

$$V_{\mathrm{LD}}(q) = E_{\mathrm{S}}(q) + E_{\mathrm{C}}(q), \tag{2}$$

$$V_{\mathrm{SH}}(q, T) = E^0_{\mathrm{shell}}(q)\Phi(T), \tag{3}$$

$$\Phi(T) = \exp\left(-\frac{aT^2}{E_{\mathrm{d}}}\right). \tag{4}$$

Here, V_{LD} is the potential energy calculated with the finite-range liquid drop model, given as a sum of of the surface energy E_{S} [7] and the Coulomb energy E_{C}. V_{SH} is the shell correction energy evaluated by Strutinski method from the single-particle levels of the two-center shell model. The shell correction have a temperature dependence expressed by a factor $\Phi(T)$, in which E_{d} is the shell damping energy chosen to be 20 MeV [8] and a is the level density parameter. At the zero temperature ($T = 0$), the shell correction energy reduces to that of the two-center shell model values E^0_{shell}. The second term on the right hand side of Eq. (1) is the rotational energy for an angular momentum ℓ [3], with a moment of inertia at q, $I(q)$.

The multidimensional Langevin equations [3] are given as

$$\begin{aligned} \frac{dq_i}{dt} &= \left(m^{-1}\right)_{ij} p_j, \\ \frac{dp_i}{dt} &= -\frac{\partial V}{\partial q_i} - \frac{1}{2}\frac{\partial}{\partial q_i}\left(m^{-1}\right)_{jk} p_j p_k - \gamma_{ij}\left(m^{-1}\right)_{jk} p_k + g_{ij} R_j(t), \end{aligned} \tag{5}$$

where $q_i = \{z, \delta, \alpha\}$ and $p_i = m_{ij} dq_j/dt$ is a momentum conjugate to coordinate q_i. The summation is performed over repeated indices. In the Langevin equation, m_{ij} and γ_{ij} are the shape-dependent collective inertia and the friction tensors, respectively. The wall-and-window one-body dissipation [9] is adopted for the friction tensor which can describe the pre-scission neutron multiplicities and total kinetic energy of fragments simultaneously [10]. A hydrodynamical inertia tensor is adopted with the Werner-Wheeler approximation for the velocity field [11]. The normalized random force $R_i(t)$ is assumed to be that of white noise, *i.e.*, $\langle R_i(t)\rangle$=0 and $\langle R_i(t_1)R_j(t_2)\rangle = 2\delta_{ij}\delta(t_1 - t_2)$. The strength of the random force g_{ij} is given by Einstein relation $\gamma_{ij}T = \sum_k g_{ij}g_{jk}$.

The temperature T is related with the intrinsic energy of the composite system as $E_{\text{int}} = aT^2$, where E_{int} is calculated at each step of a trajectory calculation as

$$E_{\text{int}} = E^* - \frac{1}{2}\left(m^{-1}\right)_{ij} p_i p_j - V(q, \ell, T = 0). \tag{6}$$

The fission events are determined in our model calculation by identifying the different trajectories in the deformation space. We consider the neutron emission in our calculation. However, we only take into account the decrease in the excitation energy of the system by neutron emission, not the change in the potential energy surface, as our first step.

3. Results

3.1 MDFF of the isotopes in actinoid nucleus over a wide range

Using the dynamical model, MDFF of $n+^{235}$U and $n+^{239}$Pu at low excitation energy $E^* =$ 20 MeV were calculated in the previous study [4]. The overall trend of the asymmetric mass distribution were reproduced.

Here, using the same parameters as these in the calculation for $n+^{235}$U, we investigate the MDFF of the isotopes in actinoid nuclei over a wide range, which is the first attempt with the Langevin calculation. Figure 1 shows the calculation results. In the calculation, we prepared 10,000 trajectories and assumed $\Phi(T) = 1$ in Eq. (3), which corresponds to the full shell correction energy, to simulate the low excitation energy introduced by thermal neutrons. The effects of $\Phi(T)$ is discussed in Ref. [4]. We can see the characteristic tendency of the MDFF with the numbers of neutron and proton. It is useful to discuss the mechanism of the fission process for each isotopes.

3.2 MDFF taking into account the effects of neutron emission

In our calculation model, we only considered the the decrease in the excitation energy of the system by neutron emission. Here, we develop the model taking into account the change of neutron number in the system by neutron emission. It means that the multi chance fission could be treated and we could compere results with the MDFF of the experimental data, directly. Using the GEF code, which is a computer code for the simulation of the nuclear fission process [12], we obtain the average rate of neutron emissions during the de-exciting process of the compound nucleus. Once we know the excitation energy and neutron number of the system, we could calculate the MDFF using the Langevin model. Then we sum up the results of MDFF with the weight coefficients at a rate of neutron emissions. The results are shown in Fig. 2 for ^{238}U at $E^* = 35$ MeV comparison with the experimental data [13]. The calculation results show that the experimental data include the multi chance fission obviously.

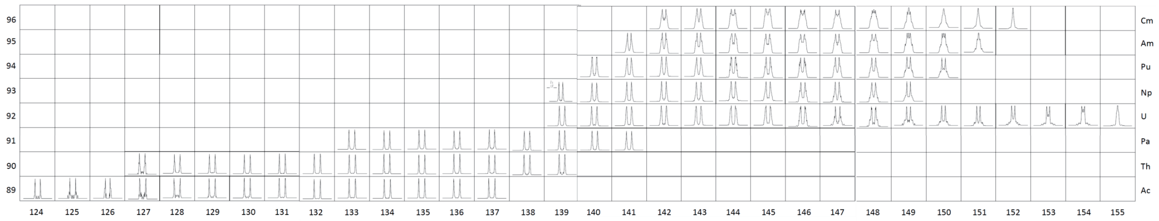

Figure 1: Calculated mass distribution of fission fragments of the isotopes in actinoid nuclei at $E^* = 20$ MeV

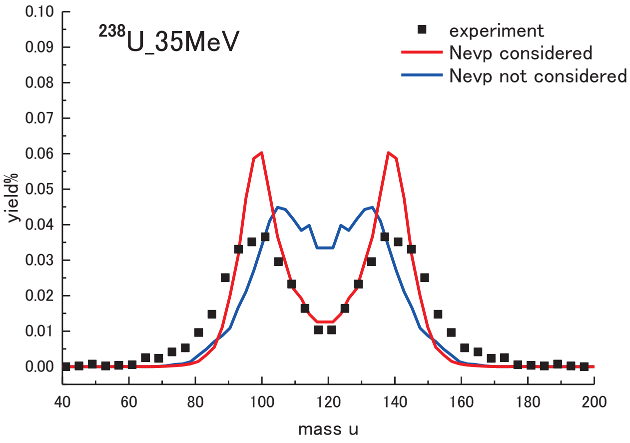

Figure 2: Calculated mass distribution of fission fragments of ^{236}U at $E^* = 35$, with and without the multi chance fission. The experimental data is shown by dots [13].

3.3 MDFF using microscopic transport coefficients

It is well-known that the collective inertia and the friction (the transport coefficients) in the dynamical equation are calculated microscopically by the linear response theory taking into account the nuclear structure [14]. The transport coefficients depend on the nuclear temperature and the friction is smaller than the one-body friction (macroscopic model) at the low temperature. Using the transport coefficients, we try to calculate the MDFF of ^{236}U. Figure 3 shows the MDFF with the microscopic transport coefficients at $E^* = 15$ and 35 MeV comparison with the macroscopic one. The difference between the results with the microscopic transport coefficients and the macroscopic one is not so much. In the fission process, we start the calculation on the assumption in a thermal equilibrium state. Therefore, we could say that the transport coefficients play an important roll when the kinetic energy of the system dissipates into the intrinsic energy, that is to say, in the fusion process and the deep inelastic collision etc.

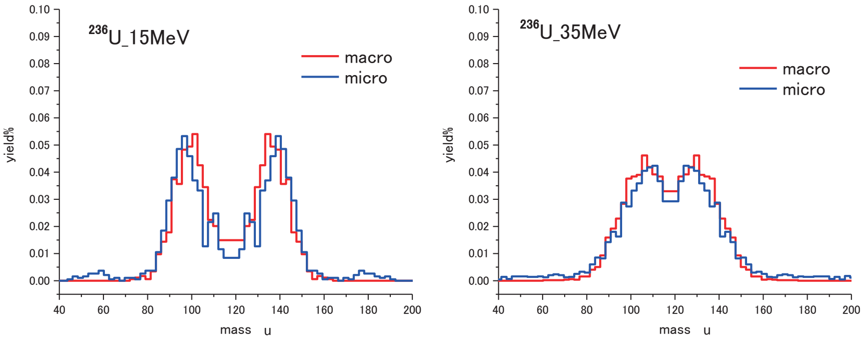

Figure 3: Calculated mass distribution of fission fragments of ^{236}U with the microscopic transport coefficients at $E^* = 15$ and 35 MeV, in comparison with the macroscopic one.

3.4 Fission process with independent deformations of fission fragments

To calculate the fission process more realistically, we introduce the independent deformations of fission fragments, since the deformations of the heavy and light fragments in the fission of U region are known to be different from each other. We investigate the fission process using the four-dimensional Langevin calculation with $q = \{z, \delta_1, \delta_2, \alpha\}$.

The results of MDFF of $n+^{235}$U at $E^* = 20$ MeV quantitatively agree with the experimental data. We calculate the average total kinetic energy of the fission fragments $\langle TKE \rangle$. We obtain $\langle TKE \rangle_{4dim} = 164.6$ MeV, which is consistent with the experimental data $\langle TKE \rangle_{exp} = 168.2 \sim 171.3$ MeV [15]. In the three-dimensional Langevin calculation, it is $\langle TKE \rangle_{3dim} = 169.4$ MeV. The configurations at the scission point are represented with $\langle \delta \rangle = -0.121$ in the three-dimensional Langevin calculation, and $\langle \delta_1 \rangle = -0.182$ and $\langle \delta_2 \rangle = 0.314$ in the four-dimensional one.

4. Summary

In this study, we investigated the fission process at low excitation energy using Langevin equations. We investigated the MDFF of the isotopes in actinoid nuclei over a wide range. We developed the model taking into account the change of the neutron number in the system by neutron emission, and investigated the multi chance fission. Moreover, we introduced the the microscopic transport coefficient in the dynamical model, and the four-dimensional Langevin calculation ($\delta_1 \neq \delta_2$). The reproduction of the experimental MDFF in this model can be considered as grounds for supporting the investigation of fission dynamics at low excitation energy. In the future, we plan to improve the model with high accuracy and to decrease the differences between the calculated MDFF and the experimental data.

The authors are grateful to Prof. T. Wada (original Langevin code) and Dr. F. Ivanyuk (microscopic transport coefficients) for their helpful suggestions and valuable discussion throughout the present work. The authors would like to thank Dr. S. Yamaji and his collaborators who developed the calculation code for potential energy with a two-center parameterization.

References

[1] O. Hahn and F. Straßmann, Naturwissenschaften **27**, 11 (1939).

[2] L. Meitner and O.R. Frisch, Nature (London) **143**, 239 (1939).

[3] Y. Aritomo and M. Ohta, Nucl. Phys. A **744**, 3 (2004).

[4] Y. Aritomo and S. Chiba, Phys. Rev. C **88**, 044614 (2013).

[5] J. Maruhn and W. Greiner, Z. Phys. **251**, 431 (1972).

[6] K. Sato, A. Iwamoto, K. Harada, S. Yamaji, and S. Yoshida, Z. Phys. A **288**, 383 (1978).

[7] H.J. Krappe, J.R. Nix, and A.J. Sierk, Phys. Rev. C **20**, 992 (1979).

[8] A.V. Ignatyuk, G.N. Smirenkin, and A.S. Tishin, Sov. J. Nucl. Phys. **21**, 255 (1975).

[9] J. Blocki, Y. Boneh, J.R. Nix, J. Randrup, M. Robel, A.J. Sierk, and W.J. Swiatecki, Ann. Phys. **113**, 330 (1978).

[10] T. Wada, Y. Abe and N. Carjen, Phys. Rev. Lett. **7**, 3538 (1993).

[11] K.T.R. Davies,A.J. Sierk, and J.R. Nix, Phys. Rev. C **13**, 2385 (1976).

[12] K.-H. Schmidt, B. Jurado, Ch. Amouroux, JEFF-Report 24, Data Bank, Nuclear-Energy Agency, OECD (2014).

[13] J. Katakura, JENDL FP Decay Data File 2011 and Fission Yields Data File 2011, JAEA-Data/Code 2011-025 (2012).

[14] F.A. Ivanyuk, H. Hofmann, V.V. Pashkevich, S. Yamaji, Phys. Rev. C **55**, 1730 (1997).

[15] R. Vandenbosh and J.R. Huizenga, Nuclear Fission, Academic Press, New York and London (1973).

20 Evaluation of Neutron Resonance Parameters for Zr Isotopes

Akira ICHIHARA
Nuclear Data Center, Japan Atomic Energy Agency
Tokai-mura, Naka-gun, Ibaraki-ken, 319-1195, Japan
e-mail: ichihara.akira@jaea.go.jp

Neutron resolved resonance parameters of Zr isotopes were reevaluated for the revision of JENDL-4.0. The resonance parameters were revised mainly by referring to the data published after the JENDL-4.0 evaluation. In this work, a negative resonance of ^{93}Zr was removed to reproduce the measured thermal capture cross section, and the resonance parameters of ^{94}Zr were altered to obtain the thermal elastic scattering cross section.

1. Introduction

In the Nuclear Data Center of Japan Atomic Energy Agency (JAEA-NDC), we are engaged in the evaluation activity for the next version of the Japanese Evaluated Nuclear Data Library, JENDL-4.0[1]. Zirconium (Zr) is an important structural material of nuclear reactors since zircaloys are employed in fuel rods. Natural Zr consists of isotopes with the mass numbers 90, 91, 92, 94 and 96 (^{90,91,92,94,96}Zr), where their abundance are 51.45, 11.22, 17.15, 17.38 and 2.80 %, respectively. Besides, ^{93}Zr is a long-lived fission product (LLFP) with a half-life of $1.61\text{x}10^6$ years.

In this work, we investigated the resolved resonance parameters (RRPs) of Zr isotopes using published data, and revised RRPs by mainly adopting the values derived by Tagliente et al. at the n_TOF facility in CERN [2-7]. This paper presents the current status of our evaluation for each Zr isotope.

2. Assessment of Resonance Parameters

^{90}Zr: In JENDL-4.0, the multilevel Breit-Wigner (MLBW) formula was used for cross sections in the thermal and resonance region. The upper limit of resonance energy (E_H) was 171 keV, and the scattering radius (R') was 7.2 fm. In the resonance energy (E_R) range from 3.86 to 68.6 keV, RRPs of Tagliente et al. [2] were adopted. Above E_R = 70 keV, the values of E_R and the neutron width (Γ_n) were taken from the data of Musgrove et al. [8] The values of radiative width (Γ_γ) were derived from the capture kernels measured by Boldeman et al. [9], where the correction factor of 0.967 according to a corrigendum by Allen et al. [10] was multiplied. The average radiative widths for the s-, p- and d-wave resonances, $<\Gamma_{\gamma 0}> = 0.19$ eV, $<\Gamma_{\gamma 1}> = 0.27$ eV and $<\Gamma_{\gamma 2}> = 0.28$ eV, were employed for undetermined radiative widths.

In the present evaluation, the neutron widths recommended by Mughabghab [11] were adopted for $E_R = 53.37$ and 57.79 keV to reproduce the measured total cross sections of Musgrove et al. [8] Also, $<\Gamma_{\gamma 0}> = 0.25$ eV and $<\Gamma_{\gamma 2}> = 0.25$ eV, obtained by averaging the known radiative widths, were employed.

^{91}Zr: In JENDL-4.0, MLBW formula was used. The values of E_H and R' were 26 keV and 7.2 fm, respectively. The RRP values were taken from the tabulation of Tagliente et al. [3] A negative resonance was employed to obtain the lower limit of the thermal radiative capture cross section of 1.5 ± 0.2 b measured by Nakamura et al. [12]

In the present work, RRPs for $E_R = 12.218$ and 15.763 keV in [3], which have not been included in JENDL-4.0, were supplemented.

^{92}Zr: In JENDL-4.0, MLBW formula was used. The values of E_H and R' were 71 keV and 7.2 fm, respectively. The RRP values were based on the data of Boldeman et al. [13] The average radiative widths for the s- and p-wave resonances, $<\Gamma_{\gamma 0}> = 0.18$ eV and $<\Gamma_{\gamma 1}> = 0.27$ eV, were applied to undetermined radiative widths. A negative resonance was employed to produce the thermal elastic scattering cross section of 7.1 b.

In this work, RRPs in 43 resonances below $E_R = 40$ keV were replaced with the data provided by Tagliente et al. [4] For E_R above 40 keV, the radiative widths were recalculated using the capture kernels of Boldeman et al. [13] multiplied by the correction factor of 0.9833 suggested by Allen et al. [10] The RRP values of Mughabghab [11] were adopted in the negative and the first s-wave ($E_R = 2689$ eV) resonances to obtain the recommended thermal capture cross section of 0.260 ± 0.080 b. Also, $<\Gamma_{\gamma 1}> = 0.24$ eV, derived from the known widths, was applied.

^{93}Zr: In JENDL-4.0, MLBW formula was used. The values of E_H and R' were 1.7 keV and 7.2 fm, respectively. The RRP values were evaluated on the bases of the data of Macklin et al. [14,15] The values of undetermined spin in the resonance states were assigned randomly. Also, undetermined orbital angular momentum of the incident neutron was estimated with the method of Bollinger and Thomas [16]. The average radiative widths $<\Gamma_{\gamma 0}> = 0.145$ eV and $<\Gamma_{\gamma 1}> = 0.25$ eV were applied to unknown radiative widths for the s- and p-wave resonances. A negative resonance was employed to reproduce the thermal capture cross section given by Mughabghab et al. [17]

In the present evaluation, the maximum of resonance energy E_H was extended to 6.8 keV, and the negative resonance in JENDL-4.0 was removed to obtain the thermal capture cross section which accords with the measured value of 0.76 ± 0.13 b by Nakamura et al. [12,18] The resonance peaks for $E_R = 4121$, 4320, 6641 eV were removed according to the suggestion of Tagliente et al. [5] who assigned them as impurity components. Also, $\langle\Gamma_{\gamma 1}\rangle$ = 0.21 eV derived from the known widths was employed.

^{94}Zr: In JENDL-4.0, MLBW formula was used. The values of E_H and R' were 53.5 keV and 7.2 fm, respectively. The RRP values were evaluated on the bases of the data of Boldeman et al. [13] and Leinweber et al. [19] The average radiative width $\langle\Gamma_{\gamma 1}\rangle$ = 0.175 eV was applied to undetermined radiative widths for the p-wave resonances. A negative resonance was employed to reproduce the thermal cross sections in [17].

In the present evaluation, RRPs in 49 resonances below E_R = 59 keV were replaced with the data provided by Tagliente et al. [6] Accordingly, the maximum of resonance energy E_H was extended to 59 keV. The RRP values in the negative and the first (E_R = 2241 eV) resonances were modified with the recommended values of Mughabghab to reproduce the thermal scattering cross section of 8.59 ± 0.41 b in [11] and the capture cross section of 0.049 b which were derived by averaging the measured data [20-25] published after 2000. The average radiative width $\langle\Gamma_{\gamma 1}\rangle$ = 0.16 eV derived from the known widths was employed.

^{96}Zr: In JENDL-4.0, MLBW formula was used. The values of E_H and R' were 100 keV and 7.2 fm, respectively. The values of RRPs were evaluated on the bases of the results of Coceva et al. [26], Musgrove et al. [27], Brusegan et al. [28], Salah et al. [29], and Leinweber et al. [19] The neutron and radiative widths (Γ_n, Γ_γ) were modified within experimental errors to obtain the better agreement with the radiative capture resonance integral of 5.28 ± 0.11 b recommended by Mughabghab [11]. The average radiative widths $\langle\Gamma_{\gamma 0}\rangle$ = 0.068 eV and $\langle\Gamma_{\gamma 1}\rangle$ = 0.17 eV were applied to undetermined radiative widths for the s- and p-wave resonances. A negative resonance was employed to reproduce the thermal capture cross section of Mughabghab [11].

In this work, the radiative widths in 15 resonances below E_R = 37 keV were replaced with the data derived by Tagliente et al. [7] The neutron and radiative widths of the negative resonance were adjusted to reproduce the thermal scattering cross section of 6.6 ± 0.4 b in [11] and the capture cross section of 0.022 b [23,25,30]. Also, $\langle\Gamma_{\gamma 0}\rangle$ = 0.08 eV and $\langle\Gamma_{\gamma 1}\rangle$ = 013 eV, obtained by averaging the known widths, were employed.

3. Thermal Cross Sections and Radiative Capture Resonance Integral

Through this work, RRPs were revised by replacing the data in JENDL-4.0 with the results derived by Tagliente et al. [4-7] at n_TOF facility in CERN. Moreover, the data were modified with the recommended data of Mughabghab [11]. Table 1 shows the thermal (0.0253 eV) cross sections for neutron elastic scattering (σ_{el}) and radiative capture (σ_γ), and the radiative capture resonance integral (I_γ). In each isotope, the JENDL-4.0 evaluations are listed in the first row, the present results are shown in the second row, and the recommended values of Mughabghab [11] are given in the third row. In ^{90}Zr and ^{91}Zr, the thermal cross sections and resonance integrals are hardly affected because of the minor changes. In ^{91}Zr, JENDL-4.0 and our σ_γ values are closer to the measured value of 1.5 ± 0.2 b by Nakamura et al. [12] than to the recommended value of Mughabghab [11]. In ^{92}Zr, the present I_γ value is smaller than the recommended value of Mughabghab. This may come from the fact that the Γ_γ values of Tagliente et al. [4] are 15 % smaller than those of Boldeman et al. [13] applied in JENDL-4.0. In ^{93}Zr, the negative resonance of JENDL-4.0 was removed in this work to reproduce the measured capture cross section of 0.76 ± 0.13 b by Nakamura et al. [12] In ^{94}Zr, the σ_{el} value was altered by referring to the recommended data of Mughabghab [11]. In ^{96}Zr, the agreement of I_γ with [11] was improved compared with the JENDL-4.0 evaluation.

In this work, remarkable difference from JENDL-4.0 appeared in the thermal capture cross section of ^{93}Zr and the elastic scattering cross section of ^{94}Zr. Figure 1 shows the averaged neutron capture cross section of ^{93}Zr. It can be seen that the present result almost overlaps the ENDF/B-VII.1 evaluation. Also, Figure 2 indicates the averaged elastic scattering cross section of ^{94}Zr. In Fig. 2, our result agrees well with both the ENDF/B-VII.1 and JEFF-3.2 evaluations in the thermal region.

4. Conclusion

The resonance parameters of Zr isotopes were reevaluated for the revision of JENDL-4.0. The data were revised by adopting RRPs derived by Tagliente et al. [4-7] at the n_TOF facility in CERN. Moreover, the data were modified with the recommended data of Mughabghab [11]. In this work, the negative resonance of ^{93}Zr was removed to produce the measured thermal capture cross section of Nakamura et al. [12], and RRPs of ^{94}Zr were adjusted to reproduce the thermal scattering cross section of Mughabghab [11]. The obtained results accord well with the evaluated data of other libraries in the thermal region.

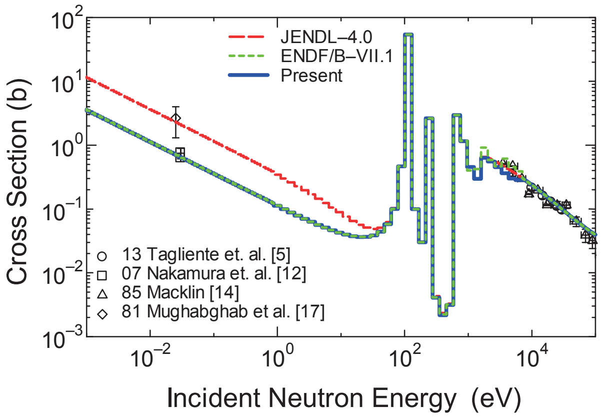

Fig.1 Averaged capture cross section of ^{93}Zr

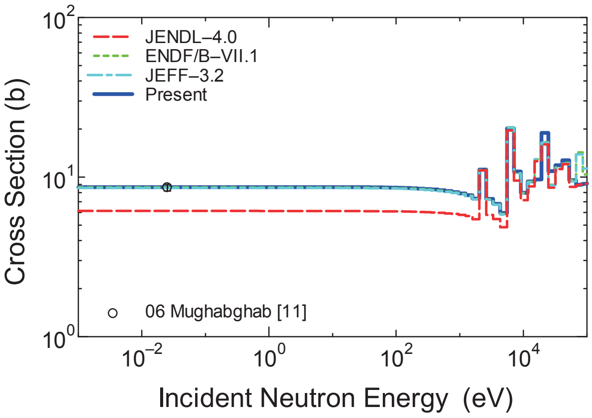

Fig.2 Averaged elastic scattering cross section of ^{94}Zr

Table 1 Thermal cross sections for neutron elastic scattering (σ_{el}) and capture (σ_{γ}), and radiative capture resonance integral (I_{γ}).

	σ_{el} (b)	σ_{γ} (b)	I_{γ} (b)
^{90}Zr			
JENDL-4.0	5.25	0.0107	0.165
Present	5.25	0.0109	0.165
Mughabghab	5.3±0.3		0.17±0.02
^{91}Zr			
JENDL-4.0	10.9	1.26	5.73
Present	10.9	1.26	5.73
Mughabghab	10.7±0.6	0.83±0.08	5.76±0.40
^{92}Zr			
JENDL-4.0	7.11	0.229	0.652
Present	7.21	0.237	0.587
Mughabghab	7.02±0.39	0.260±0.080	0.64
^{93}Zr			
JENDL-4.0	5.65	2.24	18.2
Present	5.82	0.691	17.6
Mughabghab		< 4	17.5
^{94}Zr			
JENDL-4.0	6.13	0.0507	0.287
Present	8.66	0.0490	0.283
Mughabghab	8.59±0.41	0.0494±0.0017	0.280±0.010
^{96}Zr			
JENDL-4.0	6.13	0.0203	4.23
Present	6.60	0.0222	5.29
Mughabghab	6.6±0.4	0.0229±0.0010	5.28±0.11

References

[1] K. Shibata *et al.*: J. Nucl. Sci. Technol., **48**, 1 (2011).

[2] G. Tagliente *et al.*: Phys. Rev. C, **77**, 035802 (2008).

[3] G. Tagliente *et al.*: Phys. Rev. C, **78**, 045804 (2008).

[4] G. Tagliente *et al.*: Phys. Rev. C, **81**, 055801 (2010).

[5] G. Tagliente *et al.*: Phys. Rev. C, **87**, 014622 (2013).

[6] G. Tagliente *et al.*: Phys. Rev. C, **84**, 015801 (2011).

[7] G. Tagliente *et al.*: Phys. Rev. C, **84**, 055802 (2011).

[8] A. R. de L. Musgrove, J. A. Harvey and W. M. Good: Aust. J. Phys., **30**, 379 (1977).

[9] J. W. Boldeman *et al.*: Nucl. Phys., **A246**, 1 (1975).

[10] B. J. Allen, J. W. Boldeman and R. L. Macklin: Nucl. Sci. Eng., **82**, 230 (1982).

[11] S. F. Mughabghab: *Atlas of Neutron Resonances*, Elsevier, Amsterdam, 2006.

[12] S. Nakamura *et al.*: J. Nucl. Sci. Technol., **44**, 21 (2007).

[13] J. W. Boldeman *et al.*: Nucl. Phys., **A269**, 31 (1976).

[14] R. L. Macklin: Astrophys. Space Sci., **115**, 71 (1985).

[15] R. L. Macklin, J. A. Harvey and N. W. Hill: Nucl. Sci. Eng., **92**, 525 (1986).

[16] L. M. Bollinger and G. E. Thomas: Phys. Rev., **171**, 1293 (1968).

[17] S. F. Mughabghab, M. Divadeenam and N. E. Holden: *Neutron Cross Sections*, Vol.1, Academic Press, New York, 1981.

[18] J. Hori *et al.*: “Measurements of Neutron Capture Cross Sections at J-PARC/MLF/ANNRI (2)”, JAEA-Conf 2011-002, p. 29 (2011).

[19] G. Leinweber *et al.*: Nucl. Sci. Eng., **134**, 50 (2000).

[20] X. Huang, *et al.*: Atom. Energy. Sci. Technol., **34**, 456 (2000) (EXFOR 31638005).

[21] S. Nakamura *et al.*: “Thermal Neutron Capture Cross Sections and Resonance Integrals of ^{80}Se, ^{94,96}Zr and ^{124}Sn”, INDC(JPN)-190/U, 26 (2003) (EXFOR 22834006).

[22] S. A. Jonah and U. Sadiq: “The Use of Miniature Neutron Source Reactor Facility for the Determination of Neutron-induced Cross Section Data”, INDC(NDS)-0574, p. 67 (2010).

[23] P. M. Prajapati *et al.*: Nucl. Sci. Eng., **171**, 78 (2012).

[24] F. F. Arbocco *et al.*: J. Radioanal. Nucl. Chem., **296**, 931 (2013).

[25] K. S. Krane: Appl. Radiat. Isotopes, **94**, 60 (2014).

[26] C. Coceva, P. Giacobbe and M. Magnani: “Resonance Parameters of ^{96}Zr below 40 keV”, Proc. Int. Conf. on Nuclear Cross Sections for Technology, October 22-26, 1979, Knoxville, US, p.319 (1980).

[27] A. R. De L. Musgrove, W. M. Good and J. A. Harvey: “Neutron Resonance Parameters of ^{96}Zr below 100 keV”, AAEC/E415 (1977).

[28] A. Brusegan *et al.*: “Failure of Valence-neutron Capture in ^{96}Zr”, Proc. 4th Int. Symp. on Neutron-Capture Gamma-Ray Spectroscopy and Related Topics, September 7-11, 1981, Grenoble, French, p. 406 (1982).

[29] M. M. Salah *et al.*: “Accurate Determination of the Parameters of the 292.4-eV Resonance of ^{91}Zr and the 301.1-eV Resonance of ^{96}Zr”, Proc. Int. Conf. on Nuclear Data for Basic and Applied Science, May 13-17, 1985, Santa Fe, US, p. 593 (1986).

[30] F. F. Arbocco *et al.*: J. Radioanal. Nucl. Chem., **302**, 655 (2014).

21 Evaluation of Nuclear Structure Data with Probable Spin Values for ^{124}Cd and ^{124}In in 124 Mass Chain

W.T. Leon S. Fernando, J. Katakura, K. Takahashi, T. Sasaki, T. Kikuchi and N. Harada
Nagaoka University of Technology, Nagaoka, Japan 940-2188, s155072@stn.nagaokaut.ac.jp

This study focused on the evaluation work reviewing and updating nuclear structure data of the two nuclides namely $^{124}_{48}Cd$ and $^{124}_{49}In$ belonging to the mass chain of A=124. Recent studies on these two nuclides surpass the 2008 evaluated nuclear structure. Energy levels were identified in the recent studies through the decay and reaction data were used to prepare the adopted levels for the two nuclides with some of the previous evaluated reaction and decay data.

Spin suggestions done by authors in their studies were evaluated through the multipolarity of gamma rays, systematic, LOGFT values and rotational band structure before confirming the possible spin values for the energy levels. This evaluation work assigns new spin values for the some of the energy levels which were evaluated in 2008 study. Q values of the alpha decay, beta decay and neutron and proton separation energies were also updated through recent studies.

Decay schemes for the both nuclides were developed using available decay data and reaction data using codes available in the Brookhaven National Laboratory's website were used to fit least square values for energy levels and gamma rays. Consistency was cross checked.

1. Introduction

In-depth assessments and evaluation of decay schemes is important in field of nuclear technology where those evaluated decay data will be used by different stake holders such as nuclear physicist's in determining the current knowledge of particular decay parameters and also determining the need of further studies. Medical physics will look into the some of the nuclear parameters in treating patients and also medical diagnosis through the equipment's such as X-ray. Commissioning and decommissioning of nuclear power plant technology that also need to go through the complex calculation for the operations in nuclear reactors need the proper evaluated accurate data sets [1].

Isotopes $^{124}_{48}Cd$ and $^{124}_{49}In$ belongs to the mass chain A=124 and both are close to Z=50 shell structure and recent studies regarding these two nuclides marks an evaluation compared to the previous evaluated data [2]. These data are maintained by the libraries such as Evaluated Nuclear Structure Data File (ENSDF) by National Nuclear Data Center (NNDC) in Brookhaven National Laboratory (BNL) in USA.

In the present work, an evaluation of the energy levels and spin values of the energy levels of each isotope was performed taking into account the new data available in the recent studies. Atomic Mass Evaluation AME2012 [3] is a recommended by evaluators for the ENSDF evaluation and it provides valuable information such as Q value of alpha decay, neutron, proton separation energy and etc. for all the possible nuclides on the nuclear chart and some of these information need to be included in the present evaluation work as it updates the previous information of some of the parameters in evaluating nuclides.

Previous evaluation work carried in 2008 for the A=124 needs to be updated as the many experimental data such as beta decay and some reaction data have provided new information of the nuclear structure of the nuclides ^{124}Cd and ^{124}In. This evaluation work focus on used the new information for update the nuclear structure of the ^{124}Cd and ^{124}In.

All the identified decay data of the nuclides were considered for evaluation and least square fit was done for those data sets through the GTOL code in order to derive level energies. Adopted data set for the ^{124}Cd and ^{124}In nuclides was prepared using decay and reaction data including the spin values for energy levels. Moreover, in order to preserve the consistency between the reaction, decay and adopted data sets, Pandora code were used to make cross check of mentioned data sets. Finally, ENSDAT code was used to run the adopted data set. All these codes were available in the Brookhaven National Laboratory's website [4].

According to the recently published Atomic Mass Evaluation AME2012, there will be changes in the Q values of the alpha (Q(α)), beta (Q(β-)) transitions of the two nuclides with the neutron (S(n)) and proton (S(p)) separation energies. Table 1 shows the 2008 evaluation used and recent values of the Q(α), Q(β-), S(n) and s(p) for the ^{124}Cd and ^{124}In.

Table 1: Adopted values for the Q(α), Q(β-), S(n) and S(p) for the current evaluation and 2008 evaluation (*uncertainties are given in parentheses next to the values)

		Q(α) (keV)		Q(β-) (keV)		S(n) (keV)		S(p) (keV)	
^{124}Cd	Current evaluation	-8846	(4)	4170	(30)	7359	(4)	14440	(30)
	2008 evaluation	-8990	(140)	4170	(40)	7470	(70)	14050	(210)
^{124}In	2012AME	-7640	(30)	7360	(30)	5510	(40)	10750	(30)
	2008	-7650	(90)	7360	(50)	5520	(50)	10850	(60)

AME2012 published the new energy values for neutron and proton separation from the nuclides ^{124}Cd and ^{124}In with more accuracy as the uncertainty is less comparing with the 2008 A=124 evaluation data (Table 1). Q values for the beta (Q(β-)) decay do not show the changes but the uncertainties are reduced. These values were adopted to reaction and decay data for the evaluation.

Recommended half-lives of the ^{124}Cd and ^{124}In nuclides in the 2008 evaluation was adopted for the new study as there is no study available for the half-live determination or similar. The recent studies in reaction and decay models also adopted the 2008 evaluated half-live in their studies.

2. Energy levels

In this evaluation all the recent experimental reaction and decay data were used with the previously identified experimental and reaction data. For the ^{124}Cd isotope the energy levels were identified and constructed through the identified β- decay data where recent studies show two isomers with half-lives of 191 ms and 144 ms for the low spin and high spin of ^{124}Ag [5]. Coulomb excitation [6], Alpha induced fission (^{238}U (α, Fγ)) [7] and Proton induced fission (^{238}U (p, Fγ)) [8] reaction also provide extra energy levels to the identified β- decay data. Recent studies identified new energy structure for the ^{124}In through the reaction (^{9}Be (^{238}U, Fγ)) [9].

2.1. Beta decay

The region of mass chain A = 124, trends to beta decaying and nuclei such as ^{124}Cd and ^{124}In undergoes beta decay's to become stable. So the recent studies show that beta decay of ^{124}Ag and ^{124}Cd to ^{124}Cd and ^{124}In respectively follow up with gamma transitions providing the information of the energy levels of the respective isotopes.

Isomeric of states of the odd-odd isotopes are built from the $\pi(g_{9/2})$ proton state and neutron states namely $v(h_{11/2})$ and $v(d_{3/2})$of the ^{124}Ag. This configuration shows two isomers with the spin values of (2-) for low spin state and (8-) for high spin with half-lives of 191 ms and 144 ms respectively [5]. Authors of the study suggest these spin values considering the beta feeding to the ^{124}Cd level with certain spin values. These two isomers decay to ^{124}Cd and follow with gamma transitions. Fig. 1 and 2 show respectively low spin and high spin beta decay of ^{124}Ag with following gamma's. However, nuclear configuration and similar structure to ^{124}In, was consider for this evaluation work to suggest different spin values for the low spin and high spin isomers respectively while referring the evaluation study of The NUBASE2012 evaluation of nuclear properties [10].

Through the careful consideration of this spin values with the possible nuclear configuration and similarity of the nuclear structures of ^{124}Ag and ^{124}In, the low spin isomer most probably have $\pi(g_{9/2}) \otimes \upsilon(d_{3/2})$ configuration which suggest possible (3,4,5,6)+ spin values and for high spin isomer $\pi(g_{9/2}) \otimes \upsilon(h_{11/2})$ configuration and similar nuclide structures of ^{124}In suggest spin of (7,8,9)-. With these possible spin values and similarity to ^{124}In structure, evaluation suggests the two isomers of ^{124}Ag should have (3+) and (9-)

for the low spin and high spin respectively as their spin configuration and LOGFT rules may provide better concluded evidence for these spin values in future studies.

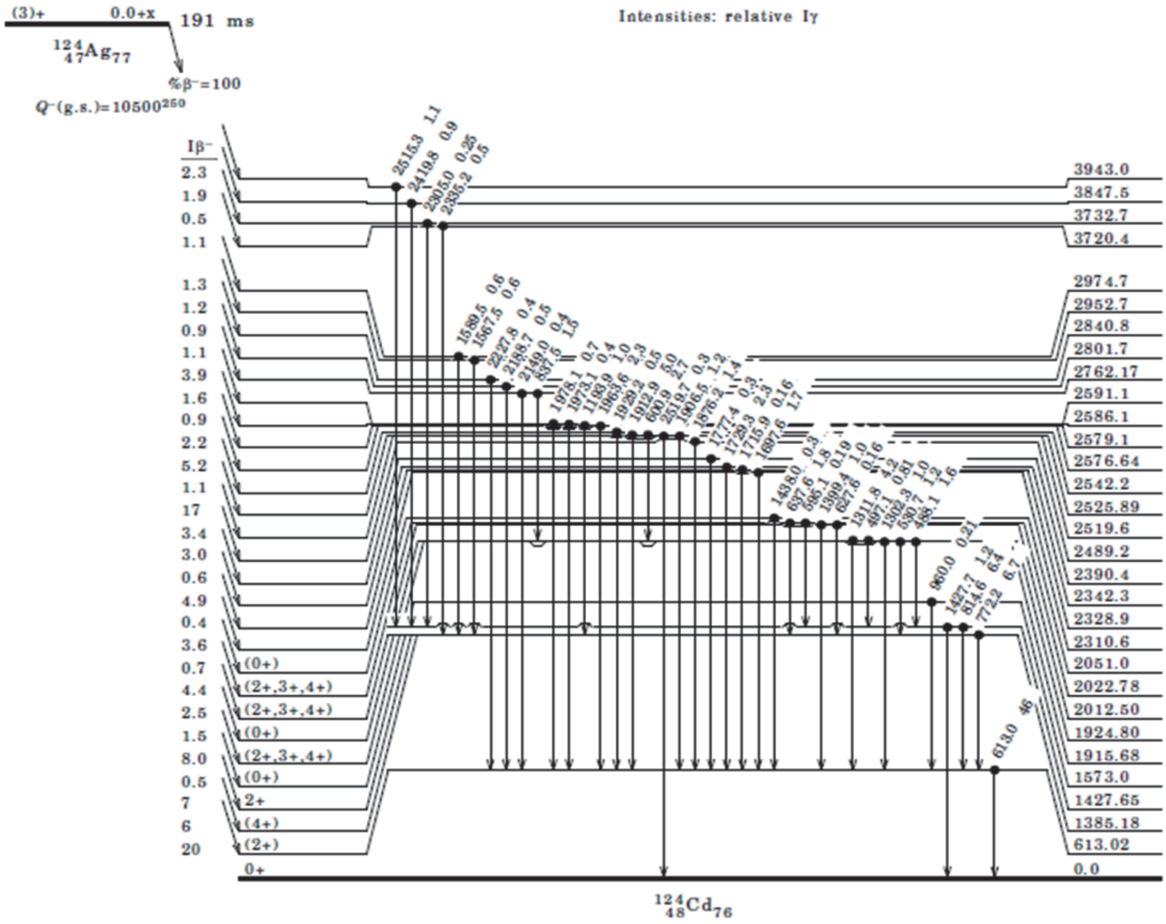

Figure 1: Decay Scheme for the ^{124}Cd from the beta decaying of low spin isomer of ^{124}Ag

3. Spin assignment

Spin assignment for the energy levels is important as it determines the properties of the gamma transitions and the type of decay from one nuclide to another. This evaluation used the available experimental data of the respective studies and their assignment as the basis of the spin assignment. However, these spin assignments were cross checked with the systematics, rotational band structure, measured multipolarity of gamma rays, LOGFT values and so on before preparing the adopted level data with assign the best possible spin values for the ^{124}Cd and ^{124}In.

3.1. Rotational band structure

When the alpha, proton or any heavy ion beam induced to the target, fission fragments of those reaction show the exotic state with rotational model and gamma transitions can be observed to the energy levels with certain spin values as define by,

$$E_j = \frac{\hbar^2}{2\mathcal{J}} J(J+1)$$

where, E_j is the energy of the jth spin value, $\hbar$ is the deduced plank constant and $\mathcal{J}$ is the moment of inertia.

Recent studies [8] suggest continuation of band structure of ^{124}Cd through the yrast level determination from the shell model calculation and experimental results. This study also suggests energy levels of 4496.3 keV, 4819.9 keV and 5039.0 keV should have spin values of (14+,15-), (16+) and (18+) respectively. However, evaluation work does not identify the continuation in these high energy levels as band structure, as the gamma transition from 4496.6 keV is questionable to carry spin difference of 2 between 4496.6 keV and 3661.7 keV energy levels. Gamma transitions data do not provide B(E2) strength or any information to consider this spin value for the energy level and study assign this information based on their simulation result comparing experimental result. Study on the Spectroscopy of neutron-rich Pd and Cd isotopes [7] shows band structure and the 2008 evaluation also identified this band structure determining the spin values of energy levels. Hence this study will adopt the 2008 evaluated band structure in the respective energy levels.

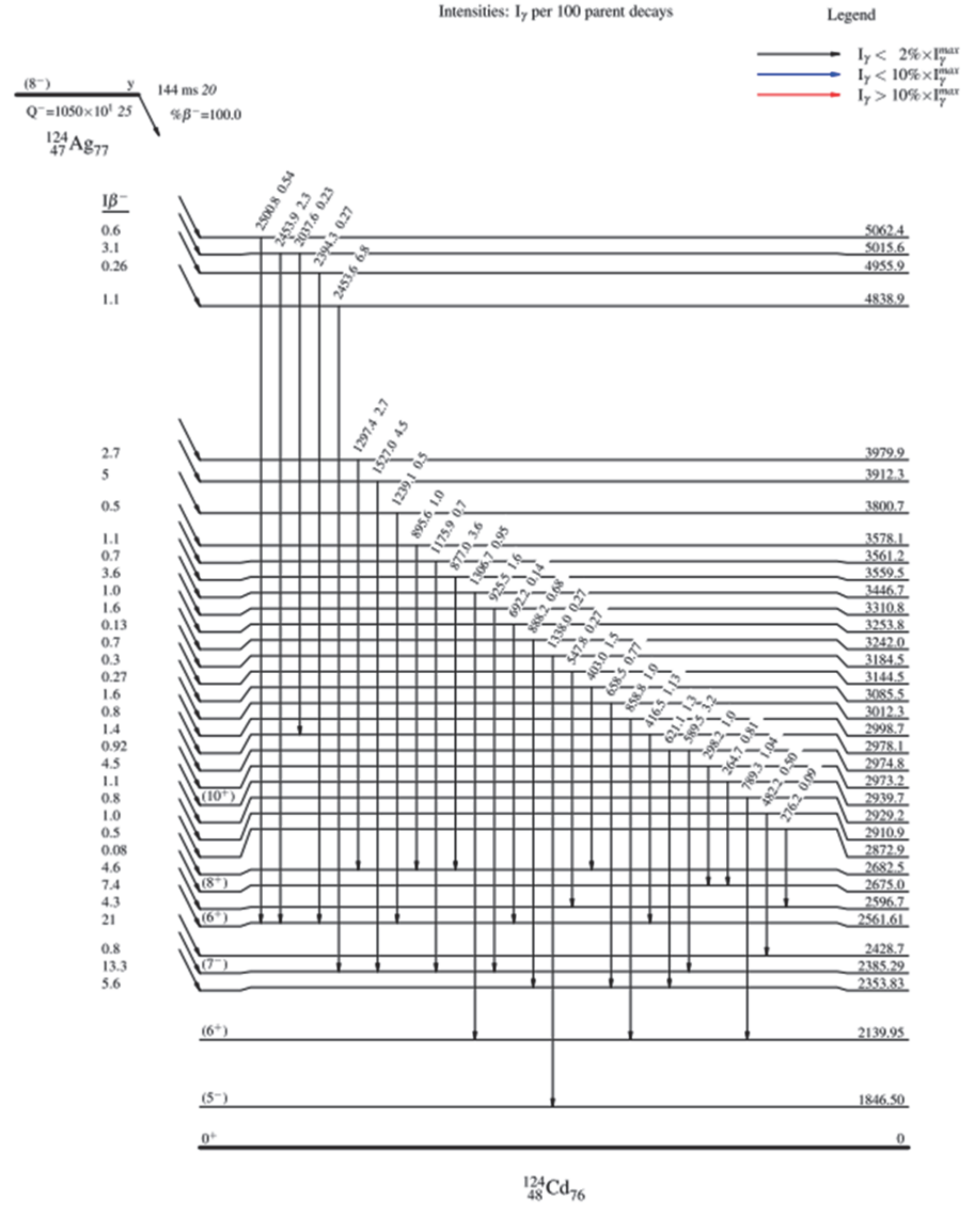

Figure 2: Decay Scheme for the ^{124}Cd from the beta decaying of high spin isomer of ^{124}Ag

3.2. Multipolarity of the gamma rays

The conservation of angular momentum (I) has provided an enormous amount of information on the structure of nuclei and plays a controlling role in the gamma ray decay process and it defines as a transition to a lower energy state from a higher energy state through emission of single photon. Both the initial (I_i) and final (I_f) states of the nuclei will have a definite angular momentum and parity and so the photon must connect the two states and conserve both parity and angular momentum with an exact integer number of angular momentum units ($\hbar$). The conservation of angular momentum and parity are different and conservation of each has a different effect on the possible properties of the emitted photon.

A photon must carry at least one unit of angular momentum so that $l = \Delta I = 0$ is forbidden for single photon emission and the angular momentum carried by the photon can take any value in the range;

$$\left|\left(I_i - I_f\right)\right| \leq l \leq \left(I_i + I_f\right)$$

The multipolarity of the photon is a quantification of the amount of angular momentum carried by the photon and the photon with l units of angular momentum is called a 2^l–pole. A shift in the distribution of charge will give rise to an electric field but a shift in the distribution of current in the nucleus will give a rise to a magnetic field. The parity of the photon depends on both the angular momentum and the type (electric or magnetic) of transition indicated in Table 2.

Table 2: Gamma ray selection rules and multipolarities

Radiation Type	Name	$l = \Delta I$	$\Delta\pi$
E1	electric dipole	1	Yes
M1	magnetic dipole	1	No
E2	electric quadrupole	2	No
M2	magnetic quadrupole	2	Yes
E3	electric octupole	3	Yes
M3	magnetic octupole	3	No
E4	electric hexadecapole	4	No
M4	magnetic hexadecapole	4	Yes

Possible spin values were assigned to energy levels of 2561.46 keV and 2747.9 keV in the ^{124}Cd considering the multipolarity of the gamma rays where dipole and quadrupole transitions were considering strong comparing to the octupole and hexadecapole. Therefore, 2747.9 keV energy level was evaluated to possible spin values of (6+,7,8+) considering the gamma transitions to follows to energy levels with spin (6+), (7-) and (8+), while 2561.46 keV energy level evaluated to possible spin values of (5-,6,7-) follows gamma transitions to energy levels contains spin values of (5-), (6+) and (7-).

For the ^{124}In energy levels of 36.53 keV possible spin values was assigned as (2+,3+,4+) considering the M1 transition to Ground State (G.S) of spin (3+). Similarly, E1 gamma transition to G.S. from 179.88 keV level assigns the spin values of (2-,3-,4-) while, 242.68 keV energy level is assigned with possible spin values of (2+,3+,4+) considering the E1 gamma transition to 179.88 keV energy level [9] [11].

3.3. LOGFT values

Beta decay constant is relating to the constant nuclear matrix element $|M|$ and can be integrated through the Fermi integral *f (Z$_D$, Q)*, which can be written with strength parameter g (other symbols have their usual meanings),

$$\lambda = \frac{g^2|M|^2 m_e^5 c^4}{2\pi^3\hbar^7} f(Z_D, Q)$$

or in terms of the half-life of the parent, $t_{1/2}$,

$$f(Z_D, Q) * t_{1/2} = ln2 \, \frac{2\pi^3\hbar^7}{g^2|M|^2 m_e^5 c^4}$$

The left hand side of this equation is called the comparative half-life or "ft value" because this value can be readily measured in experiments and should only depend on the nuclear matrix element and the beta decay strength constant. Half-lives of β decay span many orders of magnitude so the ft values will span a similarly large range and it is convenient to use the common logarithm of the ft value (with $t_{1/2}$ in seconds) to characterize observed β decays.

These LOGFT values fall into groups which can correlate with spin and parity change in the decay (Table 3) and then can be used to assign spins and parities in nuclei.

Table 3: Classification of β-decay transitions

Transition Type	Log ft	*l*	Δπ	Fermi ΔJ	GT ΔJ
Super-allowed	2.9-3.7	0	No	0	0
Allowed	4.4 - 6.0	0	No	0	0,1
First forbidden	6.0 - 10.0	1	Yes	0,1	0,1,2
Second forbidden	10.0 - 13.0	2	No	1,2	1,2,3
Third forbidden	> 15	3	Yes	2,3	2,3,4

LOGFT value (<6) measure in the [11] beta transition to known 2+ spin level of the ^{124}Sn, suggest the ΔJ=0,1 with no parity change according to GT model. So the 2008 evaluation identifies ^{124}In ground state should have spin value of (1)+, but this evaluation work identifies (3)+ as the ground state spin value considering nuclear configuration where possible spin values of (3,4,5,6)+ and confirmation through the LOGFT value.

4. Results and Discussion

Using the evaluated decay and reaction data with nuclear structure concepts, nuclear structure for ^{124}Cd shown in the Fig. 3 was developed with the assigned spin values. Energies of the gamma rays and their relative intensities were also included for the evaluation of the nuclear structure of the ^{124}Cd.

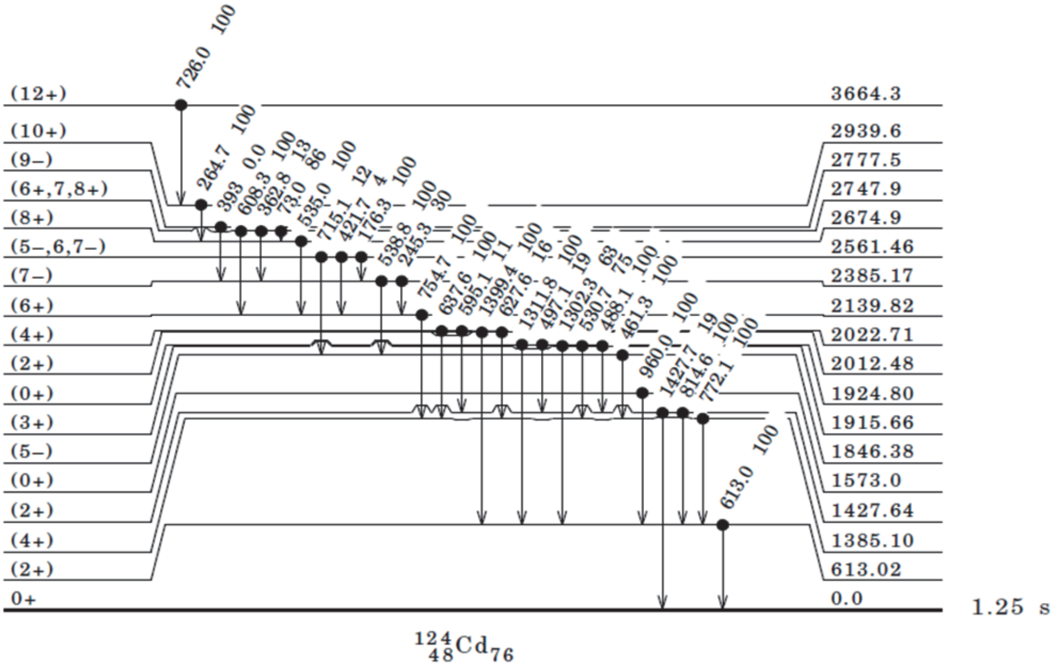

Figure 3: Evaluated decay Scheme of ^{124}Cd with assigned spin values

^{124}In nuclear structure is developed similar to the ^{124}Cd structure and shown in the Fig. 4. Multipolarity assigned from the study [9] is questionable as the authors of the study does not provide the clear back ground information as they suggest M1 for ΔJ=1 and E2 for ΔJ=2. So this evaluation assigns multipolarity values as D for M1 and Q for E2 gamma transitions.

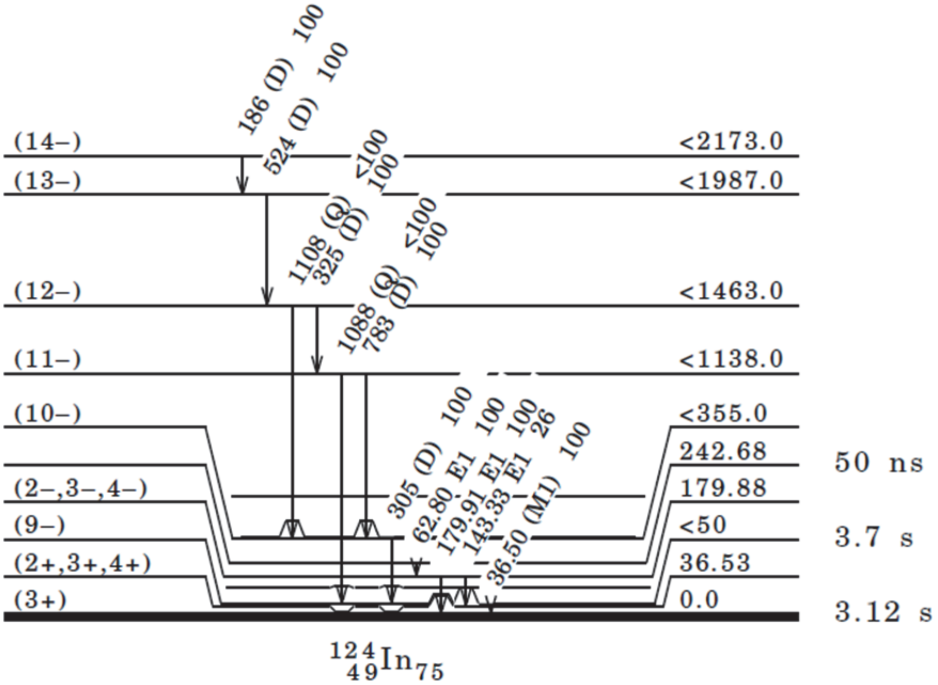

Figure 4: Evaluated decay Scheme of ^{124}In with assigned spin values

5. Conclusion

This study identifies new energy levels and spin values compared to the 2008 evaluation. Mainly ground state spin level of the ^{124}In was changed to (3)+ from (1)+ considering the nuclear configurations. Spin values suggested by the studies were considered for evaluation and some of the spin values were omitted from the assignment as their spin assignment is questionable. ^{124}In shows a major change in the spin values for the energy levels compared to the 2008 evaluation. For the ^{124}Cd nuclear structure, some of the spin assignments were similar to the 2008 evaluation, however, new energy levels were assigned with possible spin values and some of the previously assigned spin values were changed according to evaluation of the nuclide.

References

[1] A. Nichols, "Recommended decay data and evaluated databases-international perspectives," *Journal of Nuclear Science and Technology,* vol. 52, no. 1, pp. 17-40, 2015.

[2] J. Katakura and Z.D. Wu, "Nuclear Data Sheets for A =124," *Nuclear Data Sheets,* vol. 109, no. 7, pp. 1655-1877, 2008

[3] M.Wang, G. Audi, A.H. Wapstra, F.G. Kondev, M. MacCormick, X. Xu and B. Pfeiffer, "The AME2012 atomic mass evaluation*(II). Tables, graphs and references," *Chinese Physics C,* vol. 36, no. 12, pp. 1603-2014, 2012.

[4] "National Nuclear Data Center," Brookhaven National Laboratory, [Online]. Available: http://www.nndc.bnl.gov/nndcscr/ensdf_pgm/. [Accessed 2015]

[5] J. C. Batchelder, N. T. Brewer, C. J. Gross, R. Grzywacz, J. H. Hamilton, M. Karny, A. Fijalkowska, S. H. Liu, "Structure of low-lying states in 124,126Cd populated by," *Physical Review C,* vol. 89, no. 5, 2014.

[6] S. Ilieva *et al.*, "Coloumb excitation of neutron-rich Cd isotopes," *Physical Review C,* vol. 89, no. 1, 2014.

[7] M.A.Stoyer, W.B. Walters, C.Y. Wu, D. Cline, H. Hua, A.B.Hayes, R. Teng, R.M. Clark, P. Fallon, A. Goergen, A.O. Macchiavelli, K. Vetter, P. Mantica and B. Tomlin, "Spectroscopy of neutron-rich Pd and Cd isotopes near A=120," *Nuclear Physics A,* vol. 787, no. c, pp. 455-462, 2007.

[8] A. Van craeyenest, G.S. Simpson, G. Gey, P.T. Greenlees, F. Droueti, G. Kessedjian, T. Malkiewicz, M. Ramdhane, C. Sage, G. Thiamova, T. Grahn, K. Hauschild, A. Herzan, U. Jakobsson, P. Jones, R. Julin, S. Juutinen, S. Ketelhut, A. Lopez-Martens, et al., "Prompt gamma ray spectroscopy of the neutron-rich 124Cd," in *European Physics Journal Web of Conferences 62, 01004* , 2013.

[9] M. Rejmunda, A. Navin, S. Biswas, A. Lemasson, M. Caamano, E. Clementa, O. Delaune, F. Farget, G. deFrance, B. Jacquota and P. Van Isacker, "Electromagnetic properties of neutron-rich nuclei adjacent to the Z=50 shell closure," *Physics Letters B,* vol. 753, pp. 86-90, 2016.

[10] G. Audi, F.G. Kondev, M. Wang, B. Pfeiffer, X. Sun, J. Blachot and M. MacCormick, "The NUBASE2012 evaluation of nuclear properties*," *Chinese Physics C,* vol. 36, no. 12, pp. 1157-1286, 2012.

[11] B. Fogelberg, T. Nagarajan and B. GrapenGiesser, "Levels and Transition probabilities in 124In as observed in the decay of 124Cd," *Nuclear Physics A,* vol. 230, pp. 214-220, 1974.

22 FENDL-3.1b Test

Chikara KONNO[1], Saerom KWON[2], Masayuki OHTA[2] and Satoshi SATO[2]

[1]*Japan Atomic Energy Agency, Tokai-mura, Naka-gun, Ibaraki-ken 319-1195, Japan*
[2]*National Institutes for Quantum and Radiological Science and Technology, Rokkasho-mura, Kamikita-gun, Aomori-ken 039-3212, Japan*
e-mail : konno.chikara@jaea.go.jp

The revised version of FENDL-3, FENDL-3.1b, was released in October, 2015. Thus we have tested FENDL-3.1b neutron sub-library for the problems we reported to IAEA before. Most of the MATXS files above 20 MeV had no scattering matrix data of non-elastic scattering, but this problem was fixed by re-processing FENDL-3 with NJOY2012.50. As for the problem on KERMA factors and DPA data, IAEA revised the wrong Q value of the capture reaction in ^{15}N and re-calculated KERMA factors and DPA data with NJOY2012.50. It was confirmed that most of the KERMA factors and DPA data were revised correctly except for huge gas production cross-section data. However a new problem on KERMA and DPA data of $^{39\text{-}41}$K was found out. It was considered that this problem was due to a bug of NJOY. Additionally we investigated a trouble in NJOY processing of ^{116}Sn and ^{117}Sn at IAEA and specified that one of the NJOY patches caused this trouble.

1. Introduction

IAEA released the Fusion Evaluated Nuclear Data Library version 3.0 (FENDL-3.0) [1] in December, 2012. We found some problems on FENDL-3.0 neutron sub-library [2, 3]; 1) the ^{16}O data above 20 MeV caused large overestimation in the analysis of the concrete shielding experiment at JAEA/TIARA, 2) most of the MATXS files above 20 MeV had no scattering matrix data of non-elastic scattering, 3) many KERMA factors and DPA cross-section data were not correct because FENDL-3.0 was processed with the old version NJOY99.364 [4]. We reported these problems to IAEA and IAEA revised FENDL-3.0 only for the NJOY processing issues (mentioned above, 2) and 3)) three times (FENDL-3.1, FENDL-3.1a, FENDL-3.1b [5]), because IAEA had made some simple mistakes in the revisions. It should be noted that the ^{16}O data above 20 MeV were not revised because it was not an NJOY processing problem but an original data problem. Thus we have tested the latest version FENDL-3.1b neutron sub-library, which was released in October, 2015, in order to confirm whether the problems related to NJOY processing have been solved or not.

2. Problem on MATXS files above 20 MeV

The MATXS files [5] of FENDL-3.1b were re-produced by using the latest NJOY2012.50 [6] code with IAEA patch. We carried out the same simple calculation test as before [3]. The model of this calculation test was a natural iron sphere of 1 m in radius with an isotropic neutron source of 50 MeV (49 - 50 MeV, which is the sixth group of the MATXS files in FENDL-3.1b) at the center. Neutron spectra inside the sphere were calculated by using the Sn code ANISN [7] with a multigroup library, which was generated from the MATXS files of FENDL-3.1b with the TRANSX-2.15 code [8], and the Monte Carlo code MCNP5-1.40 [9] with the ACE files [5] of FENDL-3.1b. Figure 1 shows the calculated neutron spectra at the distance of 40 cm from the center of the iron sphere. The neutron spectrum with ANISN and FENDL-3.1b agrees well with that with MCNP and FENDL-3.1b, though that with ANISN and FENDL-3.0 is very different from that with ANISN and FENDL-3.1b. It is confirmed that the problem on the MATXS files above 20 MeV in FENDL-3.1b is fixed.

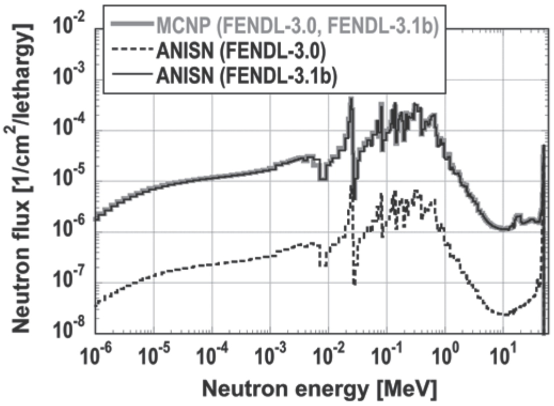

Fig. 1 Calculated neutron spectra at 40 cm from center of iron sphere

3. Problem on KERMA and DPA data

IAEA used the latest NJOY2012.50 code with IAEA patch, by which IAEA could

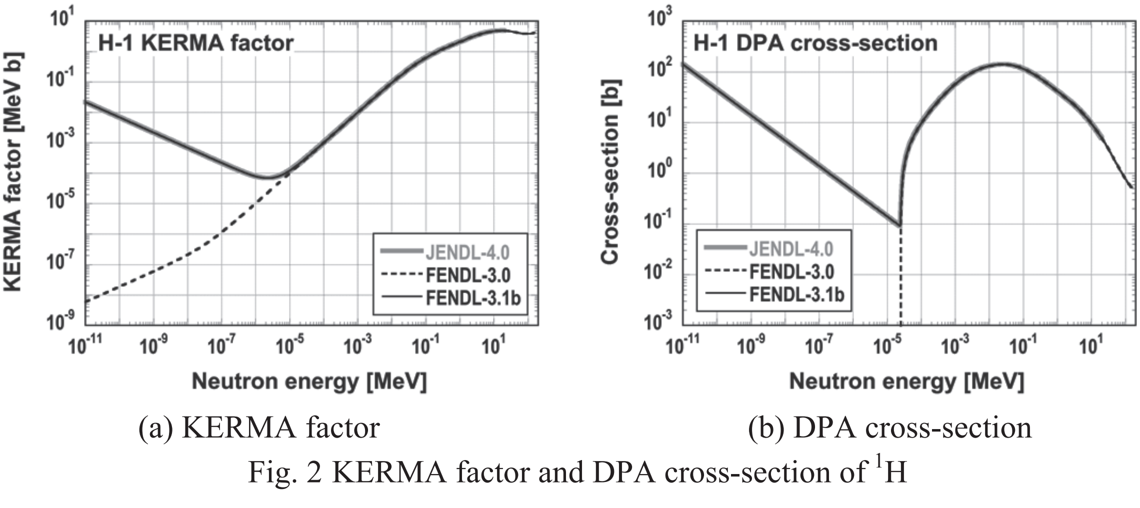

(a) KERMA factor (b) DPA cross-section

Fig. 2 KERMA factor and DPA cross-section of ^{1}H

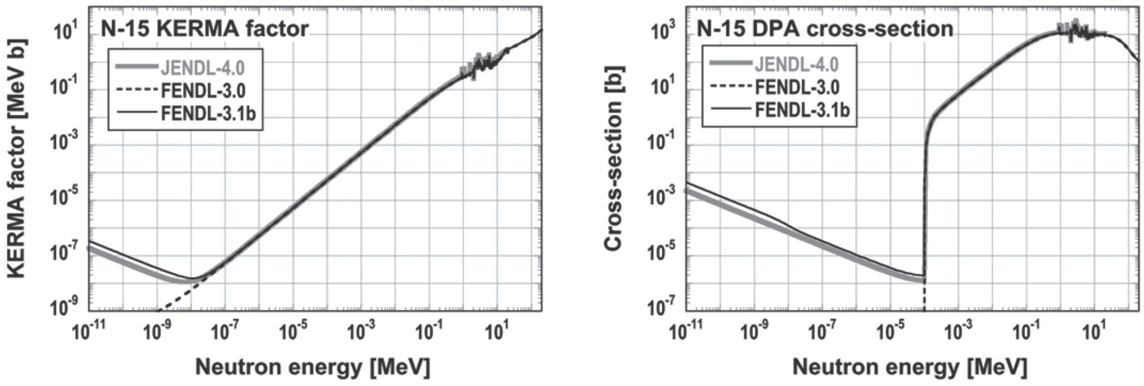

(a) KERMA factor (b) DPA cross-section

Fig. 3 KERMA factor and DPA cross-section of ^{15}N

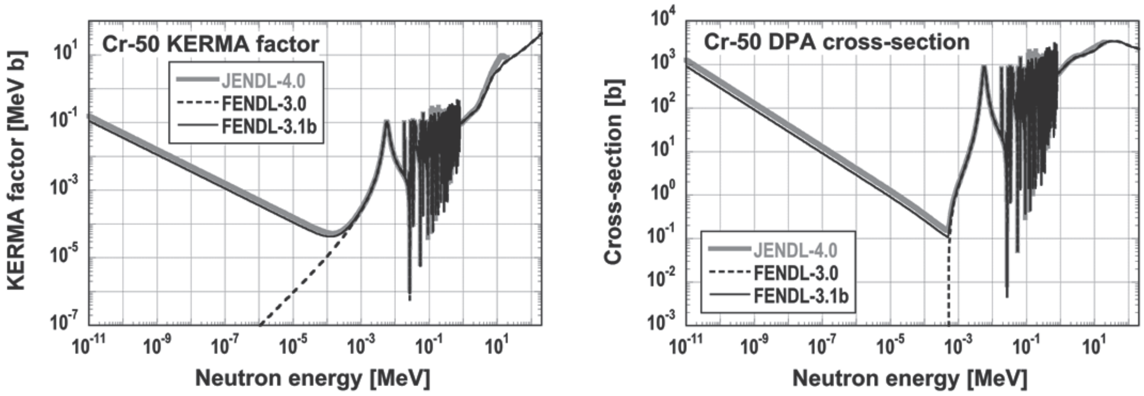

(a) KERMA factor (b) DPA cross-section

Fig. 4 KERMA factor and DPA cross-section of ^{50}Cr

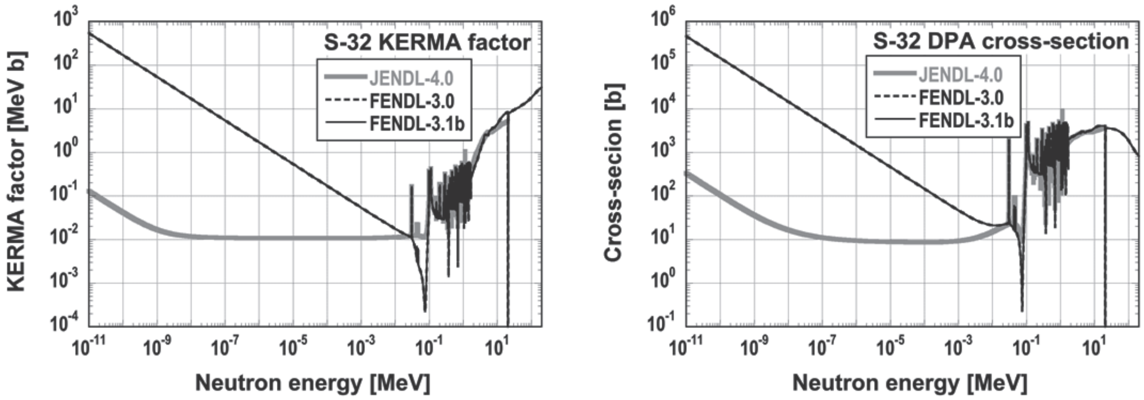

(a) KERMA factor (b) DPA cross-section

Fig. 5 KERMA factor and DPA cross-section of ^{32}S

replace energy-balance KERMAs in ACE files with kinematics-upper-limit KERMAs. IAEA revised the wrong Q value of the capture reaction in ^{15}N. The typical revised KERMA and DPA data are compared with the previous wrong ones and those of JENDL-4.0 [10] as shown in Figs. 2-5. The problems on KERMA and DPA data are fixed except for that due to huge gas production cross-section data shown in Fig. 5.

4. New problem on KERMA and DPA data

IAEA decided to adopt kinematics-upper-limit KERMA factors as KERMA factors in all the ACE and MATXS files of FENDL-3.1b in order to avoid energy-balance problem [11]. Most of the KERMA factors in the official ACE files of FENDL-3.1b seemed to have no problem. However a new problem was found out; the KERMA and DPA data of $^{39-41}$K were very different from those of JENDL-4.0, ENDF/B-VII.1 [12] and JEFF-3.2 [13] below a few keV as shown in Fig. 6. We investigated this problem. Figure 7 indicates that the kinematics KERMA factors in $^{39-41}$K do not include a partial KERMA factor of the gas production reactions. Figure 8 demonstrates that this

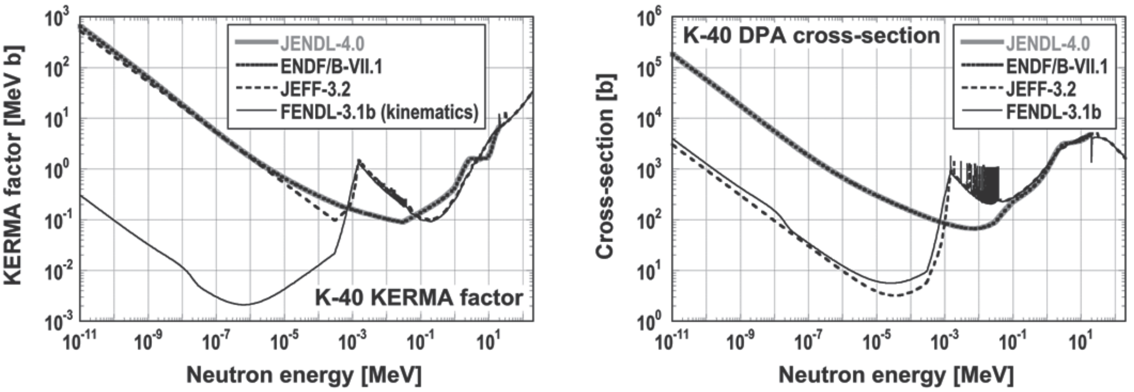

(a) KERMA factor (b) DPA cross-section

Fig. 6 KERMA factor and DPA cross-section of ^{40}K

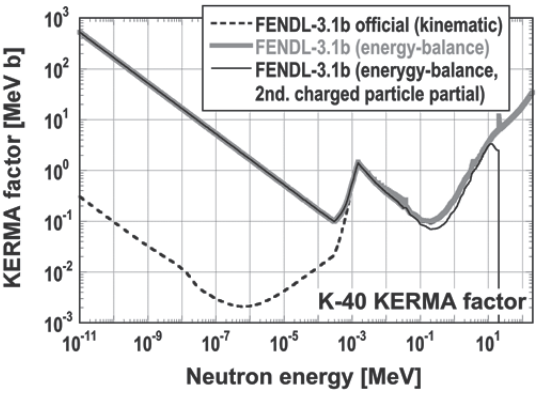

Fig. 7 Various KERMA factors (1) of ^{40}K

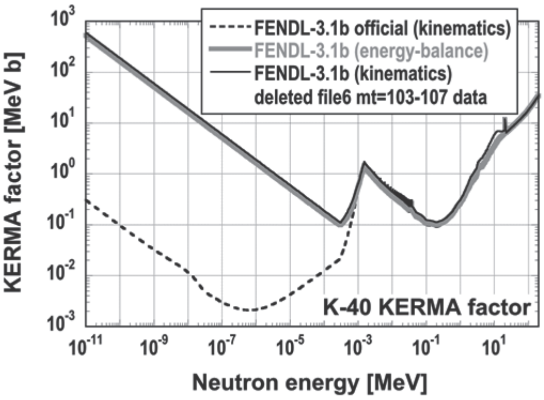

Fig. 8 Various KERMA factors (2) of ^{40}K

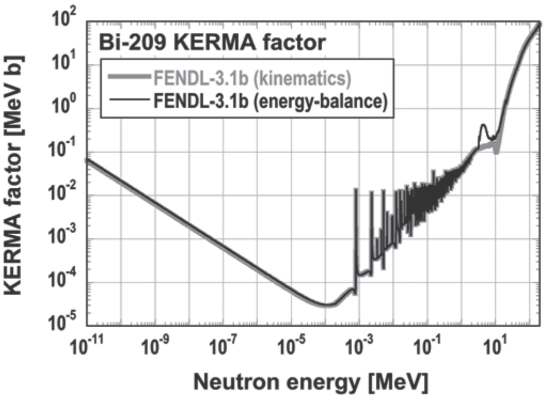

Fig. 9 KERMA factor of ^{209}Bi

problem occurs only in nuclei with mt=103 and mt=107 data in file6 (e.g. $^{39\text{-}41}$K data in FENDL-3.1b) because this problem does not appear if mt=103 and mt=107 data in file6 are deleted. Moreover this problem does not occur in nuclei with mt=600-649 and mt=800-849 in file6 (e.g. ^{209}Bi in FENDL-3.1b) as shown in Fig. 9. Therefore it is considered that NJOY2012.50 cannot process nuclei with mt=103 and mt=107 data in file6 adequately.

5. Additional problem on NJOY processing

IAEA had not been able to produce the ACE files of ^{116}Sn and ^{117}Sn in FENDL-3.1b due to a processing trouble “Segmentation fault” in the NJOY2012.50 code. Thus we investigated this issue with IAEA and Los Alamos National Laboratory (LANL). We processed ^{116}Sn and ^{117}Sn of FENDL-3.1b with NJOY2012.50 by using the gfortran compiler on the Macintosh computer and the ACE files were generated without problem. We asked IAEA about the NJOY2012 processing trouble. IAEA answered that “Segmentation fault” occurred in acefc.f90 of NJOY2012.50 with IAEA patch by using Lahey/Fujitsu FORTAN90 compiler on the Windows computer. “Segmentation fault” often occurs in the case of the array overflow. Thus we compiled NJOY2012.50 with the option “-fbound-check” on Macintosh in order to check the array overflow. Then we found out that the array overflow also occurred in processing ^{116}Sn and ^{117}Sn of FENDL-3.1b on the Macintosh computer, though “Segmentation fault” did not occur. IAEA asked LANL, the NJOY developer, about this issue. LANL pointed out that NJOY recognized the two secondary gammas of 2.64900 and 2.64901 MeV from the (n,nα) reaction of ^{116}Sn and the (n,2nα) reaction of ^{117}Sn as one gamma because secondary gammas were discriminated in acefc.f90 of NJOY2012.50 if

$$\frac{E_{i+1}}{E_i} - 1 > eps,\ \ where\ E_i : i-th\ gamma\ energy,\ \ eps : criteria\ value\ (4.6\times10^{-6})$$

and 2.64901/2.64900-1 = 3.775x10^{-6} < eps. This made an insufficient secondary gamma array in acefc.f90, which caused “Segmentation fault”. LANL had modified the “eps” value from 1.0 x 10^{-10} to 4.6 x 10^{-6} in the patch 20 of NJOY2012, but LANL proposed to omit this patch. ^{116}Sn and ^{117}Sn of FENDL-3.1b should be processed with the “eps” value less than 3.7 x 10^{-6} or without the patch 20. We reported this result to IAEA in December, 2015. IAEA released the ACE files of ^{116}Sn and ^{117}Sn of FENDL-3.1b in July, 2016.

6. Summary

We investigated if the problems in FENDL-3.0 were fixed in FENDL-3.1b. The followings were confirmed.

1) The Q-value bug of ^{15}N in FENDL-3.0 was fixed.
2) The MATXS files in FENDL-3.0 were re-processed correctly.
3) The problematic KERMA and DPA data were revised except for those due to huge gas production cross-section data.

Additionally we pointed out a new problem on the KERMA and DPA data of $^{39\text{-}41}$K in FENDL-3.1b and solved an NJOY processing trouble for ^{116}Sn and ^{117}Sn in FENDL-3.1b.

References

[1] Forrest RA, Capote N, Otsuka N, Kawano T, Koning AJ, Kunieda S, Sublet J-Ch, Watanabe Y. FENDL-3 Library – Summary documentation. INDC(NDS)-0628. Austria: International Atomic Energy Agency; 2012.

[2] Konno C, Ohta M, Asahara H, Ochiai K, Sato S. FENDL-3.0 Benchmark Test with Shielding Experiments at JAEA/TIARA. Proceedings of the 2013 Symposium on Nuclear Data, JAEA-Conf 2014-002, 2015: pp. 160-166.

[3] Konno C, Ohta M, Kwon S, Ochiai K, Sato S. Problems on FENDL-3.0. Proceedings of the 2014 Symposium on Nuclear Data, JAEA-Conf 2015-003, 2016: pp. 131-136.

[4] MacFarlane RE, Muir DW. The NJOY Nuclear Data Processing System, Version 91. LA-12740-M. USA: Los Alamos National Laboratory; 1994.

[5] https://www-nds.iaea.org/fendl/.

[6] MacFarlane RE, Kahler AC. Methods for Processing ENDF/B-VII with NJOY. Nuclear Data Sheets. 2010; 111: 2739–2890.

[7] ORNL RSICC. DOORS3.2a: One, two- and three-dimensional discrete ordinates neutron/photon transport code system. CODE PACKAGE CCC-650. USA: Oak Ridge National Laboratory; 2007.

[8] MacFarlane RE. TRANSX 2: a code for interfacing MATXS cross-section libraries to nuclear transport codes. LA-12312-MS. USA : Los Alamos National Laboratory; 1993.

[9] X-5 Monte Carlo Team. MCNP - A General Monte Carlo N-Particle Transport Code, Version 5. LA-UR-03-1987. USA: Los Alamos National Laboratory; 2005.

[10] Shibata K, Iwamoto O, Nakagawa T, et al. JENDL-4.0: a new library for nuclear science and engineering. J Nucl Sci Technol. 2011; 48: 1–30.

[11] Konno C, Ochiai K, Takakura K, Sato S. Remarks on KERMA Factors in ACE files. Nuclear Data Sheets. 2014; 118: 450–452.

[12] Chadwick MB, Herman M, Oblozinsky P, et al. ENDF/B-VII.1 Nuclear Data for Science and Technology: Cross Sections, Covariances, Fission Product Yields and Decay Data. Nuclear Data Sheets. 2011; 112: 2887–2996.

[13] https://www.oecd-nea.org/dbforms/data/eva/evatapes/jeff_32/

23 ENDF/B-VIIIβ2 benchmark test with shielding experiments at QST/TIARA

Saerom KWON[1*], Chikara KONNO[2], Masayuki OHTA[1], Satoshi SATO[1] and Kentaro OCHIAI[1]
[1]*National Institutes for Quantum and Radiological Science and Technology, Rokkasho-mura, Kamikita-gun, Aomori-ken 039-3212, Japan*
[2]*Japan Atomic Energy Agency, Tokai-mura, Naka-gun, Ibaraki-ken 319-1195, Japan*
[*]e-mail: kwon.saerom@qst.go.jp

Previously we benchmarked the iron and concrete shielding experiments with 40 and 65 MeV neutron sources at QST/TIARA by using ENDF/B-VII.1, FENDL-3.0 and JENDL-4.0/HE. We pointed out that the calculated results with ENDF/B-VII.1 excessively overestimated the measured neutron fluxes more in the thicker test shields in both of the experiments. It was confirmed that the overestimations were due to elastic and non-elastic scattering data of ^{56}Fe and ^{16}O in ENDF/B-VII.1. Several beta versions of ENDF/B-VIII were released in 2016. We analyze the same experiments with ENDF/B-VIIIβ2 (2nd beta version which was released in August, 2016) to investigate whether the ^{56}Fe and ^{16}O data in ENDF/B-VIIIβ2 are improved. In the iron experiment, the excessive overestimation in the calculated result with ENDF/B-VII.1 decreases in that with ENDF/B-VIIIβ2, due to the revision of the elastic and non-elastic scattering cross section data of ^{56}Fe in ENDF/B-VIIIβ2. However, the excessive overestimation in the calculated results with ENDF/B-VII.1 does not change in that with ENDF/B-VIIIβ2 in the concrete experiment because the ^{16}O data above 20 MeV are not revised in ENDF/B-VIIIβ2. The final version of ENDF/B-VIII should be modified based on these results.

1. Introduction

Nuclear data for high energy (i.e. above 20 MeV) neutrons have been used in nuclear analyses for International Fusion Materials Irradiation Facility (IFMIF) [1] and advanced fusion neutron sources (A-FNS: Japan [2], IFMIF/DONES: Europe [3]). FENDL-3.1b (a new extended version of Fusion Evaluated Nuclear Data Library from 20 MeV to greater than 60 MeV) [4] and JENDL-4.0/HE (an extended version of JENDL-4.0 up to 200 MeV) [5] were recently released as the higher energy nuclear data. ENDF/B-VII.1 [6] includes neutron-induced data up to 150 MeV for several nuclei. It is announced that a new version of ENDF/B-VII, ENDF/B-VIII, is going to be released in 2017. Thus several beta versions of ENDF/B-VIII were released in 2016 [7].

We have benchmarked nuclear data libraries above 20 MeV with the iron and concrete shielding experiments with 40 and 65 MeV neutrons at Takasaki Ion Accelerators for Advanced Radiation Application (TIARA) in National Institutes for Quantum and Radiological Science and Technology (QST) [8, 9]. We pointed out the following results so far: (a) Iron experiment: The calculation result with FENDL-3.0 (same as FENDL-3.1b) showed the best agreement with the measured one. That with JENDL-4.0/HE moderately agreed with the experimental data. That with ENDF/B-VII.1 excessive overestimated the measured one, which was confirmed to be due to the smaller non-elastic scattering data of ^{56}Fe in ENDF/B-VII.1. (b) Concrete experiment: The calculated result with JENDL-4.0/HE showed the best agreement with the measured one. Those with FENDL-3.0 (same as FENDL-3.1b) and ENDF/B-VII.1 excessively overestimated the measured one. It was confirmed that this overestimation was due to both the larger elastic and smaller non-elastic scattering data of ^{16}O in FENDL-3.0 and ENDF/B-VII.1.

Here we investigate whether the problems of the ^{56}Fe and ^{16}O data in ENDF/B-VII.1 are revised correctly in ENDF/B-VIIIβ2 through analyses of the iron and concrete shielding experiments with 40 and 65 MeV neutrons at QST/TIARA.

2. Experiment and Analysis

2.1 Iron and concrete shielding experiments at QST/TIARA

More than two decades ago, the iron and concrete shielding experiments at QST/TIARA were performed with quasi-mono energetic 40 and 65 MeV neutrons generated by bombarding 43 and 68 MeV protons to a ^{7}Li target [10, 11]. Figure 1 shows the experimental configuration of TIARA shielding experiment and the collimated neutrons were injected to a test shield (iron or concrete) area of 1.2 m x 1.2 m. The neutron spectra above 10 MeV at the rear part of the test shield on beam axis were measured with a BC501A scintillation detector.

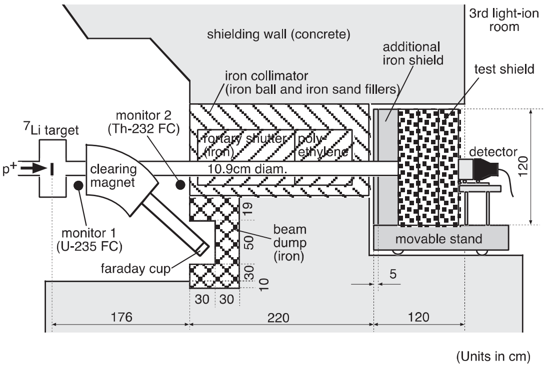

Fig. 1. Experimental configuration of the shielding experiment at QST/TIARA

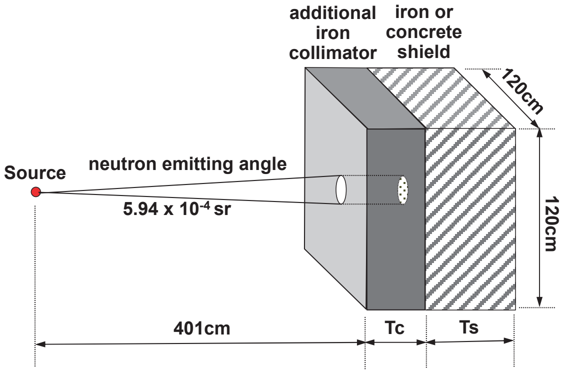

Fig. 2. Calculation model of the shielding experiments

2.2 Analysis method

We analyzed the experiments using the Monte Carlo N-Particle transport code, MCNP5-1.50 [12] with ENDF/B-VII.1, FENDL-3.1b, JENDL-4.0/HE and ENDF/B-VIIIβ2. The source files of FENDL-3.1b are the followings, (a) ^{1}H: ENDF/B-VII.1 (< 20 MeV) + JENDL/HE (> 20 MeV), (b) ^{16}O, $^{28\text{-}30}$Si, ^{54}Fe, ^{57}Fe: ENDF/B-VII.1, (c) ^{27}Al, ^{58}Fe: JEFF-3.1.1, (d) ^{40}Ca: JENDL-4.0 (< 20 MeV) + JENDL/HE-2007 (> 20 MeV) and (e) ^{56}Fe: JEFF-3.1.1 (< 20 MeV) + TENDL-2011(> 20 MeV). The ACE files from JENDL-4.0/HE and ENDF/B-VIIIβ2 were processed with the nuclear data processing code, NJOY2012.50 [13], by ourselves and used in the analysis. The ^{1}H data in FENDL-3.1b was used for the calculations with ENDF/B-VII.1 and ENDF/B-VIIIβ2, because the ^{1}H data in both the libraries have no data above 20 MeV.

In the analysis, we used the measured spectrum data of quasi-mono energetic 40 or 65 MeV neutrons as the source neutron. We modeled only the collimated neutron beam and the test shield with an additional iron collimator as shown in Fig. 2.

3. Results and discussion

3.1 Iron experiment

The experimental and calculated neutron spectra in the iron experiment with 40 MeV neutrons are shown in Fig. 3. In order to compare more precisely, the ratios (Calc./Expt.s) of the calculated continuum (10-35 MeV) and peak (35-45 MeV) neutron fluxes to the experimental ones are shown in Figs. 4 and 5. In the thinner test shield, the experimental and calculated spectra agree well with those with all the libraries. In the thicker test shield, the overestimation problem in the calculation result with ENDF/B-VII.1 is improved in that with ENDF/B-VIIIβ2, which is similar to those with FENDL-3.1b and JENDL-4.0/HE.

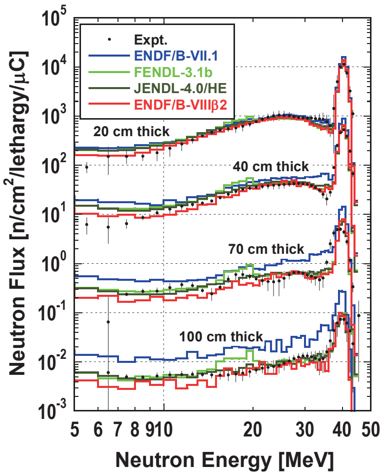

Fig. 3. Neutron spectra in the iron experiment with 40 MeV neutrons

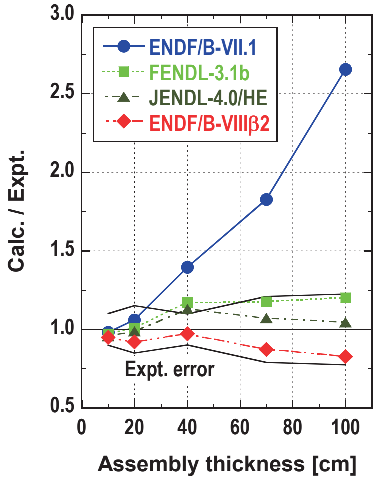

Fig. 4. Calc./Expt. for neutron fluxes of 10-35 MeV in the iron experiment

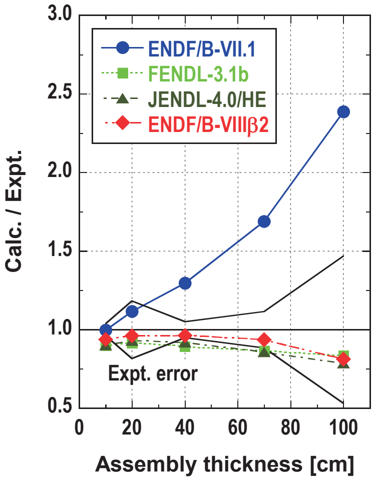

Fig. 5. Calc./Expt. for neutron fluxes of 35-45 MeV in the iron experiment

The experimental and calculated neutron spectra in the iron experiment with 65 MeV neutrons are plotted in Fig. 6. In order to compare more precisely, the Calc./Expt.s of the continuum (10-60 MeV) and peak (60-70 MeV) neutron fluxes are shown in Figs. 7 and 8. The calculated peak neutron flux with ENDF/B-VII.1 is slightly smaller than that with ENDF/B-VIIIβ2, but still overestimates.

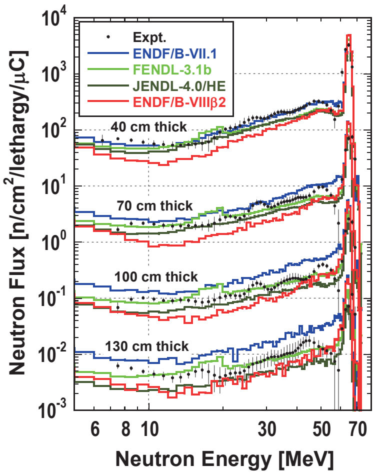

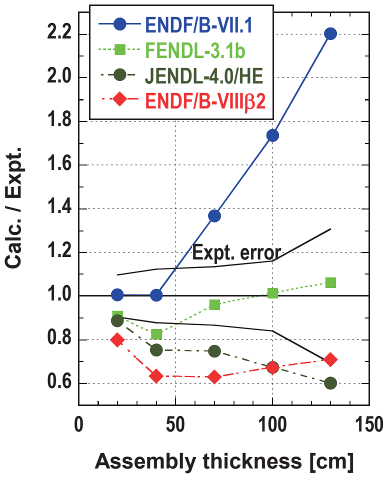

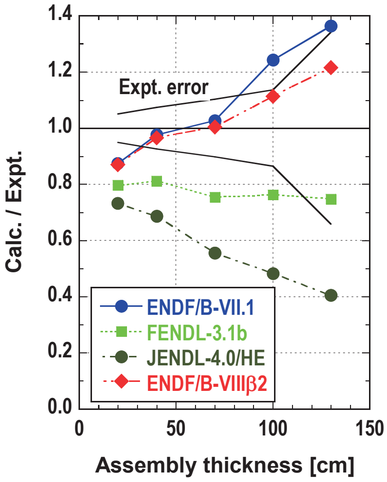

Fig. 6. Neutron spectra in the iron experiment with 65 MeV neutrons

Fig. 7. Calc./Expt. for neutron fluxes of 10-60 MeV in the iron experiment

Fig. 8. Calc./Expt. for neutron fluxes of 60-70 MeV in the iron experiment

Figures 9 and 10 show the elastic and non-elastic scattering cross sections of ^{56}Fe, respectively. ENDF/B-VIIIβ2 has similar elastic scattering cross section to JENDL-4.0/HE at both 40 and 65 MeV, and it is smaller than FENDL-3.1b. ENDF/B-VIIIβ2 has also similar non-elastic scattering cross section to FENDL-3.1b at 40 MeV, but it is smaller than FENDL-3.1b and JENDL-4.0/HE at 65 MeV. Thus the ^{56}Fe data of the elastic and non-elastic scattering cross sections for high energy neutrons are considered to be partly revised in ENDF/B-VIIIβ2.

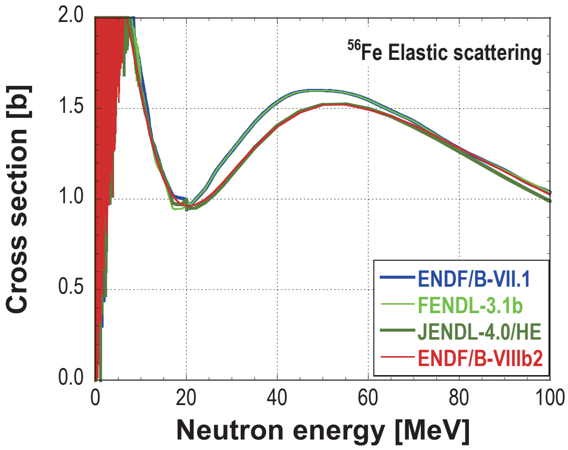

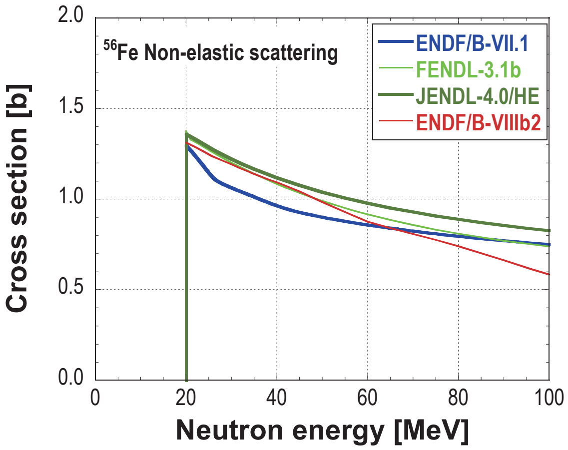

Fig. 9. Elastic scattering cross section of ^{56}Fe

Fig. 10. Non-elastic scattering cross section of ^{56}Fe

3.2 Concrete experiment

The experimental and calculated neutron spectra in the concrete experiment with 40 MeV neutrons are shown in Fig. 11. In order to compare more precisely, the Calc./Expt.s of the continuum (10-35 MeV) and peak (35-45 MeV) neutron fluxes are shown in Figs. 12 and 13. The calculation result with ENDF/B-VIIIβ2 is almost the same as that with ENDF/B-VII.1, which overestimates the measured one drastically. Only the calculated result with JENDL-4.0/HE agrees well with the measured one.

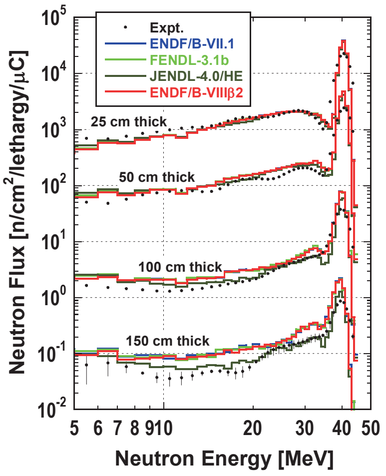

Fig. 11. Neutron spectra in the concrete experiment with 40 MeV neutrons

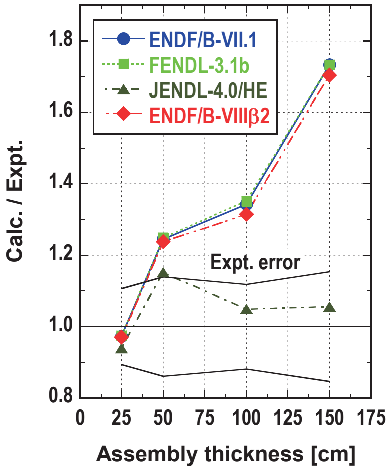

Fig. 12. Calc./Expt. for neutron fluxes of 10-35 MeV in the concrete experiment

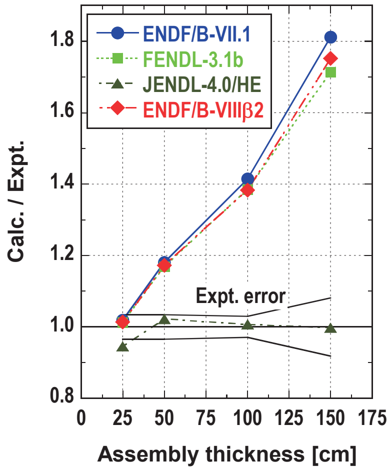

Fig. 13. Calc./Expt. for neutron fluxes of 35-45 MeV in the concrete experiment

The experimental and calculated neutron spectra in the concrete experiment with 65 MeV neutrons are plotted in Fig. 14. In order to compare more precisely, the Calc./Expt.s of the continuum (10-60 MeV) and peak (60-70 MeV) neutron fluxes are shown in Figs. 15 and 16. Note that the measured data for the assembly of 200 cm in thickness may include background neutrons. The calculation result with ENDF/B-VIIIβ2 is almost the same as that with ENDF/B-VII.1.

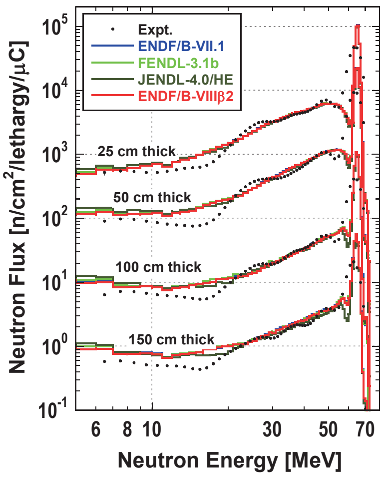

Fig. 14. Neutron spectra in the concrete experiment with 65 MeV neutrons

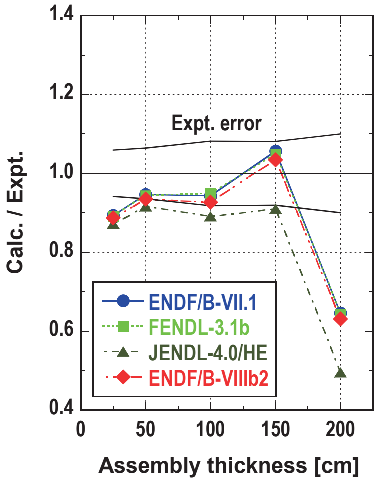

Fig. 15. Calc./Expt. for neutron fluxes of 10-60 MeV in the concrete experiment

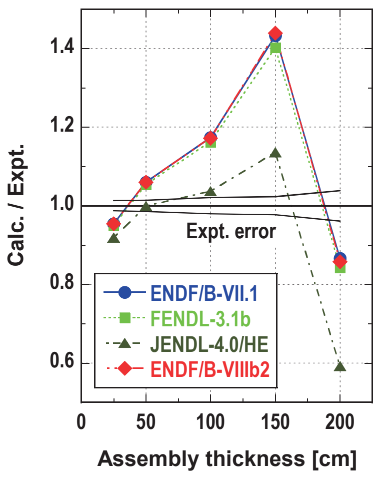

Fig. 16. Calc./Expt. for neutron fluxes of 60-70 MeV in the concrete experiment

The calculated peak neutron fluxes with ENDF/B-VIIIβ2 still overestimate the measured ones because the ^{16}O data above 20 MeV in ENDF/B-VIIIβ2 are not revised from those in ENDF/B-VII.1 as shown in Figs. 17 and 18.

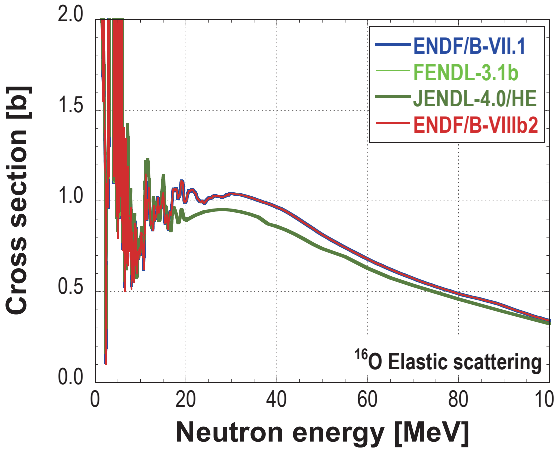

Fig. 17. Elastic scattering cross section of ^{16}O

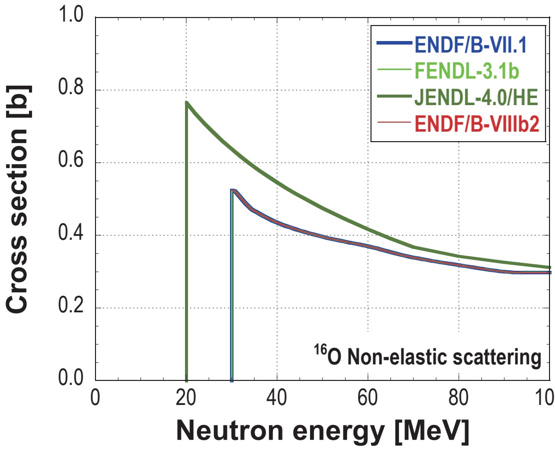

Fig. 18. Non-elastic scattering cross section of ^{16}O

4. Conclusion

We analyzed the iron and concrete shielding experiments with 40 and 65 MeV neutron sources at QST/TIARA by using ENDF/B-VIIIβ2 which was released in August, 2016 for the next version of the ENDF/B-VII library, in order to investigate how the ^{56}Fe and ^{16}O data in ENDF/B-VIIIβ2 were improved. In the iron experiment, the excessive overestimation in the calculated result with ENDF/B-VII.1 was improved in that with ENDF/B-VIIIβ2, as the result of the partly revision of the elastic and non-elastic scattering cross section data in ENDF/B-VIIIβ2. In the concrete experiment, however, the excessive overestimation in the calculated result with ENDF/B-VII.1 still remained in that with ENDF/B-VIIIβ2 because the ^{16}O data above 20 MeV were not revised in ENDF/B-VIIIβ2. The final version of ENDF/B-VIII should be modified based on these results.

References

[1] J. Knaster *et al.*, “The International Fusion Materials Irradiation Facility (IFMIF),” Nature Phys. 12, pp.424-434 (2016).
[2] K. Ochiai *et al.*, “IFMIF/EVEDA Activity of Broader Approach and Future Plan,” J. Plasma Fusion Res. 92, pp.274-277 (2016).
[3] A. Ibarra *et al.*, “A Stepped Approach from IFMIF/EVEDA Toward IFMIF,” Fusion Sci. Tech. 66, pp.252-259 (2014).
[4] http://www-nds.iaea.org/fendl/ (current as of Feb. 9, 2017).
[5] S. Kunieda *et al.*, “Overview of JENDL-4.0/HE and benchmark calculation,” JAEA-Conf. 2016-004, pp.41-46 (2016).
[6] M. B. Chadwick *et al.*, “ENDF/B-VII.1: Nuclear Data for Science and Technology,” Nucl. Data Sheets 112, pp.2887-2996 (2011).
[7] https://ndclx4.bnl.gov/gf/project/endf/ (current as of Feb. 9, 2017).
[8] C. Konno *et al.*, “Analyses of iron and concrete shielding experiments at JAEA/TIARA with JENDL/HE-2007, ENDF/B-VII.1 and FENDL-3.0,” Fusion Eng. Des. 98-99, pp.2178-2181 (2015).
[9] C. Konno *et al.*, “JENDL-4.0/HE Benchmark Test with Concrete and Iron Shielding Experiments at JAEA/TIARA,” EPJ Web of Conferences 153, 01024 (2017).
[10] H. Nakashima *et al.*, “Experiments on Iron Shield Transmission of Quasi-mono energetic Neutrons Generated by 43- and 68 MeV Protons via the ^{7}Li(p,n) reaction,” JAERI-Data/Code 96-005 (1996).
[11] N. Nakao *et al.*, “Experimental Data on Concrete Shield Transmission of Quasi-mono energetic Neutrons Generated by 43- and 68 MeV Protons via the ^{7}Li(p,n) reaction,” JAERI-Data/Code 97-020 (1997).
[12] X-5 Monte Carlo Team, “MCNP-A General Monte Carlo N-Particle Transport Code, Version 5,” LA-UR-03-1987 (2005).
[13] A. C. Kahler *et al.*, “The NJOY Nuclear Data Processing System, Version 2012,” LA-UR-12-27079 (2012).

24 Production cross sections of ^{52}Fe isotope in alpha particle induced reactions on ^{nat}Cr

Naoyuki Ukon[1], Moemi Saito[2], Masayuki Aikawa[2]

[1]Nuclear Reaction Data Center (JCPRG), Faculty of Science, Hokkaido University, Kita 10 Nishi 8, Kita-ku, Sapporo 060-0810, Japan
[2]Graduate School of Science, Hokkaido University, Kita 10 Nishi 8, Kita-ku, Sapporo 060-0810, Japan
e-mail: ukon@nds.sci.hokudai.ac.jp

^{52}Fe ($T_{1/2}$ = 8.27 h) is a medical radioisotope available for positron emission tomography. A process to produce ^{52}Fe is α-induced reactions on natural chromium. Three experimental cross sections of the reaction have previously been measured, however there is a large discrepancy among them. We have a plan to perform an experiment for the cross section measurement with a 50 MeV α beam at RIKEN AVF cyclotron and performed its simulation beforehand. We compared the simulation result with previous experimental data and theoretical data and assessed the experimental method.

1. Introduction

Positron emission tomography (PET) is a general tracer technique based on the use of positron-emitting nuclides for labelling of a wide range of tracer molecules. ^{52}Fe is a positron emitter, which decays to ^{52}Mn with a physical half-life of 8.27 h. The only iron isotope with suitable decay characteristics for PET, ^{52}Fe, has merely been used as a bone marrow tracer [1-3].

The cross sections of the selected nuclear reaction are fundamental information for applications. The literature search for existing cross section data on ^{nat}Cr(α,x)^{52}Fe reactions, which are included in the EXFOR database [4], showed that only three studies were performed previously [5-7]. However there is a large discrepancy among the previous data. Therefore, we have a plan to perform to measure the cross sections. In this study, we simulated the forthcoming experiment to measure activation cross sections of the ^{nat}Cr(α,x) reaction for ^{52}Fe and other isotope production using nickel–chromium alloy targets. The result was compared with the previous data [5-7] and the theoretical calculation of the code TALYS 1.8 as obtained from the on-line library TENDL-2015 [8].

2. Method

The experiment is planned at the RIKEN AVF cyclotron with a 50 MeV α beam. The actual incident beam energy can be measured by the time-of-flight method using plastic scintillator monitor [9]. The target consists of 64 thin metallic foils, which are 24 nickel-chromium alloy (6.73 $\mathrm{mg/cm^2}$), 20 natural nickel (4.45 $\mathrm{mg/cm^2}$) and 20 titanium (2.25 $\mathrm{mg/cm^2}$) foils, respectively. The composition of the nickel-chromium allay is nickel (79%), chromium (20%) and iron (1%). The isotopic composition of the chromium is natural and it has four stable isotopes (^{50}Cr: 4.345%, ^{52}Cr: 83.79%, ^{53}Cr: 9.50%, ^{54}Cr: 2.36%). The beam energy degraded in the stacked target is calculated using the SRIM code available online [10]. The gamma-lines expected from the activated foils are listed in Table 1 [11], which are measured by HPGe detectors. The experiment is simulated using PHITS, a Monte Carlo particle transport simulation code [12].

Table 1: Decay data and reaction and Q-value of ^{nat}Cr(α,x) reactions [11]

Nuclide	Half-life	Decay mode (%)	E_γ (keV)	I_γ (%)	Contributing reaction	Q-value (keV)
^{52}Fe	8.27 h	EC+β^+ (100)	169.00	0.992	^{50}Cr(α,αn)	-15647.14
					^{52}Cr(α,αn)	-36946.16
^{52}Mn	5.59 d	EC+β^+ (100)	744.23	0.900	^{50}Cr(α,pn)	-12490.23
			935.54	0.945	^{52}Cr(α,p3n)	-33789.25
			1434.09	1.000		
^{54}Mn	312.1 d	EC (100)	834.85	0.9998	^{52}Cr(α,pn)	-12796.95
					^{53}Cr(α,p2n)	-20736.07
					^{54}Cr(α,p3n)	-30455.19
^{56}Mn	2.58 h	β^- (100)	846.76	0.9885	^{53}Cr(α,p)	-3239.1
					^{54}Cr(α,pn)	-12958.227
^{49}Cr	42.3 m	EC+β^+ (100)	152.91	0.303	^{50}Cr(α,2p3n)	-41296.0
			90.63	0.532	^{50}Cr(α,αn)	-13000.33
					^{52}Cr(α,2αn)	-34299.36
^{51}Cr	27.7 d	EC (100)	320.08	0.099	^{50}Cr(α,2pn)	-19035.0
					^{52}Cr(α,αn)	-12038.35
					^{53}Cr(α,2αn)	-19977.47
					^{54}Cr(α,2αn)	-29696.59
^{48}V	15.97 d	EC+β^+ (100)	983.52	0.9998	^{50}Cr(α,αpn)	-21145.22
			1312.11	0.982	^{52}Cr(α,αp3n)	-42444.25

3. Results

The simulated excitation functions of the ^{nat}Cr(α,x) reactions are shown in Figs. 1 and 2. The excitation function of the ^{50}Cr(α,2n)^{52}Fe reaction, the only possible in the energy domain studied, has an effective threshold of 16.901 MeV corresponding to the theoretical one. In Hermanne et al. [5], the maximum value of about 22 mb at around 32 MeV corresponds well with the values of Levkovskij [6]. The values of Chowdhury et al. [7] are however a factor three too high and strangely peaked. The TENDL-2015 prediction [8] has a maximum that is shifted in energy by about 10 MeV. The peak position of the simulation result shows good agreement with Hermanne *et al*. [5] and Levkovskij [6] although the amplitude is large. The production cross sections of other isotopes can also be obtained in the forthcoming experiment as shown in Fig. 2.

4. Conclusions

Cross sections are fundamental information for applications. The production cross sections of a positron emitter ^{52}Fe, which is available for PET, are valuable information. We have a plan to perform an experiment for the cross section measurement of the α-induced reaction on ^{nat}Cr for ^{52}Fe production at RIKEN AVF cyclotron. In this study, we simulated the forthcoming experiment to measure the cross sections of the ^{nat}Cr(α,x) reactions using nickel-chromium alloy targets. The cross sections were obtained and compared with the previous experimental data [5-7] and theoretical calculation [8]. The obtained data can contribute the accurate estimation of ^{52}Fe production through the reaction.

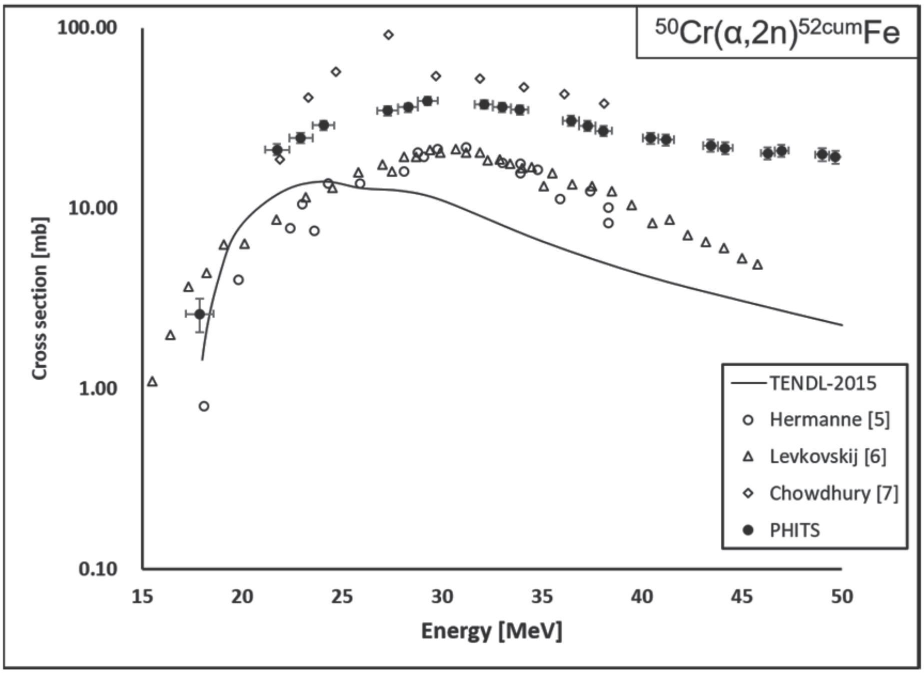

Fig. 1 Excitation function of the ^{50}Cr(α,2n)^{52cum}Fe reaction derived from PHITS simulation with previous data and TENDL-2015

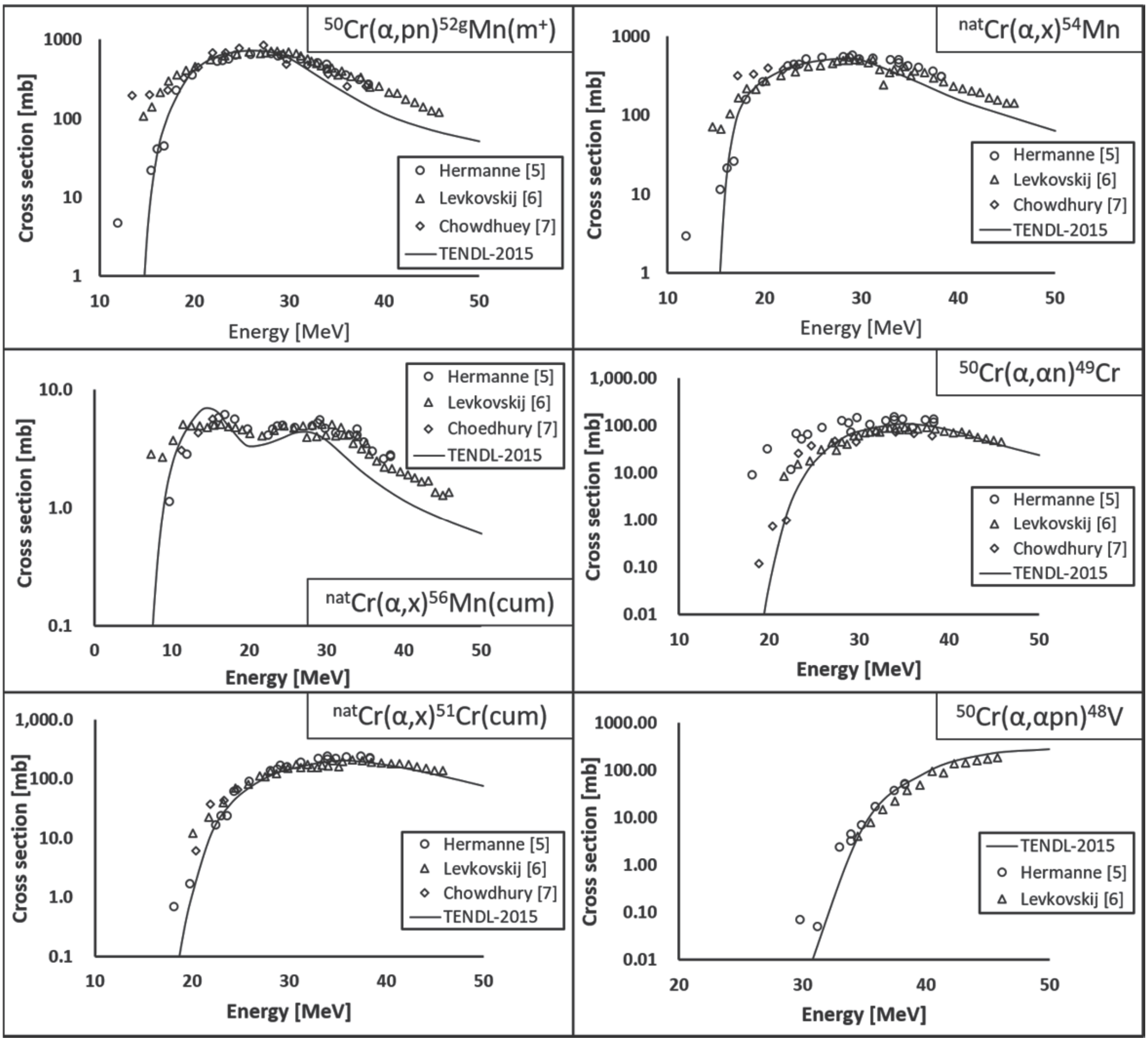

Fig. 2 Excitation functions of the $^{nat}Cr(\alpha,x)$ reactions to be measured in the forthcoming experiment with previous data and TENDL-2015

5. References

[1] Ferrant A, Cogneau M, Leners N., *et al.* ^{52}Fe for additional marrow ablation before bone marrow transplantation. Blood 1993;81: pp.3435-3439.

[2] Lubberink M, Tolmachev V, Beshara S, *et al*. Quantification aspects of patient studies with ^{52}Fe in positron emission tomography. Appl. Radiat. Isot. 1999;51: pp.707-715.

[3] Beshara S, Sorensen J, Lubberink M, *et al*. Pharmacokinetics and red cell utilization of ^{52}Fe/^{59}Fe-labelled iron polymaltose in anaemic patients using positron emission tomography. Br. J. Haematol., 2003;120: pp.853-859.

[4] Otuka N, Dupont E, Semkova V, *et al*. Towards a More Complete and Accurate Experimental Nuclear Reaction Data Library (EXFOR): International Collaboration Between Nuclear Reaction Data Centres (NRDC). Nuclear Data Sheets 2014;120: pp.272-276.

[5] Hermanne A, Adam Rebeles R, Tárkányi F, *et al.* Alpha particle induced reactions on ^{nat}Cr up to 39 MeV: Experimental cross-sections, comparison with theoretical calculations and thick target yields for medically relevant ^{52g}Fe production. Nucl. Instr. Meth. Phys. Res. B 2015;256-257: pp.28-41.

[6] Levkovskij VN. Activation cross section nuclides of average masses (A = 40-100) by proton and alpha particles with average energies (E = 10-50 MeV), Activation Cross Sections by Protons and Alphas. Moscow 1991. (EXFOR A0510)

[7] Chowdhury DP, Sujit Pal, Saha SK, *et al*. Determination of cross section of alpha-induced nuclear reaction on natural Cr and Zr by stacked foil activation for thin layer activation analysis, Nucl. Instr. Meth. Phys. Res. B 1995;103: pp.261-266. (EXFOR A0204)

[8] TENDL-2015: TALYS-based evaluated nuclear data library, Available from: https://tendl.web.psi.ch/tendl_2015/tendl2015.html

[9] Watanabe T, Fujimaki M, Fukunishi N, et al. BEAM ENERGY AND LONGITUDINAL BEAM PROFILE MEASUREMENT SYSTEM AT THE RIBF. Proc. 5th Int. Part. Accel. Conf. (IPAC2014) 2014: pp.3566-3568.

[10] Ziegler J, Biersack JP, Ziegler M, SRIM: the Stopping and Range of Ions in Matter. Available from: http://www.srim.org

[11] NuDat 2.6. National Nuclear Data Center; Available from: http://www.nndc.bnl.gov/nudat2/

[12] Sato T, Niita K, Matsuda N, *et al*. Particle and Heavy Ion Transport Code System PHITS, Version 2.52, J. Nucl. Sci. Technol. 2013;50: pp.913-923.

25 Theoretical model analysis of (*d, xn*) reactions on ^{7}Li at 25, 40, and 102 MeV

Hiroki SADAMATSU[1], Shinsuke NAKAYAMA[2], Yukinobu WATANABE[1],
Osamu IWAMOTO[2], Kazuyuki OGATA[3]
[1]*Department of Advanced Energy Engineering Science, Kyushu University, Japan*
[2]*Nuclear Science and Engineering Center, Japan Atomic Energy Agency, Japan*
[3]*Research Center for Nuclear Physics, Osaka University, Japan*
E-mail: sadamatsu@aees.kyushu-u.ac.jp

Neutron production from deuteron-induced reactions on ^{7}Li is analyzed with theoretical model calculation considering elastic and nonelastic breakup processes, proton transfer process to bound states in the residual nucleus, and statistical decay processes. The calculation results reproduce experimental double differential cross sections (DDXs) of ^{7}Li(*d, xn*) reactions at incident energies up to 102 MeV generally well, except in the low emission energy region. The nonelastic breakup process is found to be the most dominant reaction process.
This work was funded by ImPACT Program of Council for Science, Technology and Innovation (Cabinet Office, Government of Japan).

Keyword **: ImPACT, DEURACS, Lithium-7, deuteron-induced reactions, theoretical model calculation**

1. Introduction

In recent years, the demand for intense neutron sources has been increasing in various applications such as nuclear transmutation of high-level radioactive waste and medical radioisotopes production. Deuteron accelerator-based neutron sources are promised as one of the candidates. In the design of deuteron accelerator neutron sources, reliable nuclear data of deuteron-induced reactions are required for neutron converter materials (Li, Be, C, *etc*.) and accelerator structure materials (Al, Cu, Nb, *etc*.). Since it is hard to measure the whole nuclear data required over wide ranges of incident energy and target nuclei by measurements, theoretical model calculations which can complement experimental data play an important role in nuclear data evaluation.

We have been developing a code system dedicated for deuteron-induced reactions, called deuteron-induced reaction analysis code system (DEURACS) [1,2]. So far, DEURACS has been applied successfully to calculate thick target neutron yields (TTNYs) for ^{9}Be(*d, xn*) and ^{12}C(*d, xn*) reactions at energies up to 50 MeV [2]. In the present work, we focus on deuteron-induced neutron production from ^{7}Li target. Firstly, the spectroscopic factors (SFs) necessary to describe proton transfer reactions are extracted by the DWBA analysis of experimental double differential (*d, xn*) cross sections (DDXs) at incident energies of 25, 40, and 102 MeV. Then, the calculated DDXs are compared with the measured ones, and the applicability of DEURACS is discussed.

2. Models and methods

A. Calculation method of DDXs

In DEURACS, the DDXs of (*d, xn*) reactions are expressed by incoherent summation of four components:

$$\frac{d^2\sigma}{dEd\Omega} = \frac{d^2\sigma_{EBU}}{dEd\Omega} + \frac{d^2\sigma_{NBU}}{dEd\Omega} + \frac{d^2\sigma_{p-TR}}{dEd\Omega} + \frac{d^2\sigma_{SD}}{dEd\Omega} \tag{1}$$

where $d^2\sigma_{EBU}/(dEd\Omega), d^2\sigma_{NBU}/(dEd\Omega), d^2\sigma_{p-TR}/(dEd\Omega),\ and\ d^2\sigma_{SD}/(dEd\Omega)$ correspond to the DDXs for elastic breakup, nonelastic breakup, proton transfer and statistical decay reaction, respectively.

The elastic breakup (EBU) is calculated using the code based on the Continuum-Discretized Coupled-Channels method (CDCC) [3]. The Glauber model [5,6] is adopted to describe the nonelastic breakup (NBU) reaction, in which either proton or neutron in deuteron is absorbed into the target and the remaining one scatters elastically on it. The DWUCK4 code [4] based on conventional zero-range Distorted Wave Born Approximation (DWBA) is used for the proton transfer (p-TR) transition to bound states of the residual nucleus. Note that the NBU and p-TR reactions were referred to as the stripping reactions to the continuum and bound states, respectively, in our past works [1,2]. Finally, the statistical decay (SD) process is calculated using the Hauser-Feshbach and exciton models implemented in the CCONE code [7,8]. In the calculation, three different compound nuclei are considered because they can be formed by absorption of either a neutron or a proton in the incident deuteron or the deuteron itself. Therefore, the DDXs for the statistical decay are calculated in the same way as in Ref. [9]:

$$\frac{d^2\sigma_{SD}}{dEd\Omega} = R_d \frac{d^2\sigma^{CCONE}_{(d,xn)}}{dEd\Omega} + R_n \frac{d^2\sigma^{CCONE}_{(n,xn)}}{dEd\Omega} + R_p \frac{d^2\sigma^{CCONE}_{(p,xn)}}{dEd\Omega} \tag{2}$$

where R_d, R_p, and R_n denote the formation fractions of three different compound nuclei, which are calculated with the Glauber model, and $d^2\sigma^{CCONE}_{(d,xn)}/(dE d\Omega)$, $d^2\sigma^{CCONE}_{(n,xn)}/(dE d\Omega)$, $d^2\sigma^{CCONE}_{(p,xn)}/(dE d\Omega)$ are the DDXs of (*d, xn*), (*p, xn*), and (*n, xn*) reactions calculated with the CCONE code, respectively.

In the calculation of (*p, xn*) and (*n, xn*) components in Eq. (2), we assume that the incident energy of the proton and the neutron is half of the deuteron incident energy. To be exact, this assumption is not correct because the neutron or the proton absorbed in the target nucleus by the nonelastic breakup reaction has a certain energy distribution. However, we use this assumption for reduction of computational time because we confirmed that there is not a significant difference between the calculation results with this approximate and those including the energy distribution properly.

B. Input parameters of model calculations

In the CDCC and the Glauber model calculations, the nucleon optical model potentials (OMPs) of the target nucleus are necessary. In the present work, we use the global potentials of Koning and Delaroche (KD) [10] at half the incident deuteron energy. In both the CCONE and DWBA calculations, the nucleon OMPs and the deuteron OMPs are necessary. In the CCONE calculation, the KD OMPs and the An and Cai (An-Cai) global OMPs [11] are used for nucleon OMPs and deuteron OMPs, respectively. Note that these OMPs are the same as in our previous analyses [1,2]. In the DWBA calculation, the KD OMPs and the adiabatic OMPs derived from the nucleon OMP of Ye *et al* [12] are used for nucleon OMPs in the exit channel and deuteron OMPs in the entrance channel, respectively.

3. DWBA analysis of proton transfer reaction

To calculate DDXs from the ^{7}Li(*d, n*) reaction, we extract the spectroscopic factors (SFs) of single proton orbits in the residual nucleus ^{8}Be, which is necessary to determine the absolute value of differential cross sections calculated by the DWUCK4 code. The relation between the DWUCK cross section and the DWBA differential cross section for proton transfer reaction leading to each excited state *i* of residual nucleus is given by

$$\frac{d\sigma_{bound,i}^{DWBA}}{d\Omega}(E_d) = \frac{D_0^2}{10^4}\frac{2J_i+1}{2J_A+1}\frac{S_i}{2j+1}\frac{d\sigma_{bound,i}^{DWUCK4}}{d\Omega}(E_d) \tag{3}$$

where E_d is the incident deuteron energy, D_0 is a constant used in zero-range approximation and the value is $D_0^2 = 1.50 \times 10^4$, J_A and J_i are the spins of the ground state of target nucleus and the i-th state of residual nucleus, respectively, S_i is the SF for each state, j is the total spin of transferred neutron, and $\mathrm{d}\sigma_{\mathrm{bound,i}}^{DWUCK4}/\mathrm{d}\Omega$ is the differential cross section calculated with the DWUCK4 code. In this study, the ground state and the first excited state (3.03 MeV) of residual nucleus ^{8}Be are considered as discrete states in the exit channel.

The DDXs for proton transfer reaction are obtained by folding the calculated DWBA cross sections corresponding to each bound state with Gaussian function as follows:

$$\frac{d^2\sigma_{p-TR}}{dEd\Omega} = \sum_i^{I_0}\frac{1}{\sqrt{2\pi\sigma^2}}\exp\left(-\frac{(E-\mu_i)^2}{2\sigma^2}\right)\frac{d\sigma_{bound,i}^{DWBA}}{d\Omega} \tag{4}$$

where $\mathrm{d}\sigma_{p-TR}/dEd\Omega$ is the DDXs for proton transfer reaction, E is the proton emission energy, σ is the standard deviation representing experimental energy resolution, and μ_i is the emission energy corresponding to the i-th discrete peak. $d\sigma_{bound,i}^{DWBA}/d\Omega$ is the differential cross section calculated from Eq. (3).

4. Results and discussion

Figure 1 shows comparisons of calculated and experimental differential cross sections for the transition to the ground and 3.03-MeV states of ^{8}Be in the ^{7}Li(d, n)^{8}Be reaction at 25, 40 and 102 MeV. The experimental DDXs are integrated over the neutron emission energy around the observed peaks to obtain the differential cross sections. The experimental data are taken from Refs. [13-15]. The calculation shows only the DWBA component and the statistical decay contribution from compound nuclei is not considered because this component is not so large at forward angles. Each Si of the SF in Eq. (3) was extracted by fitting the calculated cross section to the corresponding experimental data for each incident energy.

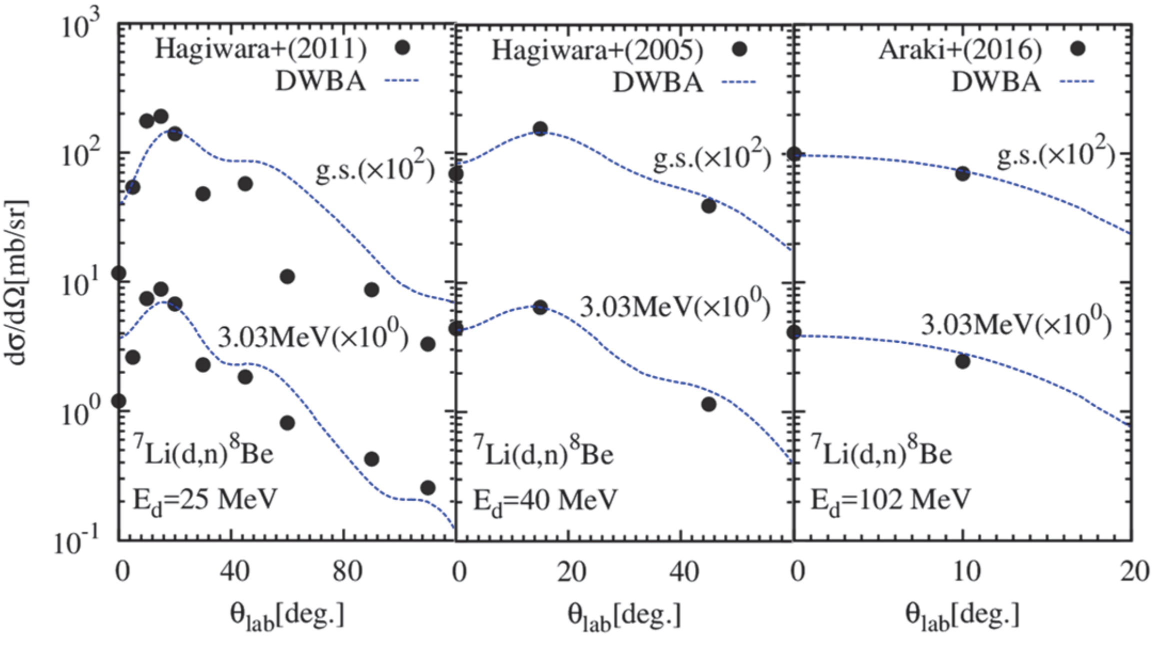

Fig. 1 Calculated and experimental differential cross sections of the ^{7}Li(d, n) reaction

In our early work of ^{12}C(d,p) reactions [1], we have reported that the S_i has an incident energy dependence given by

$$S_{i,k}(E_d) = F_i S_{C-12,1}(E_d) \qquad (5)$$

where F_i is a scaling factor depending on the excited states i of residual nucleus k, and $S_{C\text{-}12,1}(E_d)$ is the incident energy dependence of the SF value which is determined by the ^{12}C(d,p)^{13}C$_{\mathrm{g.s.}}$ reaction:

$$S_{\mathrm{C}-12,1}(E_d) = -2.18 \times 10^{-6} E_d^3 + 3.19 \times 10^{-4} E_d^2 - 1.56 \times 10^{-2} E_d + 8.20 \times 10^{-1} \qquad (6)$$

In **Fig. 2**, the extracted SFs for the ground and 3.03 MeV states of ^{8}Be are plotted as a function of incident energy and compared with the incident energy dependence given by Eqs. (5) and (6). The extracted SF of the ground state at 40 MeV is about 20% smaller than the SF predicted by Eqs (5) and (6). The extracted SF value may have a relatively large uncertainty because the two peaks seen in the measured DDX are overlapped due to poor energy resolution and the separation of the ground-state peak weaker than the 3.03-MeV state one is not sufficient.

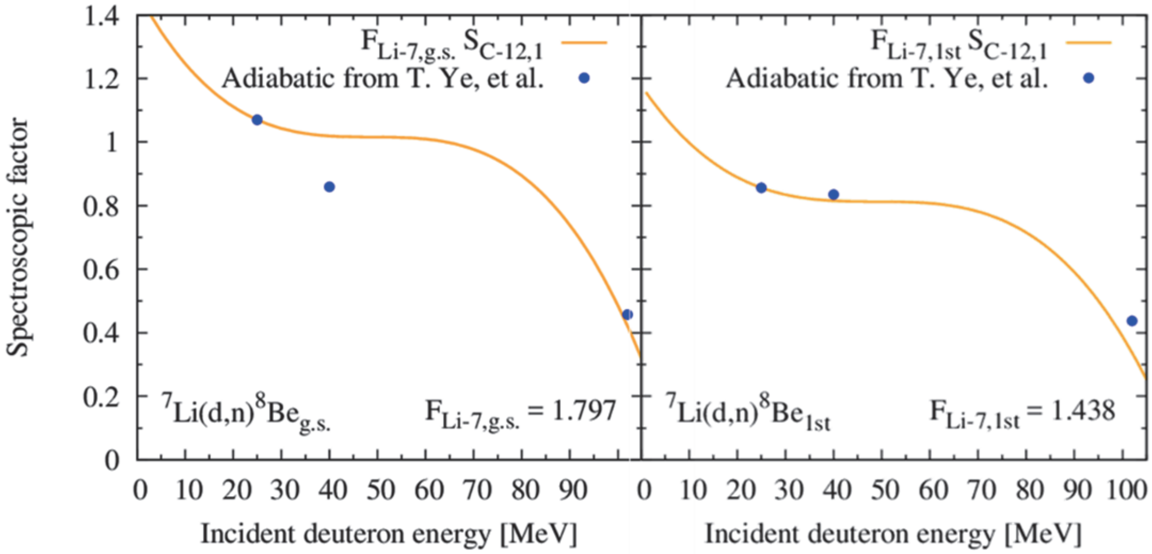

Fig. 2 Incident energy dependence of experimental SFs extracted from the ^{7}Li(d, n)^{8}Be reaction

Next, **Fig. 3** shows comparisons between the calculated and experimental DDXs of ^{7}Li for two deuteron energies of 25 MeV [13] and 40 MeV [14] at several angles. The calculation generally reproduces the experimental data, although some discrepancies are seen.

In **Fig. 4**, the calculated and experimental DDXs at 0 degree are compared for three incident energies of 25, 40 and 102 MeV [15]. The calculation reproduces generally well both the shape and magnitude of the experimental DDX data. It is found that the nonelastic breakup process is the most dominant at any incident energies and the peak structure seen in the high neutron energy end is caused by the proton transfer process. There are some discrepancies between the calculation and the experimental data. One of them is underestimation seen in the low neutron energy region smaller than 5 MeV. This underestimation might be because the CCONE code, which describes the statistical decay process, cannot deal with particle emissions from discrete states in residual nuclei. In addition, the calculation cannot reproduce the peak seen near the incident energy. Since each measurement was carried out using a natural lithium targets, the peak is expected to be formed by ^{6}Li(d, xn)^{7}Be (g.s. or 0.429 MeV) which is not involved in the calculation.

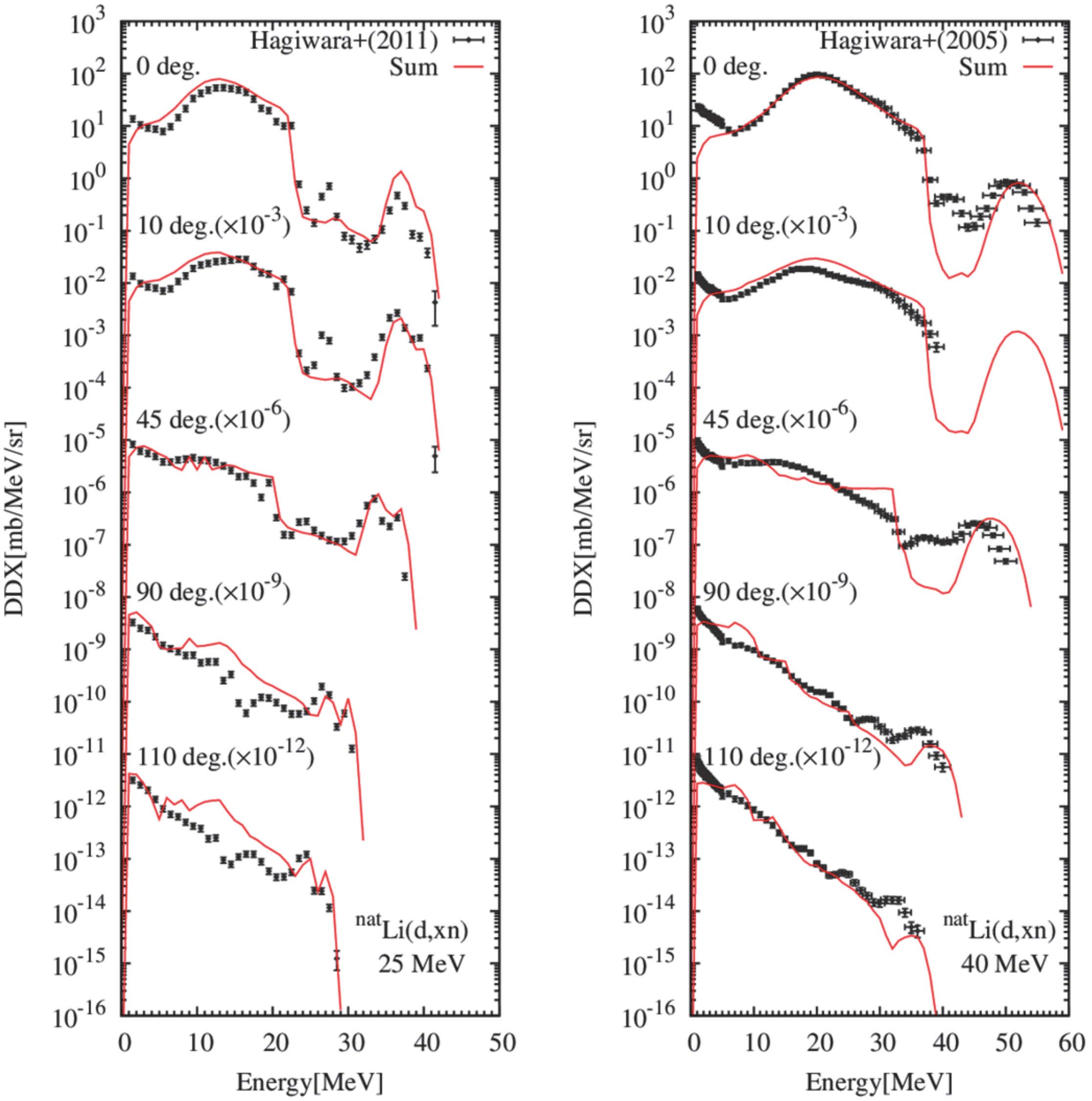

Fig. 3 Calculated and experimental DDXs of the ^{7}Li(*d, xn*) reaction at 25 and 40 MeV

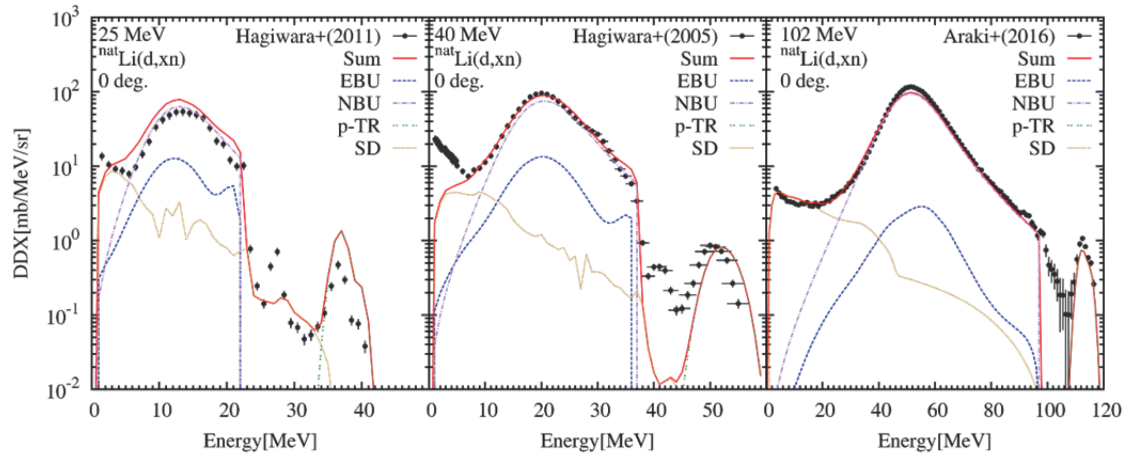

Fig. 4 Calculated and experimental DDXs at 0 degree for the ^{7}Li(*d, xn*) reaction at 25, 40, and 102 MeV

5. Conclusion and outlook

Deuteron-induced reaction analysis code system (DEURACS) was applied to calculate double differential cross sections (DDXs) for the ^{7}Li(*d, xn*) reaction at 25, 40, and 102 MeV. First, the spectroscopic factors (SFs) of single proton orbits in the residual nucleus ^{8}Be were extracted from the DWBA analysis of proton transfer reaction to the ground and 3.03-MeV states. The extracted SFs were found to have the incident energy dependence similar to that seen in the ^{12}C(*d, p*)^{13}C$_{\mathrm{g.s.}}$ reaction. The calculated DDXs reproduced the experimental ones generally well, except in the low emission energy region. Through the model analysis, it was found that the nonelastic breakup reaction described by the Glauber model is the most dominant neutron production process.

In the future, we will calculate double-differential thick target neutron yields in the same way as in Ref. [2], and compare the results with available experimental data [16,17].

References

[1] S. Nakayama and Y. Watanabe, J. Nucl. Sci. Technol., **53**, 89 (2016).
[2] S. Nakayama *et al*., Phys. Rev. C **94**, 014618 (2016).
[3] M. Yahiro *et al*., Prog. Theor. Exp. Phys. 2012, 01A206 (2012).
[4] P. D. Kunz, Computer code DWUCK4, University of Colorado, (Private Communication).
[5] T. Ye, Y. Watanabe, and K. Ogata, Phys. Rev. C **80**,014604 (2009).
[6] T. Ye, S. Hashimoto *et al*., Phys. Rev. C **84**, 054606 (2011).
[7] O. Iwamoto, J. Nucl. Sci. Technol. ,**44**, 687 (2007).
[8] O. Iwamoto *et al.*, Nucl. Data Sheets, **131**, 259 (2016).
[9] S. Nakayama *et al*., Nucl. Data Sheets, **118**, 305 (2014).
[10] A. J. Koning and J. P. Delaroche, Nucl. Phys. A **713**, 231 (2003).
[11] H. An and C. Cai, Phys. Rev. C **73**, 054605 (2006).
[12] T. Ye, Y. Watanabe, K. Ogata, S. Chiba, Phys. Rev. C **78**, 024611 (2008).
[13] M. Hagiwara *et al*., J. Nucl. Materials, **417**, 1284–1287(2011).
[14] M. Hagiwara, *et al*., Fusion Sci.Technol., **48,** 1320 (2005).
[15] S. Araki *et al.*, Nucl. Instr. and Meth. in Phys. Research A **842**, 62–70 (2017).
[16] D. L. Johnson *et al*., J. Nucl. Materials, **85**, 467 (1979).
[17] A. N. Goland *et al*., IEEE Transactions on Nucl. Sci. **22**, 1776 (1975).

26 Optimization of experimental system design for benchmarking of large angle scattering reaction cross section at 14 MeV using two shadow bars

Naoya Hayashi, Seiki Ohnishi, Yuki Fujiwara, Sachie Kusaka, Fuminobu Sato, Isao Murata
Department of Sustainable Energy and Environmental Engineering, School of Engineering,
Osaka University, 2-1 Yamadaoka, Suita, Osaka 565-0871, Japan
E-mail:n.hayashi@qr.see.eng.osaka-u.ac.jp

Abstract

At 14 MeV, it is known that the absolute value of large angle scattering cross section is small. The contribution is thus thought to be neglected in the neutronics design of fusion reactor. However, in case that a neutron source can be regarded as a beam like a neutron streaming, large angle scattering cross sections might affect the nuclear design result largely. In fact, in fusion neutronics benchmark experiments using a neutron beam so far, there was a difference observed between experiment and simulation. Also it is known that there are differences in large angle scattering cross sections among nuclear data libraries. Then we have been carrying out preliminary benchmark experiments for verification of large angle scattering reaction cross sections of iron for a few years.

The purpose of the present study is to optimize the experimental system design to realize an accurate benchmarking of large angle scattering reaction cross sections. Finally, we reached the optimized experimental system and developed the experimental procedure which was supposed to perform more accurate benchmark experiments for large angle scattering reaction cross sections.

1. Introduction

The reaction cross section of iron which is used as the main structural material is important in neutronics design of fusion reactor. However, because the large angle scattering reaction cross section is known to be small among reaction cross sections of iron, it was thought that the contribution in the result of transport calculation was small. On the other hand, it is reported that when the structure becomes as large as the fusion reactor, the activation or exposure dose in the deeper places by like neutron streaming could be affected by the effect of the large angle scattering reaction. As in the previous research, Ohnishi carried out fusion neutronics benchmark experiments using a DT neutron beam and examined the effect of the large angle scattering reaction [1]. The experimental system is shown in Fig.1. Collimated beam neutrons were bombarded to the center of the assembly. In the assembly, six

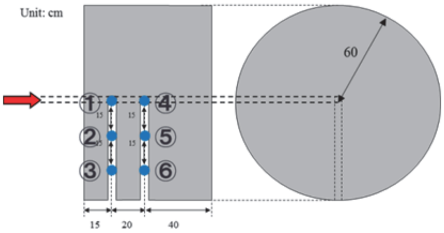

Fig. 1 The experimental system of fusion neutronics benchmark experiment

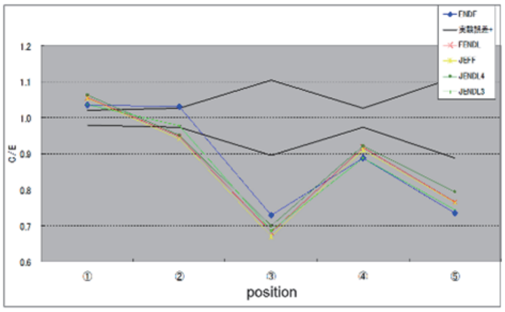

Fig. 2 The result of fusion neutronics benchmark experiment

activation foils (4×4×0.6 cm^3, niobium and indium) were arranged at positions shown in Fig.1 to confirm how neutrons are scattered by measuring the radioactivities of them. The C/E value of each activation foil is shown in Fig.2. The activation foil which was placed in a deep and off-center position, especially foils 3 and 5, shows a disagreement between calculation and experiment. We thought that this disagreement could be due to the uncertainty of large angle scattering reaction cross section.

Neutron elastic scattering reaction cross sections are included in all nuclear data libraries. However, it is known that there are differences in large angle scattering cross section among them even in the case of iron as shown in Fig.3. Under these circumstances, it would be an important task to examine a hypothesis that the differences observed in the previous research by Ohnishi would really be due to the uncertainty of the large angle scattering cross section.

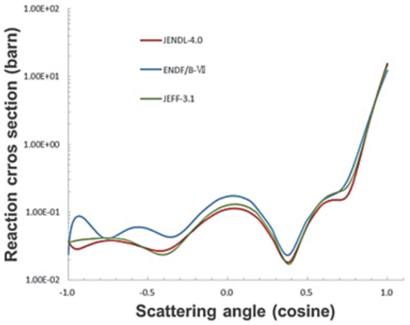

Fig. 3　Angular distribution of neutron elastic scattering of ^{56}Fe [2-5]

Then we have been carrying out preliminary numerical experiments for verification of large angle scattering reaction cross sections of iron for a few years and optimized an experimental system numerically assuming an isotopic neutron source and a shadow bar with MCNP-5[6]. The experimental system is shown in Fig.4. Using this experimental system, we can suppress the contribution of neutrons other than large angle scattered neutrons to be less than 2%. We verified theoretically that we can carry out an accurate benchmark experiment.

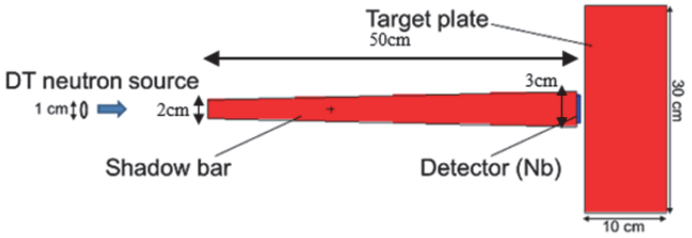

Fig. 4　Schematic experimental arrangement in previous study[6]

This experimental system was designed assuming it was in an ideal surrounding where the wall is far enough from the experimental system. However, the heavy irradiation room in OKTAVIAN, Osaka University where we will carry out our experiment is relatively small as shown in Fig.5 (4.2×4.6×4.2m^3). We thus have to consider the room-return neutrons because the wall of heavy irradiation room is near to the experimental system. The aim of the present study is to design an optimized experimental system and develop an experimental procedure using two shadow bars to benchmark the large angle scattering cross section even in a finite irradiation room.

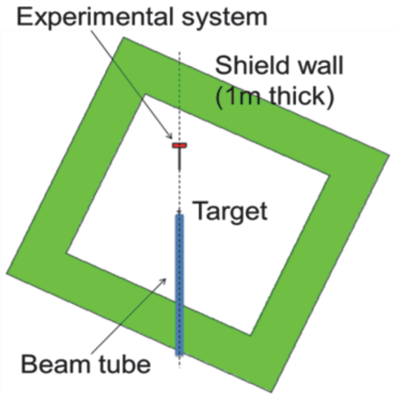

Fig.5　Experimental arrangement in the heavy irradiation room in OKTAVIAN, Osaka University

2. Experimental system design procedure

According to the discussion in Chap. 1, we designed the experimental system in order to extract the contribution of large angle scattering reaction especially for iron. In the simulation, MCNP-5 was used as a calculation code and JENDL-4.0, ENDF/B-VII and JEFF-3.1 were used as a nuclear data library. As a result of physical considerations, the basic experimental arrangement was decided as shown in Fig.6. S1 is a shadow bar which we used in our previous study. However, the contribution of room-return neutrons was too large to determine the contribution of large angle scattered neutrons accurately. Then we designed a shadow bar S2 to be used with S1 to remove the contribution of room-return neutrons and to extract that of large angle scattering.

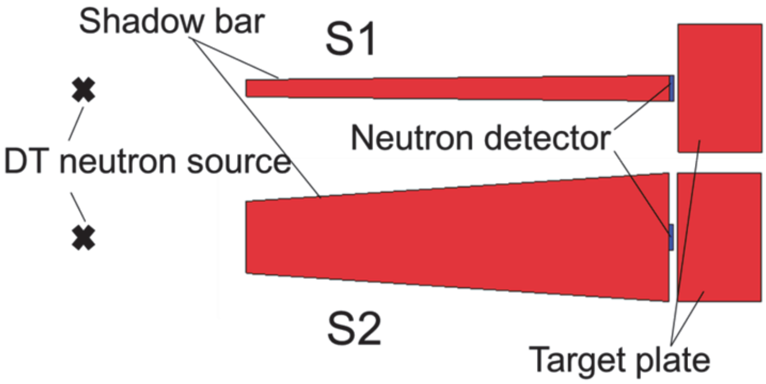

Fig. 6 Schematic experimental arrangement

In this experiment, the two shadow bars play an important role to suppress direct incidence of 14 MeV DT neutrons. In addition, shadow bar S1 measures all the contributions of neutrons except direct incidence. It means it also includes contribution of large angle scattered neutrons. On the other hand, S2 suppresses all the neutrons from the neutron source in order to measure only the contribution of room-return neutrons. The thickness of an iron target plate is set to be thin (as thin as 2 MFP) so that neutrons scattered to forward directions can mostly go through the target plate. The large angle scattered neutrons in the plate are incident to a niobium foil, which is placed just behind the shadow bar, in order to count large angle scattered neutrons. The induced radioactivity is measured by a Ge detector.

Detail of the experimental system

We assume the DT neutron source to be an isotopic disk neutron source (1 cm in diameter). This specification is fixed to simulate the specification of the intense 14 MeV neutron source facility, OKTAVIAN in Osaka University where we plan to carry out practical benchmark experiments. In this calculation, the beam intensity is 1.0×10^{10} (neutron/s).

The dimensions of the iron target plate are 15 cm in diameter and 10 cm in thickness. By making the target plate thin, i.e., around 2 MFP, we can reduce the number of scattering reaction inside the target plate and make the contribution of the large angle scattering reaction relatively dominant.

The thickness of the niobium foil is 5 mm-thick and 3cm in diameter. The reason why we chose niobium is that the energy threshold of ^{93}Nb(n,2n)^{92m}Nb reaction is as high as 9MeV and also the reaction cross section is enough high as 0.464 barn. Therefore, the niobium foil can count only large angle scattered neutrons of around 13.5 MeV, having no sensitivity to neutrons moderated in the shadow bar.

The shadow bar material is iron because the macroscopic cross section at 14 MeV is large to attenuate the 14 MeV neutrons. The shadow bars are circular truncated cones and the dimensions of the shadow bar S1 are 50cm in length, 2cm in upper diameter and 3cm in bottom diameter and those of S2 are 50cm in length, 8.3cm in upper diameter and 15cm in bottom diameter. These dimensions are optimized by parameter survey calculations by MCNP-5.

The distance between the DT neutron source and the upper base of the shadow bar is also optimized as 55cm. This distance depends on the shape of the shadow bar.

3. Simulation Result

We carried out four numerical experiments with MCNP-5 using S1 and S2. Practically, for each shadow bar, two experiments were performed with and without the target plate. F4 tally was used to calculate the reaction rate of Nb foil.

In the design, we considered six paths of neutrons to the Nb foil in order to extract the contribution of large angle scattered neutrons. The separation is shown in Fig.7. Neutron ① only passes through the shadow bar, ② passes the shadow bar and reflect in the target plate, ③ reflects only in the target plate, ④ reflects in the wall and reach the Nb foil via the shadow bar, ⑤ reflects in the wall and reach the Nb foil via the target plate and ⑥ reflects only in the wall. The large angle scattered neutrons are neutron ③ and we finally determine the contribution of neutron ③ by the four experiments.

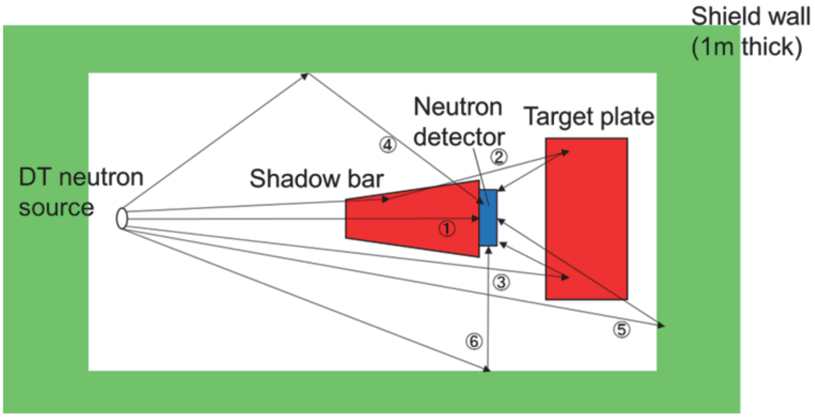

Fig.7 Separation of the paths of neutrons

Table 1 shows an example of calculation summary in case of using JENDL-4.0. Suffix “it” and “nt” means experiments with and without the target plate, respectively. The numbers ①~⑥ correspond to the separated path of neutrons shown in Fig.7.

Table 1 Reaction rate in each experiment using JENDL-4.0 (unit: reaction/source neutron)

	S1it	S2it	S1nt	S2nt	S1it - S1nt	S1it - S2it - (S1nt - S2nt)
①	0.02×10^{-9}	0.12×10^{-9}	0.01×10^{-9}	0.12×10^{-9}	0.01×10^{-9}	0.01×10^{-9}
②	0.10×10^{-9}	0.01×10^{-9}	0	0	0.09×10^{-9}	0.09×10^{-9}
③	4.04×10^{-9}	0	0	0	4.04×10^{-9}	4.04×10^{-9}
④	1.01×10^{-9}	0.57×10^{-9}	1.02×10^{-9}	0.56×10^{-9}	-0.01×10^{-9}	-0.02×10^{-9}
⑤	1.05×10^{-9}	1.06×10^{-9}	2.98×10^{-9}	2.97×10^{-9}	-1.93×10^{-9}	-0.02×10^{-9}
⑥	0.75×10^{-9}	0.23×10^{-9}	0.81×10^{-9}	0.23×10^{-9}	-0.06×10^{-9}	-0.06×10^{-9}
sum	6.97×10^{-9}	1.99×10^{-9}	4.82×10^{-9}	3.88×10^{-9}	2.14×10^{-9}	4.04×10^{-9}

In our previous study, we tried to determine the contribution of large angle scattered neutrons by calculation of the reaction rate of Nb foil; (S1it)-(S1nt). However, as shown in Table 1, the contribution of neutron ⑤ still remains in case of (S1it)-(S1nt). Then in the present study, we designed shadow bar S2 and extracted the contribution of large angle scattered neutrons by these four experiments. The contribution of large angle scattered neutrons (③) is included in the foil of S1it. However, other contributions are also contained. The other contributions can be compensated because the contributions are contained in other three foils. As a result, the contribution of large angle scattered neutrons (③) can finally be deduced by the four Nb reaction rates with the equation; (S1it) - (S2it) - ((S1nt) - (S2nt)). By this calculation, other contributions still remain, but these are small enough compared to that of large angle scattered neutrons as shown in Table 1. Therefore, if we carry out these four experiments, we can determine the contribution of large angle scattered neutrons by a simple calculation of the four reaction rates of Nb foil.

Next we show a calculation summary in case of using ENDF/B-VII and JEFF-3.1 in Tables 2 and 3. By these results, the contribution of large angle scattered neutrons (③) was 4.04×10^{-9}, 6.26×10^{-9} and 3.85×10^{-9} (reaction/source) for JENDL-4.0, ENDF/B-Ⅶ and JEFF-3.1, respectively. The result indicates that a significant difference exists between ENDF/B-Ⅶ and others. We think we can make clear the cause of the difference by this measuring technique.

Table 2 Reaction rate in each experiment using ENDF/B-Ⅶ(unit: reaction/source neutron)

	S1it	S2it	S1nt	S2nt	S1it - S2it - (S1nt - S2nt)
①	0.01×10^{-9}	0.09×10^{-9}	0.01×10^{-9}	0.09×10^{-9}	0
②	0.23×10^{-9}	0.03×10^{-9}	0	0	0.20×10^{-9}
③	6.26×10^{-9}	0	0	0	6.26×10^{-9}
④	0.98×10^{-9}	0.62×10^{-9}	1.03×10^{-9}	0.62×10^{-9}	-0.05×10^{-9}
⑤	1.06×10^{-9}	1.11×10^{-9}	2.95×10^{-9}	2.97×10^{-9}	-0.03×10^{-9}
⑥	0.74×10^{-9}	0.24×10^{-9}	0.80×10^{-9}	0.23×10^{-9}	-0.07×10^{-9}
sum	9.28×10^{-9}	2.09×10^{-9}	4.79×10^{-9}	3.91×10^{-9}	6.31×10^{-9}

Table 3 Reaction rate in each experiment using JEFF-3.1(unit: reaction/source neutron)

	S1it	S2it	S1nt	S2nt	S1it - S2it - (S1nt - S2nt)
①	0.01×10^{-9}	0.10×10^{-9}	0.02×10^{-9}	0.10×10^{-9}	-0.01×10^{-9}
②	0.12×10^{-9}	0.02×10^{-9}	0	0	0.10×10^{-9}
③	3.85×10^{-9}	0	0	0	3.85×10^{-9}
④	1.03×10^{-9}	0.64×10^{-9}	1.03×10^{-9}	0.66×10^{-9}	0.02×10^{-9}
⑤	1.08×10^{-9}	1.09×10^{-9}	2.97×10^{-9}	2.98×10^{-9}	0
⑥	0.74×10^{-9}	0.24×10^{-9}	0.81×10^{-9}	0.25×10^{-9}	-0.06×10^{-9}
sum	6.83×10^{-9}	2.09×10^{-9}	4.83×10^{-9}	3.99×10^{-9}	3.90×10^{-9}

4. Conclusion

We finally designed and optimized the experimental system and procedure for benchmarking of large angle scattering reaction cross section. Now one of the four experiments with an iron target plate was already done. Continuously we will carry out other three experiments for the complete benchmarking of iron. Then, we will examine how the results of this experiment can contribute to improvement of the accuracy of the evaluated nuclear data libraries.

References

[1] Seiki Ohnishi *et al.*: “New integral experiments for large angle scattering cross section data benchmarking with DT neutron beam at JAEA/FNS”, *Fusion Engineering and Design*, **87**, pp. 695-699 (2012).

[2] K. Shibata, O. Iwamoto, T. Nakagawa, N. Iwamoto, A. Ichihara, S. Kunieda, S. Chiba, K. Furutaka, N. Otuka, T. Ohsawa, T. Murata, H. Matsunobu, A. Zukeran, S. Kamada, and J. Katakura: "JENDL-4.0: A New Library for Nuclear Science and Engineering," J. Nucl. Sci. Technol. 48(1), pp.1-30 (2011).

[3] K. Shibata, O. Iwamoto, T. Nakagawa, N. Iwamoto, A. Ichihara, S. Kunieda, S. Chiba, N. Otuka, and J. Katakura: "JENDL-4.0: A New Library for Innovative Nuclear Energy Systems," Proc. the 2010 International Conference on Nuclear Data for Science and Technology (ND2010), J. Korean. Phys. Soc., 59(23), pp.1046-1051 (2011).

[4] Arjan Koning et al.: “The JEFF-3.1 Nuclear Data Library” *JEFF report 21*, OECD (2006).

[5] M.B. Chadwick et al.: “ENDF/B-VII.0: Next Generation Evaluated Nuclear Data for Nuclear Science and Technology”, *Nucl. Data Sheets*, **102**, pp.2931-3060 (2006).

[6] N. Hayashi, S. Ohnishi, F. Sato, I. Murata, “Optimization of Experimental System Design for Benchmarking of Large Angle Scattering Reaction Cross section at 14 MeV Using A Shadow Bar”, *Proc. of the 2015 Symposium on Nucl. Data*, Nov. 19-20, 2015, Ibaraki Quantum Beam Research Center, Tokai-mura, Ibaraki, Japan, JAEA-Conf 2016-004(INDC(JPN)-202), pp. 205-210 (2016).

27 Verification and Estimation of Thermal Neutron Capture Cross Section of ^{102}Ru

Atsunori TERASHIMA[1,2,]*, Mikael NILSSON[2], Masaki OZAWA[3], Satoshi CHIBA[3]
[1]Department of Nuclear Engineering, Graduate School of Science and Engineering, Tokyo Institute of Technology,
2-12-1-N1-9 Ookayama, Meguro-ku, Tokyo 152-8550, Japan
[2]Department of Chemical Engineering and Materials Science, The Henry Samueli School of Engineering,
University of California, Irvine, 916 Engineering Tower, Irvine, CA 92697-2575, USA
[3]Laboratory for Advanced Nuclear Energy, Institute for Innovative Research, Tokyo Institute of Technology,
2-12-1-N1-9 Ookayama, Meguro-ku, Tokyo 152-8550, Japan
*e-mail: terashima.a.aa@m.titech.ac.jp

The Aprés ORIENT research program proposes to create valuable elements by nuclear transmutation of fission products in nuclear reactors. Although the uncertainty of the reaction rate of ^{102}Ru(n, γ)^{103}Ru would become important to estimate the efficiency of such transmutation around light platinum group elements, there is a big deviation of the evaluated value of thermal neutron capture cross section of ^{102}Ru between JENDL-4.0 and other evaluated nuclear data libraries. In this study, both the neutron activation analysis on ^{102}Ru(n, γ)^{103}Ru and the corresponding burnup calculation had been performed for verification of the evaluated values in each library. As a relative C/E evaluation, proposed in this paper, of the number density of ^{103}Ru created by the neutron capture reaction of ^{102}Ru, the possibility was pointed out that the evaluated value of thermal neutron capture cross section of ^{102}Ru in JENDL-4.0 could be overestimated more than 20%. Then, based on the C/E values obtained in this study, it was estimated as 1.204±0.059 b. This estimated value roughly supported both JENDL/AD-201X (1.178 b) and the latest measured value (1.241(1) b).

1. Introduction

The Après ORIENT research program [1] is aiming at creating stable, highly-valuable elements (defined as secondary nuclear rare metals; NRMs) by nuclear transmutation from fission products (FPs) separated from spent nuclear fuels. In our previous studies [2, 3] to analyze the efficiency of creation of NRMs and to estimate the radioactivity of created NRMs by (n, γ) reaction followed by β^- decay of FPs in nuclear reactors, a simple burnup calculation had been performed by using ORLIBJ40 package [4]. Then, as a comprehensive evaluation of created NRMs from viewpoints of the efficiency of transmutation, the radioactivity of products, and importance of products as resources, light platinum group elements were specially selected as most important NRMs, which should be much researched in the future works for realization of this advanced nuclear fuel cycle [3].

For such future works, the uncertainty of ^{102}Ru(n, γ)^{103}Ru would become one of the most important quantities to estimate the efficiency of such transmutation around light platinum group elements. However, as shown in Figure 1, it was found that there was a big deviation of the evaluated value of thermal neutron capture cross section of ^{102}Ru between JENDL-4.0 [5] and other evaluated nuclear data libraries. In addition, from Figure 1, it turned out that there was also a big deviation among measured or evaluated values recorded in EXFOR [6]. Thus, a precise measurement of the cross section and verification of these evaluated values in each library are strongly required. Therefore, in the present study, both the neutron activation analysis for Ru and the corresponding burnup calculation were performed for verification of these evaluated values of thermal neutron capture cross section in each evaluated nuclear data library and for estimation of the much probable value of it.

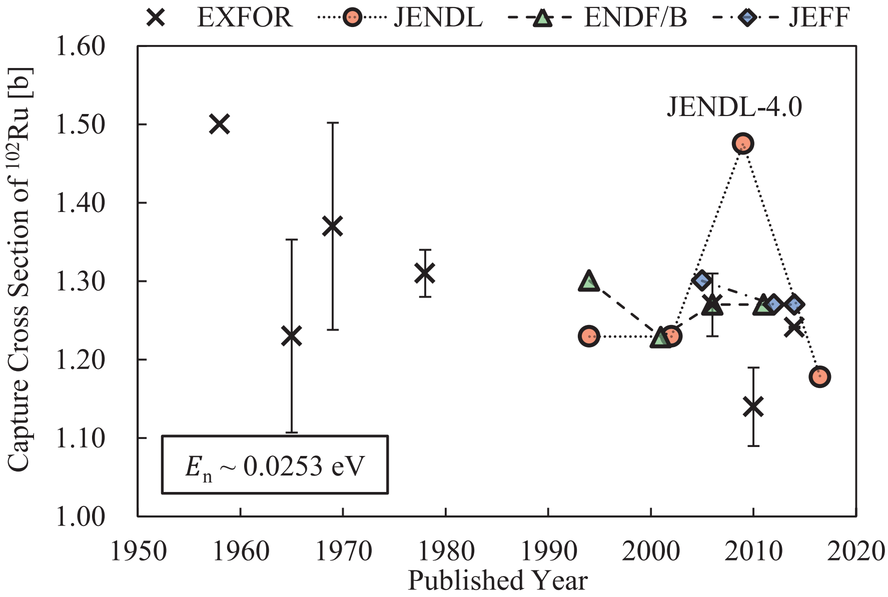

Figure 1: Transition and comparison of the thermal neutron capture cross section data of ^{102}Ru. The latest data of JENDL is based on JENDL/AD-201X [7].

2. Methods

2.1 Irradiation experiment

A solution containing approximately 1,000 ppm of cation of Ru in dilute nitric acid was prepared from Ru atomic absorption standard solution (Fluka). 1mL of it was put in a short poly vial EP338-NAA (LA Container), and then it was also put in a long poly vial EP290-NAA (LA Container). Moreover, it was put in a dedicated polyethylene container for the TRIGA® reactor at University of California, Irvine (UC Irvine).

For the position of the targets in the TRIGA reactor, the rotary rack facility was selected, which is slowly rotated around just outside the reactor core but inside the graphite reflector surrounding the core. Then, thermal neutron flux is dominant at the position. The target was irradiated in the facility for 1 hour at 250 kW, which was stationary maximum thermal power of TRIGA reactor at UC Irvine.

After irradiation, gamma rays accompanying radioactive decay of ^{103}Ru (E_γ = 497.1 keV) and ^{105}Ru (E_γ = 724.3 keV) were measured by a high-purity Germanium (HPGe) detector GC4018 (CANBERRA) and analyzed by gamma analysis software Genie 2000 (CANBERRA). From the count per second of the representative gamma ray, the number of nucleus of each radioactive nuclide at the time of the end of the irradiation was calculated based on their decay history and the detector efficiency calibration.

From the measurement of the gamma rays accompanying radioactive decay of ^{103}Ru (^{105}Ru), the number density of ^{103}Ru (^{105}Ru) $N(t_i)$ [/cm^3] at the time of the end of the irradiation t_i [s] was calculated by equation (1);

$$N(t_i) = \frac{1}{\lambda} \times \frac{CPS(t_d)}{I \times \varepsilon} \times \exp[\lambda\{t_d - t_i\}] \times \frac{\lambda\{t_c - t_d\}}{1 - \exp[-\lambda\{t_c - t_d\}]} \quad . \quad (1)$$

where, t_d [s] is the time of the beginning of the counting the gamma ray, t_c [s] is the time of the end of the counting the gamma ray, I [%] is the intensity of the gamma ray from ^{103}Ru (^{105}Ru) [8], λ [/s] is the decay constant of ^{103}Ru (^{105}Ru) [8], and ε [%] is the efficiency of the detector depending on the position and the shape of the sample and energy of the gamma ray. It should be noted, in this paper, following four uncertainties were considered; from experiment, (i) count per second *CPS* and (ii) detector efficiency ε; from nuclear data, (iii) intensity I and (iv) decay constant λ.

2.2 Burnup calculation

In accordance with the above condition of the irradiation experiment by using TRIGA reactor at UC Irvine, a predictive simulation was performed by using MVP-BURN code [9] with a burnup calculation module added to 3-dimensional Monte Carlo code based on continuous energy methods; MVP-III (beta-version) [10]. The 3-dimensional geometry in the simulation was constructed based on the actual reactor design [11-13]. Main information for burnup calculation in this paper was summarized in Table 1. It should be noted that the burnup chain data of MVP-BURN (ChainJ40; u4cm6fp119bp14T_J40) was modified around target nuclides in order to handle the radioactive nuclides with short half-life. It enabled to reproduce the experiment of neutron activation analysis on short-lived radioactive nuclides by MVP-BURN code.

Basically, MVPlib_nJ40 [14] based on JENDL-4.0 was used as a cross section library of all nuclides. On the other hand, for ^{104}Ru in the target region, not only MVPlib_nJ40 but also MVPlib_nB70 based on ENDF/B-VII.0 [15] were especially used. Moreover, for ^{102}Ru in the same region, 8 libraries were used such as MVPlib_nJ40, MVPlib_nB70, MVPlib_nJ33 [16] based on JENDL-3.3 [17], JENDL/AD-201X which is a new activation cross section file for decommissioning of LWRs [7], and 4 modified libraries based on JENDL-4.0. These modified libraries with the same energy of the only negative resonance to JENDL-4.0 and the different width of it had made by the authors. A difference among these 4 libraries and JENDL-4.0 is almost only the value of thermal neutron capture cross section. It should be noted that from Table 2, for ^{102}Ru and ^{104}Ru, the combination of JENDL-4.0 and ENDF/B-VII.0 enables to compare among three latest evaluated libraries such as JENDL-4.0, ENDF/B-VII.1 [18], and JEFF-3.2 [19].

The number of history of neutron per batch was 160,000, and the number of skip batch and effective batch were 100 and 1,000, respectively. The number of burnup step was 1 per hour. The number of sub-step was 120 per burn step. In the above calculation condition, the number of nucleus of each the corresponding radioactive nuclide, namely ^{103}Ru and ^{105}Ru, at the time of the end of the irradiation was calculated.

Table 1: Main information for burnup calculation in this paper

Code	MVP-BURN (MVP-III beta-version, 64bit MPI, 8CPU)				
Burnup chain data	ChainJ40 (u4cm6fp119bp14T_J40) modified around Ru to handle the radioactive isotopes with short half-lives				
Input parameter	The number of neutron history				16,000 / batch
	The number of skipped batch				100
	The number of effective batch				1,000
	The number of burn step				1 / hour
	The number of sub-step				120 / burn step
Averaging	3 cases using the deferent initial random number				
Calculated quantity	The number density of created ^{103}Ru and ^{105}Ru at t_i				
Considered uncertainty	Statistical error of the calculated number density of ^{103}Ru and ^{105}Ru				
Cross section library	Nuclide	Library		σ_c (0.0253eV)	MVPlib
	^{102}Ru	JENDL-4.0		1.475 b	MVPlib_nJ40
		Modified	#1	1.234 b	➤Based on JENDL-4.0
			#2	1.214 b	➤Changing the nega. res. para.
			#3	1.197 b	➤Made by LICEM [14,16]
			#4	1.164 b	(ENDF file -> MVPlib)
		JENDL/AD-201X		1.178 b	Made by LICEM
		JENDL-3.3		1.230 b	MVPlib_nJ33
		ENDF/B-VII.0		1.270 b	MVPlib_nB70
	^{104}Ru	JENDL-4.0		0.469 b	MVPlib_nJ40
		ENDF/B-VII.0		0.472 b	MVPlib_nB70
	Others	JENDL-4.0			MVPlib_nJ40

Table 2: Comparison of the evaluating laboratory and thermal neutron capture cross section of ^{102}Ru, ^{104}Ru, and ^{96}Ru in three latest evaluated nuclear data libraries and JENDL-3.3

	Laboratory having evaluated the nuclear data Thermal neutron capture cross section [b]		
	JENDL-4.0 (JENDL-3.3)	ENDF/B-VII.1	JEFF-3.2
^{102}Ru	JNDC	CNDC	CNDC
	1.48 (1.230)	1.27 same to ENDF/B-VII.0	1.27 same to ENDF/B-VII.0
^{104}Ru	JNDC	CNDC	CNDC
	0.469 (0.328)	0.472 same to ENDF/B-VII.0	0.472 same to ENDF/B-VII.0
^{96}Ru	JNDC	JNDC	NEA
	0.271 (0.290)	0.290 same to JENDL-3.3	0.249

2.3 Relative C/E evaluation of ^{102}Ru$(n, \gamma)^{103}$Ru reaction normalized by ^{104}Ru$(n, \gamma)^{105}$Ru reaction

As the concentration of cation of Ru in the atomic absorption standard solution was not good precision, correcting the concentration is required before comparison between calculation and experiment. As one method of the correction, the relative evaluation can be applied, which the reaction rate of an isotope is normalized by that of another isotope.

From Table 2, the thermal neutron capture cross section of ^{104}Ru has comparatively small difference as 1% among three latest evaluated libraries. Thus, even if another evaluated library as standard for the relative evaluation is used, only a little change from the default result could be caused. Therefore, in the present study, ^{104}Ru$(n, \gamma)^{105}$Ru reaction was used as a normalization factor for ^{102}Ru$(n, \gamma)^{103}$Ru reaction. Then, the relative simulated value $^{A}C_{\mathrm{rel}}$ of the number density of ^{A}Ru was defined by the following equations;

$${}^{105}_{\ \ j}C_{\mathrm{rel},i} \equiv {}^{105}E\ , \qquad {}^{103}_{\ \ j}C_{\mathrm{rel},i} \equiv {}^{103}_{\ \ j}C_{i} \times \frac{{}^{105}E}{{}^{105}_{\ \ j}C_{i}}\ . \quad (2\text{ and }3)$$

where, ^{A}C is the number density of ^{A}Ru calculated by MVP-BURN code, ^{A}E is the number density of ^{A}Ru measured by the neutron activation analysis, and index i and j indicate the name of the used cross section library for ^{102}Ru and ^{104}Ru, respectively. As a result of this normalization, it could be considered that some errors between ^{103}C and ^{103}E were disappeared such as for the concentration of Ru and for the neutron flux at the sample region.

3. Results and Discussion

As a result of the relative C/E evaluation of the number density of ^{103}Ru, a deviation between the values of ($^{103}C_{\mathrm{rel}}/^{103}E$-1) using the same library for ^{102}Ru and the different libraries for ^{104}Ru were lower than 1 % in any cases. Thus, it could be permitted to average these 2 C/E values using the different libraries for ^{104}Ru (JENDL-4.0 and ENDF/B-VII.0). In this paper, these averaged C/E value named as X was defined by equation (4);

$$X_i \equiv \frac{1}{2}\left\{\left(\frac{{}^{103}_{\mathrm{J40}}C_{\mathrm{rel},i}}{{}^{103}E_i} - 1\right) + \left(\frac{{}^{103}_{\mathrm{B70}}C_{\mathrm{rel},i}}{{}^{103}E_i} - 1\right)\right\} = \frac{1}{2}\frac{{}^{105}E_i}{{}^{103}E_i}\left(\frac{{}^{103}_{\mathrm{J40}}C_i}{{}^{105}_{\mathrm{J40}}C_i} + \frac{{}^{103}_{\mathrm{B70}}C_i}{{}^{105}_{\mathrm{B70}}C_i}\right) - 1\ . \quad (4)$$

Then, comparison of each X value is shown in Figure 2.

From Figure 2, it turned out that the evaluated value of thermal neutron capture cross section of ^{102}Ru in JENDL-4.0 could be overestimated more than 20% because the Maxwellian distribution of thermal neutron spectrum is dominant in the target area. In addition, the evaluated value in ENDF/B-VII.0 could be also overestimated approximately 7%. On the other hand, the range of the error bar of X value in the case of JENDL/AD-201X included $X = 0\%$ although the X value was slightly lower than 0%. Therefore, it could be considered that the evaluated value of thermal neutron capture cross section of ^{102}Ru in JENDL/AD-201X was much more reasonable than those in JENDL-4.0 and ENDF/B-VII.0, namely three latest evaluated nuclear data libraries such as JENDL-4.0, ENDF/B-VII.1, and JEFF-3.2.

Finally, as the results of 4 X values in the cases of Modified#1-4, it could be predicted that the value of thermal neutron capture cross section of ^{102}Ru around 1.20 b would make the X value 0%. Then, estimation of the much probable value of thermal neutron capture cross section of ^{102}Ru was performed using these X values. From comparison between X_i and the corresponding value of thermal neutron capture cross section of ^{102}Ru $\sigma_{\mathrm{c,th},i}$, it turned out that there was a good linear relation in the cases of 7 libraries based on JENDL, which libraries have only the difference in the negative resonance parameter of ^{102}Ru. Thus, one estimated value of thermal neutron capture cross section of ^{102}Ru ${}^{\mathrm{est}}\bar{\sigma}_{\mathrm{c,th}}$ was calculated using these 7 X values except for that based on ENDF/B-VII.0 by the following equations;

$$ {}^{\mathrm{est}}\sigma_{\mathrm{c,th},i} \equiv \frac{\sigma_{\mathrm{c,th},i}}{(1+X_i)},\ \left(\Delta {}^{\mathrm{est}}\sigma_{\mathrm{c,th},i}\right)^2 \equiv \left(\frac{\partial {}^{\mathrm{est}}\sigma_{\mathrm{c,th},i}}{\partial X_i}\right)^2 (\Delta X_i)^2\ , \tag{5} $$

$$ {}^{\mathrm{est}}\bar{\sigma}_{\mathrm{c,th}} \equiv \frac{\sum_{i=1}^{n} {}^{\mathrm{est}}\sigma_{\mathrm{c,th},i}}{n},\ \left(\Delta {}^{\mathrm{est}}\bar{\sigma}_{\mathrm{c,th}}\right)^2 \equiv \frac{\sum_{i=1}^{n}\left(\Delta {}^{\mathrm{est}}\sigma_{\mathrm{c,th},i}\right)^2}{n}\ . \tag{6} $$

Then, the estimated value was 1.204±0.059 b, which roughly supported both JENDL/AD-201X (1.178 b) and the latest measured value (1.241(1) b) [20].

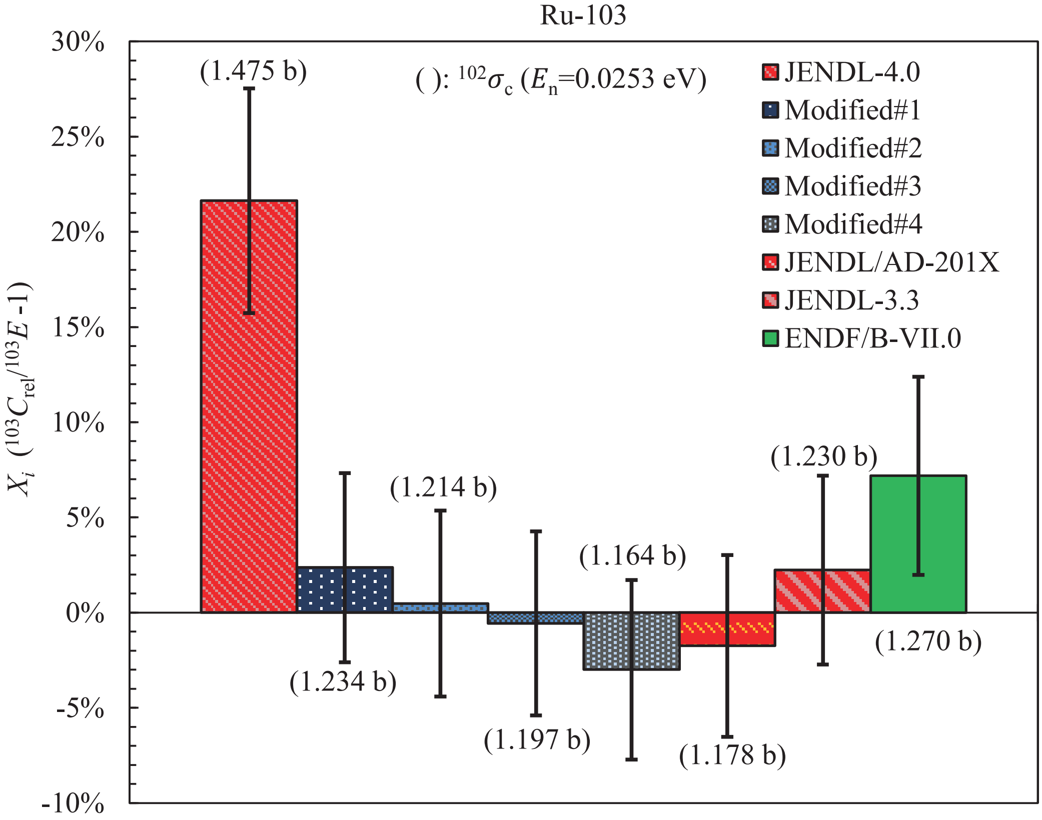

Figure 2: Comparison of the C/E values of the number density of ^{103}Ru created by capture reaction of ^{102}Ru in the case of using each library. The value in the brackets means the corresponding value of thermal neutron capture cross section of ^{102}Ru in the library.

4. Conclusion

Both a burnup calculation using MVP-BURN code and the neutron activation analysis on Ru at UCI-TRIGA reactor had been performed. As a relative C/E evaluation of the number density of ^{103}Ru created by ^{102}Ru(n, γ)^{103}Ru reaction normalized by ^{104}Ru(n, γ)^{105}Ru reaction, the possibility was pointed out that the evaluated value of thermal neutron capture cross section of ^{102}Ru in JENDL-4.0 could be overestimated more than 20%. On the other hand, it turned out that the evaluated value in JENDL/AD-201X could be much reasonable although the relative C/E value was slightly lower than 0%. Based on 7 values of C/E except for the case of ENDF/B-VII.0, the thermal neutron capture cross section of ^{102}Ru was estimated as 1.204±0.059 b. This estimated value roughly supported both JENDL/AD-201X (1.178 b) and the latest measured value (1.241(1) b).

Acknowledgement

The authors would like to sincerely thank Dr. Yasunobu Nagaya (Japan Atomic Energy Agency) for his many more technical advices about calculation by MVP code. This work was a part of the research supported by JSPS KAKENHI Grant Number 15J12066 (Grant-in-Aid for JSPS Fellows) and Academy for Co-creative Education of Environment and Energy Science (ACEEES), Tokyo Institute of Technology, Japan.

References

[1] M. Ozawa, C. Y. Han, T. Kaneshiki, M. Nilsson: “Aprés ORIENT, A P&T-based New Resource Strategy in Nuclear Fuel Cycle,” Proc. Int. Nuclear Fuel Cycle Conf. (GLOBAL 2013), Sep.29-Oct.3, 2013, Salt Lake City, Utah, USA, pp.1499-1503 (2013).
[2] A. Terashima, M. Ozawa: *Nucl. Sci. Tech.* **26**, S010311 (2015).
[3] A. Terashima, M. Ozawa: *Prog. Nucl. Energy* **93**, 177-185 (2016).
[4] K. Okumura, K. Sugino, K. Kojima, T. Jin, *et al.*: “A Set of ORIGEN2 Cross Section Libraries Based on JENDL-4.0: ORLIBJ40,” JAEA-Data/Code 2012-032 (2013).
[5] K. Shibata, O. Iwamoto, T. Nakagawa, N. Iwamoto, *et al.*: *J. Nucl. Sci. Technol.* **48**, 1-30 (2011).
[6] Experimental Nuclear Reaction Data (EXFOR) Database Version of 2016-12-12, IAEA, https://www-nds.iaea.org/exfor/exfor.htm (Last access: Dec. 28, 2016).
[7] K. Shibata, N. Iwamoto, S. Kunieda, F. Minato, *et al.*: “Activation Cross-section File for Decommissioning of LWRs,” JAEA-Conf 2016-004, pp.47-52 (2016).
[8] Live Chart of Nuclides, IAEA, https://www-nds.iaea.org/relnsd/vcharthtml/VChartHTML.html (Last access: Dec. 28, 2016).
[9] K. Okumura, T. Mori, M. Nakagawa, K. Kaneko: *J. Nucl. Sci. Technol.* **37**, 128-138 (2000).
[10] Y. Nagaya, K. Okumura, T. Mori, M. Nakagawa: “MVP/GMVP : General Purpose Monte Carlo Codes for Neutron and Photon Transport Calculations based on Continuous Energy and Multigroup Methods,” JAERI 1348 (2005).
[11] J. R. Humphries: “TRIGA Mark I 250-kW Pulsing Reactor Mechanical Maintenance and Operating Manual for The University of California, Irvine,” GA 9389 (1969).
[12] G. E. Miller: “Safety Analysis Report Revision 1,” University of California, Irvine (1999).
[13] J. Crozier: “Nuclear Analysis of the University of California – Irvine TRIGA® Reactor,” GA 911196 (2010).
[14] K. Okumura, Y. Nagaya: “Production of Neutron Cross Section Library based on JENDL-4.0 to Continuous-energy Monte Carlo Code MVP and Its Application to Criticality Analysis of Benchmark Problems in the ICSBEP Handbook,” JAEA-Data/Code 2011-010 (2011).
[15] M. B. Chadwick, P. Obložinský, M. Herman, N. M. Greene, *et al.*: *Nucl. Data Sheets* **107**, 2931-3060 (2006).
[16] T. Mori, Y. Nagaya, K. Okumura, K. Kaneko: “Production of MVP Neutron Cross Section Libraries Based on the Latest Evaluated Nuclear Data Files,” JAERI-Data/Code 2004-011 (2004).
[17] K. Shibata, T. Kawano, T. Nakagawa, O. Iwamoto, *et al.*: *J. Nucl. Sci. Technol.* **32**, 1125-1136 (2002).
[18] M. B. Chadwick, M. Herman, P. Obložinský, M. E. Dunn, *et al.*: *Nucl. Data Sheets* **112**, 2887-2996 (2011).
[19] JEFF-3.2 evaluated data library - Neutron data, OECD-NEA, https://www.oecd-nea.org/dbforms/data/eva/evatapes/jeff_32/ (Last access: Dec. 28, 2016).
[20] F. F. Arboccò, P. Vermaercke, K. Smits, L. Sneyers, *et al.*: *J. Radioanal. Nucl. Chem.* **302**, 655-672 (2014).

28 Activation cross sections of alpha-induced reactions on natural zinc for ^{68}Ge production

M. Aikawa[1], M. Saito[1], S. Ebata[1], Y. Komori[2], H. Haba[2]
[1] Graduate School of Science, Hokkaido University, Sapporo 060-0810, Japan
[2] Nishina Center for Accelerator-Based Science, RIKEN, Wako 351-0198, Japan
e-mail: aikawa@sci.hokudai.ac.jp

Germanium-68 ($T_{1/2}$ = 270.95 d) is a generator of a positron emitter, ^{68}Ga ($T_{1/2}$ = 67.71 min), which is available for the positron emission tomography (PET). Two independent cross section measurements are available for the $^{\mathrm{nat}}$Zn(α,x)^{68}Ge reaction, however the amplitudes are slightly different from each other. Therefore, we measured cross sections of the alpha-induced reactions on natural zinc for the ^{68}Ge production using the stacked foil technique and the activation method. The experiment was performed using a 51.5-MeV alpha beam at the RIKEN AVF cyclotron. The derived cross sections were compared with the previous experimental data and theoretical calculations. Our results show slightly larger amplitude than the previous data at the peak although the position at around 30 MeV is consistent with them.

1. Introduction

A variety of radioactive isotopes are used in nuclear medicine for therapy and diagnosis. A positron emitter, ^{68}Ga ($T_{1/2}$ = 67.71 min), is available for the positron emission tomography (PET) [1]. In addition to ^{68}Ga, the production of its long-lived parent, ^{68}Ge ($T_{1/2}$ = 270.95 d), is worthy of investigation for production of a ^{68}Ga generator [2]. A possible reaction route to produce ^{68}Ge (Z = 32) is alpha-induced reactions on zinc isotopes (Z = 30). The alpha capture reactions on ^{64}Zn have energetically been investigated due to interests in astrophysics [3-4] and nuclear physics [5-8]. However, the cross sections of the capture reaction are very small (less than a few mb). On the other hand, cross sections of the alpha-induced reactions on natural zinc exceed 100 mb at the peak around 30 MeV incident energy [9,10]. However, the amplitudes of the previous data are slightly different from each other. We therefore measured cross sections of the alpha-induced reactions on natural zinc for ^{68}Ge production.

2. Method

The experiment was performed at the AVF cyclotron of the RIKEN RI Beam Factory by using the stacked foil technique and the activation method. Natural zinc foils (purity: 99.9%, Nilaco, Japan) were used with ^{nat}Ti monitor foils (purity: 99.6%, Nilaco, Japan). The thicknesses of the Zn and Ti foils were estimated from measured area and weight of large foils (50 × 50 mm^2 and 50 × 100 mm^2) and found to be 18.64 mg/cm^2 and 2.25 mg/cm^2, respectively. The stacked target consisted of 14 sets of the Zn-Ti-Ti foils (8 × 8 mm^2) cut off from the large foils. The Ti monitor foils at the downstream side of the beam is assumed to compensate losses of recoil products. The target was irradiated for 2 hours by a 51.5-MeV alpha beam with the average intensity of 41.0 pnA, which was measured by a Faraday cup. The beam energy was measured by the time-of-flight method using a plastic scintillator monitor [11]. The γ-lines from the irradiated foils were measured by HPGe detectors.

Table 1: Reaction and decay data of ^{68}Ge and ^{68}Ga [12,13]

Nuclide	Half-life	Decay mode (%)	E_γ (keV)	I_γ (%)	Contributing reaction	Q-value (keV)
^{68}Ge	270.95 d	EC (100)			^{64}Zn(α,γ)	3399.9
					^{66}Zn(α,2n)	-15638.0
					^{67}Zn(α,3n)	-22690.3
					^{68}Zn(α,4n)	-32888.4
					^{70}Zn(α,6n)	-48588.9
^{68}Ga	67.71 min	EC+β^+ (100)	1077.34	3.22	^{68}Ge(ε)	

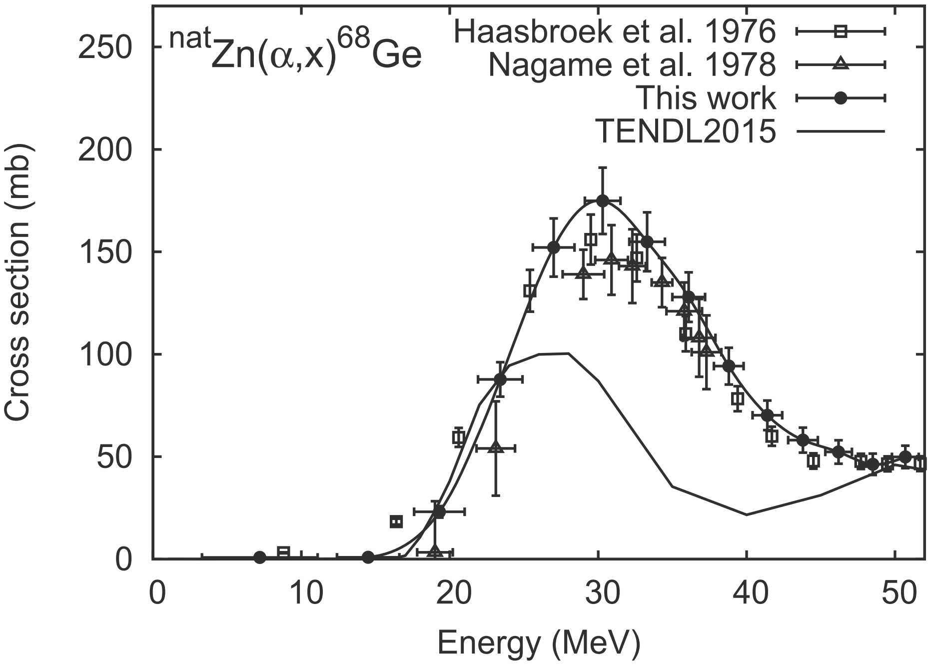

Fig. 1: The excitation function of the ^{nat}Zn(α,x)^{68}Ge reaction. The result is compared with the previous experimental data [9,10] and TENDL-2015 [14].

3. Result

The reaction and decay data [12,13] are summarized in Table 1. The measurement of the 1077.34 keV γ-line (3.22%) from the ^{68}Ga decay, which was in equilibrium with that of its parent ^{68}Ge, was performed after a long cooling time of about 80 days. Each Zn foil with its Ti catcher foil was simultaneously measured to collect the recoiling products. In the cooling time, all ^{68}Ga produced directly through the ^{nat}Zn(α,x) reaction could be considered to decay out completely. The cross sections derived from the measurement is shown in Fig. 1 together with the previous experimental data (open squares and triangles) [9,10] and the TENDL-2015 data (dashed line) [14]. The result shows slightly different from the previous data, although the peak position at around 30 MeV is consistent with them. On the contrary, the TENDL-2015 data shows different tendency from the experimental data probably due to underestimation of the contribution from the ^{67}Zn(α,3n) reaction.

4. Summary

We performed the experiment of the alpha-induced reactions on natural zinc to produce ^{68}Ge, a generator of a positron emitter, ^{68}Ga. The excitation function of the ^{nat}Zn(α,x)^{68}Ge reaction was measured up to 51.5 MeV and found that the peak position is consistent with previous experiments.

Acknowledgements

This work was performed at the RI Beam Factory operated by the RIKEN Nishina Center and CNS, University of Tokyo.

References

[1] Banerjee SR, Pomper MG. Clinical applications of Gallium-68. Appl. Radiat. Isot. 2013;76:2-13.

[2] Rösch F. Past, present and future of ^{68}Ge/^{68}Ga generators. Appl. Radiat. Isot. 2013;76:24-30.

[3] Basunia MS, Shugart HA, Smith AR, *et al*. Measurement of cross sections for a-induced reactions on ^{197}Au and thick-target yields for the (α,γ) process on ^{64}Zn and ^{63}Cu. Phys. Rev. C 2007;75:015802.

[4] Gyürky G, Mohr P, Fülöp Z, *et al*. Relation between total cross sections from elastic scattering and α-induced reactions: The example of ^{64}Zn. Phys. Rev. C 2012;86:041601.

[5] Porile NT. Excitation Functions for Alpha-Induced Reactions on Zinc-64. Phys. Rev. 1959;115:939-948.

[6] Ruddy FH, Pate BD. FORMATION AND DECAY OF THE COMPOUND NUCLEUS ^{68}Ge (I). Experiment and the independence hypothesis. Nucl. Phys. A 1969;127:305-322.

[7] Di Pietro A, Figuera P, Amorini F, *et al*. Reactions induced by the halo nucleus 6He at energies around the Coulomb barrier. Phys. Rev. C 2004;69:044613.

[8] Scuderi V, Di Pietro A, Figuera P, *et al*. Fusion and direct reactions for the system ^{6}He + ^{64}Zn at and below the Coulomb barrier. Phys. Rev. C 2011;84:064604.

[9] Haasbroek FJ, Burdzik GF, Cogneau M, *et al*. Excitation functions and thick-target yields for Ga-67, Ge-68/Ga-68, Cd-109 and In-111 induced in natural zinc and silver by 100 MeV alpha particles. Council for Scientific and Industrial Research (Pretoria); 1976. (Report FIS 91).

[10] Nagame Y, Unno M, Nakahara H, *et al*. Production of ^{67}Ga by Alpha Bombardment of Natural Zinc. Appl. Radiat. Isot. 1978;29:615-619.

[11] Watanabe T, Fujimaki M, Fukunishi N, *et al*. BEAM ENERGY AND LONGITUDINAL BEAM PROFILE MEASUREMENT SYSTEM AT THE RIBF. Proc. 5th Int. Part. Accel. Conf. (IPAC2014) 2014:3566-3568.

[12] NuDat 2.6. National Nuclear Data Center; Available from: http://www.nndc.bnl.gov/nudat

[13] Q-value calculator. National Nuclear Data Center; Available from: http://www.nndc.bnl.gov/qcalc

[14] TENDL-2015: TALYS-based evaluated nuclear data library, Available from: https://tendl.web.psi.ch/tendl_2015/tendl2015.html

29 Development of an artificial neural network code for unfolding neutron spectra measured by multiple foils activation method

Yukimasa SANZEN[1], Tadahiro KIN[1], Masaki KAMIDA[1], Katsumi AOKI[2],
Naoto ARAKI[2], Yukinobu WATANABE[1]
[1]*Department of Advanced Energy Engineering Science, Kyushu University*
[2]*Faculty of engineering, Kyushu University*
E-mail: kin@aees.kyushu-u.ac.jp

We have developed a new unfolding code based on artificial neural network (ANN) in order to derive neutron energy spectrum by the multiple foils activation method. In the ANN unfolding code, the backpropagation algorithm is used for learning process. The ANN code was applied to measurement of thick target neutron yield (TTNY) from a carbon target irradiated by 20-MeV deuterons. The resultant TTNY was compared with the TTNY derived by an existing unfolding code, GRAVEL as well as a theoretical model calculation. The present ANN result is found to be in good agreement with the GRAVEL result and the calculated one.

1. Introduction

Neutron irradiation is applied to various fields (e.g., nondestructive inspection, boron neutron capture therapy, and medical RIs production). Highly reliable neutron energy spectra are required for safety design and estimation of RI production yield. The neutron energy spectra are commonly measured by using multiple foils activation method and such neutron detectors as Bonner spheres and liquid scintillators. In the present work, we adopt the multiple foils activation method among them. Unfolding method is necessary to derive the neutron spectrum in the method. Production yields of N_i (i: reaction ID) can be expressed by the following equation:

$$N_i \approx \sum_j R_{ij}\phi_j \, , \tag{1}$$

where R_{ij} and ϕ_j are the production rate and neutron yield corresponding to the neutron energy group j. In the multiple foils activation method, the equation cannot be solved analytically because the number of the reactions of interest is generally less than the number of neutron energy group. Therefore, the unfolding method is necessary to derive the neutron spectrum ϕ.

Many unfolding techniques have so far been developed, e.g., the iterative approximation method, the maximum entropy method, and the Monte Carlo based method. However, there are still problems on initial guess dependency and error evaluation [1]. An unfolding code based on artificial neural network (ANN) technique has the potential to resolve the problems. We have developed a new ANN unfolding code and validated the code in the present work.

2. Artificial neural network

ANN is a mathematical model of the human brain and designed to “think” like human through learning process. Fig. 1 shows a schematic view of the mathematical model of a single neuron of ANN, where x is the input signal, w is the weight, Y is the output signal.

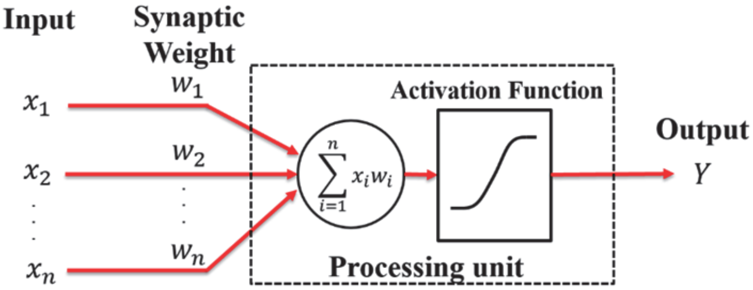

Fig. 1 Schematic view of the mathematical model of a single neuron

Each input signal x_i is weighted by w_i, and all of them are summed. An output signal of a neuron, Y is obtained as the output of a certain activation function f.

$$
\begin{aligned}
Y &= f(u) \\
&= f(\sum x_i w_i) \qquad (2)
\end{aligned}
$$

There are some activation functions (e.g., step function and sigmoid function and ramp function) as shown in Fig. 2.

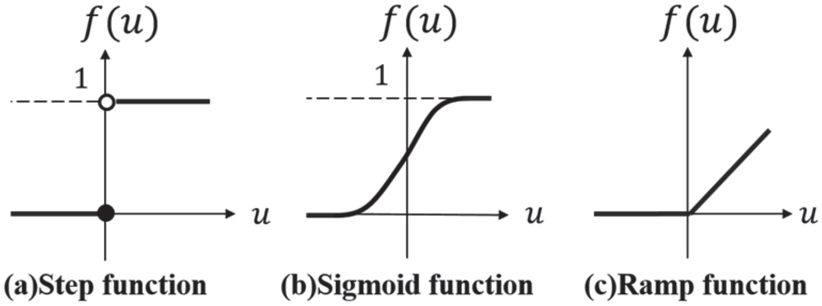

Fig. 2 Three examples of the general activation function used in the ANN

Neural network models consist of many artificial neurons. A schematic view of a generally applied ANN model, called the feedforward neural network, is shown in Fig. 3. The neural network system consists of an input layer, several hidden layers and an output layer. The input signals are propagated to only the forward direction (left to right).

To train the ANN, supervised learning technique is used. In the supervised learning, the training data including a set of input signals and the corresponding output signals are necessary. The output signal corresponding to the input signal of the training data is called the teacher signal.

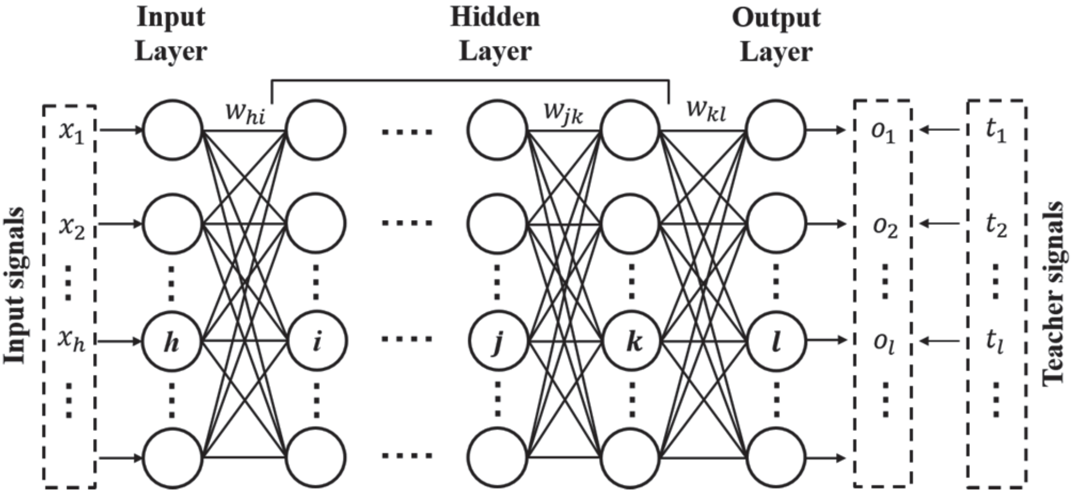

Fig. 3 Schematic view of a general architecture of the feedforward neural network

3. Development of unfolding code

3.1 Adopted ANN Model

We have developed an ANN unfolding code for the multiple foils activation method. Nuclear production yields at the end of irradiation (EOI) and neutron yields of each neutron energy group correspond to the input signals and the output signals of the ANN, respectively. The developed feedforward neural network has three layers as shown in Fig. 4. The sigmoid function was adopted as the activation function. To train the ANN, the backpropagation method [3] is used. In the algorithm, the weights are modified repeatedly based on the gradient descent method. To minimize the loss function $E(w)$, we use the following equation:

$$E(w) = \frac{1}{2}\sum(o_i - t_i)^2 \tag{3}$$

$$\Delta w = -\varepsilon \frac{\partial E}{\partial w} \tag{4}$$

where o_i is the output signal, t_i is the teacher signal, w is the weights, and ε is the learning rate. By modifying the weights through iterative calculation, the gradient of the loss function is close to zero. After the learning process is completed, the most probable weights are derived.

The learning parameters (e.g., learning rate, slope of sigmoid function, number of neurons of the hidden layer) are generally optimized by trial and error. We can obtain a solution of unknown output signals from measured input signals only with the completed ANN. Thus, the initial guess spectrum is unnecessary in the ANN unfolding method.

3.2 Validation of the Developed ANN Unfolding Code

To prepare the training dataset, firstly, random neutron spectra using Gaussian shaped functions were generated as teacher signals by the following equation:

$$f(x) = a \times \exp\left(-\frac{(x-\bar{x})^2}{2\sigma^2}\right) \tag{5}$$

where a is the magnitude, $\bar{x}$ is the position of the peak, σ is the standard deviation. To make multiple datasets, $a, \bar{x},$ and σ are randomly generated.

Secondly, the input signals were calculated by multiplying the neutron spectra by production rate function. The production rate of R_{ij} were calculated by following equation:

$$R_{ij} = \sigma_{ij} N_i Q \Omega \frac{1-e^{-\lambda t}}{\lambda t} \tag{6}$$

where R_{ij} is the production rate of reaction ID i and the neutron energy group j, σ_{ij} is the cross section of nuclide, N_i is the number of atoms at EOI, Q is the beam current, Ω is the solid angle of irradiation samples, λ is the decay constant of nuclide, and t is the beam irradiation time.

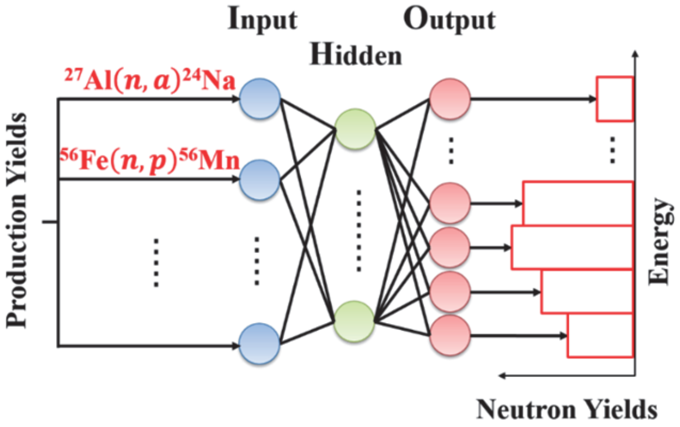

Fig. 4 Schematic view of the system of the developed ANN unfolding code

To validate the code, a test experiment with the multiple foils activation method was performed at Cyclotron and Radioisotope Center (CYRIC), Tohoku University. A carbon thick target was irradiated by 20-MeV deuterons to produce accelerator-based neutrons. By using the multiple foils activation method, the thick target neutron yield (TTNY) of the $\mathrm{C}(d,n)$ reaction at 20 MeV was obtained. The schematic diagram of the experimental system and the results of the nuclear production yields at EOI are shown in Fig. 5 and Table 1, respectively. The production yields obtained by the experiment were used as the input signals in the ANN unfolding code. The production rate functions are calculated using the cross sections stored in JENDL-4.0 [4]. The production rate functions are shown in Fig. 6. Since the production rate functions have an independent shape each other, they are appropriate to the unfolding method in the energy range of several to 20 MeV.

To train the ANN, five hundred Gaussian shaped neutron spectra were generated, and the production yields were calculated for each of the nine reactions. The weights were derived by repeating the calculation with the backpropagation method ten thousand times. The numbers of neurons in input, hidden, and output layers were 9, 30, and 101, respectively.

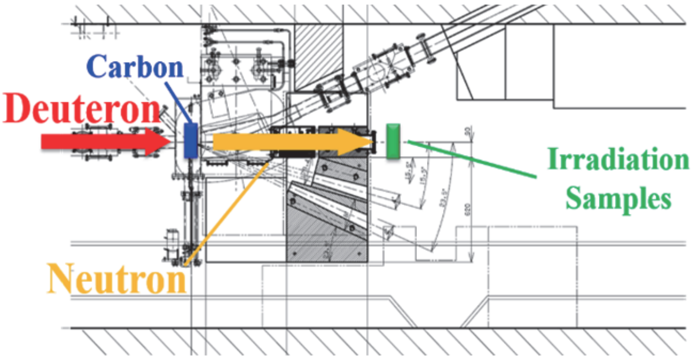

Fig.5 Schematic diagram of the experimental system

Table 1 The reactions used for unfolding process and the production yields at EOI

No.	Reaction	Yields
1	^{27}Al(n,a)^{24}Na	5.30(34) × 10^7
2	^{56}Fe(n,p)^{56}Mn	1.28(9) × 10^7
3	^{59}Co(n,a)^{56}Mn	1.90(13) × 10^7
4	^{59}Co(n,p)^{59}Fe	2.68(17) × 10^8
5	^{58}Ni(n,2n)^{57}Ni	1.24(9) × 10^7
6	^{64}Zn(n,p)^{64}Cu	6.91(51) × 10^8
7	^{67}Zn(n,p)^{67}Cu	7.59(53) × 10^6
8	^{96}Zr(n,2n)^{95}Zr	7.00(50) × 10^7
9	^{96}Mo(n,p)^{96}Nb	1.63(12) × 10^6

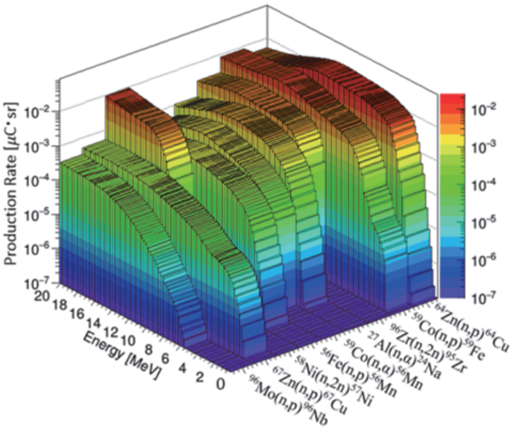

Fig. 6 Production rate functions for the interested reactions

4. Results and discussion

By using the completed ANN, the experimental yields shown in Table 1 were used as the input signals to obtain TTNY as the output signal. The obtained TTNY is shown with results of the GRAVEL code [5] and theoretical calculation by DEURACS [6] in Fig. 7. Note that, since DEURACS can accurately reproduce the TTNY in the present experimental condition, the calculated TTNY was used for the initial guess spectrum of the GRAVEL code. As a result, we found that the ANN result is in a good agreement with others.

Finally, we calculated production yields by folding the obtained TTNY with the production rate function for comparison with the experimental yields. The C/E value is shown in Fig. 8. Since the values distribute around 1.0, we concluded that the developed ANN code has sufficient ability to derive TTNY with the multiple foils activation method.

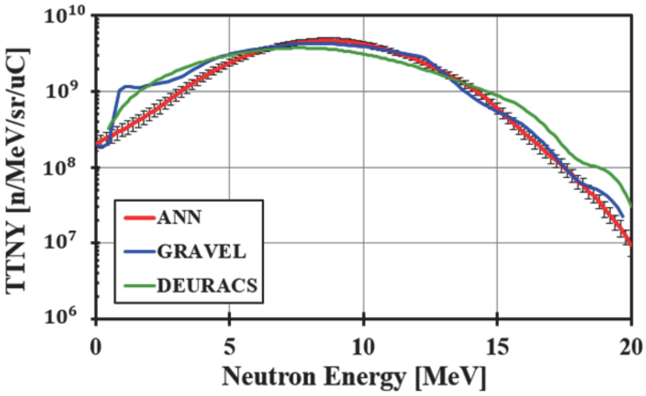

Fig. 7 The unfolded TTNY compared with the GRAVEL code and the DEURACS

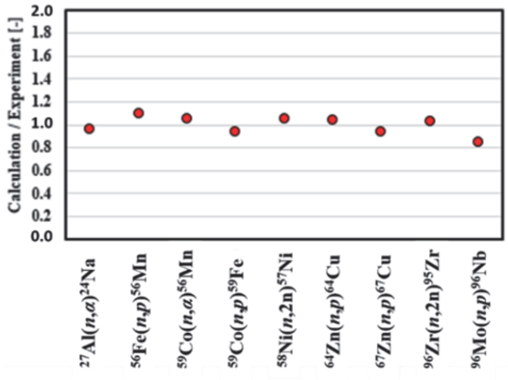

Fig. 8 The C/E value of the number of the atoms at EOI

5. Summary and conclusion

We have developed an artificial neural network (ANN) code for unfolding neutron spectra measured by multiple foils activation method. The ANN code was applied to measurement of thick target neutron yield (TTNY) from a carbon target irradiated by 20-MeV deuterons. To train the ANN, random neutron spectra using Gaussian shaped functions were used as teacher signals. We found that the result of ANN unfolding code is in a good agreement with that of the GRAVEL code and the calculation with DEURACS.

In the future, we plan to compare the TTNY obtained by the ANN unfolding code with the other experimental method (e.g., TOF method) for further validation of the code. Moreover, we will perform the optimization of the learning parameters and quantitative evaluation to improve the accuracy of final spectrum.

Reference

[1] M. Shigetaka, T. Iguchi, J. Nucl. Sci. Technol.,**10**, No. 2, 63-75 (2011).

[2] Warren S. McCulloch, Walter Pitts. Bulletion of Mathematical Biophysics, 5, 115 (1943).

[3] Rumelhart, David E.; Hinton, Geoffrey E., Williams, Ronald J. Nature 323, 533-536 (1986).

[4] K. Shibata, O. Iwamoto, T. Nakagawa, N. Iwamoto, A. Ichihara, S. Kunieda, S. Chiba, K. Furutaka, N. Otuka, T. Ohsawa, T. Murata, H. Matsunobu, A. Zukeran, S. Kamada, and J. Katakura: "JENDL-4.0: A New Library for Nuclear Science and Engineering," J. Nucl. Sci. Technol. **48**(1), 1-30 (2011).

[5] M. Matzke, Report PTB-N-19, Unfolding of pulse height spectra: the HEPRO program system (1994).

[6] S. Nakayama and Y. Watanabe, J. Nucl. Sci. Technol. , **53**, No. 1, 89-101 (2016).

30 Resonance Analysis of Cross Section Data Measured by J-PARC/MLF using the Modified REFIT Code

Kazuhito Mizuyama, Nobuyuki Iwamoto, Osamu Iwamoto, Kazushi Terada and Taro Nakao
Nuclear Science and Engineering Center, Japan Atomic Energy Agency
Tokai-mura, Naka-gun, Ibaraki-ken 319-1195, Japan
e-mail: mizuyama.kazuhito@jaea.go.jp

For the purpose of the precise energy calibration of the TOF measurements by ANNRI at J-PARC MLF, we determined the flight lengths from the recent TOF data of ^{197}Au, neutron transmission and capture cross section using the modified REFIT code and the nuclear data libraries, JENDL-4.0 and JEFF-3.2. By using the modified REFIT code with the obtained flight lengths, we performed resonance analysis. Preliminary resonance parameters were obtained up to 300 eV.

1. Introduction

In the project entitled as Research and development for Accuracy Improvement of neutron nuclear data on Minor ACtinides (AIMAC), the cross section data of MAs (^{241,243}Am, ^{237}Np) have been measured by the ANNRI installed at the neutron time-of-flight (TOF) beam line in the J-PARC MLF. High precision data are expected even in the case of small amount sample because the reaction rates are strongly increased by the high intensity pulsed neutron beam of J-PARC MLF.

We are going to analyze those cross section data by using the least-squares multilevel R-matrix code REFIT [1]. For precise analysis of the cross section data measured by ANNRI, it is necessary to take into account the energy resolution function. In this study, we therefore adopt the modified version of REFIT [2] which treats the energy resolution function for ANNRI. Note that the Ikeda-Carpenter resolution function [3] and its parameters at certain operational condition of J-PARC MLF [4] were adopted in the modified REFIT code.

The determination of the flight length is crucial for the energy calibration of the TOF data. The nominal values of the flight length of ANNRI are known, but those are not the values based on the cross section measurements. We, therefore, determined the flight lengths from the neutron transmission and capture cross section data of ^{197}Au measured by ANNRI under the same operational condition of J-PARC MLF, because resonance parameters are thought to be well known.

In Sec.2, we determine the flight lengths from the TOF measurements of ^{197}Au and present the obtained flight lengths for ANNRI. In Sec.3, we perform the resonance analysis of ^{197}Au using the obtained flight lengths and derive the resonance parameters. The current problem and the future subject are also presented.

2. Determination of the flight length

In the recent measurements by ANNRI at J-PARC, the neutron transmission and capture cross section of ^{197}Au were measured up to 1 keV by the TOF method with Li-glass scintillator and Ge spectrometer, respectively. The proton beam of J-PARC was supplied by 200 kW power in the single-bunch mode. The dead-time correction and the background subtraction were carried out in order to obtain the data of neutron transmission and capture cross section. The self-shielding and the multiple scattering correction were taken into account in the analysis by using the options of the REFIT code. The TOF channel width was 4 ns and 10 ns for the neutron transmission and capture cross section data respectively.

The nominal values of the flight length are given by 28.7 m and 21.5 m for Li-glass scintillator and Ge spectrometer, respectively. In this study, we determined the flight lengths L from the measured data the neutron transmission and capture cross section by using the evaluated data and the modified REFIT code. The energy resolution parameter for the ANNRI at J-PARC derived by Kino et al. [4] was adopted in order to take into account the pulsed neutron shape effect. Adjusting L to reproduce the resonance energies of evaluated data below 1 keV for those of the experimental data by using the modified REFIT code, the flight length for Li-glass scintillator was obtained as 28.5959(4) m and 28.6310(4) m using JENDL-4.0 [5] and JEFF-3.2 [6] respectively. Note that the number in parentheses is the fitting error, The flight length for Ge spectrometer was obtained as 21.4916(1) m and 21.5149(1) m using JENDL-4.0 and JEFF-3.2 respectively.

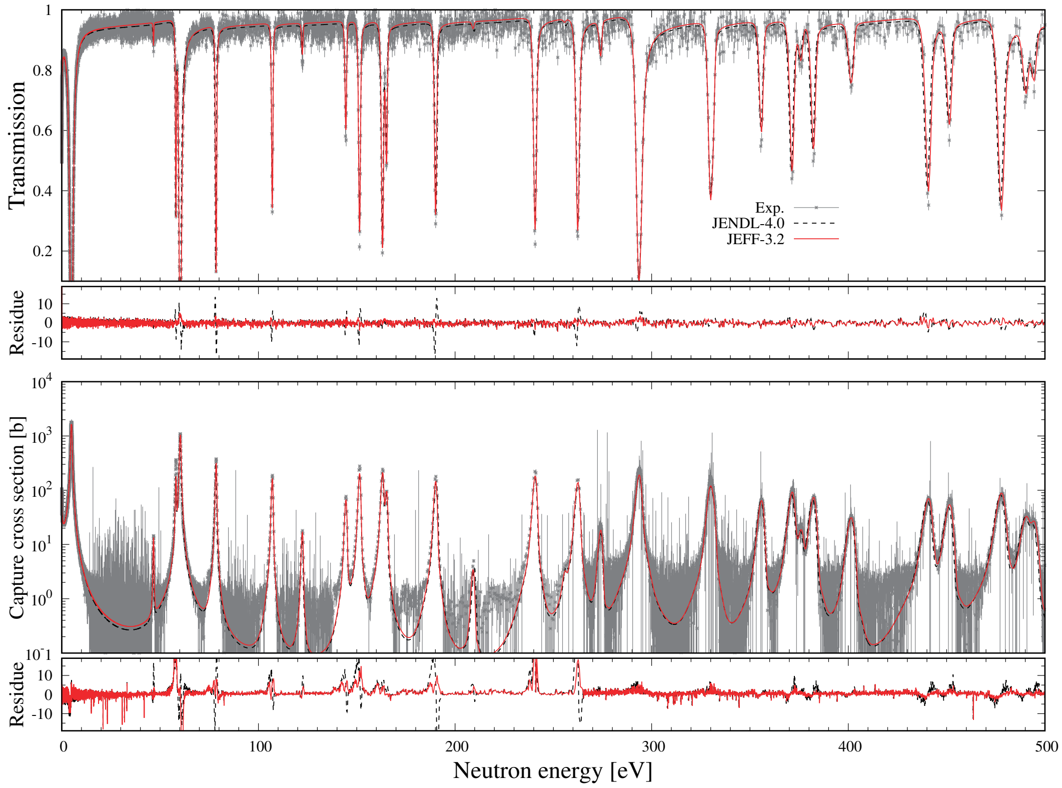

Figure 1. An overview of the neutron transmission and capture data of ^{197}Au below 500 eV. The experimental data were measured by ANNRI at J-PARC, and the calculated results were obtained by the modified REFIT code with the adjusted flight length and the nuclear data, JENDL-4.0 (dashed curve) and JEFF-3.2 (solid curve). The residue is defined as $(F^{exp} - F^{cal})/\delta F$, where $F^{exp} \pm \delta F$ and F^{cal} are the measured and calculated quantities.

In Fig.1, we show the transmission (upper panel) and capture cross section (lower panel) below 500 eV calculated by the modified REFIT code with JENDL-4.0 (dashed curve) and JEFF-3.2 (solid curve) using the obtained L. The calculated data of JEFF-3.2 was better than those of JENDL-4.0 in the sense of the agreement with the experimental data. In the calculation with JENDL-4.0, there were several mismatching of the resonance energies. The data of JEFF-3.2 was very good agreement with the transmission of the experiment data, however, the residue associated the resonance width was still large in the capture cross section. We, therefore, adopted the flight length obtained by using JEFF-3.2 (28.6310 m for Li-glass scintillator, and 21.5149 m for Ge spectrometer) for the resonance analysis.

3. Resonance analysis

The resonance parameters, neutron width Γ_n, radiation width Γ_γ, and resonance energy E_0 of ^{197}Au below 300 eV were determined by the simultaneous fitting to the transmission and the capture cross section data measured by ANNRI using the modified REFIT code. The initial resonance parameters were taken from those of JEFF-3.2 for this analysis. Preliminary fitting results were shown in Fig.2 and Fig.3. The calculated results with JEFF-3.2 were also shown for comparison as the results before fitting procedure. Both data of the transmission and the capture cross section were fitted reasonably well to the experimental data except the resonances around 60 eV. The resonances around 60 eV could not be fitted because there was large inconsistency between the transmission and the capture cross section in the experimental data. The reanalysis of the data is still in progress.

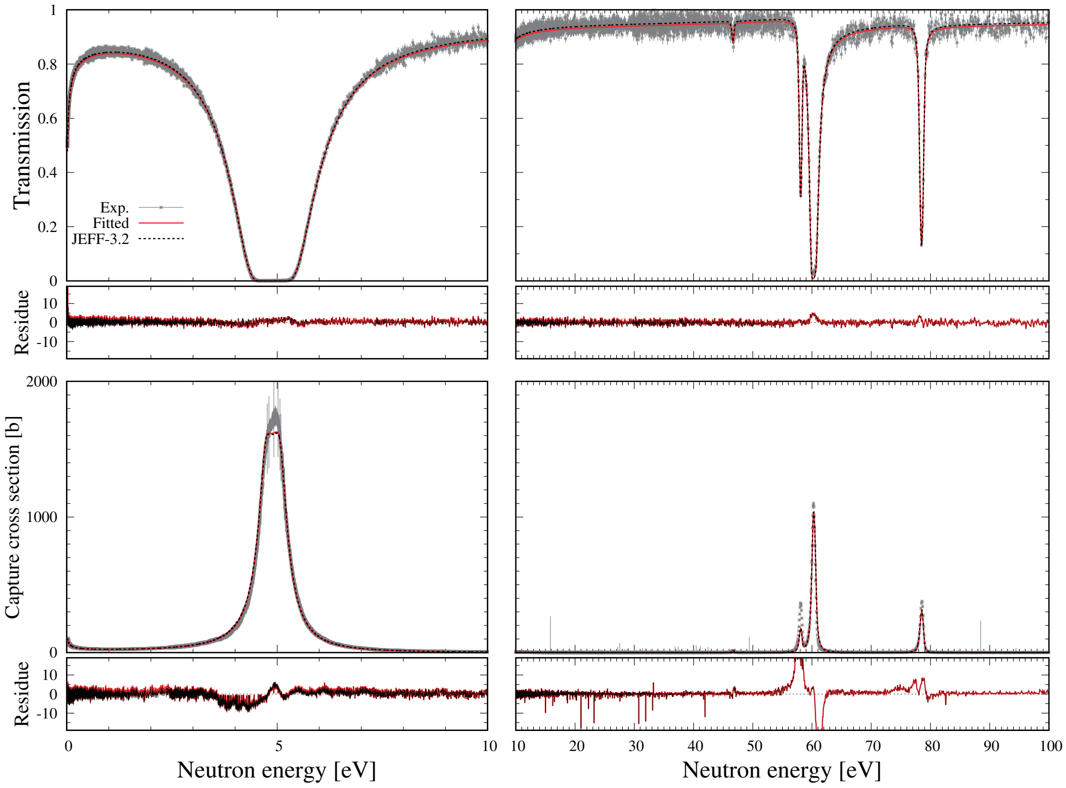

Figure 2. Simultaneous fitted results below 100 eV. Simultaneous fitting procedures were performed by the modified REFIT code for neutron transmission and capture cross section. The residue is defined as $(\sigma^{exp} - \sigma^{fit})/\delta\sigma$, where $\sigma^{exp} \pm \delta\sigma$ and σ^{fit} are the measured and fitted cross sections.

The obtained preliminary results of resonance parameters below 300 eV were listed in Table 1. The resonance parameters provided by JEFF-3.2 were also listed for comparison. Note that the resonance parameters in parentheses were not adjusted, since the resonances with the peak capture

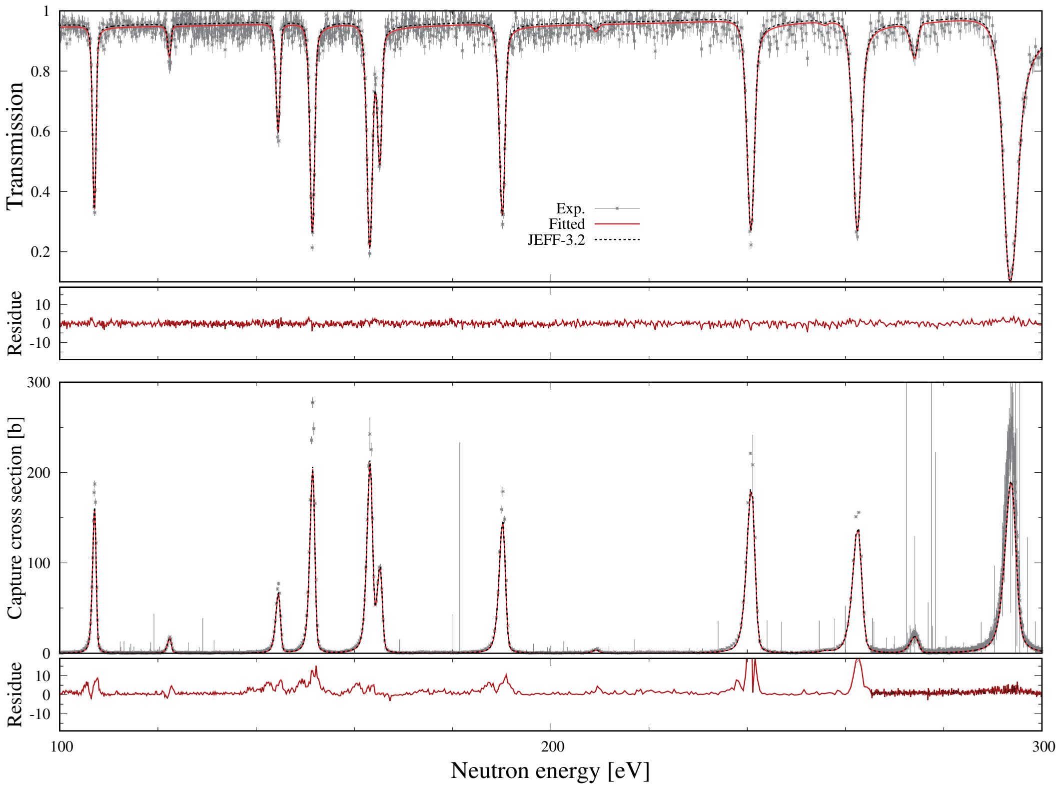

Figure 3. Simultaneous fitted results in the 100 to 300 eV region

cross sections smaller than 50 b were excluded from the fitting procedure. In addition, the most of the resonance energies were not adjusted because the resonance energies provided by JEFF-3.2 were in good agreement with both data of the transmission and the capture cross section measured by ANNRI. The energy of the first resonance was adjusted together with the parameters of the negative resonance in order to adjust the data in the thermal energy region.

The obtained resonance parameters were in mostly good agreement with those of JEFF-3.2, but there were some differences especially in higher energy region. In order to discuss these differences or the accuracy of the fitting results, it is necessary to take care of the reliability of the resolution function. Because the effect of the resolution function is expected to appear in the cross sections above 10 eV [4], and the currently adopted parameters for the resolution function was optimized to the operational condition of the 17.5 kW proton beam power in contrast to 200 kW. The appropriate resolution parameters corresponding to the operational condition may be necessary for more precise resonance analysis. This would be a future subject.

4. Summary

We analyzed new neutron transmission and capture data of ^{197}Au measured by ANNRI using the modified REFIT code which takes into account the energy resolution function of J-PARC. Before the resonance analysis, we determined the flight lengths using the modified REFIT code with the data of the libraries, JENDL-4.0 and JEFF-3.2. From the sense of the agreement with the experimental data, we adopted the flight length obtained by the adjustment using JEFF-3.2. Applying it to the simultaneous R-matrix fitting of the resonance parameters to measured neutron transmission and

Table 1. Resonance parameters of ^{197}Au below 300 eV

Fitted result				JEFF-3.2			
E_0 [eV]	J	Γ_n[eV]	Γ_γ[eV]	E_0 [eV]	J	Γ_n[eV]	Γ_γ[eV]
-6.1100E+01	1	3.2900E-01	1.2430E-01	-6.1100E+01	1	3.2900E-01	1.2430E-01
-1.4837E+01	2	1.8116E-02	1.2700E-01	-5.2966E+01	2	3.6577E-01	1.2700E-01
4.9144E+00	2	1.5136E-02	1.2140E-01	4.8997E+00	2	1.4960E-02	1.2140E-01
(4.6669E+01	1	2.2000E-04	1.2700E-01	4.6669E+01	1	2.2000E-04	1.2700E-01)
(5.8078E+01	1	4.3100E-03	1.1300E-01	5.8078E+01	1	4.3100E-03	1.1300E-01)
(6.0291E+01	2	7.0660E-02	1.1800E-01	6.0291E+01	2	7.0660E-02	1.1800E-01)
7.8508E+01	1	1.9233E-02	1.2121E-01	7.8500E+01	1	1.7000E-02	1.2400E-01
1.0703E+02	2	8.8812E-03	1.2300E-01	1.0703E+02	2	7.8300E-03	1.2300E-01
(1.2230E+02	2	9.0000E-04	1.2100E-01	1.2230E+02	2	9.0000E-04	1.2100E-01)
1.4441E+02	1	1.0773E-02	1.2100E-01	1.4441E+02	1	9.0700E-03	1.2100E-01
1.5139E+02	2	3.0132E-02	1.2100E-01	1.5139E+02	2	2.2260E-02	1.2100E-01
1.6307E+02	1	6.1904E-02	1.2900E-01	1.6307E+02	1	5.5160E-02	1.2900E-01
1.6508E+02	2	9.9706E-03	1.2100E-01	1.6508E+02	2	9.9830E-03	1.2100E-01
1.9003E+02	1	6.2329E-02	1.2100E-01	1.9003E+02	1	4.9080E-02	1.2100E-01
2.0922E+02	1	1.1487E-03	1.2100E-01	2.0905E+02	1	8.6000E-04	1.2100E-01
2.4061E+02	2	8.5361E-02	1.7405E-01	2.4061E+02	2	7.4164E-02	1.2100E-01
(2.5560E+02	1	5.6080E-04	1.2400E-01	2.5560E+02	1	5.6080E-04	1.2400E-01)
2.6226E+02	1	1.3984E-01	1.8234E-01	2.6226E+02	1	1.4400E-01	1.2900E-01
(2.7386E+02	2	4.8282E-03	1.2100E-01	2.7386E+02	2	4.8282E-03	1.2100E-01)
2.9346E+02	2	3.2122E-01	1.9272E-01	2.9346E+02	2	3.6398E-01	1.2600E-01

capture data, the reasonable fitted results and the resonance parameters were obtained except resonances around 60 eV in which there were large inconsistency between measured neutron transmission and capture data. Reanalysis of the experimental data is still in progress.

Acknowledgement

The authors are grateful for the financial support of “Research and development for Accuracy Improvement of neutron nuclear data on Minor ACtinides (AIMAC)” project entrusted to Japan Atomic Energy Agency by Ministry of Education, Culture, Sport, Science and Technology of Japan (MEXT).

References

[1] M. C. Moxon, T. C. Ware, C. J. Dean: UKNSF(2010)P243.

[2] H. Hasemi, et al.: Nucl. Instrum. Meth. Phys. Res. A773, 137 (2015).

[3] S. Ikeda and J. M. Carpenter: Nucl. Instrum. Methods, A239, 536 (1985).

[4] K. Kino et al.: Nucl. Instrum. Meth. Phys. Res. A736, 66 (2014).

[5] K. Shibata et al.: J. Nucl. Sci. Technol., 48, 1(2011).

[6] https://www.oecd-nea.org/dbforms/data/eva/evatapes/jeff_32/.(accessed 2014).

31 Measurement and Simulation of the Neutron Capture Reaction using NaCl Samples

Kaoru Y. HARA1)*, Nobuya FUJII1), Takashi KAMIYAMA1), Yuki NARITA1),
Hirotaka SATO1), Shoji NAKAMURA2), and Yosuke TOH2)

1) Faculty of Engineering, Hokkaido University, Sapporo 060-8628, Japan
2) Nuclear Science and Engineering Center, Japan Atomic Energy Agency, Ibaraki-ken 319-1195, Japan
*e-mail: hara.kaoru@eng.hokudai.ac.jp

To determine the neutron capture cross section of ^{35}Cl in the energy range from 0.02 eV to 1 keV, the measurements and simulations of the neutron capture reaction for NaCl samples were performed with an ANNRI-NaI(Tl) spectrometer at J-PARC MLF.

1. Introduction

A long-lived nucleus ^{36}Cl (half-life 3×10^5 yr) is produced by the neutron capture reaction of a stable nucleus ^{35}Cl, which is an impurity in a coolant of nuclear reactor and structural material of accelerator facility such as water and concrete. The neutron capture cross section of ^{35}Cl is required to evaluate the production yields of the ^{36}Cl nuclei. As shown in Fig. 1, the available data are however scarce in the neutron energy region from 0.03 eV to 1 keV. The previous data of the neutron capture cross section of ^{35}Cl are plotted at the thermal neutron energy and the keV region by square [1], triangle [2], circle [3], and cross [4] in Fig. 1, where the evaluated cross section of JENDL-4.0 [5] and ENDF/B-VII.1 [6] are also plotted by the solid line and dashed line, respectively. To determine the neutron capture cross section of ^{35}Cl in the energy region below 1 keV, the neutron capture reactions for sodium chloride (NaCl) samples were measured with the neutron time-of-flight (TOF) method.

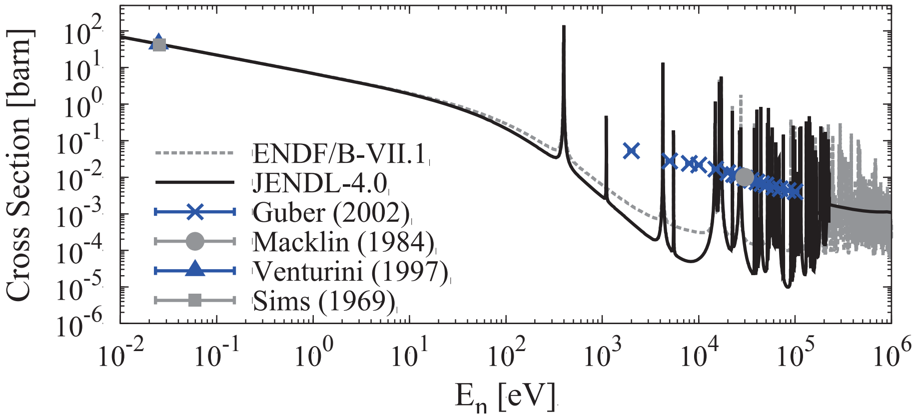

Figure 1: Neutron capture cross section of ^{35}Cl

2. Measurement using an ANNRI-NaI(Tl) spectrometer

The experiment was performed using an NaI(Tl) spectrometer in the Accurate Neutron-Nucleus Reaction measurement Instrument (ANNRI) in the Materials and Life Science Experimental Facility (MLF) at the Japan Proton Accelerator Research Complex (J-PARC). The proton beam power was about 400 kW and the repetition rate of the proton beam pulses was 25 Hz. The experimental setup of the ANNRI-NaI(Tl) spectrometer is shown in Fig. 2. Two NaI(Tl) detectors with the anti-Compton suppress plastic detectors were located at angles of 90° and 125° with respect to the neutron beam axis [7]. The detectors were shielded from neutron and γ-ray backgrounds by the borated rubber, borated polyethylene, cadmium, lead, enriched ^{6}LiH, and enriched $^6Li_2CO_3$. A sample was placed at a 28-m distance from a liquid hydrogen moderator. Disk-shaped NaCl samples were used in the measurements, where NaCl powder with a weight of 0.15 g was molded into a disk with a diameter of 1 cm. Since the natural abundances of ^{35}Cl and ^{37}Cl are 76% and 24%, respectively, the ^{23}Na and ^{37}Cl nuclei which are involved in the NaCl samples contribute to the background of the TOF measurements. The stable isotope of sodium is only ^{23}Na. To estimate the background due to ^{37}Cl and ^{23}Na, three NaCl samples with the different isotopic compositions of ^{35}Cl that were 99% (^{35}Cl-enriched), 2% (^{37}Cl-enriched), and 76% (natural Cl) were used. To obtain the energy distribution of neutron beam, $^{10,\mathrm{nat}}$B samples were also used.

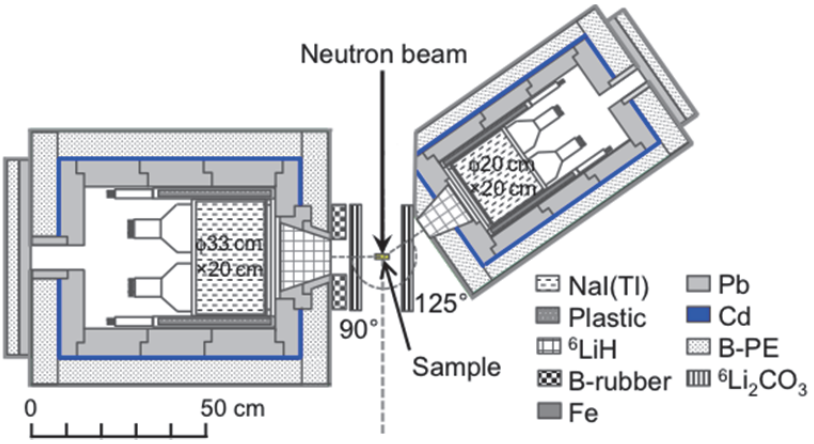

Figure 2: Experimental setup of the ANNRI-NaI(Tl) spectrometer at J-PARC MLF

3. Simulation and data analysis

3.1 Simulation using the PHITS code

The γ-ray pulse height spectra and the neutron TOF spectra for the ^{35}Cl-enriched NaCl sample were calculated using the PHITS code [8]. In the simulation, a pencil-like neutron beam with a diameter of 1 cm was defined in order to irradiate the NaCl sample and induce the ^{35}Cl(n,γ) reaction. The distance between the initial position of neutron source and the sample was 28 m. The tally cells for the γ-ray energy deposit were set in two crystals of NaI(Tl) scintillator that were located at the angles of 90° and 125° with respect to the neutron beam axis, where the results for the NaI(Tl) at 90° are only reported in this paper. The result of the simulation for pulse height indicates that the background due to scattering neutrons relatively increases with the incident neutron energy [9] except the energy of the 0.4-keV resonance of ^{35}Cl. For example, the calculated pulse height spectra for the ^{35}Cl-enriched sample at the incident neutron energies of 0.4 and 2.9 keV are shown in Fig. 3 (a) and (b), respectively. The gray solid, black solid, dot-dashed, and dotted lines present the pulse height spectra for NaCl, ^{35}Cl, ^{37}Cl, and ^{23}Na, respectively. The 0.5-MeV peaks which arise from the ^{10}B(n,$\alpha\gamma$)^{7}Li reaction with the elastic scattering neutrons are observed in the both figures, where the boron is involved in the neutron shields around the detector. In contrast with Fig. 3 (b), the background due to scattering neutrons is negligible in in Fig. 3 (a) because the neutron capture cross section of ^{35}Cl is dominant against the elastic scattering cross section of ^{23}Na (or ^{35}Cl) at 0.4 keV.

Based on the simulation for pulse height, the higher discrimination level is preferable in order to reduce the background component in the data analysis. For a qualitative demonstration, the neutron TOF spectrum was calculated by using the tally of the γ-ray energy deposit in the energy range from 0.01 eV to 50 keV when the discrimination level of the pulse height was set at 0.9 MeV (or 0.3 MeV). The calculated TOF spectra in the neutron energy region of 5 eV – 50 keV are shown at the discrimination levels of 0.3 (lower) and 0.9 MeV (higher) by the dotted and solid lines, respectively, in Fig. 4 (a). As expected, the number of counts for the resonance of ^{23}Na is relatively suppressed at the higher discrimination level in comparison with one at the lower discrimination level.

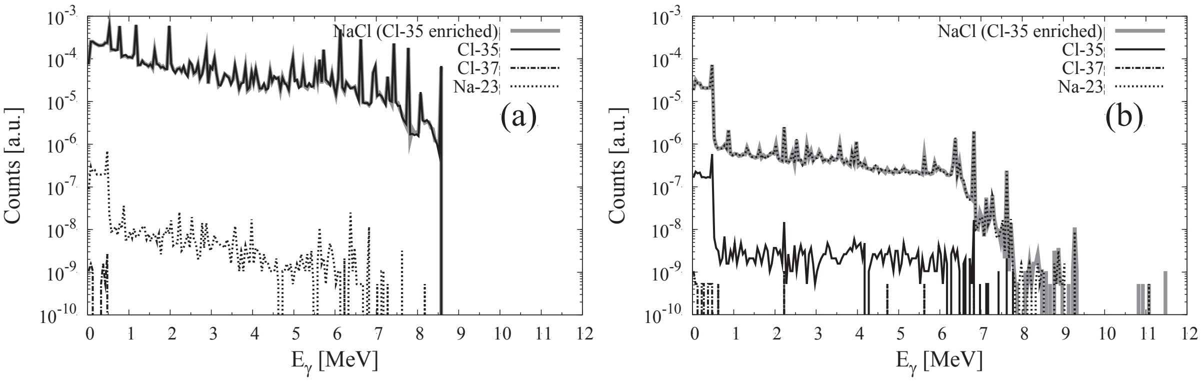

Figure 3: Calculated pulse height spectra for the NaCl sample at the incident neutron energies of 0.4 keV (a) and 2.9 keV (b)

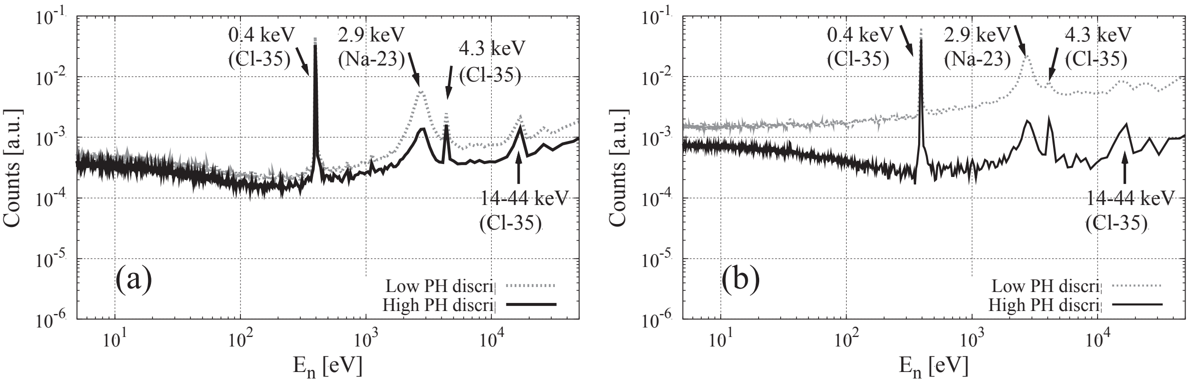

Figure 4: Calculated TOF spectra for the NaCl sample (a) and measured ones (b)

3.2 Data analysis

The TOF spectra for the NaCl samples were measured by the ANNRI-NaI(Tl) spectrometer in the neutron energy region from 0.01 eV to 50 keV. In the data analysis, the background component was reduced in the TOF spectrum by setting the higher discrimination level for the pulse height. At the lower and higher discrimination levels, the measured TOF spectra of the enriched-^{35}Cl sample are plotted by the dotted and solid lines in Fig. 4 (b), respectively, where the lower and higher discrimination levels are about 0.3 and 0.9 MeV, respectively. The resonances of

^{35}Cl are enhanced in comparison with the resonance of ^{23}Na in the TOF spectrum at the higher discrimination level. A resonance of ^{37}Cl is not observed because ^{37}Cl was depleted in the enriched-^{35}Cl sample.

The neutron capture cross sections of NaCl was preliminary obtained in the neutron energy range of 0.01 eV – 50 keV, where they were normalized using a cross section of natural NaCl at 0.025 eV. The data of $^{10,\mathrm{nat}}$B samples was used to deduce the energy distribution of incident neutron beam. Only the data which were measured with the NaI(Tl) detector at 90° were used here. The pulse-height weighting technique was not applied to this data analysis yet. The solid, dotted, and dashed lines present the neutron capture cross sections of NaCl for enriched-^{35}Cl, enriched-^{37}Cl, and natural Cl, respectively, in Fig. 5. For determining the neutron capture cross section of ^{35}Cl involved in the neutron capture cross section of NaCl, the data analysis is in progress.

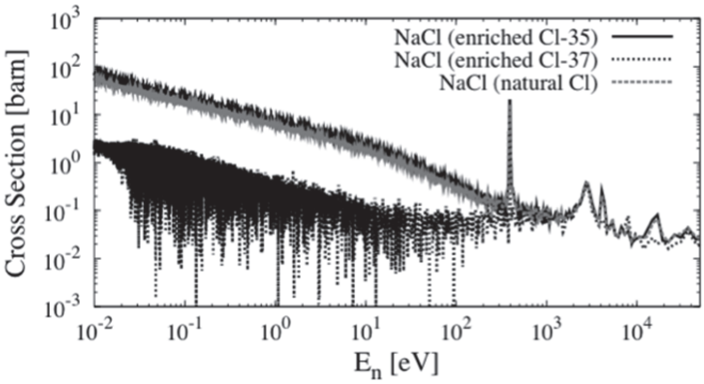

Figure 5: Measured neutron capture cross sections for NaCl

4. Conclusion

The measurements of the neutron capture cross reaction of NaCl were performed with the ANNRI-NaI(Tl) spectrometer in at J-PARC MLF. The enriched ^{35}Cl, ^{37}Cl, and natural Cl samples in chemical form of NaCl were used. For the data analysis, the γ-ray pulse height and neutron TOF spectra for the NaCl samples were calculated using the PHITS code. Based on the simulation results, the background compositions due to the scattering neutrons in the measured TOF spectra were suppressed by setting the appropriate discrimination level for the pulse height. The preliminary results of the neutron capture cross sections of NaCl was presented in the neutron energy range of 0.01 eV – 50 keV. The neutron capture cross section of ^{35}Cl will be determined from the neutron capture cross section of NaCl.

Acknowledgments

The work is supported by JSPS KAKENHI Grant Number 26820411.

References

[1] Sims GHE and Juhnke DG. The thermal neutron capture cross section and resonance capture integral of ^{35}Cl for (n,γ) and (n,p) reactions. J. Inorg. Nucl. Chem. 1969;31:3721-3725.

[2] Venturini L and Pecequilo BRS. Thermal neutron capture cross-section of ^{48}Ti, ^{51}V, ^{50,52,53}Cr and ^{58,60,62,64}Ni. Appl. Radiat. Isot. 1997;48:493-496.

[3] Macklin RL. Resonance neutron capture by ^{35,37}Cl. Phys. Rev. 1984;C29:1996-2000.

[4] Guber KH, Sayer RO, Valentine TE, Leal LC, Spencer RR, Harvey JA, Koehler PE, and Rauscher T. New Maxwellian averaged neutron capture cross sections for ^{35,37}Cl. Phys. Rev. 2002;C65:058801-1-4.

[5] Shibata K, Iwamoto O, Nakagawa T, Iwamoto N, Ichihara A, Kunieda S, Chiba S, Furutaka K, Otuka N, Ohsawa T, Murata T, Matsunobu H, Zukeran A, Kamada S, Katakura J. JENDL-4.0: a new library for nuclear science and engineering. J Nucl Sci Technol. 2011;48:1-30.

[6] Chadwick MB, Herman M, Obložinský P, Dunn ME, Danon Y, Kahler AC, Smith DL, Pritychenko B, Arbanas G, Arcilla R, Brewer R, Brown DA, Capote R, Carlson AD, Cho YS, Derrien H, Guber K, Hale GM, Hoblit S, Holloway S, Johnson TD, Kawano T, Kiedrowski BC, Kim H, Kunieda S, Larson NM, Leal L, Lestone JP, Little RC, McCutchan EA, MacFarlane RE, MacInnes M, Mattoon CM, McKnight RD, Mughabghab SF, Nobre GPA. ENDF/B-VII.1 Nuclear Data for Science and Technology: Cross Sections, Covariances, Fission Product Yields and Decay Data. Nucl. Data Sheets 2011;112;2887-2996.

[7] Katabuchi T, Matsuhashi T, Terada K, Arai T, Furutaka K, Hara KY, Harada H, Hirose K, Hori J, Igashira M, Kamiyama T, Kimura A, Kino K, Kitatani F, Kiyanagi Y, Koizumi M, Mizumoto M, Nakamura S, Oshima M, and Toh Y. Pulse-width analysis for neutron capture cross-section measurement using an NaI(Tl) detector. Nucl. Instr. Meth. 2014;A764:369-377.

[8] Sato T, Niita K, Matsuda N, Hashimoto S, Iwamoto Y, Noda S, Ogawa T, Iwase H, Nakashima H, Fukahori T, Okumura K, Kai T, Chiba S, Furuta T and Sihver L. Particle and Heavy Ion Transport Code System PHITS, Version 2.52. J. Nucl. Sci. Technol. 2013;50:913-923.

[9] Hara KY, Fujii N, Kamiyama T, Narita Y, Sato H, Nakamura S, and Toh Y. Measurement of the Cl-35(n,γ) reaction cross section in ANNRI at J-PARC. 2016; JAEA-Conf 2016-004;193-198.

32

Dependence of activation products for decommissioning on fission neutron spectra

Hiroki JOJIMA[1], Ken-ichi TANAKA[2,1] and Satoshi CHIBA[1]
[1] *Tokyo Institute of Technology, 2-12-1 Ookayama, Meguro-ku, Tokyo 152-8550, Japan*
[2] *The Institute of Applied Energy, Shinbashi SY Bldg 14-2 Nishi-Shinbashi 1-Chome, Minato-Ku,Tokyo 105-0003, Japan*
Email: joujima.h.aa@m.titech.ac.jp

Impacts of fission neutron spectra (FNS) on calculation of activation products for decommissioning of LWR plants are investigated systematically. We calculated FNS using Los Alamos Model (LAM), taking into account changes of fuel composition by fuel burnup and impacts of the modification on the calculation was investigated. We also calculated uncertainty of the calculation by propagating that of FNS.

1. Introduction

It is expected that number of LWR plants to be decommissioned will increase in several decades. To make decommissioning tasks safe and effective, a reliable calculation of radioactive products due to neutron irradiation in primary containment vessels is needed [1]. One of the important quantity which will affect such calculations is fission neutron spectrum (FNS), calculation of which still suffers from large uncertainties [2]. In addition, dependence of the results on fuel composition and uncertainty of FNS are not considered in such calculations usually [1]. Difference of calculated results makes significant change of cooling time that radioactive level decrease to clearance level (Fig.1), so impacts of fuel composition and FNS on such calculation have to be investigated.

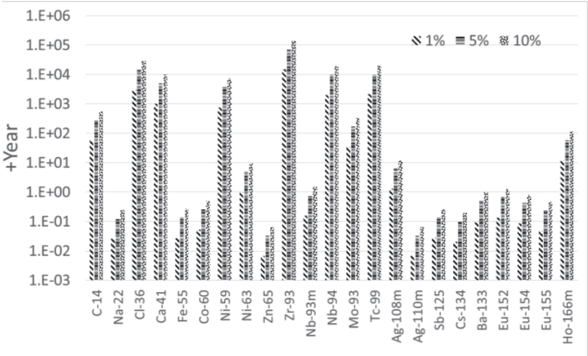

Fig.1 Dependence of cooling time that radioactive level decreases to clearance level on amount of radioactive change by 1%, 5%, and 10%.

To achieve these objects, we modified FNS theoretically, taking account of fuel composition change by fuel burnup and investigated impacts of the modification on calculation of activation products. We also calculated uncertainty of the calculation by propagating that of FNS.

2. Methods

2.1 Modification of fission neutron spectrum

To calculate FNS, we used Los Alamos Model (LAM)[3]. In this theory, FNS of center-of-mass system(CMS) $\phi(\varepsilon)$ is given as

$$\phi(\varepsilon) = \mathrm{k}(\mathrm{T})\sigma_c(\varepsilon)\exp(-\varepsilon/T). \tag{1}$$

Here, ε is emitted neutron energy in CMS, k(T) is normalization factor, and $\sigma_c(\varepsilon)$ is inverse reaction cross section. The symbol T is temperature of compound nucleus (CN) which is related to excitation energy of CN E^* approximately by Fermi-gas model:

$$E^* = Q - TKE = aT^2. \tag{2}$$

Here, Q is total energy release of fission and TKE is total kinetic energy of fission fragments, and a is level density parameter which is usually defined as

$$a = A/C \tag{3}$$

A is mass number of CN and C ranges from 8 to 11. Optical model is used to calculate $\sigma_c(\varepsilon)$. If neutrons were emitted before the fragments reach their full acceleration, emission in CMS could be anisotropic.

$$\phi(\varepsilon,\theta) = \phi(\varepsilon)(1 + bcos^2\theta)/(1 + b/3) \tag{4}$$

where θ is given in CMS and b is a parameter describing the degree of anisotropy. FNS in laboratory system $\chi(\mathrm{E})$ is expressed as

$$\chi(\mathrm{E}) = \int_{\varepsilon_-}^{\varepsilon_+} d\varepsilon \frac{\phi(\varepsilon)[1 + b\left(E - \varepsilon - E_f\right)^2/(4\varepsilon E_f)]}{4\left(\varepsilon E_f\right)^{\frac{1}{2}}(1 + b/3)} \tag{5}$$

where E denotes emitted neutron energy in laboratory system. The symbol E_f denotes kinetic energy per nucleon of accelerated fragments and $\varepsilon_\pm$ are defined as

$$\varepsilon_\pm = (\sqrt{E} + \sqrt{E_f})^2 \tag{6}$$

We adjusted parameters, C, TKE, and b by using least-squares method to reproduce experimental data.

2.2 Dependence of fission neutron spectra on fuel composition change by burnup

As fuel burnup proceeds, FNS will change because contribution to FNS of another fissile, for example, ^{239}Pu, will become significant. So we calculated fuel composition change of each burnup steps by ORLIBJ40 package [4], and combined FNS of each fissile as described below;

$$\chi_{MIX} = \frac{\sum_{i=1}^{N} \nu^i\ \Sigma_f^i \chi^i}{\sum_{i=1}^{N} \nu^i\ \Sigma_f^i} \tag{7}$$

where i means index of fissile, and N is total number of fissile. The symbols ν and Σ_f are total number of prompt neutrons and macroscopic fission cross section, respectively, while $\nu^i\ \Sigma_f^i$ means contribution to prompt neutrons of fissile i.

2.3 Error propagation

Variance of calculated activation products R[Bq/g] was calculated by propagating that of FNS according to law of error propagation:

$$V_R = \sum_{g} \sum_{g'} S_g S_{g'} cov(\chi_g, \chi_{g'}) \tag{8}$$

Here, S_g is sensitivity coefficient defined as

$$S_g = \partial R / \partial \chi_g \tag{9}$$

Relative sensitivity coefficient is also defined as

$$S_{g,rel} = (\partial R/R)/(\partial \chi_g / \chi_g) \tag{10}$$

χ_g is fission neutron spectrum in neutron energy g group. $cov(\chi_g, \chi_{g'})$ is covariance matrix for χ_g and $\chi_{g'}$.

In order to investigate the impacts of these methods on calculation of activation products for decommissioning of LWR plants, we applied these methods to the calculation by neutron irradiation in primary containment vessel[1] of Tsuruga Unit 1. Neutron flux and activation products were calculated by DORT [5] and ORIGEN-S(scale6.1)[6], respectively. Figure 2 and Table 1 show calculation object conditions.

Table1 Information of calculation object

Nuclear reactor name	Tsuruga Power Plant Unit 1
Type of Reactor	Boiling Water Reactor
Thermal Power	1070MWt
Irradiation period	373days
Uranium Enrichment	U-238:97w% , U-235:3w%
Radiation mesurments	Au-197(n,γ)Au-198, Ni-58(n,p)Co-58 (Foils in Fig.2)

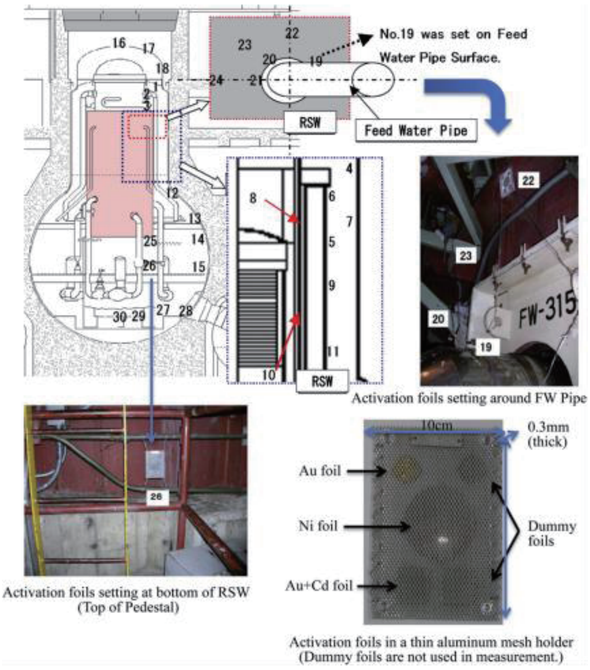

Fig.2 Overview of calculation object and measurement points [1]

3. Results

After adjusting parameters, we obtained modified FNS of $^{235}U(n_{th},f)$ reaction that reproduce experimental data better than JENDL-4.0[7] especially at low emission energy (Fig.3). In the modification, instead of increasing spectrum at low emission energy, we decreased spectrum at high emission energy within experimental data error in order to normalize spectrum to a unity (Fig. 4).

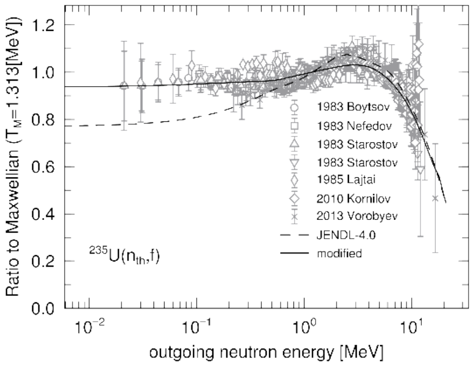

Fig.3 Modified FNS of $^{235}\mathrm{U}(n_{th},f)$ reaction

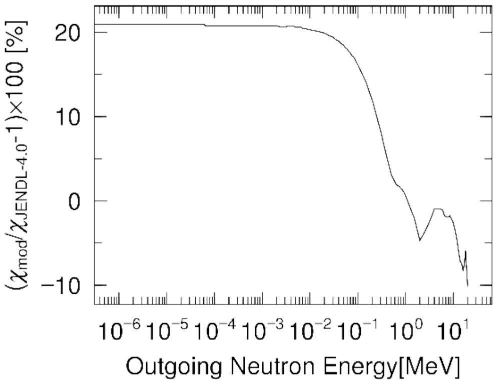

Fig.4 Difference between modified FNS and JENDL-4.0 FNS of $^{235}\mathrm{U}(n_{th},f)$ reaction

We also modified FNS of $^{239}\mathrm{Pu}(n_{th},f)$ reaction in the same way which is also dominant for thermal reactor system (Figs. 5 and 6).

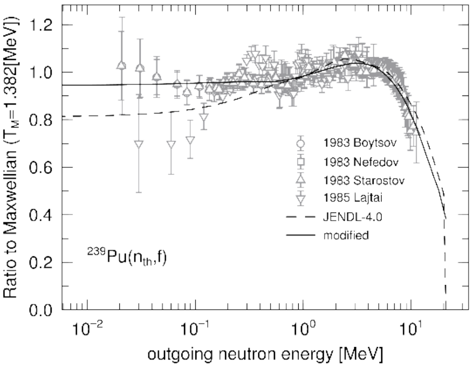

Fig.5 Modified FNS of $^{239}\mathrm{Pu}(n_{th},f)$ reaction

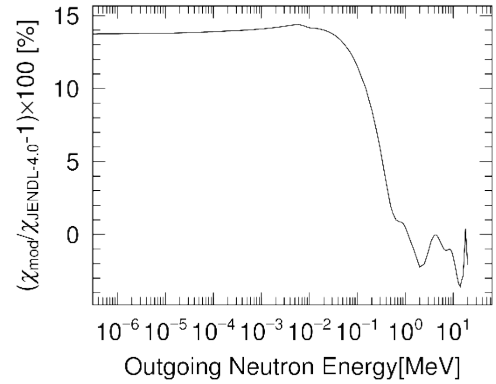

Fig.6 Difference between modified FNS and JENDL-4.0 FNS of $^{239}\mathrm{Pu}(n_{th},f)$ reaction

In order to combine FNS of $^{235}\mathrm{U}(n_{th},f)$ reaction and $^{239}\mathrm{Pu}(n_{th},f)$ reaction in accordance with eq. (7), we calculated ratio of $\nu\Sigma_f$ for each burnup steps (BOC; Beginning Of Cycle, MOC; Middle Of Cycle, EOC; End Of Cycle) (Table2). Here, atom density was calculated by ORLIBJ40, and ν and micro fission cross section σ_f at thermal neutron energy were obtained from JENDL-4.0. After combination, we defined FNS at BOC, MOC, and EOC as χ_{BOC}, χ_{MOC}, and χ_{EOC}, respectively. Then we used these FNS for calculation of activation products R[Bq/g] and the results were shown in Figs. 7 and 8.

Table.2 Ratio of $\nu\Sigma_f$ for each burnup steps

	Ratio of ν Σ f [%]		
	BOC	MOC	EOC
235U	1.00E+02	9.27E+01	8.55E+01
239Pu	0.00E+00	7.30E+00	1.45E+01

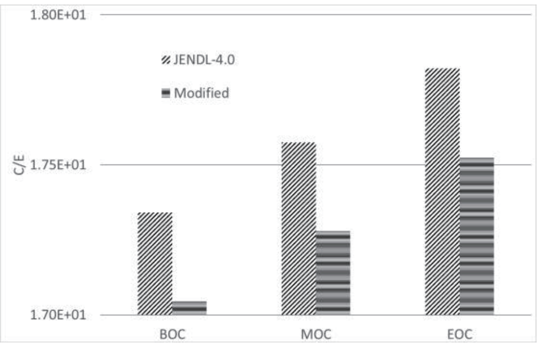

Fig.7 Comparison of calculated activation productrs(C) with experimental data(E) [2]. At BOC, MOC, and EOC, we used χ_{BOC}, χ_{MOC}, and χ_{EOC}, respectively

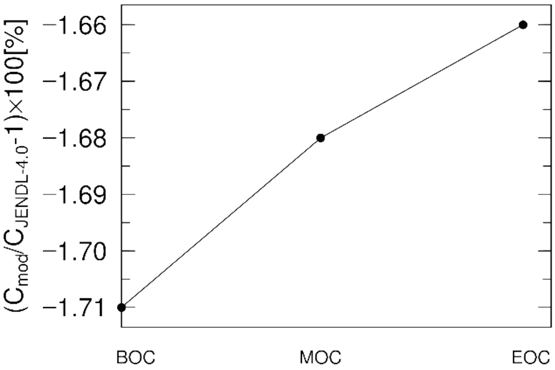

Fig.8 Difference between results of modified and JENDL-4.0 in Fig.7

Figures 7 and 8 showed the results of only ^{197}Au(n,γ)^{198}Au reaction at location number 1 (Fig. 2), because another results showed almost same behavior. The modification of FNS made R lower by ~1.7% because we decreased spectrum at high emission energy (Figs. 4 and 6), so the number of neutrons penetrating pressure vessel became lower. As fuel burnup proceeds, calculated results became higher due to contribution of ^{239}Pu(n$_{th}$,f) whose FNS is harder than that of ^{235}U(n$_{th}$,f).

Next, we calculated relative sensitivity coefficient (Fig. 9) and obtained relative uncertainty for calculated activation products of ^{197}Au(n,γ)^{198}Au and ^{58}Ni(n,p)^{58}Co reactions at location number 1 in accordance with eqs. (8) and (10). Covariance data of JENDL-4.0 was used. As a result, the uncertainties were 9.16% and 11.2%, respectively. If this uncertainty is common for another calculated activation products, the required cooling time that radioactive level decreases to clearance level will change significantly (Fig. 1). So, the uncertainty of calculated activation products caused by that of FNS is not negligible.

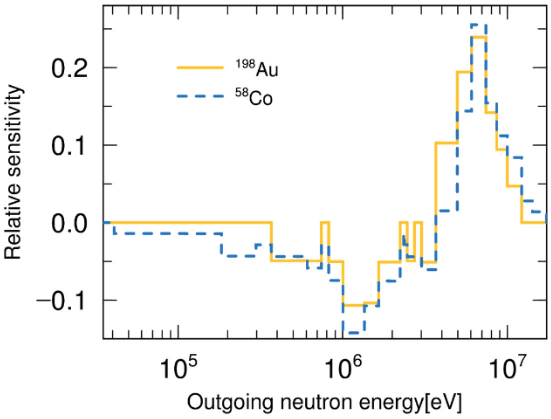

Fig.9 Relative sensitivity coefficient of calculated activation products of ^{197}Au(n,γ)^{198}Au and ^{58}Ni(n,p)^{58}Co reactions at location number 1 (Fig.2)

4. Summary

We modified FNS using LAM and took into account fuel composition change by fuel burnup. As fuel burnup proceeds, FNS will change and the amount of activation products will be larger due to contribution of FNS of ^{239}Pu(n$_{th}$,f). Uncertainty of calculated activation products by propagating that of FNS was also investigated and we found the uncertainty was not negligible.

References

[1]K.Tanaka, J.Ueno, S.Chiba," Improvement of a calculation procedure of neutron-flux distribution for radioactivity inventory estimation for decommissioning of nuclear power plants," Progress in Nuclear Energy 85, pp.254-270(2015).

[2] R.Capote, Y.-J.Chen, F.-J.Hambsch, N.V.Kornilov, J.P.Lestone, O.Litaize, B.Morillon, D.Neudecker, S.Oberstedt, T.Ohsawa, N.Otuka, V.G.Pronyaev, A.Saxena, O.Serot, O.A.Shcherbakov, N.-C.Shu, D.L.Smith, P.Talou, A.Trkov, A.C.Tudora, R.Vogt, A.S.Vorobyev, "Prompt Fission Neutron Spectra of Actinides," Nuclear Data Sheets 131(2016), pp.1-106.

[3]D.G.Madland and J.R.Nix,"New Calculation of Prompt Neutron Spectra and Average Prompt Neutron Multiplicities," Nucl.Sci.Eng.81(1982),pp.213-271 .

[4] K. Okumura, K. Sugino, K. Kojima, T.Jin, T.Okamoto, J.Katakura, "A Set of ORIGEN2 Cross Section Libraries Based on JENDL-4.0: ORLIBJ40," JAEA-Data/Code 2012-032 (2013) [in Japanese].

[5] W.A.Rhoades and R.L.Childs,"The DORT Two-dimensional Discrete Ordinates Transport Code System," RSICC-CCC-444,Oak Ridge National Laboratory(1996).

[6] Scale: A Comprehensive Modeling and Simulation Suite for Nuclear Safety Analysis and Design,ORNL/TM-2005/39,(2011).

[7] K. Shibata, O. Iwamoto, T. Nakagawa, N. Iwamoto, A. Ichihara, S. Kunieda, S. Chiba, K. Furutaka, N. Otuka, T. Ohsawa, T. Murata, H. Matsunobu, A. Zukeran, S. Kamada, and J. Katakura, " JENDL-4.0: A New Library for Nuclear Science and Engineering," J. Nucl. Sci. Technol. 48(1), pp.1-30(2011).

33

Measurement of Double Differential Cross Section for Evaporated Charged Particles from Proton-induced Reactions

Yuji YAMAGUCHI[1], Toshiya SANAMI[2] and Yusuke UOZUMI[1]
[1]Department of Applied Quantum Physics and Nuclear Engineering, Kyushu University
744 Motooka, Nishi-ku, Fukuoka-shi, Fukuoka-ken 819-0395 Japan
[2]High Energy Accelerator Research Organization
1-1 Oho, Tsukuba-shi, Ibaraki-ken 305-0801 Japan
e-mail: yyamaguchi@nucl.kyushu-u.ac.jp

Bragg curve counters (BCCs) with two built-in solid-state detectors (SSDs) were developed and tested by using 70-MeV incident protons for the measurement of double differential cross sections (DDXs) covering the evaporation energy region. The charged particles were identified by using the BCC with self particle identification capability and applying the ΔE–E method. The design value of threshold energy for proton identification is 1.5 MeV. The identification of hydrogen isotopes is confirmed from two-dimensional plots. The resultant DDX for the Au(p,p'x) reaction at 15 degrees is compared with that by Bertrand et al. It is confirmed that the threshold energy is lowered from 4.0 MeV to 1.5 MeV.

1. Introduction

Double differential cross sections (DDXs) for evaporated charged particles are important to evaluate energy deposition and residual nucleus production for developing various technologies of the accelerator driven system and particle radiation therapy. Since the evaluation is made by employing model calculation, it is necessary that nuclear reaction models have high predictive power for DDXs of light charged particle production.

The light charged particle production from intermediate energy proton-nucleus interactions is well described by using a two-stage model of the intra-nuclear cascade (INC) model and the generalized evaporation model (GEM) [1] in most cases. GEM, which is based on the Weisskopf-Ewing model [2], has been thought to have high predictive power for DDXs of evaporated particle emission from various nuclear reactions. However, due to the recent improvement in accuracy of the INC model, it has been revealed that GEM fails to predict DDXs accurately for some nuclear reactions [3, 4]. The inaccurate prediction of GEM is remarkable on proton emission from a heavy target. Thus, necessity for improvement of GEM has been pointed out, and a theoretical study on low energy proton emission [5] is starting in order to improve GEM. For the improvement, experimental data covering low energy particle emission for various targets and angles are required.

The experimental data taken by Bertrand et al. [6] are available as the existing data. However, the data for heavy targets are inconvenient to improve GEM because of scattered behavior in the low energy region and lack of low energy data and measured angles. In addition to this, the data by Bertrand et al. are less accurate around the threshold energy of detection. Thus, new series of experimental data covering low energy particle emission for various targets and angles are required.

To obtain the data, we develop Bragg curve counters (BCCs) [7, 8] with two built-in SSDs, which are expected to provide lower energy threshold than two silicon detectors can provide. The detectors are tested for measurement of DDXs on light to heavy targets.

2. Experiment

The test of BCCs with two built-in SSDs was performed at Cyclotron facility of National Institute of Radiological Sciences. The schematic view of the experimental setup is shown in Fig. 1. A scattering chamber was connected directly to the beam duct of the cyclotron and evacuated to less than 10^{-3} Pa. Incident protons from the cyclotron hit a target located inside the scattering chamber and entered a Faraday cup consisting of a stainless–steel pipe and a graphite beam dump. We chose the combinations of protons with energy of 70-MeV and targets of ^{9}Be, ^{nat}C, ^{27}Al, ^{nat}Cu, and ^{197}Au for the measurement of proton-induced light charged particle production DDXs. The targets were mounted on a target changer. Secondary charged particles emitted from the target were detected with two sets of detectors placed at 15 and 120 degrees in the laboratory system.

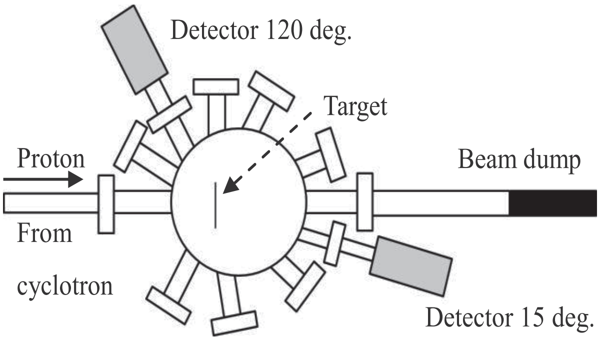

Figure 1. Schematic view of experimental setup. Incident protons come from the left side of this view.

The schematic drawing of the detector, BCC with two built-in SSDs is shown in Fig. 2. By combining BCC with SSDs, the threshold energy of 1.5 MeV for protons is expected. This is because the BCC has a thin entrance window and self particle identification capability, as will be described below.

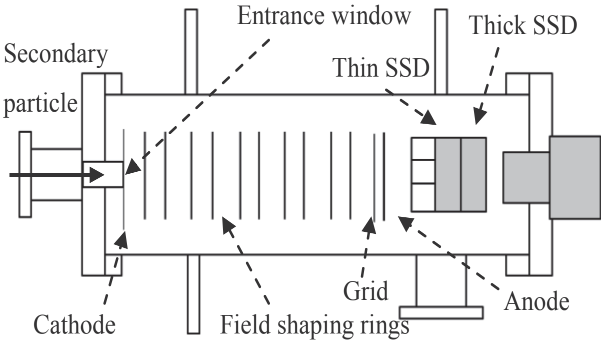

Figure 2. Schematic drawing of the BCC with two built-in SSDs. Secondary particles come from the left side of this drawing and pass through the entrance window.

The BCC is a parallel plate ionization chamber with a grid. The chamber is cylindrically shaped and sealed using

O-rings to keep 53.3 kPa (400 Torr) Ar + 10 % CH_4 gas as a counting gas. The gas pressure was adopted for detection of evaporated protons. The inside electrodes of the BCC consist of the cathode, field shaping rings, grid, and anode. The distances from the cathode to the grid and from the grid to the anode were set to 150 mm and 5 mm, respectively. The distances of 146 mm and 9 mm were also used to improve the ratio of the anode signal to noise for detection of protons. The anode plate is a round stainless-steel plate with a central hole 32 mm in diameter. The hole is covered with a 5-μm-thick aluminum foil which is connected with the stainless-steel plate electrically. Thus, the anode allows energetic secondary particles to penetrate with small energy loss, as will be described later. The field shaping rings are arranged at equal intervals to maintain a uniform electric field. The electric field is formed by providing high voltage for the cathode, field shaping rings and grid. The cathode is a round stainless-steel plate with a central hole 10 mm in diameter covered with a 2.5-μm-thick aluminized Mylar film. Since the aluminized surface and the stainless-steel plate are connected electrically, the cathode plays the role of a thin entrance window, which introduces secondary charged particles with small energy loss.

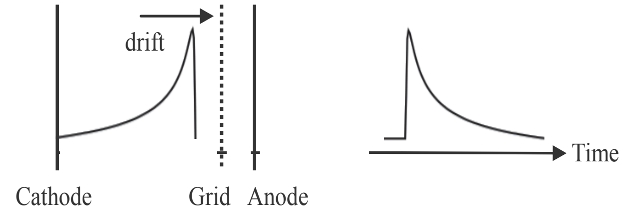

Figure 3. The distribution of electrons produced in the BCC (left) and the time distribution of the anode signal (right).

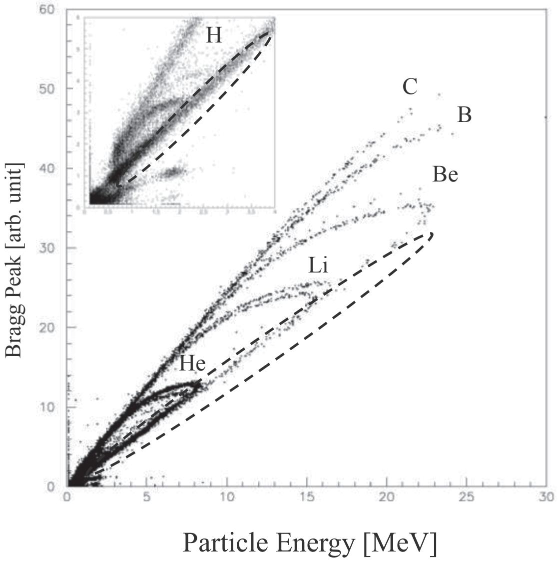

Figure 4. Secondary particle energy vs Bragg peak (atomic number) two-dimensional plot. The inset shows the plot in low energy region up to 4 MeV. The identified secondary particles from H to C are shown. Particles penetrating the anode are identified inside dashed circles.

The secondary particle stopped in front of the grid produces electron-ion pairs along its trajectory by ionizing the counting gas. Since the number of electrons is proportional to the energy deposited by the secondary particle, distribution of electrons corresponds to Bragg curve. Keeping the distribution, the electrons drift toward the grid due to the electric field, and then all the electrons pass through the grid and reach the anode. In this case, time distribution of the anode signal has inverse shape of the original distribution of electrons (Fig.3). Therefore, the energy and the atomic number of the secondary particle can be deduced from integral and peak height of the anode signal, respectively.

Fig. 4 shows the secondary particle energy vs Bragg peak (atomic number) two-dimensional plot for the carbon target. Secondary particles with enough energy to form the Bragg peak are identified. For the high energy side of hydrogen, helium, lithium and beryllium, particles penetrating through the anode are observed within dashed circles in Fig.4. These particles are also detected with SSDs behind the anode and identified by applying the *ΔE*–*E* method. Since the SSDs are 150 μm- and 2 mm-thick silicon surface-barrier detectors, the upper limit energy of the measurement is limited to be 15 MeV for protons.

The measured data were corrected to remove the effects of energy loss in the target, the entrance window, and the anode, and then DDXs were obtained by normalizing the data with solid angle, the number of target atoms and the number of incident protons.

3. Results and discussion

Fig. 5 shows the secondary particle energy vs Bragg peak (atomic number) two-dimensional plot for the beryllium target. In this figure, the high energy region is not shown, but the low energy region is focused to discuss self particle identification capability for hydrogen. In the energy range from 1 MeV to 3 MeV, the hydrogen isotopes of protons, deuterons and tritons are identified because the Bragg peak height depends on the mass number of the charged particle as well as the atomic number. It should be noted that the threshold energy of proton identification is 1.5 MeV, as mentioned in the previous section.

Fig. 6 shows *ΔE* (BCC) vs *E* (thin SSD) two-dimensional plot for the beryllium target. The hydrogen isotopes are also identified in this figure in the energy range from 0.5 MeV to 6 MeV due to good energy resolution of the BCC. The helium isotopes penetrating through the thin SSD are observed as a folding back line from the maximum energy deposited in the SSD and the line overlaps partially with lines of identified proton, deuteron and triton. This overlap can be removed analytically by using the signal of the thick SSD.

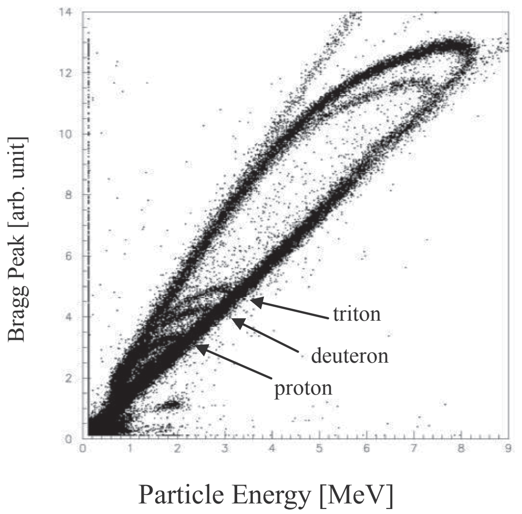

Figure 5. Secondary particle energy vs Bragg peak (atomic number) two-dimensional plot. The only low energy region up to 9 MeV is displayed. The identified particles of proton, deuteron and triton are shown.

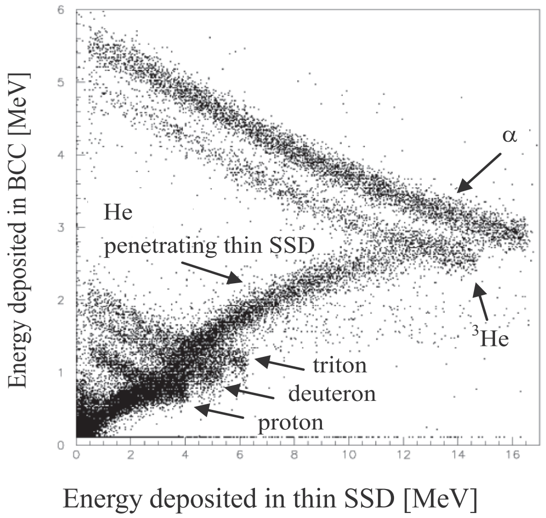

Figure 6. *ΔE* (BCC) vs *E* (thin SSD) two-dimensional plot. The identified particles of proton, deuteron, triton, ^{3}He and α are shown. The helium penetrating thin SSD is displayed.

Fig. 7 shows the experimental result of DDX for the Au(p, p’x) reaction at 15 degrees. Since the upper limit of present data is limited to be 15 MeV, the only low energy region below 20 MeV is displayed. The result for 61.5–MeV incident protons taken by Bertrand et al. [6] is also plotted in this figure. For the threshold energy, present data are down to 1.5 MeV whereas data taken by Bertrand et al. exist down to 4.0 MeV. The threshold energy is lowered as expected. Both data by present and Bertrand et al. show increasing cross sections toward low energies below 5 MeV, in contrast to the expected behavior under the Coulomb barrier (8 MeV). For the large values, further studies are needed since it is impossible to rule out a possibility of the effect caused by background components for the present. From 5 MeV to 10 MeV, present data gradually increases, while data taken by Bertrand et al. jumps sharply. Above 10 MeV, present data shows increment with secondary proton energy, which is the same behavior as data by Bertrand et al.

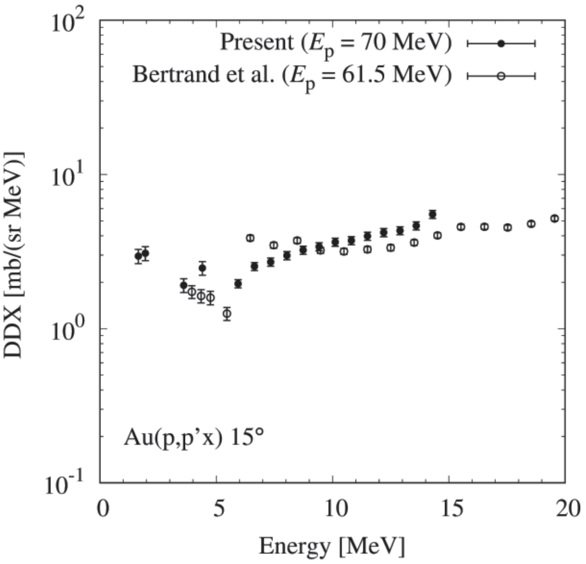

Figure 7. DDX for the Au(p, p’x) reaction at 15 degrees. The closed circles indicate present data for incident energy E_p = 70 MeV and open circles data taken by Bertrand et al. for E_p = 61.5 MeV.

4. Conclusion

We developed BCCs with two built-in SSDs to obtain experimental data covering low energy particle emission. The detectors were tested for measurement of DDXs on light to heavy targets. By combining BCC with SSDs, the energy threshold was lowered to 1.5 MeV for secondary protons. The result of DDX for the Au(p, p’x) reaction at 15 degrees was obtained down to lower energy than existing data. For the data below 5 MeV, further studies are needed to rule out the possibility of the effect by background components.

References

[1] S. Furihata: Nucl. Instr. and Meth. B 171, 251 (2000).
[2] V. Weisskopf: Phys. Rev. 52, 295 (1937).
[3] Y. Uozumi, T. Yamada and M. Nakano: J. Nucl. Sci. Technol. 52, 264 (2014).
[4] Y. Uozumi, T. Mori, A. Sonoda and M. Nakano: EPJ Web of Conference 122, 1 (2016).
[5] Y. Yamaguchi, Y. Uozumi and M. Nakano: EPJ Web of Conference 122, 1 (2016).
[6] F. E. Bertrand and R. W. Peelle: Phys. Rev. C 8, 1045 (1973).
[7] T. Sanami, M. Hagiwara, T. Oishi, M. Baba and M. Takada: Nucl. Instr. and Meth. A 589, 193 (2008).

[8] M. Hagiwara, T. Sanami, T. Oishi, M. Baba and M. Takada: Nucl. Instr. and Meth. A 592, 73 (2008).

34 Consistency check of experimental data using evaluated photonuclear data

Nobuyuki Iwamoto
Nuclear Data Center, Nuclear Science and Engineering Center, Japan Atomic Energy Agency, Tokai, Ibaraki 319-1195, Japan
e-mail: iwamoto.nobuyuki@jaea.go.jp

Evaluation of photon-induced nuclear data on ^{90}Zr, ^{117,120,124}Sn, ^{133}Cs, ^{159}Tb, ^{165}Ho and ^{181}Ta was performed, using the CCONE code, together with covariance estimation made by the KALMAN code in the incident energies up to 30 MeV. The evaluated photoneutron cross sections and derived neutron-multiplicity transition (NMT) functions were compared with the experimental data of two pioneering groups.

The cross sections obtained by these groups are consistent for ^{117,120,124}Sn and ^{165}Ho over the threshold energy of the $(\gamma, 2n)$ reaction. In contrast, those of ^{90}Zr, ^{133}Cs, ^{159}Tb and ^{181}Ta have differences in the region. These disagreements lead to large evaluation errors. The NMT functions being the ratio of partial photoneutron to neutron yield cross sections reveal the uncertainty of the experimental data present above ∼20-25 MeV, compared with the evaluated results.

1. Introduction

A series of experimental survey for the photonuclear cross sections was carried out in the 1960-80s. Main efforts were made by two groups of Lawrence Livermore in USA and Saclay in France. Subsequently, it was found for some nuclides that there was inconsistency between the data measured by these groups. Hence, reliability of the data was questioned.

Recently, Varlamov et al. [1] introduced neutron-multiplicity transition (NMT) functions to investigate the validity of partial photoneutron cross sections. The NMT functions F_i were defined as the ratio of partial photoneutron cross section $\sigma(\gamma, inx)$ to the neutron yield cross section $\sigma(\gamma, xn)$:

$$F_i = \frac{\sigma_{(\gamma,inx)}}{\sigma_{(\gamma,xn)}} = \frac{\sigma_{(\gamma,inx)}}{\sigma_{(\gamma,1nx)} + 2\sigma_{(\gamma,2nx)} + 3\sigma_{(\gamma,3nx)} + ...}, \tag{1}$$

where i represents the neutron multiplicity. The NMT functions of F_1 and F_2 for the $(\gamma, 1nx)$ and $(\gamma, 2nx)$ reactions (i.e. one neutron and two neutrons emission reactions including, for example, $(\gamma, 1n)$ and $(\gamma, 1np)$ reactions and $(\gamma, 2n)$ and $(\gamma, 2np)$ reactions, respectively) take values smaller than 1 and 0.5, respectively, as a rule. According to this expression, Varlamov et al. pointed out that the measured cross sections of the Livermore and Saclay groups for $(\gamma, 1nx)$ and $(\gamma, 2nx)$ reactions had the values being “physically not allowed”.

Evaluation of photonuclear data has been performed by relying on available measured data, whose experimental techniques and analytical method are examined in the evaluation. In this work, we adopted the NMT functions and checked whether the measured data can be used to evaluate the photoneutron cross sections. In order to do this, the photon-induced reaction cross sections were calculated by using a nuclear reaction calculation code CCONE, and then, the NMT functions were derived from the partial photoneutron cross sections. In addition, the covariance was evaluated, considering the propagation of model parameter uncertainties to the cross sections.

2. Evaluation methods

2.1 Cross sections

Photon-induced reaction cross sections were calculated from the Hauser-Feshbach statistical model and pre-equilibrium two-component exciton model [2] in the CCONE code [3]. The incident energy ranges from 1 to 140 MeV. The discrete nuclear levels were taken from the RIPL-3 database [4]. The nuclear levels in the excitation energy higher than the upper energy of the discrete levels were described by the composite level density formulation of Gilbert and Cameron [5], in which the expression of Mengoni-Nakajima [6] was adopted for the Fermi-gas model. The E1 photon strength function is important to represent the giant dipole resonance. The modified Lorentzian form was adopted to give the E1 transition strength [7]. The M1 and E2 transitions of gamma-rays are also possible. The strength was described by the standard Lorentzian form [8]. The particle emissions of neutrons, protons, deuterons, tritons, ^{3}He, and alpha were taken into account. The parameters of optical model potential (OMP), which expresses the particle transmission coefficients, were employed from Koning and Delaroche [9] for neutrons and protons, Han et al. [10] for deuteron, folding form based on the Koning-Delaroche OMP for triton, Xu et al. [11] for ^{3}He, and Avrigeanu and Avrigeanu [12] for alpha particle.

2.2 Covariance

The covariance estimate in the incident energy region up to 30 MeV was performed with the KALMAN code [13], which employs a generalized least-squares fitting method based on the Bayesian technique. The posterior covariance matrix was calculated from the prior model parameter and experimental covariances. The uncertainties were considered for the following model parameters: pre-equilibrium model, level density, photon strength function, neutron and proton OMPs. The experimental errors were set to cover the spread of measured data, instead of formally adopting the given errors. The statistical and systematic components of the error were assumed to have equal fraction [14].

3. Results

The calculated results were compared to the measured data of Livermore and Saclay groups in **Figs. 1-8**. The top panel of Fig. 1 shows the photoneutron cross sections for $(\gamma, 1nx)$, $(\gamma, 2nx)$ and (γ, xn) reactions of ^{120}Sn. The present evaluation well explains the energy dependence of the measured cross sections. The $(\gamma, 1nx)$ reaction cross section of the Livermore group increases and undulates above 22 MeV, whereas there is no remarkable change in the $(\gamma, 2nx)$ reaction cross section. Although the $(\gamma, 1np)$ and $(\gamma, 1n\alpha)$ reaction channels are already open, their cross sections are still small in this energy region, according to the present results (e.g., their contribution to the $(\gamma, 1nx)$ reaction cross section is only 1% at 25 MeV). Hence, this characteristic is hard to be explained in the current framework. The middle panel represents the evaluated errors. Taking account of the cross sections measured by the two groups, the errors in the considered energy range are 10-50% and 20-30% for $(\gamma, 1nx)$ and $(\gamma, 2nx)$ reactions, respectively. The bottom panel illustrates the NMT functions F_1 and F_2. The estimated errors almost cover the measured F_1 and F_2 functions below 22 MeV, above which the experimental data have negative values for the $(\gamma, 1nx)$ and $(\gamma, 2nx)$ reactions and larger values than 0.5 for the $(\gamma, 2nx)$ reaction. The latter defect comes from the limitation of the NMT function. It is found that the NMT functions provides an additional information to judge the validity of a set of experimental data. In this comparison, most of these data, however, are still valid, considering the given large errors.

Figures 2-8 are the same ones as Fig. 1, but for ^{90}Zr, ^{117,124}Sn, ^{133}Cs, ^{159}Tb, ^{165}Ho and ^{181}Ta, respectively. The experimental data of the Saclay group were multiplied by 0.88 for ^{90}Zr.

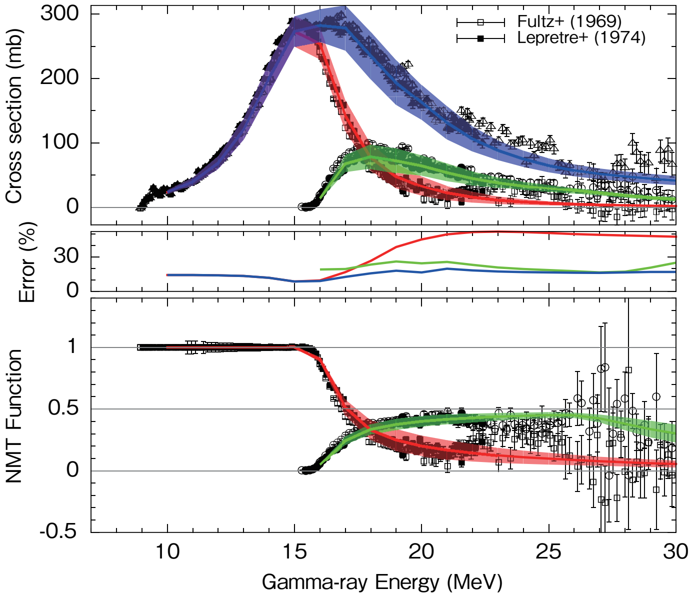

Figure 1: Comparisons of the calculated results with experimental data of Livermore (open symbols) and Saclay (filled symbols) groups for ^{120}Sn. (top panel) The cross sections of $(\gamma, 1nx)$, $(\gamma, 2nx)$ and (γ, xn) reactions shown by squares, circles and triangles for the measured data and solid, dashed and dotted lines for the calculated ones, respectively. (middle panel) The evaluated errors in percent. (bottom panel) The NMT functions for $(\gamma, 1nx)$ and $(\gamma, 2nx)$ reactions.

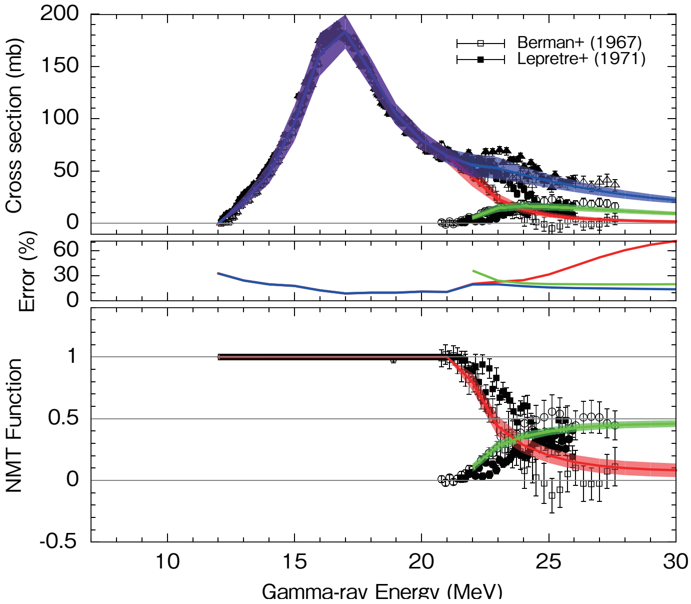

Figure 2: Same as Fig. 1, but for ^{90}Zr

The correction factor was recommended by Berman et al. [15]. The data of the Livermore group were also multiplied by 1.09, 1.08, 1.16 and 1.22 for ^{133}Cs, ^{159}Tb, ^{165}Ho and ^{181}Ta, respectively. The values for the first three nuclides were empirically fixed so as to coincide with the $(\gamma, 1nx)$ reaction cross section of the Saclay data, taking account of the fact that the Livermore data were typically underestimated. The factor for ^{181}Ta was taken from Lee et al. [16].

The Saclay data for $(\gamma, 1nx)$ reaction of ^{90}Zr have bump around 23 MeV as shown in the top panel of Fig. 2, in contrast to the Livermore data which do not indicate such structure.

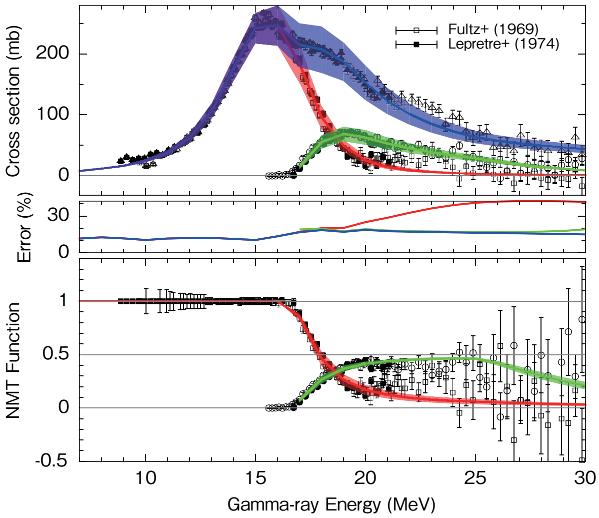

Figure 3: Same as Fig. 1, but for ^{117}Sn

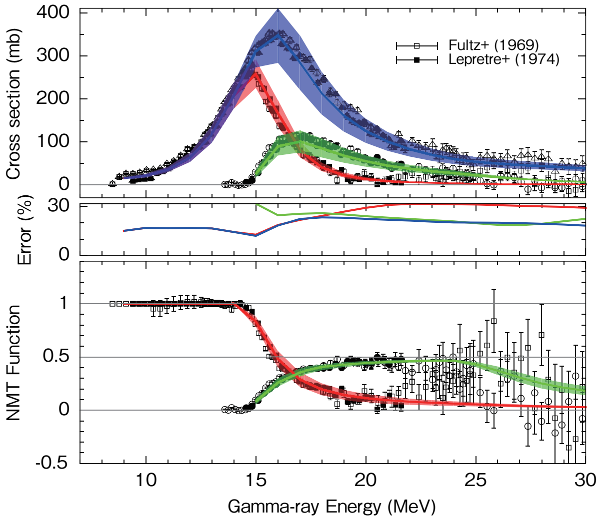

Figure 4: Same as Fig. 1, but for ^{124}Sn

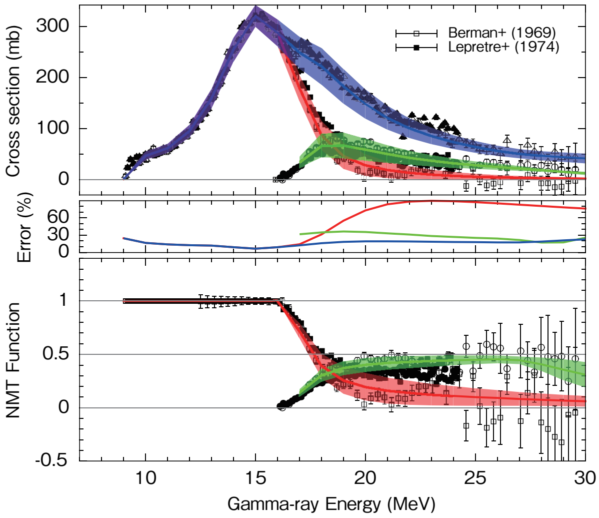

Figure 5: Same as Fig. 1, but for ^{133}Cs

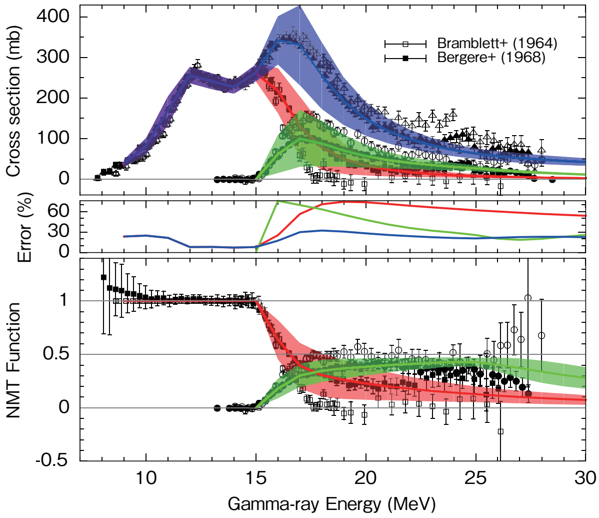

Figure 6: Same as Fig. 1, but for ^{159}Tb

This leads to small cross sections of $(\gamma, 2nx)$ reaction. The present evaluation supports the Livermore data. The Saclay data exceed the range of the derived error. Hence, we cannot give results simultaneously explaining the Livermore and Saclay data. This bump might be ascribed to incorrect neutron multiplicity sorting. The same characteristic above 21 MeV can also be found in the F_1 and F_2 functions. The evaluated results are in reasonable agreement with the Livermore data.

The similar differences encountered in the evaluation of ^{90}Zr are present between the Livermore and Saclay data for ^{133}Cs, ^{159}Tb and ^{181}Ta above the threshold energy of $(\gamma, 2n)$ reaction. In fact, these are well-known trend that the cross sections of the Livermore group for $(\gamma, 1nx)$ reaction are small, and, in contrast, those for $(\gamma, 2nx)$ reaction are large, compared to those of the Saclay group. As a result, the evaluated errors are large (over 60%). On the other hand, the photoneutron cross sections of ^{117,120,124}Sn and ^{165}Ho have consistency between the both groups. The experimental data, however, have a high dispersion with large errors above ~25 MeV as highlighted by the NMT functions. This characteristic is almost true for the measured data of the considered nuclides as already mentioned in the case of ^{120}Sn. Therefore, when the measured data of the Livermore groups were available, attention should be paid to the reliability of

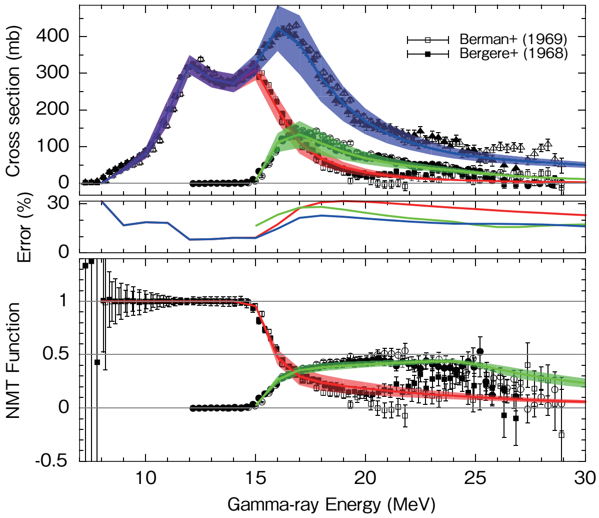

Figure 7: Same as Fig. 1, but for ^{165}Ho

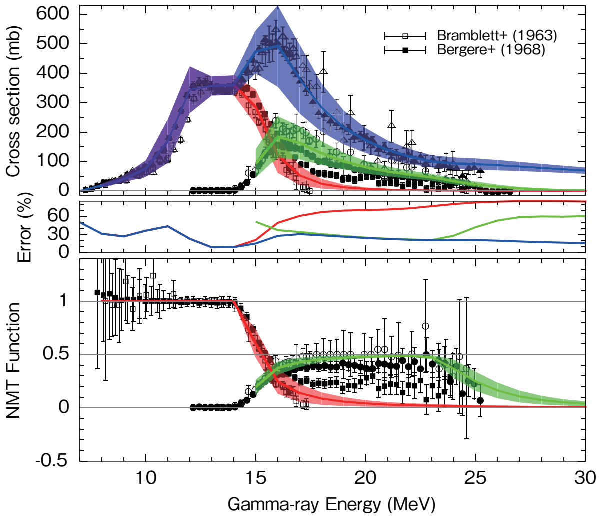

Figure 8: Same as Fig. 1, but for ^{181}Ta

photoneutron cross sections in the energy region especially higher than ~20-25 MeV.

4. Conclusion and summary

Evaluation of photon-induced nuclear data on ^{90}Zr, ^{117,120,124}Sn, ^{133}Cs, ^{159}Tb, ^{165}Ho and ^{181}Ta was performed, using the CCONE code. The covariance of photoneutron cross sections was also estimated in the incident energies up to 30 MeV by using the KALMAN code. The calculated results for the partial photoneutron and neutron yield cross sections and NMT functions were compared with the data measured by the groups of the Lawrence Livermore in USA and Saclay in France.

The large differences in the cross sections are seen between the Livermore and Saclay groups for ^{90}Zr, ^{133}Cs, ^{159}Tb and ^{181}Ta above the threshold energy of $(\gamma, 2n)$ reaction, above which the estimated errors exceed 60%. It is expected to measure these partial photoneutron cross sections more carefully, in order to enhance the accuracy of those photonuclear data. In contrast, the cross sections of ^{117,120,124}Sn and ^{165}Ho by the Livermore group are consistent with those by the Saclay group even above the $(\gamma, 2n)$ reaction threshold energy. The NMT functions based on their experimental data represent fiuctuation being less clear in the cross sections above ~20-25 MeV, in comparison with the evaluated results, and have values contradicting with the definition as seen also in the other nuclides. In the present cases, most of these data, however, are consistent with the limitation of NMT functions because they are given with large uncertainties.

Acknowledgments

This work was supported by JSPS KAKENHI Grant Number 26420876.

References

[1] V.V. Varlamov et al., Eur. Phys. J. A50, 114 (2014).

[2] A.J. Koning, M.C. Duijvestijn, Nucl. Phys. A744, 15 (2004).

[3] O. Iwamoto, Nuclear Data Sheets, 131, 259-288 (2016).

[4] R. Capote et al., Nucl. Data Sheets 110, 3107 (2009).

[5] A. Gilbert, A.G.W. Cameron, Canadian J. Phys. 43, 1446 (1965).

[6] A. Mengoni, Y. Nakajima, J. Nucl. Sci. Technol. 31, 152 (1994).

[7] V.A. Plujko et al., J. Nucl. Sci. Technol. Suppl. 2, 811 (2002).

[8] J. Kopecky, M. Uhl, Phys. Rev. C41, 1941 (1990).

[9] A.J. Koning, J.P. Delaroche, Nucl. Phys. A713, 231 (2003).

[10] Y. Han et al., Phys. Rev. C 74, 044615 (2006).

[11] Y. Xu et al., Sci. China, Phys. Mech. & Astron., 54, 2005 (2011).

[12] M. Avrigeanu, V. Avrigeanu, Phys. Rev. C82, 014606 (2010).

[13] T. Kawano, K. Shibata, JAERI-Data/Code 97-037 (1997) [in Japanese].

[14] N. Iwamoto, EPJ Web of Conferences, 111, 03002 (2016).

[15] B.L. Berman et al., Phys. Rev. C36, 1286 (1987).

[16] Y.-O. Lee, T. Fukahori, J. Chang, J. Nucl. Sci. Technol. 35, 685 (1998).

35 Gamma strength function of Ca-40 below the particle threshold for medical-physics applications

A. Makinaga[1, 2], R. Schwengner[3], S. Reinicke[3], R. Depalo[4], L. Wagner[3], T. Koegler[3] and A. Wagner[3]

[1]Jein Institute for Fundamental Science, 606-8638, Kyoto, Japan
[2]Hokkaido University, 060-0810, Sapporo, Japan
[3]Helmholtz-Zentrum Dresden-Rossendorf, 01328 Dresden, Germany
[4]INFN and University of Padova, 35131 Padova, Italy
*E-mail: makinaga@nucl.sci.hokudai.ac.jp

Abstract

Photo-absorption experiment on Ca-40 up to the neutron threshold at 15.6 MeV was measured at the bremsstrahlung facility of γELBE in Helmholtz-Zentrum Dresden Rossendorf. Gamma strength function of Ca-40 which is one of the main component in the human body is basic physical quantity in the radiation treatment. In this study, we performed the precise measurement of gamma-ray transitions from excited Ca-40 to evaluate information related to the nuclear structure.

1. Introduction

Photon strength of Ca-40 is an important parameter to estimate the photoabsorption cross section. The Ca-40 isotope, which is the main component of bone in the human body, is important from the view point of medical physics. For example, X-ray scanning systems using the nuclear resonance fluorescence (NRF) technique have been investigated for gamma simulated emission computed tomography (GSECT) because NRF imaging can get the information of not only elemental but also nuclear characteristic properties. GSECT is also said to be effective to detect a bias of material components of cancer cells in the normal tissue [1]. For another example, in case of the radiation therapy using real-time tracking radiation therapy (RTRT) and image-guided radiation therapy (IGRT), the effect of photonuclear reactions including photon scattering in the body influences the precision of the perspective image and radiation treatment results [2].

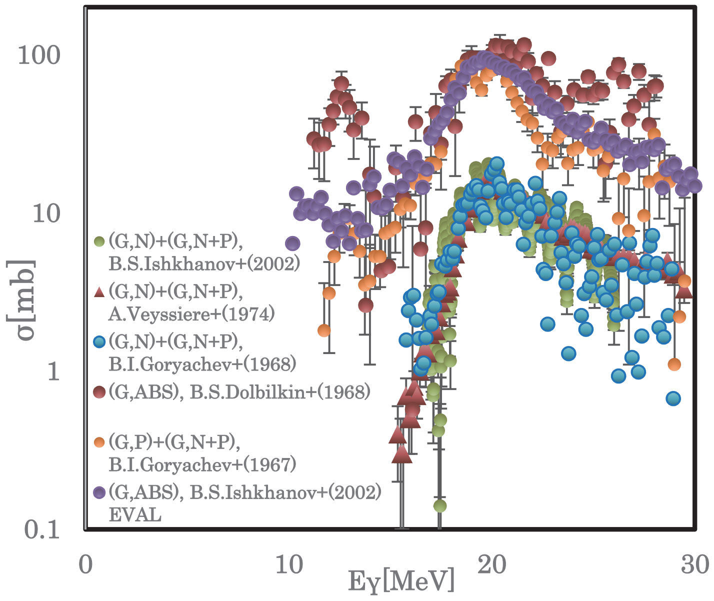

Figure 1 Photonuclear reaction cross section for Ca-40

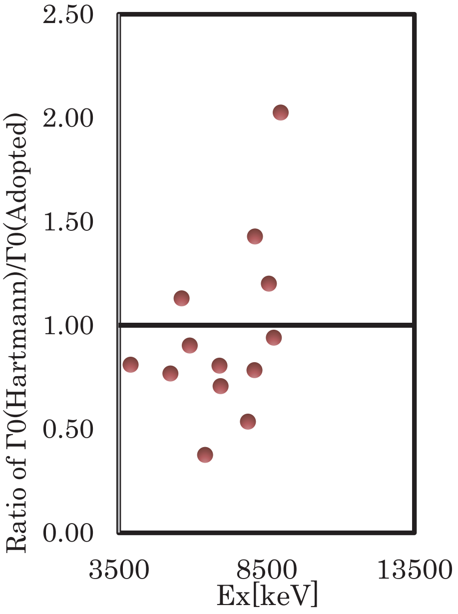

Figure 2 Ratio of gamma width of T.Hartman et al. [14] and ENSDF [21] for Ca-40

Concretely speaking for the photon therapy, ICRP Publication 86 reported the estimated relative standard uncertainties, which consist of 4 stages, as follows. 1) Absolute dose determination at the reference point in a water phantom (beam calibration) (2.2%), 2) Relative dosimetry (water or plastic phantom measurements) (2.1%), 3) Dose calculation to the patient (3.7%), 4) Dose delivery (along complete treatment) (3.4%) [3]. The combined standard uncertainty in all steps is 5.9 %. Furthermore, considering the clinical situation, a combined standard uncertainty is estimated about 5%. For nuclear data, we should especially care about the effect on the "step 3" as mentioned above. A more precise requirement of the dose calculation is also published as AAPM TG53 [4]. While photonuclear reactions themselves contribute only a few percent in the radiation treatment for x-ray, precise analysis of uncertainties from the view point of nuclear data is not performed yet.

From the view point of nuclear physics, low-energy electric dipole (E1) excitations, especially below the particle-separation energy, have been actively studied using the photon-scattering method [5-12]. In particular, Ca isotopes are suitable to search for the extra enhancement near the particle threshold called pygmy dipole resonance (PDR) and for well-studied relation between the PDR and neutron skin thickness [13]. For the Ca-40 isotope, the (γ,p) channel opens at Sp = 8.329 MeV + some energy, at which tunneling through the Coulomb barrier starts. The height of the Coulomb barrier is about 4 MeV. There is work by T. Hartmann et al., [14]. Only 3 states with spin 1 but 9 states with spin 2 were found up to 9 MeV. Finally, for the nuclear data for Ca-40, there is only one experimental data set for photoabsorption data, and one evaluation was done by B. S. Ishkhanov et al., using old photon-induced particle emission data [15] (see Figure 1). The existing other experimental data are also very old and have large uncertainties [16-21]. Additionally, the gamma decay widths Γ_0 have still some differences between recent results [14] and ENSDF adopted values in Ref. [21] (see Figure 2).

In this study, the dipole strength distribution of Ca-40 was studied in a photon-scattering experiment using bremsstrahlung produced with an electron energy of 15.6 MeV at the linear accelerator ELBE. We investigated with the sensitive setup γELBE whether there are more transitions deexciting states with small intensity.

2. Photon-scattering experiment at γELBE

The photon-scattering cross section $\sigma_{\gamma f}(E_R)$ can be measured via the γ–ray transition from a given excited level E_R and de-excitation to a level E_f in the target. In case of non-overlapping resonances, photon scattering is described to process via a compound nucleus reaction with uncorrelated channels f characterized by the partial width Γ_f, so the photon-scattering cross section $\sigma_{\gamma f}(E_R)$ can be described as:

$$\sigma_{\gamma f}(E_R)=\sigma_{\gamma}(E_R)\frac{\Gamma_f}{\Gamma} \qquad (1)$$

Here, all partial widths contribute to the total level width $\Gamma=\Sigma\Gamma_f$.

$$I_S = \int_0^{\infty}\sigma_{\gamma\gamma}(E)dE = \frac{2J_R+1}{2J_0+1}\left(\frac{\pi\hbar c}{E_R}\right)^2\Gamma_0\frac{\Gamma_f}{\Gamma} \qquad (2)$$

I_S is the integral over the scattering cross section for the level R and Γ_f is the partial width for a transition from R to a level f. The measured intensity of γ-rays emitted to the ground state at $E_\gamma=E_R$ at an angle θ can be expressed as:.

$$I_\gamma(E_\gamma,\theta)=I_s(E_R)\Phi(E_R)\varepsilon(E_\gamma)N_{at}W(\theta)\frac{\Delta\Omega}{4\pi} \qquad (3)$$

Here, N_{at} is number of the target nuclei per area unit, $\varepsilon(E_\gamma)$ is the absolute full-energy peak efficiency at E_γ , $\Phi(E_R)$ is the absolute photon flux at E_R, $W(\theta)$ is the angular correlation of this transition, and $\Delta\Omega$ is solid angle of the detector.

If the electron energy is high enough above a particular level, the experiments with bremsstrahlung lead to the possibility of the population of a level by a feeding transition from a higher-lying level. Such feeding increases the intensity of the transition to the ground state from the considered resonance R. The intensity of the transition to the ground state becomes a superposition of the rate of elastic scattering and the intensity of the transitions feeding level R. The cross-section integral I_{s+f} can be expressed as:

$$\begin{aligned} I_{s+f} &= \int_0^{\infty}\sigma_{\gamma\gamma}(E)dE + \sum\nolimits_{i>R}\sigma_{\gamma i}\frac{\Gamma_0}{\Gamma}dE \\ &= \frac{2J_R+1}{2J_0+1}\left(\frac{\pi\hbar c}{E_R}\right)^2\frac{\Gamma_0^2}{\Gamma} + \sum\nolimits_{i>R}\frac{\Phi(E_i)}{\Phi(E_R)}\frac{2J_i+1}{2J_0+1}\left(\frac{\pi\hbar c}{E_i}\right)^2\Gamma_0^i\frac{\Gamma_R^i}{\Gamma^i}\frac{\Gamma_0}{\Gamma} \qquad (4)\end{aligned}$$

Where, summation over i>R is that the energy E_i of a level which feeds the considered resonance R is higher than the energy E_R of this resonance. Γ_i, Γ_{i0}, and Γ^i_R are the total width of the level E_i, the partial width of the transition to the ground state and the partial width of the transition to the level R, respectively. Details of the experimental method are shown in Refs. [5-12].

The photon-scattering cross section measurement on Ca-40 was performed at the superconducting electron accelerator ELBE of the Research Center Dresden-Rossendorf. Bremsstrahlung was produced by hitting 7 μm niobium radiator with electron beams of 15.6 MeV electron kinetic energy and average currents of 300 μA. The produced bremsstrahlung was collimated by an Al collimator with a length of 2.6 m and an opening angle of 5 mrad. A cylindrical Al absorber of 10 cm length was placed between the radiator and the collimator to reduce the low-energy part of the bremsstrahlung spectrum. The scattered photons were measured with four 100% HPGe detectors surrounded by BGO escape-suppression shields. Two

Ge detectors were placed at 90 degrees relative to the photon-beam direction. The other two HPGe detectors placed at 127 degrees were used to deduce angular distributions of the γ rays. To reduce the low-energy part of background photons, absorbers of 8 mm Pb plus 3 mm Cu were placed in front of the detectors at 127 degrees and 13 mm Pb plus 3 mm Cu were used for the detectors at 90 degrees. A natural $CaCO_3$ target of 2 g was irradiated with bremsstrahlung. ^{11}B (99.5% enrichment) was used to determine the photon flux. In photon-scattering experiments, experimental spectra also include contributions of inelastic and cascade transitions. Figure 3 shows the gamma-ray spectrum detected with a HPGe detector at 127 degrees. Spectra of scattered photons were measured for 72 hours.

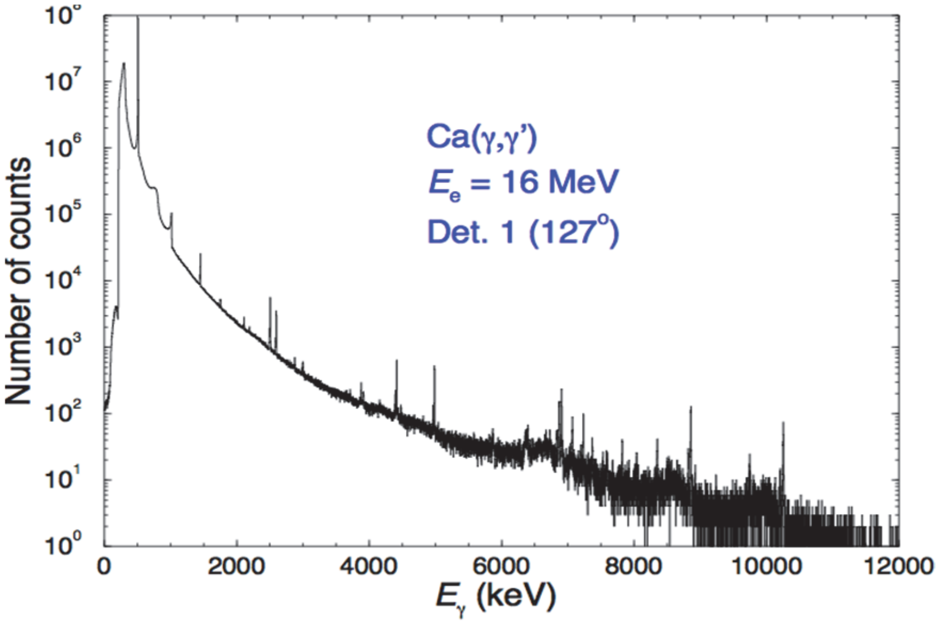

Figure 3 Gamma-ray spectrum of Ca-40 using an HPGe detector at 127 degrees

3. Summary

Photon-scattering on Ca-40 was measured at the bremsstrahlung facility γELBE of the Research Center Dresden-Rossendorf at an electron kinetic energy of 15.6 MeV. We successfully measured spectra of gamma rays scattered from Ca-40 with HPGe detectors. Further data analysis is in progress.

Acknowledgments

We thank the staff of the ELBE accelerator for their cooperation during the experiments. We also thank to T. Shizuma for his discussion of Ca-40 NRF experiment at New Subaru. A. M. also thanks Prof. M. Bando (JIFS, Kyoto Univ. and Osaka Univ.), and Prof. T. Wada (Kansai Univ.) for their interesting and warm discussion of radiation medical physics and radiation biology. This work was supported by Helmholtz Zentrum Dresden – Rossendorf and Hokkaido University.

References

[1] M. D. Belly, W. P. Segars and A. J. Kapadia, Med. Phys. 41, (6), 063902(2014).
[2] H. Shirato *et al.*, Int. Radiat. Oncol. Biol. Phys. 48, (2), 435(2000).

[3] ICRP Publication 86, Ann. ICRP 30(30) (2000).
[4] AAPM Task Group 53, Med. Phys. 25, (10), 1773(1998).
[5] R. Schwengner *et al.*, Phys. Rev. C 76, 034321(2007).
[6] G. Rusev *et al.*, Phys. Rev. C 77, 064321(2008).
[7] R. Schwengenr *et al.*, Phys. Rev. C 78, 064314(2008).
[8] N. Benouaret *et al.*, Phys. Rev. C 79, 014303(2009).
[9] G. Rusev *et al.*, Phys. Rev. C 79, 061302(R)(2009).
[10] R. Schwengner et al., Phys. Rev. C 81, (2009).
[11] A. Makinaga *et al.*, Phys. Rev. C 82, 024314(2010).
[12] A. Makinaga *et al.*, Phys. Rev. C 90, 044301(2014).
[13] T. Inakura *et al.*, Phys. Rev. C 84, 021302(R)(2011).
[14] T. Hartman *et al.*, Phys. Rev. C 65, 034301(2002).
[15] B. S. Ishkhanov *et al.*, Rep. Moscow State Univ. Inst. of Nucl.Phys. Reports, No. 2002, 27(2002).
[16] A. Veyssiere *et al.*, Nucl. Phys. A 227, 513(1974).
[17] B. I. Goryachev, *et al.*, Soviet Jour. of Nucl. Phys. 7 698(1968).
[18] B. I. Goryachev *et al.*, JTEP letters 5, 180(1967).
[19] B. S. Ishkhanov *et al.*, Sov. Jour. of Nucl. Phys. 13 655(1971).
[20] B. S. Dolbilkin *et al.*, Bull. Russ. Acad. Sci. 30, (2), 354(1966).
[21] ENSDF database, NNDC Online Data Service:　https://www.nndc.bnl.gov/ensdf/

This is a blank page.

36

Measurement of the neutron capture cross-section of ^{133}Cs as a part of the ImPACT project

*Brian Hales, Shoji Nakamura, Atsushi Kimura, Osamu Iwamoto
Nuclear Data Center, Japan Atomic Energy Agency
Tokai-mura, Naka-gun, Ibaraki-ken 319-1195 Japan
e-mail: hales.brian@jaea.go.jp

As a part of the ImPACT project, the neutron capture cross-section of ^{133}Cs in the energy region from thermal to approx. 1.5 keV was experimentally measured. Measured results show good agreement with JENDL-4.0[1] in the energy region below 10 eV. Resonances registered in JENDL-4.0 at 133 eV, 142 eV, 193 eV 373 eV were not observed. Detailed analysis is ongoing and must be concluded before assessing JENDL-4.0 accuracy elsewhere.

This work was funded by ImPACT Program of Council for Science, Technology and Innovation (Cabinet Office, Government of Japan).

Keywords: ImPACT, transmutation, Cesium-133, capture cross section, J-PARC MLF ANNRI

1. Introduction

It is currently planned to measure the neutron cross-section of the ^{135}Cs (half-life 2.3×10^{6} y), a long-lived fission product (LLFP), using the Accurate Neutron-Nucleus Reaction measurement Instrument (ANNRI), and the high-intensity pulsed neutron beam at the Material and Life Science Experimental Facility (MLF) at the Japan Proton Accelerator Research Complex (J-PARC), currently the highest intensity pulsed neutron beam in the world. Both ^{133}Cs (natural Cs, stable) and radioactive ^{137}Cs (half-life 30.0 y) are unavoidable contaminants in the ^{135}Cs sample. In working towards the measurement of ^{135}Cs, a measurement of non-radioactive ^{133}Cs has been conducted.

2. Experiment

Using the neutron time-of-flight (TOF) method and beamline #4, ANNRI, at the MLF in J-PARC, we have measured the neutron capture cross-section of ^{133}Cs from thermal up to epithermal energies (0.0253–2000 eV), with clear resonance resolution up to 1000 eV. The neutron flight-length from neutron moderator to Cs sample was 21.5 m. The gamma-rays emitted from the sample were measured by an array of 12 high purity germanium (HPGe) detectors. Details on the parameters of the beamline, detectors, and sample placement, can be found in Kimura, et al[2]. The beam was run in single-bunch mode for this experiment. Detector events were stored on a per-event basis, recording the pulse-height (PH) and TOF data of each event, and these data were saved for offline processing. The ^{133}Cs sample was natural monoisotopic Cs in the chemical form of Cs_2CO_3 powder, pressed into pellet form and wrapped in a fluorinated ethylene-propylene (FEP) film. The sample dimensions were diameter 5.04 mm, thickness 0.329 mm, and the sample weight was 17.2 mg. The sample's chemical purity was >99.99%. A blank sample of empty FEP film was used to subtract detector counts from sources other than the sample. Additionally, to account for the effects of scattering, a ^{208}Pb sample ($\sigma_{(n,n')} >> \sigma_{(n,\gamma)}$[1]) was also measured. The beam time of each run is indicated in **Table 1**. The beam power was 150 kW.

3. Analysis

The measured TOF spectra for the Cs, Au, Pb, and blank samples were recorded individually. To reduce the effects of electrical noise, and gamma-rays captured by H, Al, and Fe in and around the laboratory, only events in the energy range of 2.300 MeV < E_γ < 6.950 MeV were tallied. For comparison of the energies of various significant gamma-rays, see **Table 2**. The measured PH spectra are shown in **Fig. 1**. The measured TOF spectra are shown in **Fig. 2**.

Table 1 Beam time for each measurement

Sample	Time (hours)
^{133}Cs	16
^{197}Au	3
^{208}Pb	14
Blank	15

Table 2 Notable energies of various significant gamma-rays[3]

Reaction	Energy (MeV)	Source
^{28}Al β-decay	1.779	^{27}Al(n,γ) in beamline
^{1}H(n,γ)	2.223 25	Neutron moderator
(Gate lower bound)	2.300	
^{133}Cs(n,γ) max	6.891 39	Sample
(Gate upper bound)	6.950	
^{56}Fe(n,γ)	7.631 18	Experiment room
^{56}Fe(n,γ)	7.645 58	Experiment room
^{27}Al(n,γ)	7.724 03	Beam duct

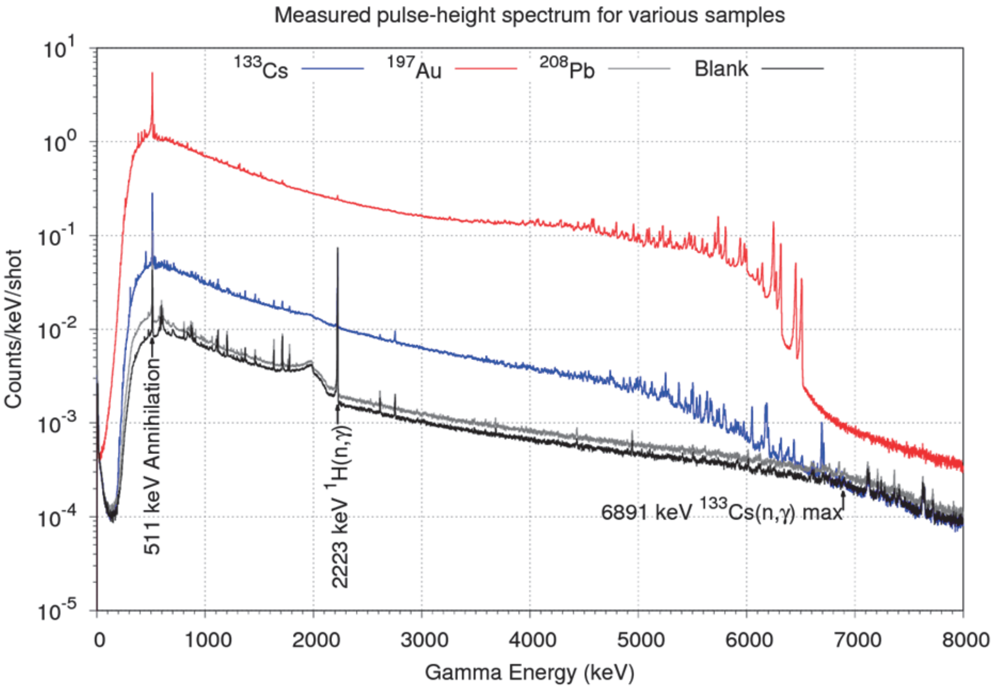

Figure 1 Measured pulse-height spectra of various runs. Most unlabeled peaks are from neutron capture of Al or Fe.

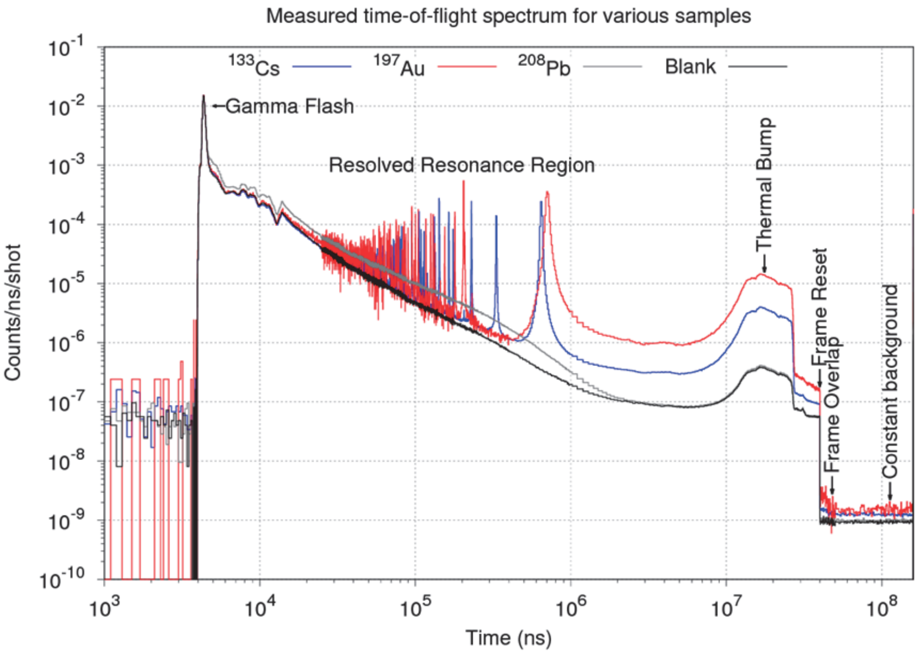

Figure 2　Measured TOF spectra of various runs

The effects of detector dead-time were negligible (<0.02% in largest resonances), but still accounted for.

For each 62 shots of the accelerator, only 58 are directed to our beamline and then 4 are directed to a neighboring facility. The count rate during this 4 shot rest was taken to be a combination of frame overlap and constant background rate, and the constant background was calculated and subtracted accordingly. The neutron flux of each run was assumed to be proportional to the integral of the beam current during each experiment, and spectra were normalized to neutron flux in this way. The effects of counts resulting from sources other than the sample were removed by subtracting the TOF spectrum of the blank measurement. Conversion from time to energy was done by examining the times of Au's resonances and comparing them with registered values in JENDL-4.0.

The neutron energy spectrum of the experiment was assumed to be unchanged from that of a previous experiment.

The effects of self-shielding were accounted for by simulating the system in PHITS v2.840[4] and comparing the average neutron flux within a given sample with that of the neutron flux upon the sample.

The number of counts due to scattering effects were accounted for by using ^{208}Pb measurement, and applying the following equation,

$$c_{Cs,scat.} = (c_{Pb-208} - c_{blank})\left(\frac{N_{Cs}}{N_{Pb-208}}\right)\left(\frac{\sigma_{Cs,scat.}}{\sigma_{Pb-208,scat.}}\right),$$

where $c_{Cs,scat.}$ is the number of counts due to scattering, $c_{Pb\text{-}208}$ is the number of counts measured in the ^{208}Pb run, c_{blank} is the number of counts measured in the blank run, N_{Cs} is the number of Cs atoms in the Cs sample, $N_{Pb\text{-}208}$ is the number of ^{208}Pb atoms in the ^{208}Pb sample, and $\sigma_{Cs,scat.}$ and $\sigma_{Pb\text{-}208,scat.}$ are the scattering cross-sections of Cs and ^{208}Pb, respectively (taken from JENDL-4.0[1]).

This un-normalized neutron cross-section was then normalized to the currently registered value in JENDL-4.0. As there are already a large number of measurements of the (n,γ) cross-section at 0.0253 eV, we chose to normalize to JENDL's value at 0.0253 eV of 28.90 b.

4. Conclusion

We have measured the neutron capture cross-section of ^{133}Cs from thermal energies up to around 1.5 keV. The measured cross-section data is shown in **Figs. 3** and **4**. While most resonances registered in JENDL-4.0 were observed, resonances at 133 eV, 142 eV, 193 eV, and 373 eV were not observed. Detailed analysis is ongoing, and is necessary to be completed before assessing JENDL-4.0's accuracy elsewhere. Particularly the effects of energy resolution must be properly assessed.

5. Future plans

Current methods used in the analysis are planned to be replaced with more accurate methodologies. Particularly, the effects of frame overlap have not yet been properly accounted for. Additionally, currently a previous experiment's measured neutron spectrum is assumed to be the neutron spectrum of this experiment, and this is planned to be replaced by the derived neutron spectrum from the ^{10}B measurement (data already taken). Also, a proper measurement and analysis of the time resolution function needs to be conducted before a full assessment of JENDL-4.0's accuracy can be made. Additionally, currently the absolute cross-section was derived by normalizing to JENDL-4.0's thermal cross-section, but it is planned to instead use the results of either the ^{197}Au measurement or a thickened ^{137}Cs sample measurement via the saturation method. Finally, in the time region just after the gamma-flash, it is not clear which counts are due to gamma-ray scattering, and which are due to (n,γ) reactions. A clear upper limit on the measured neutron cross-section cannot be made until such analysis is finalized.

Acknowledgements

The authors would like to thank the accelerator and technical staff at J-PARC for operation of the accelerator and the neutron production target and for the other experimental supports.

References

[1] K. Shibata, *et al.*: "JENDL-4.0: A New Library for Nuclear Science and Engineering," J. Nucl. Sci. Technol., **48**(1), pp.1-30 (2011).

[2] A. Kimura, *et al.*: "Neutron-capture cross-sections of ^{244}Cm and ^{246}Cm measured with an array of large germanium detectors in the ANNRI at J-PARC/MLF," J. Nucl. Sci. Technol., **49**(7), pp.708-724 (2012)

[3] J.K. Tuli, B. Pritychenko: "Thermal Neutron Capture g's (CapGam); 2018". Available from http://www.nndc.bnl.gov/capgam/.

[4] T. Sato, *et al.*: "Particle and Heavy Ion Transport Code System PHITS, Version 2.52," J. Nucl. Sci. Technol., **50**(9), pp.913-923 (2013)

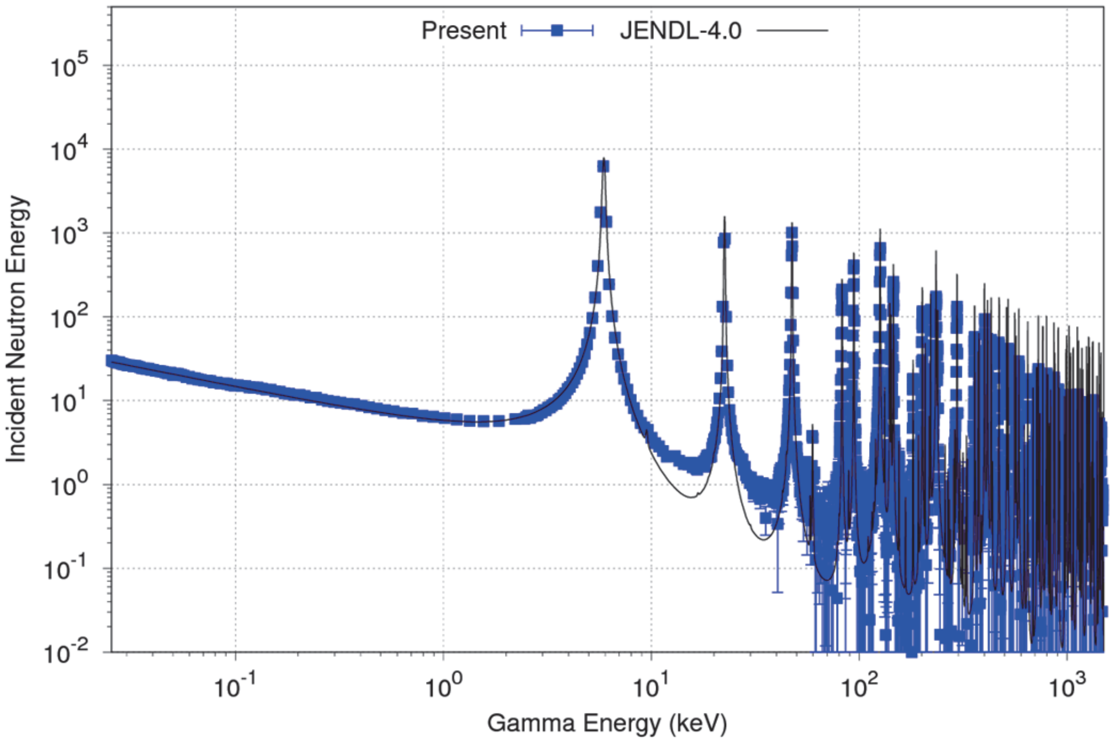

Figure 3 Derived cross-section of ^{133}Cs, energy range of 0.0253 eV to 1.5 keV

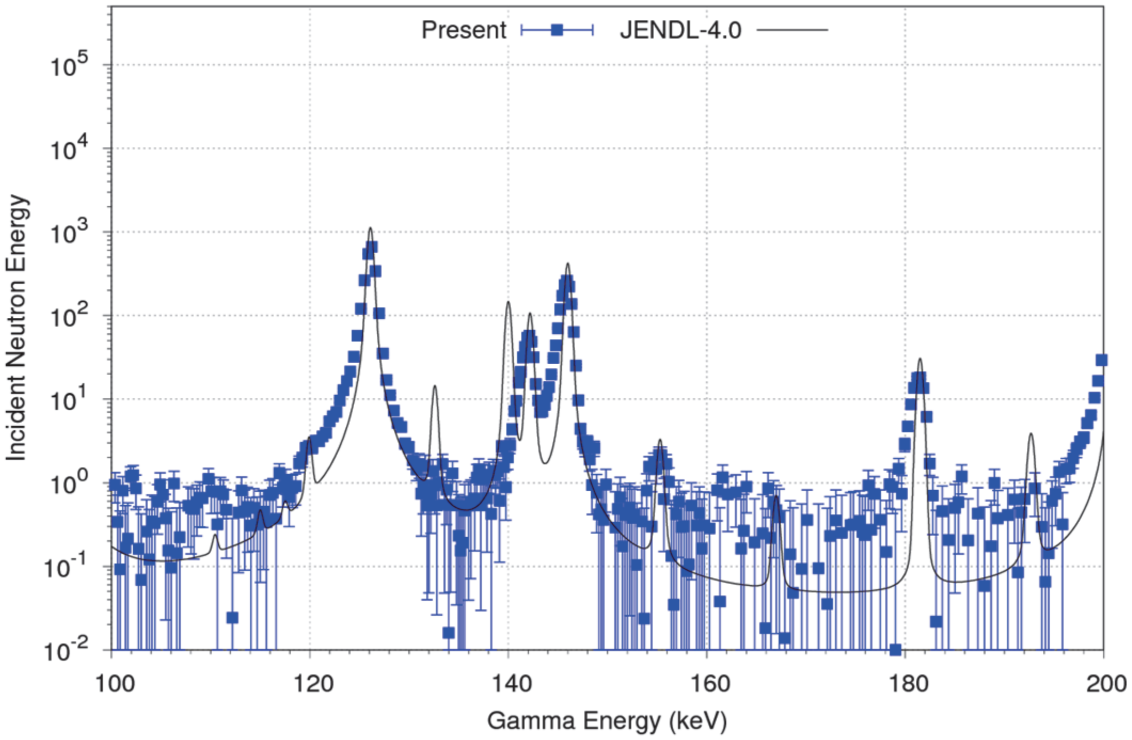

Figure 4 Derived cross-section of ^{133}Cs, energy range of 100 to 200 eV.
Note missing resonances at133 eV, 142 eV, and 193 eV.

This is a blank page.

37 Improvement of Gross Theory of Beta-decay on Single particle Treatment

Hiroyuki Koura[1,*)], Tadashi Yoshida[2)], Takahiro Tachibana[3)] and Satoshi Chiba[2)]
1) Advanced Science Research Center, Sector of Nuclear Science Research, Japan Atomic Energy Agency, Tokai, Ibaraki 319-1195, Japan
2) Laboratory for Advanced Nuclear Energy, Institute of Innovative, Research, Tokyo Institute of Technology, 2-12-1, Ookayama, Megro-ku, Tokyo 152-8550, Japan
3) Research Institute for Science and Engineering, Waseda University
Okubo 3-4-1, Shinjuku-ku, Tokyo 169-8555, Japan
*e-mail: koura.hiroyuki@jaea.go.jp

Abstract:

An improvement of the single-particle structure is carried out to the gross theory, a global beta-decay model. The gross theory is based on the sum rule of the intensity of the beta-decay transition and a strength function. This model gives reasonable results for global trend of beta-decay rates and delayed neutrons in the entire nuclear mass region. An attempt is made to improve the gross theory of nuclear beta-decay by consideration of the change in parity at the single-particle level of ground-state nuclei. In this treatment, the nuclear matrix elements are suppressed when the parity of the single neutron and proton levels is different for the allowed transition. The assignment of parity is done by using the Woods-Saxon-type single-particle potential. The discrepancies from experimental half-lives, which appeared in the vicinity of the magic number of neutrons and protons, are systematically improved in the nuclear mass region.

1. Introduction

Beta decay occurs due to the weak interaction and a nucleus in a neutron-rich nuclear mass region releases an electron, a gamma-ray, and an anti-neutrino. The beta-minus decay process occurs in neutron-rich nuclei, and it plays an important role in nuclear astrophysics, such as in the r-process nucleosynthesis in stars or when manipulating a nuclear reactor with delayed neutrons, which are emitted as an accompanying process. In order to theoretically estimate the β-decay rate and the delayed neutron probability, it is necessary to calculate the nuclear matrix elements of the beta decay. The gross theory is a macroscopic model that describes various types of β decay. It is based on the sum rule of the β-decay strength function, and it treats the transitions to all the final nuclear levels in a statistical manner. The gross theory has been successful in describing beta decay for the entire range of nuclear mass [1–7]. The results of the gross theory provide a guide to experiments on β decay, especially for newly measured nuclear data, such as very neutron-rich nuclei, and for purely theoretical nuclei that are extremely far from known nuclei. Due to its statistical treatment, the gross theory only describes macroscopic features, and it ignores microscopic properties, such as spin and the parity of relevant nuclei.

In this paper, we introduce a microscopic correction to the gross theory, and we discuss its effect on the half-lives of β decay. In particular, we focus on the parity change when interchanging a ground-state neutron and proton in a single-particle state. We estimate a single-particle state with a global single-particle potential, and we suppress the allowed transition of the β decay. The essential difference in this model is its treatment of the β-decay strength function, which corresponds to the squared transition matrix element.

2. Beta decay

The decay constant of the β-decay can be divided by the types of β-decay operators, Ω, and the decay constant is obtained as the sum of partial decay constants, λ_Ω. If we take in to account the allowed and first forbidden transitions, the total β-decay rate is expressed as

$$\lambda_\beta = \lambda_F + \lambda_{G-T} + \lambda_{\text{first-forbidden}} + \cdots \quad (1)$$

where the right-handed sides represents the decay rates of the Fermi transition, Gamow-Teller transition, and the first-forbidden transitions. The first two terms are the allowed transitions.

Under the usual approximation, each decay rate can be written with the nuclear matrix element, $|M_\Omega(E)|$, which can be calculated in the framework of the nuclear physics, and the integrated Fermi function, f, which represents a distortion of wave functions due to the Coulomb force. The decay constant is obtained as an integral of the product of the nuclear matrix element and the integrated Fermi function overall energy ranging from $-Q$ to 0 measured from the parent nucleus.

The nuclear matrix elements and the integrated Fermi function are required for theoretical calculation of the β-decay rate and the delayed neutron emission probability. Regarding the integrated Fermi function, the numerical values can be rather easily and precisely obtained. The calculation of the nuclear matrix element, is however, difficult because of a complexity of the nuclear many body problem with the complicated nuclear force. Historically, two types of approaches have been studied: One is the 'microscopic' approach currently known as the quasi-random phase approximation (QRPA). The other is the 'macroscopic approach' known as the gross theory (GT), discussed in the following.

3. Gross theory

The gross theory is constructed under a consideration that the sum of strengths of the transition from the initial state to the sum of the final states in the quantum mechanics. The ß decay also obeys such a sum (and an energy- weighted sum) rule.

In the gross theory, a one-particle strength function, D_Ω, is introduced, and the nuclear matrix element can be written as

$$|M(E)_\Omega|^2 = \int_{\epsilon_{\min}}^{\epsilon_{\max}} D_\Omega(E,\epsilon) W(E,\epsilon) \frac{dn_1}{d\epsilon} d\epsilon$$

where ε is the one particle energy of the decaying nucleons, and E is the transition energy measured from the parent state. The function $W(E, \varepsilon)$ is a weight function to take into account the Pauli exclusion principle, and $dn_1/d\varepsilon$ the one-particle energy distribution of the decaying nucleons. The actual explicit form is given in Ref. [2]. The one- particle function, $D(E, \varepsilon)$ is a smooth function and also satisfied the sum and energy-weighted sum rules as the same as for the case of $|M(E)|^2$. This is the essential idea of the gross theory.

4 . Improvement

Suppose single-particle level for neutron and proton of the ground-sate at the Fermi surface. If the parities of the neutron and the proton on the ground-state is different, the allowed transition is forbidden. If the parity of surface neutron and proton are different, the allowed transition of the ß decay from ground-state to the ground-state should not occur. Figure 1 shows examples for $^{131}\mathrm{In}_{82}$ and $^{132}\mathrm{In}_{83}$.

In the case of $^{131}\mathrm{In}_{82}$, single-neutron level of the ground-state is $2d_{3/2}$ with positive parity, while single-proton levels of the ground-state is $1g_{9/2}$ with positive parity: which is the same parity. In the case of $^{132}\mathrm{In}_{83}$, however, single-neutron level of the ground-state changes to $2f_{7/2}$ with negative parity, and resulting the allowed transition cannot occur. In the actual ß-decaying nucleus, the decay rate is the sum of all corresponding transitions of possible levels between neutrons and protons though the ground-to-ground state is generally dominant.

We introduce such a hindrance for the allowed transition into the gross theory. We estimate the spin-parity of the ground-state single-particle levels, and then treat the case of parity-mismatching between neutron and proton of the ground-state to be suppressed for the allowed transition. In the gross theory, nuclear levels are treated as the continuum with one discrete level at the Fermi surface with the Fermi gas model [2]. The nuclear matrix element is therefore composed as four parts:

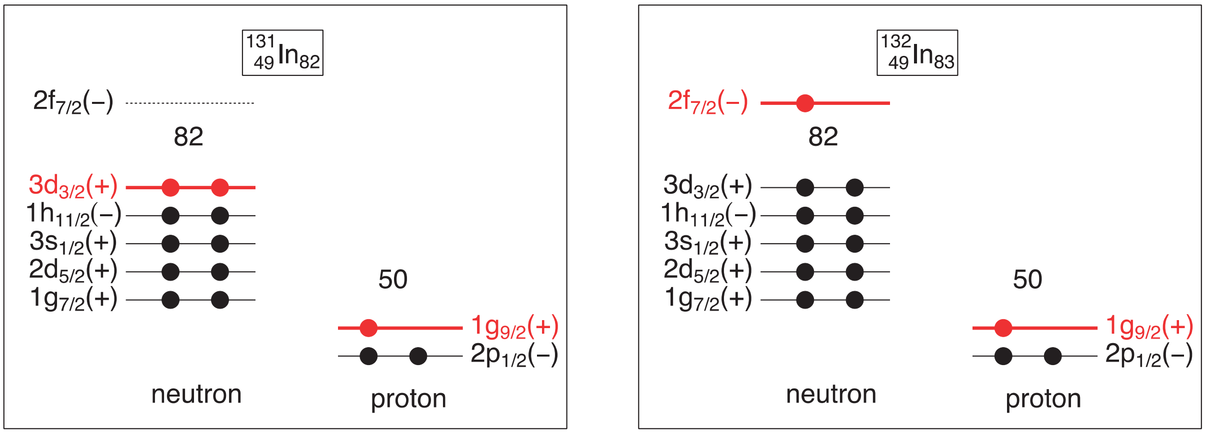

Figure 1: Schematic view of single-particle levels for $^{131}In_{82}$ and $^{132}In_{83}$. The red part red part represents the ground-state level.

$$|M_{\Omega}(E)|^2 = |M_{\Omega S\to l}(E)|^2 + |M_{\Omega S\to C}(E)|^2 + |M_{\Omega C\to C}(E)|^2 + |M_{\Omega C\to l}(E)|^2$$

Here, 'S' represents the discrete level of neutron (the surface level), 'l' represents the discrete level of proton (the lowest level), and 'C' represent the continuum of levels for the β^- case (See Ref. [2]). We sustain the intensity for the continuum-to-continuum component, $|M(E)_{\Omega C\to C}|^2$, and other three components are suppressed in the work. We emphasize that this treatment is applied for all nuclei: even-even, odd-A and odd-odd nuclei. Therefore considered spin and parity is different from experimental spin and parity of the ground-state for even-even (0^+ in total), odd-odd (integer) and odd-A with large deformations.

For the estimation of spin-parity, we adopt a modified Woods-Saxon potential applied for spherical nuclei in the entire region of nuclear chart [7]. The treatment is only done for small nuclear shapes, therefore we estimate nuclear deformation from global calculation of ground-state nuclear masses. We apply the KTUY mass formula [8] for the estimation. The threshold deformation parameter is determined so as to reproduce experimental trends, and we adopt the parameter α_2=0.05.

5. Results

5.1 Half-lives

Figure 2 shows β^--decay half lives for silver to tin isotopes in the neutron-rich mass region. The region above $N = 82$, half-lives from the previous gross theory [6] with the KTUY mass model [8] (thin line) systematically slopes down and underestimates. The improved gross theory (thick lines) enhances half-lives in these region and consequently gives gradually slopes and follows experimental trend. The result of FRDM + QRPA calculation [9] is also plotted and these results rather diverges from experimental trend and sometimes gives kink line.

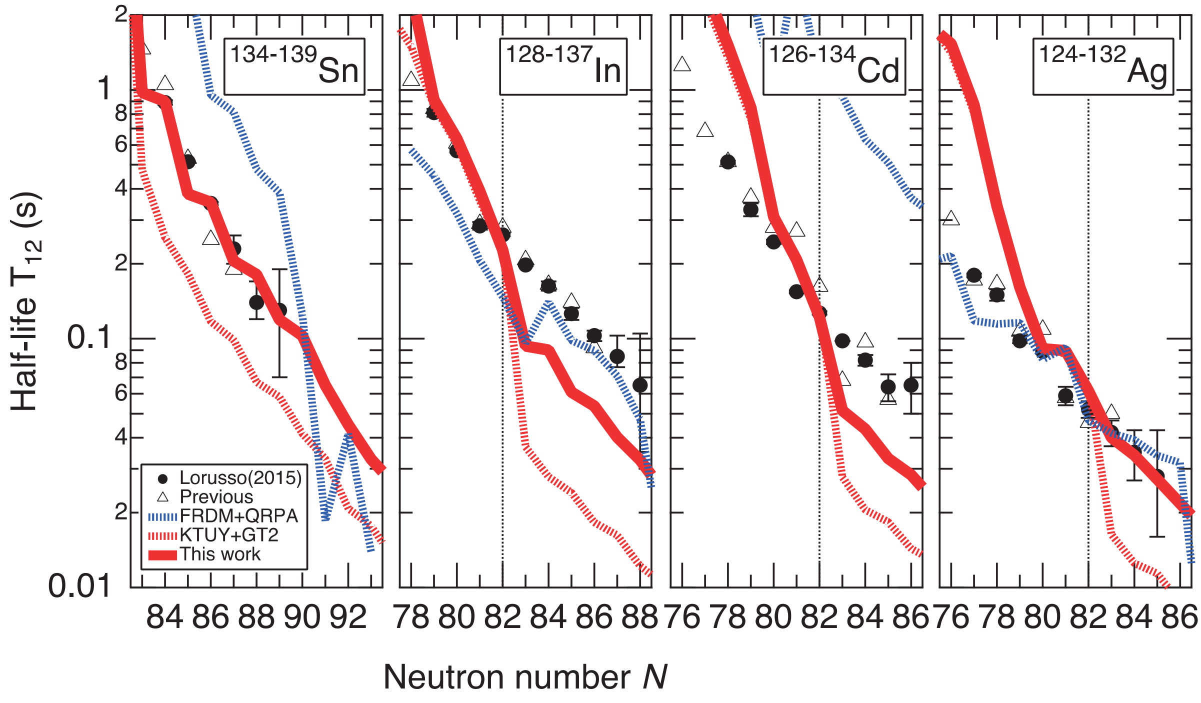

Figure 2: β⁻-decay half lives for silver to tin isotopes in the neutron-rich mass region. Thin red line: previous gross theory [6] with the KTUY mass model [8]. Thick red line: this work. Blue dashed line: FRDM+QRPA [9]. Filled circle: experiment till 2015. Open triangle: experiment in 2015 [10].

6. Summary

In conclusion, the gross theory of the β-decay is improved on the parity-changes in the allowed transition. In this treatment, the nuclear matrix elements are suppressed when the parity between single neutron and proton is different for the allowed transition. The assignment of parity is done by using the Woods-Saxon type single-particle potential and the KTUY nuclear mass model. The discrepancies from experimental half-lives, which appeared in the vicinity on the magic number of neutrons and protons, are improved. Despite the improvement, delayed neutron probabilities changes slightly to the lower.

In the treatment of this work, the sum rule of β-decay squared matrix element is not considered, and therefore these quantities may lower as expected for the corresponding nuclei. This point will deal with in the next work.

Acknowledgement

Present study is the results of “Comprehensive study of delayed-neutron yields for accurate evaluation of kinetics of high-burn up reactors" entrusted to Tokyo Institute of Technology by the Ministry of Education, Culture, Sports, Science and Technology of Japan (MEXT).

References

[1] K. Takahashi and M. Yamada, Prog. Theor. Phys. 41, 1470 (1969).

[2] S. Koyama, K. Takahashi and M. Yamada, Prog. Theor. Phys. 44, 663 (1970).

[3] K. Takahashi, M. Yamada and T. Kondoh, Atom. Dat. Nucl. Dat. Tab. 12, 101 (1973).

[4] T. Kondoh, T. Tachibana and M. Yamada., Prog. Theor. Phys. 74, 708 (1985).

[5] T.Tachibana,M.YamadaandY.Yoshida,Prog.Theor. Phys. 84, 641 (1990).

[6] T. Tachibana and M. Yamada, *Proc. Inc. Conf. on Exotic Nuclei and Atomic Masses, ENAM95*, (Editions Frontueres, Gif-sur-Yvette, 2015), p. 763.

[7] H. Koura and M. Yamada, Nucl. Phys. A 671, 96 (2000).

[8] H. Koura, T. Tachibana, M. Uno and M. Yamada, Prog. Theor. Phys. 113, 305 (2004).

[9] P.Möller, J.R.Nix and K.-L.Kratz, Atom. Dat. Nucl. Dat. Tab. 66, 131 (1997).

[10] G. Lurusso *et al.*, Phys. Rev. Lett. 114, 192501 (2015).

38 Nondestructive Determination of Water Content in Concrete by Foil Activation Method

-Feasibility study by Numerical Simulation-

Yasuhiro Nishiyama, Sachie Kusaka, Fuminobu Sato, Isao Murata,
Department of Sustainable Energy and Environmental Engineering, School of Engineering,
Osaka University, 2-1 Yamadaoka Suita, Osaka 565-0871, Japan

1. Introduction

Concrete is often used in a nuclear facility, because of its architectural usability and radiation shield performance. However, concrete loses its contained water as time passes. Then the strength of concrete may become weaker because of fissures grown by drying, and the change of the density and the amount of hydrogen in concrete will affect the radiation shield ability largely. Measurement technique of water content in concrete will thus be valuable for simulation of a radiation shield experiment using concrete, for predicting the radiation shield ability of the concrete wall in a nuclear facility, and so on.

At present, to measure the concrete content we have to carry some small concrete sample to the place where an analysis instrument is equipped. As well known, it is normally difficult for a nuclear facility. So in the present study, a new technique is proposed to nondestructively determine water content in concrete in a nuclear facility. The measurement principle is as follows. First, a gold foil is attached on a concrete, the content of which is not known. With an Am-Be neutron source, the foil is activated. In this case, the incident fast neutrons are thermalized by hydrogen in the concrete mainly. In other words, the amount of thermal neutrons depends on the amount of hydrogen in the concrete. So, by preparing the calibration curve of the amount of gold foil activation for the amount of water contained in the concrete, the absolute amount of water in the concrete can be estimated.

However, concrete normally has a different density and abundance of contained elements, and sometimes it contains carbon having a large moderating power next to hydrogen. These will affect the calibration curves.

In this study, numerical simulations were carried out to precisely investigate the above problems. The feasibility of this method was examined by practically making the calibration curves.

2. Simulation

Three numerical simulations were carried out. In Simulation 1, for some concretes the calibration curves were made to confirm the feasibility of the method. In Simulation 2 and 3, effects of contained carbon were precisely examined.

All the simulations were carried out with MCNP5 **[1]**.

2.1 Simulation 1

The system used in the simulation is shown in Fig.1. Concretes used in the simulation have different elemental components as shown in Table 1. For these concretes, the amount of water was artificially changed. A gold foil and Am-Be source are set as in Fig. 1 and the foil is irradiated for one day. The Am-Be neutron source emits fast neutrons. The fast neutrons are thermalized by hydrogen in concrete. So it would be possible to measure the amount of water in concrete. After calculating the amount of gold foil activity, the calibration curve is made.

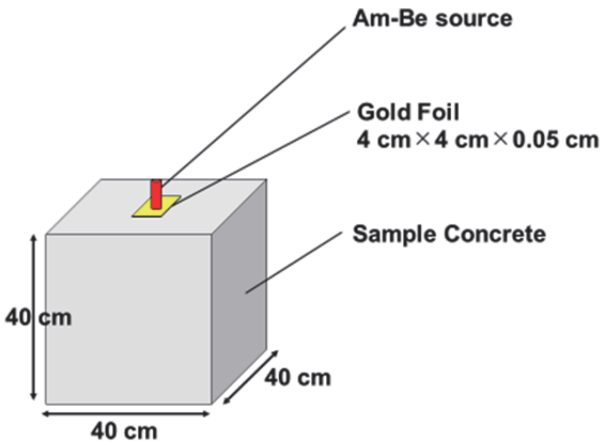

Figure 1 System used in Simulation 1

Table 1 Elemental composition of concretes [2]

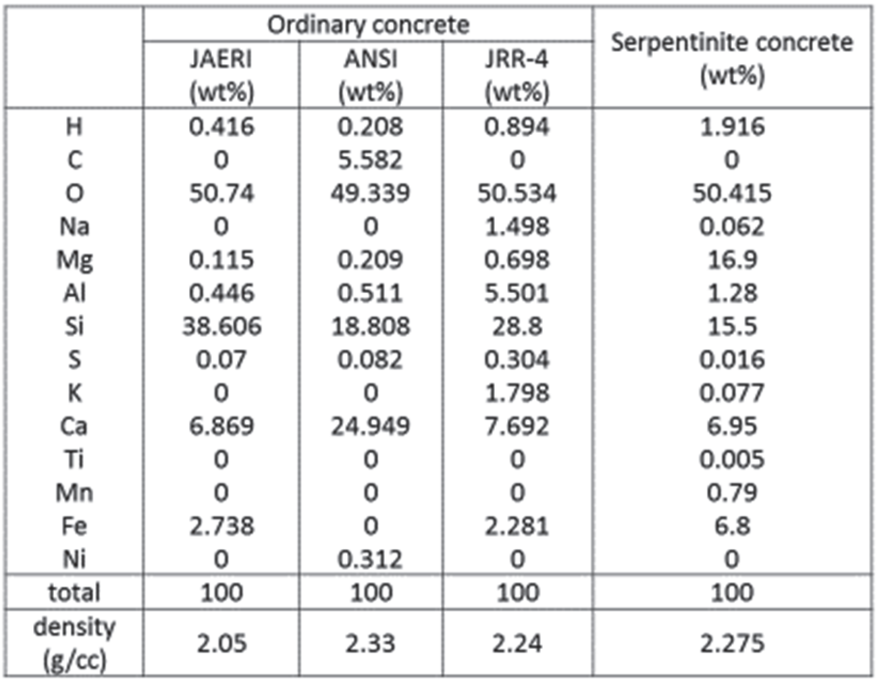

	Ordinary concrete			Serpentinite concrete (wt%)
	JAERI (wt%)	ANSI (wt%)	JRR-4 (wt%)	
H	0.416	0.208	0.894	1.916
C	0	5.582	0	0
O	50.74	49.339	50.534	50.415
Na	0	0	1.498	0.062
Mg	0.115	0.209	0.698	16.9
Al	0.446	0.511	5.501	1.28
Si	38.606	18.808	28.8	15.5
S	0.07	0.082	0.304	0.016
K	0	0	1.798	0.077
Ca	6.869	24.949	7.692	6.95
Ti	0	0	0	0.005
Mn	0	0	0	0.79
Fe	2.738	0	2.281	6.8
Ni	0	0.312	0	0
total	100	100	100	100
density (g/cc)	2.05	2.33	2.24	2.275

2.2 Simulation 2

Next, the effect of carbon in concrete was investigated. Carbon has a large moderating power next to hydrogen in concrete. Carbon may affect the calibration curve. Polyethylene moderator is very useful to expand the effect of carbon so that the effect can be discussed more easily as shown in the next chapter. The system used in the simulation is showed in Fig.2. A polyethylene sheet was placed between an Am-Be neutron source and gold foil. The calibration curve was made by changing the amount of water in concrete.

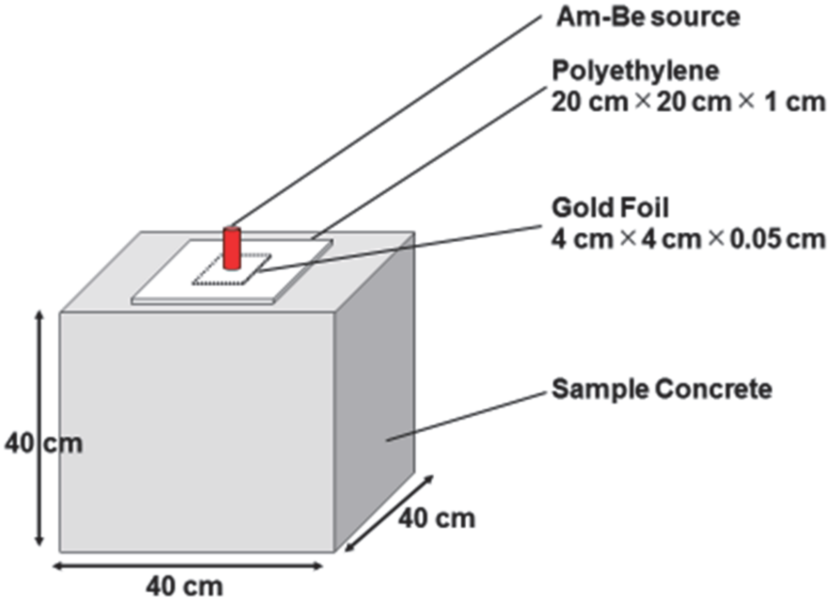

Figure 2 System used in simulation 2

2.3 Simulation 3

Finally, similar simulation was carried out with concretes in Table 1 added the same amount of carbon as ANSI. From these result, it can be found whether the effect of carbon is different depending on type of concrete. The system used in the simulation is shown in Fig.3.

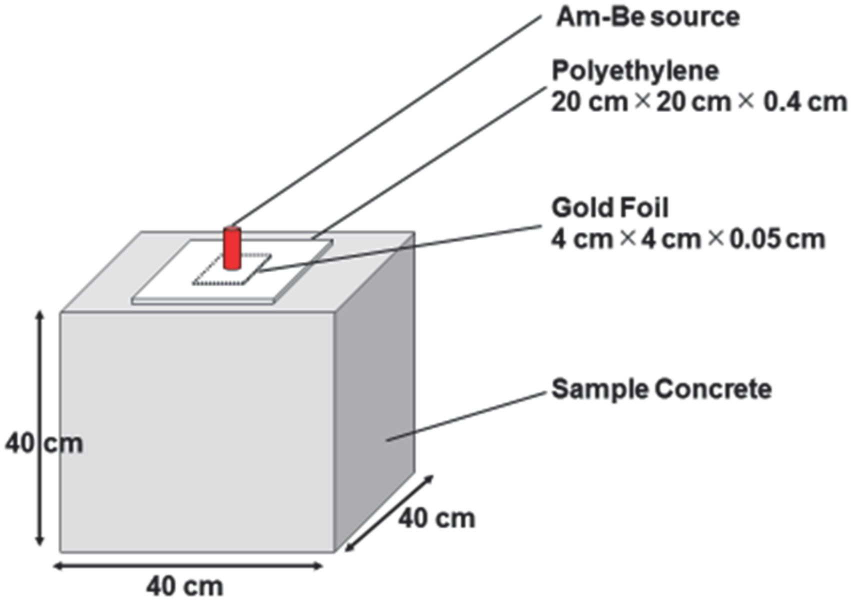

Figure 3 System used in simulation 3

3. Simulation result

Firstly, the result of Simulation 1 is shown in Fig. 4. The figure shows the calibration curves of concretes in Table.1. From the figure, it is found that the calibration curves of concretes containing no carbon are almost the same. This is because neutrons generated by (α,n) reaction in the Am-Be neutron source are a fast neutron so that heavier elements in concrete than hydrogen and carbon may not contribute to thermalize neutrons largely. And it is also an advantage that concrete contain no serious elements which absorb neutrons strongly. Besides, because the bulk of concrete is normally large enough, the difference in the calibration curve due to the density difference is not observed. The amount of the gold foil activity in the calibration curve of concrete having carbon is larger than the others.

Secondly, the result of Simulation 2 is shown in Fig. 5. The calibration curves in the lower side in the figure are the same as Fig.4. It can be found from this result that if using a polyethylene sheet the gold foil activities become much larger than without polyethylene. This is because neutrons are thermalized by hydrogens in the polyethylene sheet.

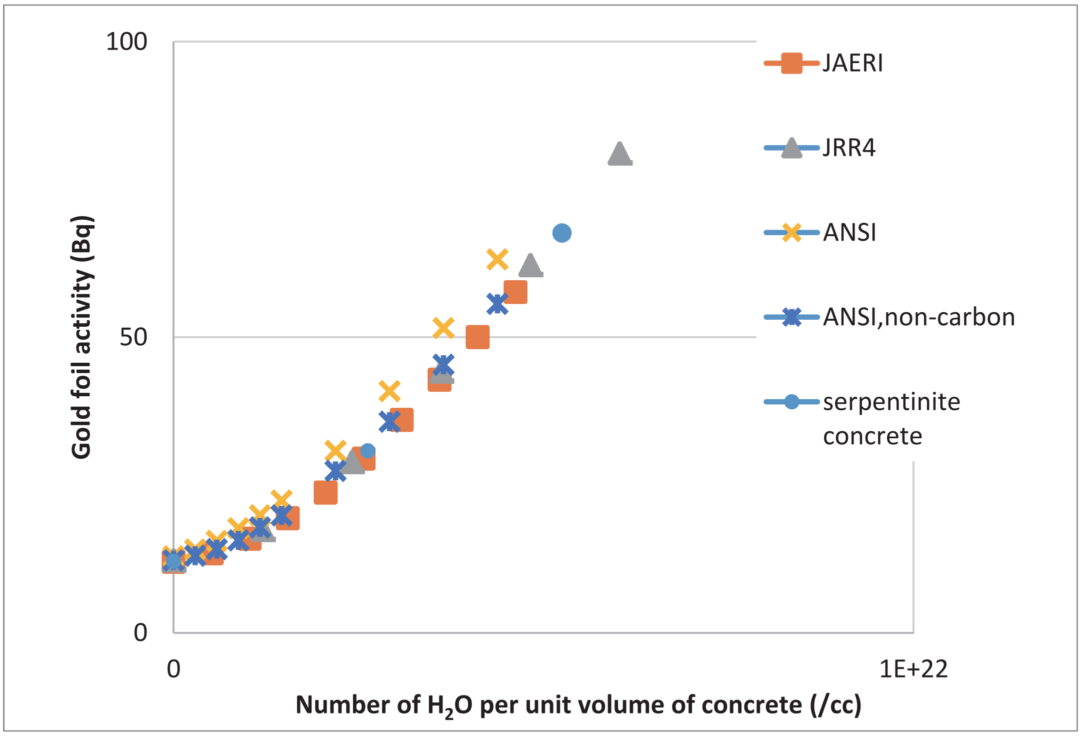

Figure 4 Calibration curves of several type of concretes

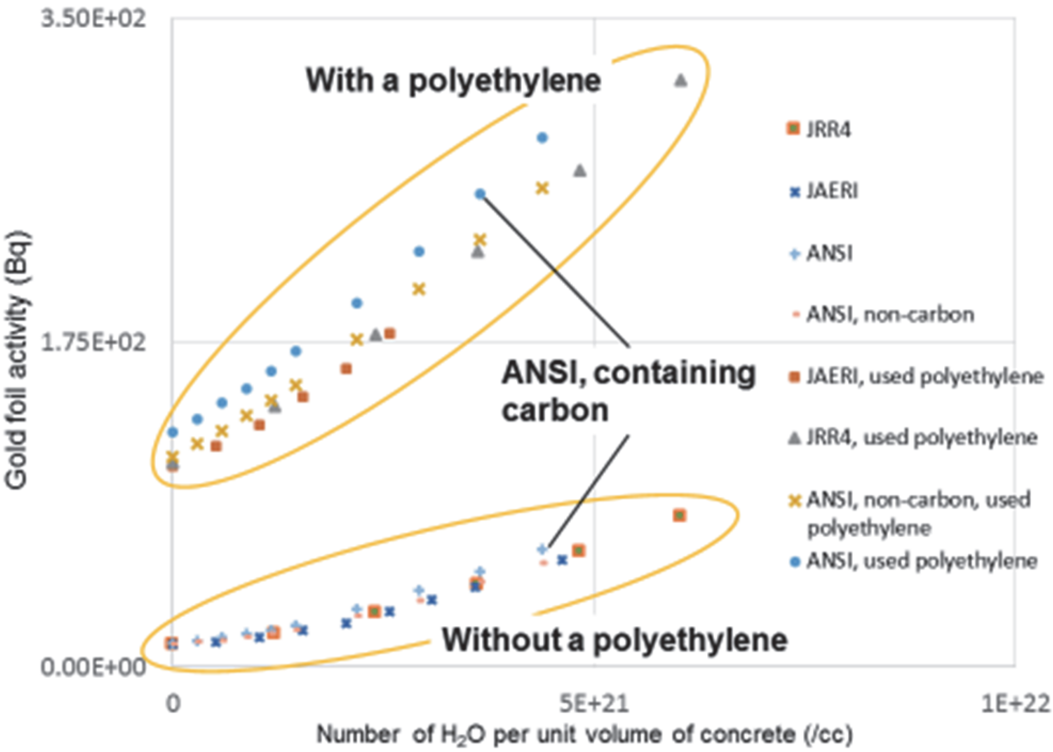

Figure 5 Comparison of calibration curves with and without a polyethylene

Finally, calibration curves of concretes, which are added the same amount of carbon as ANSI in Table 1, are shown in Fig. 6. From the result, it is found that the calibration curves containing the same amount of carbon are the same for each group with and without a polyethylene sheet. Therefore, it is found that the change of calibration curve depends on the amount of carbon in the concrete.

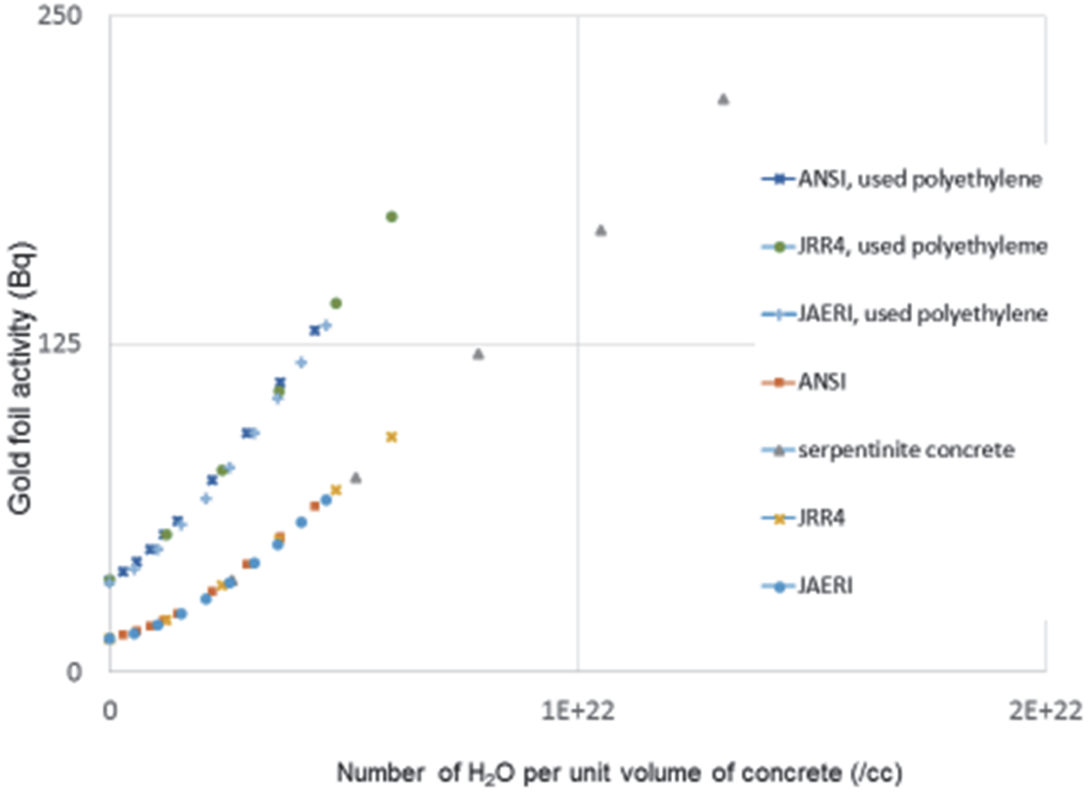

Figure 6 Calibration curves of concretes to which the same amount of carbon is added

4. Discussion

From the results described in Chap. 3, the calibration curves of concretes not containing carbon are the same regardless of its density and elemental composition except hydrogen. It means measurement of the amount of water in concrete not containing carbon is possible with this method.

Besides, it is found that the difference of the calibration curves with and without carbon depends on the amount of carbon in the concrete, and in addition using a polyethylene sheet the calibration curve difference can be expanded so as to discriminate the calibration curves of concretes with and without carbon. In other words, using polyethylene, the amount of water and carbon in concrete can be determined relatively. Concretely, the calibration curves of concretes containing various amounts of carbon are prepared beforehand with and without polyethylene. Thereafter, experiments are carried out with and without polyethylene for unknown concrete. If the concrete does not contain carbon, the two estimated amounts of water for the cases with and without polyethylene will be the same. On the other hand, in the case that concrete contains carbon, the two estimated values will not be the same. However, the difference of the two values depends on the amount of carbon in concrete. A procedure to estimate the amount of water and carbon will be examined in the next step.

5. Conclusion

In this paper, feasibility of nondestructive determination of water content in concrete using Am-Be neutron source was investigated. As the result, the difference of component elements and density in concrete cannot affect the result largely. And it is found that the calibration curve of concrete containing carbon is different from the one containing no carbon. From the two types of calibration curves with and without polyethylene, the amount of water and carbon can be estimated relatively.

For the future, we will establish the method of calculating absolute value of the amount of water and carbon, and carry out an experimental test of several sample concretes containing different amounts of water.

References

[1] Los Alamos National Laboratory, "A General Monte Carlo N-Particle Transport Code ver.5".

[2] D. Ito, "Monte Carlo Calculation Hand Book", AESJ, p.224 (2006).

This is a blank page.

39 Measurement of residual activities induced in copper by 148 MeV carbons

Hiroshi YASHIMA[1], Masayuki HAGIWARA[2], Toshiya SANAMI[2], Shunsuke YONAI[3]
[1]*Research Reactor Institute, Kyoto University,*
2-1010 Asashiro-nishi, Kumatori, Sennan, Osaka 590-0494, Japan
[2]*High Energy Accelerator Research Organization (KEK), 1-1 Oho, Tsukuba, Ibaraki 305-0801, Japan*
[3]*National Institutes for Quantum and Radiological Science and Technology,*
4-9-1, Anagawa, Inage-ku, Chiba-shi, Chiba, 263-8555, Japan
E-mail: yashima@rri.kyoto-u.ac.jp

The activation cross sections of residual nuclides in Cu for 148 MeV carbon irradiation were measured. Irradiation experiment was performed at cyclotron facility, National Institutes for Quantum and Radiological Science and Technology. Gamma-ray spectra from activation samples were measured with a HPGe detector. From the gamma-ray spectra, we obtained the variation of reaction cross sections of ^{73}Se, ^{71}As, ^{69}Ge, ^{68}Ge, ^{65}Zn and ^{61}Cu in Cu sample with Cu target thickness. These results generally agree with ACSELAM library within a factor of 2, but there are some difference between our results and ACSELAM library.

1. Introduction

The decommissioning of old accelerator facilities requires activation cross section data to estimate the residual activities induced in the accelerator components. But experimental data of activation cross section are very scarce for low energy (lower than several tens MeV) heavy ions which were required for decommissioning of accelerator facilities such as tandem accelerator and cyclotron. IRAC code was developed for estimation of residual activities. [1] The activation cross section database, ACSELAM library [1] was compiled with ALICE-F [2] calculation in IRAC code. But ACSELAM library is not validated enough for heavy ions, because experimental data of activation cross section are very scarce. We therefore irradiated 148 MeV (12.3 MeV/nucleon) carbon ions onto a Cu target to obtain experimental data of residual radioactivities for low energy heavy ions.

2. Measurement

Irradiation experiment was performed at cyclotron facility (NIRS-930), National Institutes for Quantum and Radiological

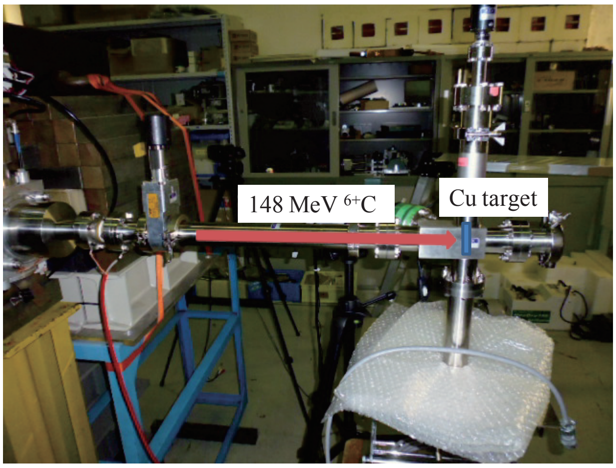

Fig.1 Schematic view of the experimental set-up

Science and Technology. A schematic view of the experimental set-up is shown in Fig. 1. The Cu target was composed of a stack of fifteen 15 mm x 15 mm x 0.01 mm natural Cu foils and total thickness of Cu target was thicker than the range of projectile carbon ions. The beam current on the Cu target was recorded with a current integrator, connected to a multichannel scaler to monitor the fluctuations of the carbon beam. The average carbon beam intensity was 5 pnA (30nA) and irradiation time was 1 hour. After irradiation, we measured the gamma-ray spectra from Cu samples with a HPGe detector.

3. Data analysis

The reaction rates of radionuclides produced in Cu samples were determined by a gamma-ray spectroscopy, where the peak efficiency of the HPGe detector and the accumulated beam dose were taken into account in the analysis. The peak efficiency of the HPGe detector was determined by using standard gamma-ray sources and Monte Carlo code EGS4 [3] and PHITS [4].

The reaction rate per projectile ion R (C ion^{-1}), corrected for beam current fluctuation is expressed by

$$R = \frac{\lambda C I_f}{\varepsilon \gamma I e^{-\lambda t_c}(1-e^{-\lambda t_m})(1-e^{-\lambda t_i})},$$

where λ is the decay constant (s^{-1}), C is the total counts of gamma-ray peak area, ε is the peak efficiency, γ is the branching ratio of gamma-rays, t_c is the cooling time (s), t_m is the measurement time (s), t_i is the irradiation time (s), I is the average beam intensity (C ion per second) and I_f is the correction factor for beam current flactuation.

The cross sections σ (mb) in the Cu samples by taking into account the projectile energy degradation in the target are obtained as follows:

$$\sigma = \frac{R}{N_d t},$$

$$E(d) = E_0 - \int_0^d \frac{dE}{dx} dx,$$

where N_d is the atomic density of Cu sample (atom/cm^3), t is thickness of Cu

Table 1 The physical properties of radioactive nuclides [6]

Product	Gamma-ray energy [keV]	Branching ratio [%]	Half life
^{73}Se	360.8	100	7.15h
^{71}As	175	82	65.28h
^{69}Ge	1107	36	39.05h
^{68}Ge	1077.4^{a}	3^{a}	270.8d
^{65}Zn	1115.5	50.6	244.26d
^{61}Cu	283	12.2	3.333h

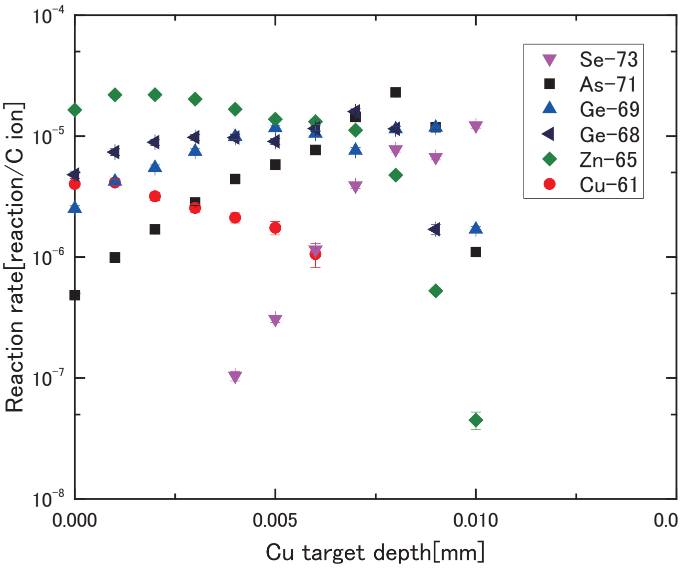

Fig.2 The spatial distribution of residual activities

sample (cm), $E(d)$ is the energy of projectile ions through target thickness d (MeV), E_0 is the incident energy of projectile ions (MeV), and dE/dx is the stopping power calculated by SRIM code [5] (MeV/cm).

The physical properties of the radioactive nuclides measured in this study are listed in Table 1. Because there is no gamma-ray emission from ^{68}Ge decay, radio activity of ^{68}Ge was estimated from that of ^{68}Ga after secular equilibrium establishment.

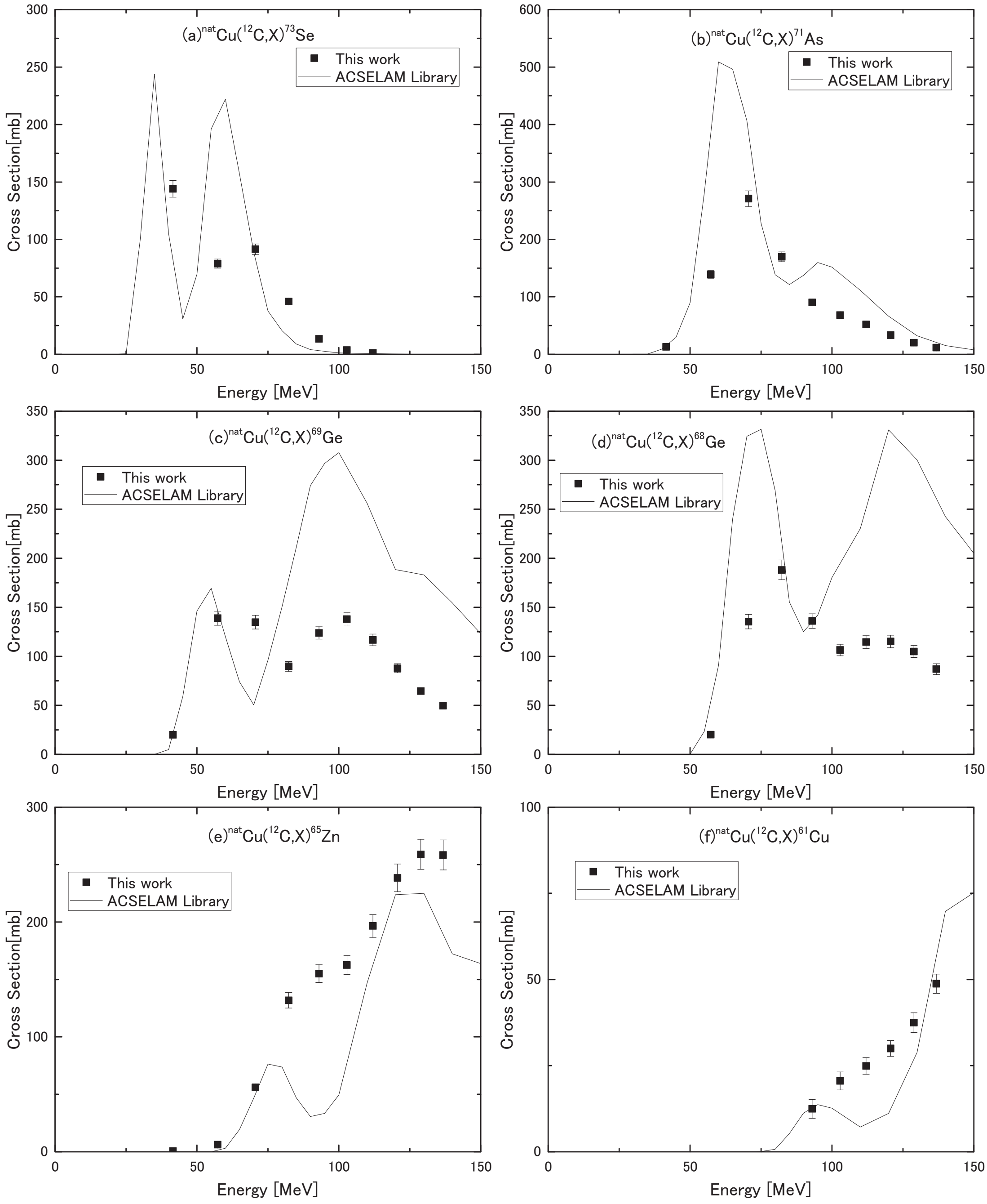

Fig.3 The excitation functions of nuclides produced in Cu for 148 MeV carbon irradiation experiment

4. Results

The spatial distribution of residual activities of ^{73}Se, ^{71}As, ^{69}Ge, ^{68}Ge, ^{65}Zn and ^{61}Cu in Cu target are shown in Fig 2. In Fig 2, residual activities increase with the Cu target thickness for heavier mass products than Cu. On the other hand, residual activities decrease with the Cu target thickness for lighter mass products than Cu.

The excitation functions of ^{nat}Cu(C, X)^{73}Se, ^{nat}Cu(C, X)^{71}As, ^{nat}Cu(C, X)^{69}Ge, ^{nat}Cu(C, X)^{68}Ge, ^{nat}Cu(C, X)^{65}Zn and ^{nat}Cu(C, X)^{61}Cu reactions are shown in Figs. 3(a)-3(f), respectively. The cross section data in ACSELAM library are also shown in Figs. 3(a)-3(f) to compare experimental results and calculated results. In Figs. 3(a)-3(f), our results generally agree with ACSELAM library within a factor of 2, but there are some difference between our results and ACSELAM library. Further systematic experimental studies are required for evaluation of activation cross sections for low energy (lower than several tens MeV) heavy ions.

5. Conclusion

The excitation functions of ^{73}Se, ^{71}As, ^{69}Ge, ^{68}Ge, ^{65}Zn and ^{61}Cu in Cu for 148 MeV carbon irradiation were measured. Our results generally agree with ACSELAM library within a factor of 2, but there are some difference between our results and ACSELAM library. The present results will be useful as benchmark data to evaluate nuclear data and investigate the accuracy of calculation codes.

Acknowledgment

The authors express their gratitude to the accelerator staff of NIRS-930 for generous support during this experiment.

References

[1] S. Tanaka et al., JAERI-Data/Code 97-019 (1997). (in Japanese).

[2] T. Fukahori, JAERI-M 92-039, pp.114-122 (1992).

[3] H. Hirayama, W. R. Nelson, D. W. O. Rogers: SLAC-265, Stanford Linear Accelerator Center, Stanford University (1985).

[4] T. Sato *et al.*, J. Nucl. Sci. Technol. 50:9, pp.913-923 (2013).

[5] James F. Ziegler, http://www.srim.org/.

[6] R.B. Firestone, V.S. Shirley (Eds.), John Wiley and Sons, New York (1996).

国際単位系（SI）

表１．SI 基本単位

基本量	SI 基本単位	
	名称	記号
長さ	メートル	m
質量	キログラム	kg
時間	秒	s
電流	アンペア	A
熱力学温度	ケルビン	K
物質量	モル	mol
光度	カンデラ	cd

表２．基本単位を用いて表されるSI組立単位の例

組立量	SI 組立単位	
	名称	記号
面積	平方メートル	m^2
体積	立方メートル	m^3
速さ，速度	メートル毎秒	m/s
加速度	メートル毎秒毎秒	m/s^2
波数	毎メートル	m^{-1}
密度，質量密度	キログラム毎立方メートル	kg/m^3
面積密度	キログラム毎平方メートル	kg/m^2
比体積	立方メートル毎キログラム	m^3/kg
電流密度	アンペア毎平方メートル	A/m^2
磁界の強さ	アンペア毎メートル	A/m
量濃度(a)，濃度	モル毎立方メートル	mol/m^3
質量濃度	キログラム毎立方メートル	kg/m^3
輝度	カンデラ毎平方メートル	cd/m^2
屈折率(b)	（数字の） 1	1
比透磁率(b)	（数字の） 1	1

(a) 量濃度（amount concentration）は臨床化学の分野では物質濃度（substance concentration）ともよばれる。

(b) これらは無次元量あるいは次元１をもつ量であるが、そのことを表す単位記号である数字の１は通常は表記しない。

表３．固有の名称と記号で表されるSI組立単位

組立量	SI 組立単位			
	名称	記号	他のSI単位による表し方	SI基本単位による表し方
平面角	ラジアン(b)	rad	1 (b)	m/m
立体角	ステラジアン(b)	sr(c)	1 (b)	m^2/m^2
周波数	ヘルツ(d)	Hz		s^{-1}
力	ニュートン	N		$m\ kg\ s^{-2}$
圧力，応力	パスカル	Pa	N/m^2	$m^{-1}\ kg\ s^{-2}$
エネルギー，仕事，熱量	ジュール	J	N m	$m^2\ kg\ s^{-2}$
仕事率，工率，放射束	ワット	W	J/s	$m^2\ kg\ s^{-3}$
電荷，電気量	クーロン	C		s A
電位差（電圧），起電力	ボルト	V	W/A	$m^2\ kg\ s^{-3}\ A^{-1}$
静電容量	ファラド	F	C/V	$m^{-2}\ kg^{-1}\ s^4\ A^2$
電気抵抗	オーム	Ω	V/A	$m^2\ kg\ s^{-3}\ A^{-2}$
コンダクタンス	ジーメンス	S	A/V	$m^{-2}\ kg^{-1}\ s^3\ A^2$
磁束	ウエーバ	Wb	Vs	$m^2\ kg\ s^{-2}\ A^{-1}$
磁束密度	テスラ	T	Wb/m^2	$kg\ s^{-2}\ A^{-1}$
インダクタンス	ヘンリー	H	Wb/A	$m^2\ kg\ s^{-2}\ A^{-2}$
セルシウス温度	セルシウス度(e)	℃		K
光束	ルーメン	lm	cd sr(c)	cd
照度	ルクス	lx	lm/m^2	$m^{-2}\ cd$
放射性核種の放射能(f)	ベクレル(d)	Bq		s^{-1}
吸収線量, 比エネルギー分与, カーマ	グレイ	Gy	J/kg	$m^2\ s^{-2}$
線量当量, 周辺線量当量, 方向性線量当量, 個人線量当量	シーベルト(g)	Sv	J/kg	$m^2\ s^{-2}$
酸素活性	カタール	kat		$s^{-1}\ mol$

(a)SI接頭語は固有の名称と記号を持つ組立単位と組み合わせても使用できる。しかし接頭語を付した単位はもはやコヒーレントではない。

(b)ラジアンとステラジアンは数字の１に対する単位の特別な名称で、量についての情報をつたえるために使われる。実際には、使用する時には記号rad及びsrが用いられるが、習慣として組立単位としての記号である数字の１は明示されない。

(c)測光学ではステラジアンという名称と記号srを単位の表し方の中に、そのまま維持している。

(d)ヘルツは周期現象についてのみ、ベクレルは放射性核種の統計的過程についてのみ使用される。

(e)セルシウス度はケルビンの特別な名称で、セルシウス温度を表すために使用される。セルシウス度とケルビンの単位の大きさは同一である。したがって、温度差や温度間隔を表す数値はどちらの単位で表しても同じである。

(f)放射性核種の放射能（activity referred to a radionuclide）は、しばしば誤った用語で”radioactivity”と記される。

(g)単位シーベルト（PV,2002,70,205）についてはCIPM勧告2（CI-2002）を参照。

表４．単位の中に固有の名称と記号を含むSI組立単位の例

組立量	SI 組立単位		
	名称	記号	SI 基本単位による表し方
粘度	パスカル秒	Pa s	$m^{-1}\ kg\ s^{-1}$
力のモーメント	ニュートンメートル	N m	$m^2\ kg\ s^{-2}$
表面張力	ニュートン毎メートル	N/m	$kg\ s^{-2}$
角速度	ラジアン毎秒	rad/s	$m\ m^{-1}\ s^{-1}=s^{-1}$
角加速度	ラジアン毎秒毎秒	rad/s^2	$m\ m^{-1}\ s^{-2}=s^{-2}$
熱流密度，放射照度	ワット毎平方メートル	W/m^2	$kg\ s^{-3}$
熱容量，エントロピー	ジュール毎ケルビン	J/K	$m^2\ kg\ s^{-2}\ K^{-1}$
比熱容量，比エントロピー	ジュール毎キログラム毎ケルビン	J/(kg K)	$m^2\ s^{-2}\ K^{-1}$
比エネルギー	ジュール毎キログラム	J/kg	$m^2\ s^{-2}$
熱伝導率	ワット毎メートル毎ケルビン	W/(m K)	$m\ kg\ s^{-3}\ K^{-1}$
体積エネルギー	ジュール毎立方メートル	J/m^3	$m^{-1}\ kg\ s^{-2}$
電界の強さ	ボルト毎メートル	V/m	$m\ kg\ s^{-3}\ A^{-1}$
電荷密度	クーロン毎立方メートル	C/m^3	$m^{-3}\ s\ A$
表面電荷	クーロン毎平方メートル	C/m^2	$m^{-2}\ s\ A$
電束密度，電気変位	クーロン毎平方メートル	C/m^2	$m^{-2}\ s\ A$
誘電率	ファラド毎メートル	F/m	$m^{-3}\ kg^{-1}\ s^4\ A^2$
透磁率	ヘンリー毎メートル	H/m	$m\ kg\ s^{-2}\ A^{-2}$
モルエネルギー	ジュール毎モル	J/mol	$m^2\ kg\ s^{-2}\ mol^{-1}$
モルエントロピー, モル熱容量	ジュール毎モル毎ケルビン	J/(mol K)	$m^2\ kg\ s^{-2}\ K^{-1}\ mol^{-1}$
照射線量（Ｘ線及びγ線）	クーロン毎キログラム	C/kg	$kg^{-1}\ s\ A$
吸収線量率	グレイ毎秒	Gy/s	$m^2\ s^{-3}$
放射強度	ワット毎ステラジアン	W/sr	$m^4\ m^{-2}\ kg\ s^{-3}=m^2\ kg\ s^{-3}$
放射輝度	ワット毎平方メートル毎ステラジアン	$W/(m^2\ sr)$	$m^2\ m^{-2}\ kg\ s^{-3}=kg\ s^{-3}$
酵素活性濃度	カタール毎立方メートル	kat/m^3	$m^{-3}\ s^{-1}\ mol$

表５．SI 接頭語

乗数	名称	記号	乗数	名称	記号
10^{24}	ヨタ	Y	10^{-1}	デシ	d
10^{21}	ゼタ	Z	10^{-2}	センチ	c
10^{18}	エクサ	E	10^{-3}	ミリ	m
10^{15}	ペタ	P	10^{-6}	マイクロ	µ
10^{12}	テラ	T	10^{-9}	ナノ	n
10^9	ギガ	G	10^{-12}	ピコ	p
10^6	メガ	M	10^{-15}	フェムト	f
10^3	キロ	k	10^{-18}	アト	a
10^2	ヘクト	h	10^{-21}	ゼプト	z
10^1	デカ	da	10^{-24}	ヨクト	y

表６．SIに属さないが、SIと併用される単位

名称	記号	SI 単位による値
分	min	1 min=60 s
時	h	1 h =60 min=3600 s
日	d	1 d=24 h=86 400 s
度	°	1°=(π/180) rad
分	’	1’=(1/60)°=(π/10 800) rad
秒	”	1”=(1/60)’=(π/648 000) rad
ヘクタール	ha	$1\ ha=1\ hm^2=10^4m^2$
リットル	L，l	$1\ L=1\ l=1\ dm^3=10^3cm^3=10^{-3}m^3$
トン	t	$1\ t=10^3\ kg$

表７．SIに属さないが、SIと併用される単位で、SI単位で表される数値が実験的に得られるもの

名称	記号	SI 単位で表される数値
電子ボルト	eV	$1\ eV=1.602\ 176\ 53(14)\times10^{-19}J$
ダルトン	Da	$1\ Da=1.660\ 538\ 86(28)\times10^{-27}kg$
統一原子質量単位	u	1 u=1 Da
天文単位	ua	$1\ ua=1.495\ 978\ 706\ 91(6)\times10^{11}m$

表８．SIに属さないが、SIと併用されるその他の単位

名称	記号	SI 単位で表される数値
バール	bar	$1\ bar=0.1MPa=100\ kPa=10^5Pa$
水銀柱ミリメートル	mmHg	1 mmHg≈133.322Pa
オングストローム	Å	$1\ Å=0.1nm=100pm=10^{-10}m$
海里	M	1 M=1852m
バーン	b	$1\ b=100fm^2=(10^{-12}cm)^2=10^{-28}m^2$
ノット	kn	1 kn=(1852/3600)m/s
ネーパ	Np	SI単位との数値的な関係は、対数量の定義に依存。
ベル	B	
デシベル	dB	

表９．固有の名称をもつCGS組立単位

名称	記号	SI 単位で表される数値
エルグ	erg	$1\ erg=10^{-7}\ J$
ダイン	dyn	$1\ dyn=10^{-5}N$
ポアズ	P	$1\ P=1\ dyn\ s\ cm^{-2}=0.1Pa\ s$
ストークス	St	$1\ St=1cm^2\ s^{-1}=10^{-4}m^2\ s^{-1}$
スチルブ	sb	$1\ sb=1cd\ cm^{-2}=10^4cd\ m^{-2}$
フォト	ph	$1\ ph=1cd\ sr\ cm^{-2}=10^4lx$
ガル	Gal	$1\ Gal=1cm\ s^{-2}=10^{-2}ms^{-2}$
マクスウエル	Mx	$1\ Mx=1G\ cm^2=10^{-8}Wb$
ガウス	G	$1\ G=1Mx\ cm^{-2}=10^{-4}T$
エルステッド(a)	Oe	$1\ Oe \triangleq (10^3/4\pi)A\ m^{-1}$

(a) ３元系のCGS単位系とSIでは直接比較できないため、等号「 ≙ 」は対応関係を示すものである。

表10．SIに属さないその他の単位の例

名称	記号	SI 単位で表される数値
キュリー	Ci	$1\ Ci=3.7\times10^{10}Bq$
レントゲン	R	$1\ R=2.58\times10^{-4}C/kg$
ラド	rad	$1\ rad=1cGy=10^{-2}Gy$
レム	rem	$1\ rem=1\ cSv=10^{-2}Sv$
ガンマ	γ	$1\ \gamma=1\ nT=10^{-9}T$
フェルミ		1フェルミ=1 fm=10^{-15}m
メートル系カラット		1メートル系カラット= 0.2 g = 2×10^{-4}kg
トール	Torr	1 Torr = (101 325/760) Pa
標準大気圧	atm	1 atm = 101 325 Pa
カロリー	cal	1 cal=4.1858J（「15℃」カロリー），4.1868J（「IT」カロリー），4.184J（「熱化学」カロリー）
ミクロン	µ	$1\ \mu=1\mu m=10^{-6}m$

（第8版，2006年）